INL/EXT-08-14767
Rev. 2

# Evaluation of the Start-Up Core Physics Tests at Japan's High Temperature Engineering Test Reactor (Fully-Loaded Core)

John D. Bess
Nozomu Fujimoto
Barbara H. Dolphin
Luka Snoj
Atsushi Zukeran

March 2010


The INL is a U.S. Department of Energy National Laboratory
operated by Battelle Energy Alliance

INL/EXT-08-14767
Rev. 2

# Evaluation of the Start-Up Core Physics Tests at Japan's High Temperature Engineering Test Reactor (Fully-Loaded Core)

John D. Bess
Nozomu Fujimoto[1]
Barbara H. Dolphin
Luka Snoj[2]
Atsushi Zukeran[3]

[1]Japan Atomic Energy Agency
[2]Jozef Stefan Institute
[3]Senior Reactor Physics Consultant

March 2010

Idaho National Laboratory
Idaho Falls, Idaho 83415

http://www.inl.gov

Prepared for the
U.S. Department of Energy
Office of Nuclear Energy
Under DOE Idaho Operations Office
Contract DE-AC07-05ID14517

NEA/NSC/DOC(2006)1

Gas Cooled (Thermal) Reactor - GCR

HTTR-GCR-RESR-001
CRIT-SUB-REAC-***COEF-KIN***-RRATE

# EVALUATION OF THE START-UP CORE PHYSICS TESTS AT JAPAN'S HIGH TEMPERATURE ENGINEERING TEST REACTOR
## (FULLY-LOADED CORE)

**Evaluators**

**John D. Bess**
**Idaho National Laboratory**

**Nozomu Fujimoto**
**Japan Atomic Energy Agency**

**Internal Reviewers**

**Barbara H. Dolphin**
**Idaho National Laboratory**

**Independent Reviewers**

**Luka Snoj**
**Jozef Stefan Institute**

**Atsushi Zukeran**
**Senior Reactor Physics Consultant**

Gas Cooled (Thermal) Reactor - GCR

HTTR-GCR-RESR-001
CRIT-SUB-REAC-*COEF-KIN*-RRATE

**Status of Compilation / Evaluation / Peer Review**

| Section 1 | Compiled | Independent Review | Working Group Review | Approved |
|---|---|---|---|---|
| 1.0 DETAILED DESCRIPTION | YES | YES | YES | YES |
| 1.1 Description of the Critical and / or Subcritical Configuration | YES | YES | YES | YES |
| 1.2 Description of Buckling and Extrapolation Length Measurements | NA | NA | NA | NA |
| 1.3 Description of Spectral Characteristics Measurements | NA | NA | NA | NA |
| 1.4 Description of Reactivity Effects Measurements | YES | YES | YES | YES |
| 1.5 Description of Reactivity Coefficient Measurements | YES | YES | YES | YES |
| 1.6 Description of Kinetics Measurements | YES | YES | YES | YES |
| 1.7 Description of Reaction-Rate Distribution Measurements | YES | YES | YES | YES |
| 1.8 Description of Power Distribution Measurements | NA | NA | NA | NA |
| 1.9 Description of Isotopic Measurements | NA | NA | NA | NA |
| 1.10 Description of Other Miscellaneous Types of Measurements | NA | NA | NA | NA |
| **Section 2** | **Evaluated** | **Independent Review** | **Working Group Review** | **Approved** |
| 2.0 EVALUATION OF EXPERIMENTAL DATA | YES | YES | YES | YES |
| 2.1 Evaluation of Critical and / or Subcritical Configuration Data | YES | YES | YES | YES |
| 2.2 Evaluation of Buckling and Extrapolation Length Data | NA | NA | NA | NA |
| 2.3 Evaluation of Spectral Characteristics Data | NA | NA | NA | NA |
| 2.4 Evaluation of Reactivity Effects Data | YES | YES | YES | YES |
| 2.5 Evaluation of Reactivity Coefficient Data | NA | NA | NA | NA |
| 2.6 Evaluation of Kinetics Measurements Data | NA | NA | NA | NA |
| 2.7 Evaluation of Reaction Rate Distributions | YES | YES | YES | YES |
| 2.8 Evaluation of Power Distribution Data | NA | NA | NA | NA |
| 2.9 Evaluation of Isotopic Measurements | NA | NA | NA | NA |
| 2.10 Evaluation of Other Miscellaneous Types of Measurements | NA | NA | NA | NA |

| Section 3 | Compiled | Independent Review | Working Group Review | Approved |
|---|---|---|---|---|
| 3.0 BENCHMARK SPECIFICATIONS | YES | YES | YES | YES |
| 3.1 Benchmark-Model Specifications for Critical and / or Subcritical Measurements | YES | YES | YES | YES |
| 3.2 Benchmark-Model Specifications for Buckling and Extrapolation Length Measurements | NA | NA | NA | NA |
| 3.3 Benchmark-Model Specifications for Spectral Characteristics Measurements | NA | NA | NA | NA |
| 3.4 Benchmark-Model Specifications for Reactivity Effects Measurements | YES | YES | YES | YES |
| 3.5 Benchmark-Model Specifications for Reactivity Coefficient Measurements | NA | NA | NA | NA |
| 3.6 Benchmark-Model Specifications for Kinetics Measurements | NA | NA | NA | NA |
| 3.7 Benchmark-Model Specifications for Reaction-Rate Distribution Measurements | YES | YES | YES | YES |
| 3.8 Benchmark-Model Specifications for Power Distribution Measurements | NA | NA | NA | NA |
| 3.9 Benchmark-Model Specifications for Isotopic Measurements | NA | NA | NA | NA |
| 3.10 Benchmark-Model Specifications of Other Miscellaneous Types of Measurements | NA | NA | NA | NA |
| **Section 4** | **Compiled** | **Independent Review** | **Working Group Review** | **Approved** |
| 4.0 RESULTS OF SAMPLE CALCULATIONS | YES | YES | YES | YES |
| 4.1 Results of Calculations of the Critical or Subcritical Configurations | YES | YES | YES | YES |
| 4.2 Results of Buckling and Extrapolation Length Calculations | NA | NA | NA | NA |
| 4.3 Results of Spectral Characteristics Calculations | NA | NA | NA | NA |
| 4.4 Results of Reactivity Effect Calculations | YES | YES | YES | YES |
| 4.5 Results of Reactivity Coefficient Calculations | NA | NA | NA | NA |
| 4.6 Results of Kinetics Parameter Calculations | NA | NA | NA | NA |
| 4.7 Results of Reaction-Rate Distribution Calculations | YES | YES | YES | YES |
| 4.8 Results of Power Distribution Calculations | NA | NA | NA | NA |
| 4.9 Results of Isotopic Calculations | NA | NA | NA | NA |
| 4.10 Results of Calculations of Other Miscellaneous Types of Measurements | NA | NA | NA | NA |
| **Section 5** | **Compiled** | **Independent Review** | **Working Group Review** | **Approved** |
| 5.0 REFERENCES | YES | YES | YES | YES |
| Appendix A: Computer Codes, Cross Sections, and Typical Input Listings | YES | YES | YES | YES |

Gas Cooled (Thermal) Reactor - GCR

HTTR-GCR-RESR-001
CRIT-SUB-REAC-*COEF-KIN*-RRATE

# EVALUATION OF THE START-UP CORE PHYSICS TESTS AT JAPAN'S HIGH TEMPERATURE ENGINEERING TEST REACTOR (FULLY-LOADED CORE)

**IDENTIFICATION NUMBER:** HTTR-GCR-RESR-001
CRIT-SUB-REAC-***COEF*-*KIN***-RRATE

**KEY WORDS:** axial reaction rate, critical configuration, excess reactivity, graphite-moderated, graphite-reflected, helium coolant, HTTR, low enriched uranium (LEU), pin-in-block fuel, prismatic fuel, shutdown margin, subcritical configuration, thermal reactor, TRISO, uranium oxide fuel

## SUMMARY INFORMATION

## 1.0 DETAILED DESCRIPTION

The High Temperature Engineering Test Reactor (HTTR) of the Japan Atomic Energy Agency (JAEA) is a 30 MWth, graphite-moderated, helium-cooled reactor that was constructed with the objectives to establish and upgrade the technological basis for advanced high-temperature gas-cooled reactors (HTGRs) as well as to conduct various irradiation tests for innovative high-temperature research. The core size of the HTTR represents about one-half of that of future HTGRs, and the high excess reactivity of the HTTR, necessary for compensation of temperature, xenon, and burnup effects during power operations, is similar to that of future HTGRs. During the start-up core physics tests of the HTTR, various annular cores were formed to provide experimental data for verification of design codes for future HTGRs (Ref. 1, p. 310).

The Japanese government approved construction of the HTTR in the 1989 fiscal year budget; construction began at the Oarai Research and Development Center in March 1991 and was completed May 1996. Fuel loading began July 1, 1998, from the core periphery. The first criticality was attained with an annular core on November 10, 1998 at 14:18, followed by a series of start-up core physics tests (Figure 1.1) until a fully-loaded core was developed on December 16, 1998. Criticality tests were carried out into January 1999. The first full power operation with an average core outlet temperature of 850ºC was completed on December 7, 2001, and operational licensing of the HTTR was approved on March 6, 2002. The HTTR attained high temperature operation at 950 ºC in April 19, 2004. After a series of safety demonstration tests, it will be used as the heat source in a hydrogen production system by 2015. A short history of the HTTR project is shown in Figure 1.2, and a plan for the future of the HTTR project is shown in Figure 1.3 (Ref. 3, pp. 12-14).

A very high temperature reactor critical assembly (VHTRC) was constructed[a] to provide reactor physics experiments to study the detailed neutronic characteristics of the HTTR core design (Ref. 15, pp. 21-23). Seven different core designs were employed (Ref. 3, p. 19). Further summary of the validation efforts using the VHTRC is discussed elsewhere.[bcd]

---

[a] H. Yasuda, et al., "Construction of VHTRC (Very High Temperature Reactor Critical Assembly," JAERI-1305, Japan Atomic Energy Research Institute, Tokaimura, 1986.

[b] I. Murata, K. Yamashitta, S. Maruyama, R. Shindo, N. Fujimoto, Y. Sudo, and T. Nakata, "Evaluation of Local Power Distribution with Fine-Mesh Core Model for High Temperature Engineering Test Reactor (HTTR),"*J. Nucl. Sci. Tech.*, **31**(1): 62-72 (January 1994).

[c] N. Fujimoto, N. Nojiri, and K. Yamashita, "Validation of the Nuclear Design Code System for the HTTR using the Criticality Assembly VHTRC," *Nucl. Eng. Des.*, **233**: 155-162 (2004).

[d] F. Akino, M. Takeuchi, T. Ono, and Y. Kaneko, "Experimental Verification and Analysis of Neutron Streaming Effect through Void Holes for Control Rod Insertion in HTTR," *J. Nucl. Sci. Tech.*, **34**(2): 185-192 (February 1997).

Hot zero-power critical,[a] Rise-to-power,[b] irradiation tests,[c] and safety demonstration testing[d,e] have also been performed with the HTTR, representing additional means for computational validation efforts. Power tests were performed in steps from 0 to 30 MW, with various tests performed at each step to confirm core characteristics, thermal-hydraulic properties, and radiation shielding (Ref. 13, p. 284). The high-temperature test operation at 950 ºC represented the fifth and final phase of the rise-to-power tests.[f] The safety tests demonstrated inherent safety features of the HTTR such as slow temperature response during abnormal events due to the large heat capacity of the core and the negative reactivity feedback.[g] A more detailed summary of the rise-to-power with safety tests is shown in Table 1.1.

The experimental benchmark performed and currently evaluated in this report pertains to the data available for the fully-loaded core critical from the initial six isothermal, annular and fully-loaded, core critical measurements performed at the HTTR. Additional experiments performed during the start-up physics tests include reactivity worth (excess reactivity, shutdown margin, and control rods), isothermal temperature coefficient, and reaction rate measurements. A subcritical evaluation of the fully-loaded core was also recorded. Evaluation of the start-up core physics tests specific to the annular core loadings is compiled elsewhere (HTTR-GCR-RESR-002).

---

[a] J. C. Kuijper, X. Raepsaet, J. B. M. de Haas, W. von Lensa, U. Ohlig, H-J. Ruetten, H. Brockmann, F. Damian, F. Dolci, W. Bernnat, J. Oppe, J. L. Kloosterman, N. Cerullo, G. Lomonaco, A. Negrini, J. Magill, and R. Seiler, "HTGR Reactor Physics and Fuel Cycle Studies," *Nucl. Eng. Des.*, **236**: 615-634 (2006).

[b] S. Nakagawa, Y. Tachibana, K. Takamatsu, S. Ueta, and S. Hanawa, "Performance Test of HTTR," *Nucl. Eng. Des.*, **233**: 291-300 (2004).

[c] T. Shibata, T. Kikuchi, S. Miyamoto, and K. Ogura, "Assessment of Irradiation Temperature Stability of the First Irradiation Test Rig in the HTTR," *Nucl. Eng. Des.*, **223**: 133-143 (2003).

[d] Y. Tachibana, S. Nakagawa, T. Takeda, A. Saikusa, T. Furusawa, K. Takamatsu, K. Sawa, and T. Iyoku, "Plan for the First Phase of Safety Demonstration Tests of the High Temperature Engineering Test Reactor (HTTR)," *Nucl. Eng. Des.*, **224**: 179-197 (2003).

[e] S. Nakagawa, K. Takamatsu, Y. Tachibana, N. Sakaba, and T. Iyoku, "Safety Demonstration Tests using High Temperature Engineering Test Reactor," *Nucl. Eng. Des.*, **233**: 301-308 (2004).

[f] S. Fujikawa, H. Hayashi, T. Nakazawa, K. Kawasaki, T. Iyoku, S. Nakagawa, and N. Sakaba, "Achievement of Reactor-Outlet Coolant Temperature of 950 ºC in HTTR," *J. Nucl. Sci. Tech.*, **41**(12): 1245-1254 (December 2004).

[g] S. Nakagawa, D. Tochio, K. Takamatsu, M. Goro, and T. Takeda, "Improvement of Analysis Technology for High Temperature Gas-Cooled Reactor by using Data Obtained in High Temperature Engineering Test Reactor," *J. Power Energy Syst.*, **2**(1): 83-91 (2008).

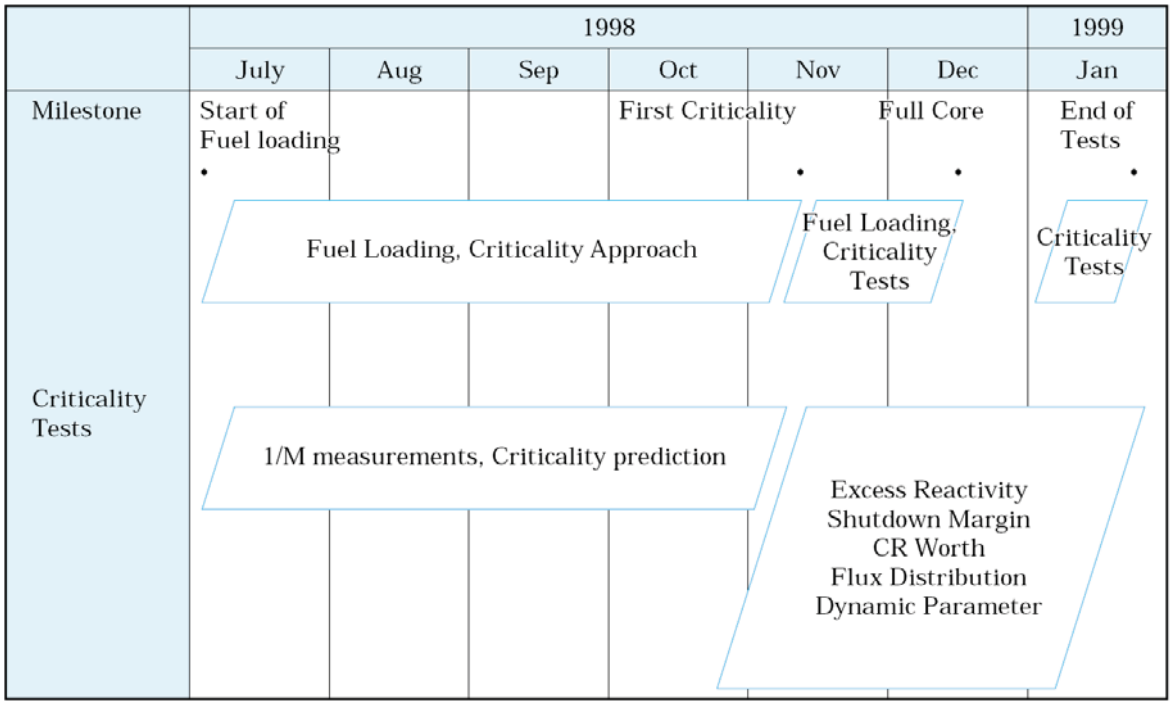


Figure 1.1. Progress of Start-Up Core Physics Tests.[a]

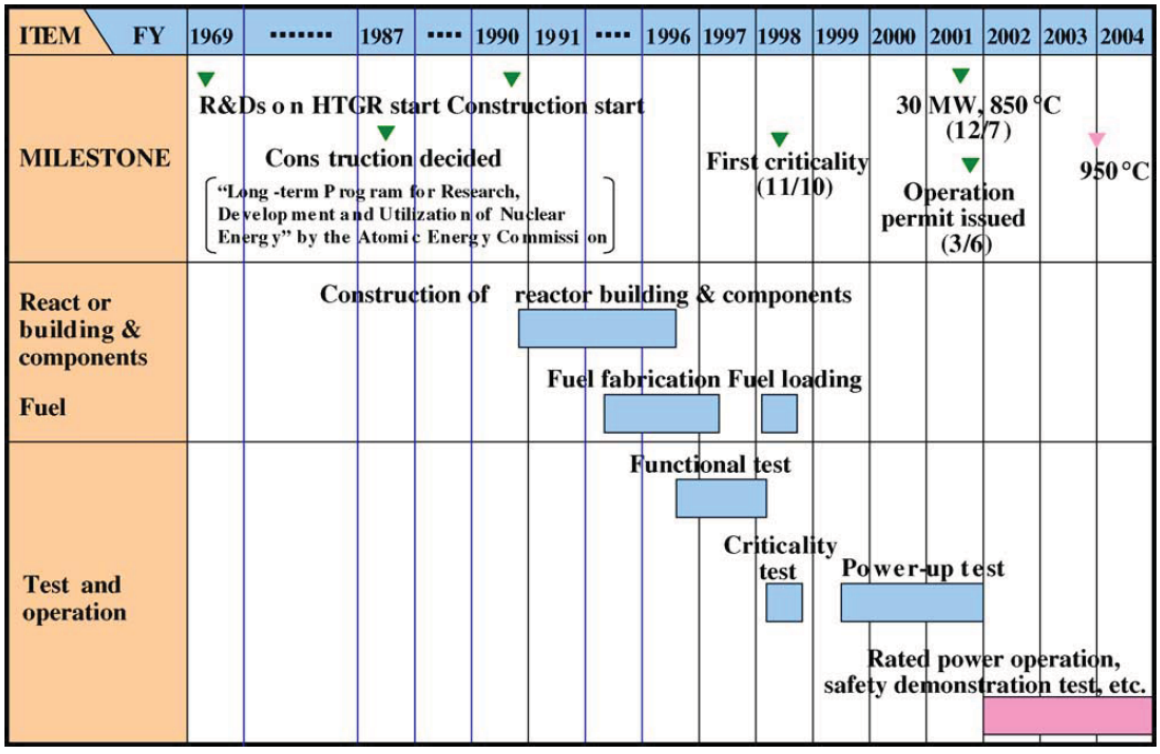


Figure 1.2. History of the HTTR Project (Ref. 3, p. 12).

[a] "Present Status of HTGR Research and Development," Japan Atomic Energy Research Institute, Tokaimura, March 2004.

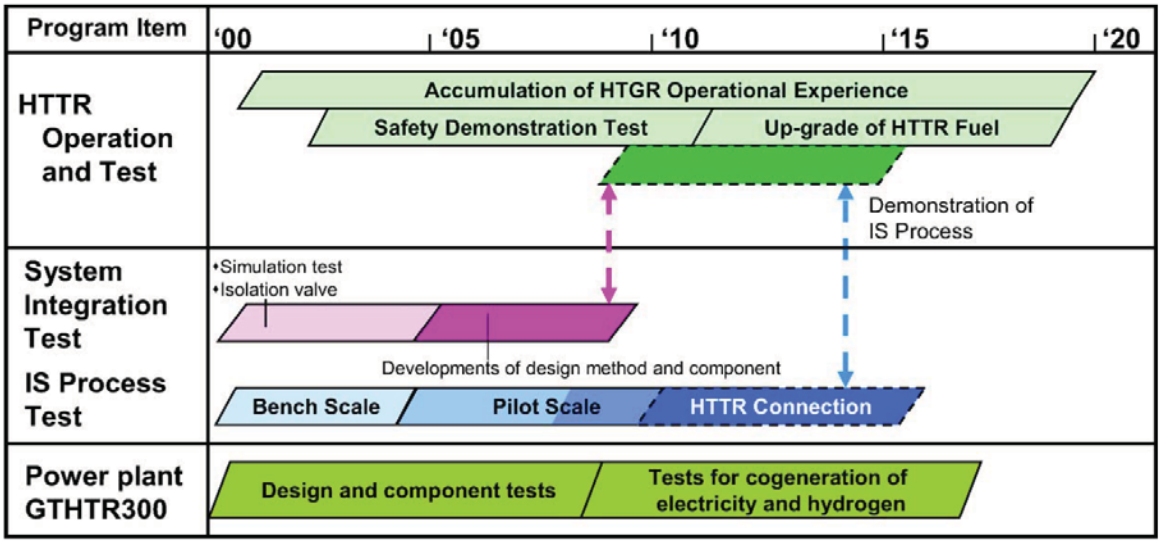


Figure 1.3. Present and Future Plans of the HTTR Project (Ref. 3, p. 13).

Table 1.1. HTTR Rise-to-Power and Safety Operation History.[a]

| Operation name | Operation mode | | Max. reactor thermal power (MW) | Duration | Operation time (MWd) | Remarks |
|---|---|---|---|---|---|---|
| 1st phase rise-to-power test (PT-1) | ● | ▲ | 9 | 23 April–8 May 2000 | | |
| | | | | 11–26 May 2000 | 193 | |
| | | ◆ | 9 | 30 May–6 June 2000 | | |
| 2nd phase rise-to-power test (PT-2) | ● | ▲ | 20 | 3–8 July 2000 | 63 | a) |
| | | | | 29 January–12 February 2001 | 423 | |
| | | ◆ | 20 | 16 February–1 March 2001 | | |
| 3rd phase rise-to-power test (PT-3) | ■ | ▲ | 20 | 14 April–7 May 2001 | | |
| | | ◆ | 20 | 11–16 May 2001 | 689 | b) |
| | | | | 21 May–8 June 2001 | | |
| 4th phase rise-to-power test (PT-4) | ● | ▲ | 30 | 23 October–14 December 2001 | 1,293 | Achievement of 850°C, 30 MW |
| | | ◆ | 30 | 25 January–6 March 2002 | 984 | Operation permit issued. |
| 1st operation cycle (RP/RS-1) | ● | ◆ | 30 | 30 May–17 June 2002 | 370 | |
| | | ▲ | 9 | 21 June–1 July 2002 | 92 | Safety demonstration test |
| 2nd operation cycle (RS-2) | ● | ▲ | 30 | 5 February–14 March 2003 | 658 | Safety demonstration test |
| 3rd operation cycle (RP-3) | ● | ◆ | 20 | 16–21 May 2003 | 72 | a) |
| 4th operation cycle (RS-4) | ● | ▲ | 9 | 8–11 August 2003 | 25 | Safety demonstration test |
| 5th operation cycle (RS-5) | ● | ▲ | 30 | 27 anuary–25 February 2004 | 549 | Safety demonstration test |
| | | | 18 | 29 February–5 March 2004 | | Safety demonstration test |
| 5th phase rise-to-power test (PT-5) | ■ | ▲ | 30 | 31 March–1 May 2004 | 679 | Achievement of 950°C, 30 MW |
| | | ◆ | 30 | 2 June–2 July 2004 | 626 | Operation permit issued. |
| Total operation time (include other operations, *i.e.* core physics tests) | | | | | 6,717 | |

●: Rated operation mode, ■: High-temperature test operation mode, ▲: Single-loaded operation mode, ◆: Parallel-loaded operation mode
a) Automatically reactor shut-down caused by a signal of PPWC flow-rate low
b) Automatically reactor shut-down caused by a loss of off-site electric power by a thunderbolt

[a] S. Fujikawa, H. Hayashi, T. Nakazawa, K. Kawasaki, T. Iyoku, S. Nakagawa, and N. Sakaba, "Achievement of Reactor-Outlet Coolant Temperature of 950 ºC in HTTR," *J. Nucl. Sci. Tech.*, **41**(12): 1245-1254 (December 2004).

## 1.1 Description of the Critical and / or Subcritical Configuration

### 1.1.1 Overview of Experiment

The initial start-up core physics tests for the High Temperature Engineering Test Reactor were performed between the months of July 1998 and January 1999. The HTTR facility is at the Oarai Research and Development Center of the Japan Atomic Energy Agency.

Core physics tests, including start-up and power-up operations, were planned in order to ensure core performance and reactor safety of an HTGR. Results were obtained for a core burn-up of up to 5 GWD/t. During these tests, the critical approach, the excess reactivity, the shutdown margin, the control rod worth, the reactivity coefficient, the neutron flux distribution, and the power distribution were measured and compared with the calculated results (Ref. 13, p. 283).

First criticality was attained on November 10, 1998, and the core was fully loaded in December 1998. During the fuel loading period, various tests were conducted under cold clean conditions as the start-up core physics tests. During these tests, the power was limited to below 30 W and the helium pressure was 1 bar. The tests for the critical approach, excess reactivity, shutdown margin, neutron flux distribution and control rod worth were conducted (Ref. 13, p. 284). Elsewhere the pressure is listed as 1 atmosphere (Ref. 1, p. 312). One atmosphere is equal to $1.01325 \times 10^5$ Pa, or 1.01325 bar.

Of the initial six isothermal, annular and fully-loaded, core critical measurements that were performed, only the fully-loaded core was evaluated in this benchmark analysis. It was determined to have a total uncertainty between -0.60 and +0.71 % Δk. Dominant uncertainties are the impurities in the IG-110 graphite blocks and impurities in the PGX graphite blocks. Comprehensive biases could not be determined for all aspects of this experiment.

Currently the calculations performed using the benchmark model have a $k_{eff}$ about 1.5 to 2.1 % greater than experimental benchmark value and within 4σ. It is currently difficult to obtain the necessary information to further improve the confidence in the benchmark model and effectively reduce the overall uncertainty and bias; the necessary data is proprietary and its released is being restricted, because the benchmark configuration of the HTTR core is the same that is currently in operation. Once this information is made available, the HTTR benchmark can be adjusted as appropriate.

The evaluated subcritical configuration of the fully-loaded core also has a computational bias in $k_{eff}$ of between 1.5 to 2.3 % and a total uncertainty in the benchmark of ±1.04 %.Δk. The subcritical configurations developed during initial core loading were not evaluated.

A warm critical configuration was recorded in Reference 2 but does not represent a valid benchmark experiment.

### 1.1.2 Geometry of the Experiment Configuration and Measurement Procedure

Section 1.1.2.1 discusses the HTTR site and facility as gathered from the references. Section 1.1.2.2 contains information regarding many of the internal mechanisms of the HTTR. Both of these sections are useful in understanding the overall HTTR description. However, most of the information pertinent to this benchmark evaluation of the reactor core can be found in Section 1.1.2.3 through Section 1.1.2.6.

*1.1.2.1 Facility Description*

## Site and Facility

The HTTR is located on JAEA's Oarai Research and Development Center, which is approximately 100 kilometers north of the Tokyo metropolitan area, near the Pacific Ocean (Figure 1.4 and 1.5). The plant area is 200 m by 300 m in size (Figure 1.6). The 48 m by 50 m reactor building is situated in the central area of the plant with an 80-m high exhaust stack to the north, as shown in Figure 1.7 (Ref. 2, p. 5). Air cooling towers are located on the roof of the reactor building (Ref. 15, p.9).

Typically important Japanese buildings must be built on base rock material. The HTTR reactor building, however, is supported on an Ishizaki-layer, which is a sand layer formed during the Quaternary era. Boring and seismic surveys demonstrated strength and support of this layer equivalent to that of base rock; therefore, the seismic safety of the facility was recognized.[a] Significant seismic design guidelines were incorporated into the HTTR such that all anticipated earthquakes would not cause a severe accident.[b]

Construction of the HTTR took approximately 7 years (Figure 1.8). The reactor building is comprised of five levels, three of which are underground, as shown in Figures 1.9 and 1.10. The major design specifications of the HTTR are provided in Table 1.2.


Figure 1.4. Location of JAEA's Oarai Research and Development Center.

[a] K. Kunitomi and S. Shiozawa, "Safety Design," *Nucl. Eng. Des.*, **233**: 45-58 (2004).

[b] K. Iigaki and S. Hanawa, "Seismic Design," *Nucl. Eng. Des.*, **233**: 59-70 (2004).

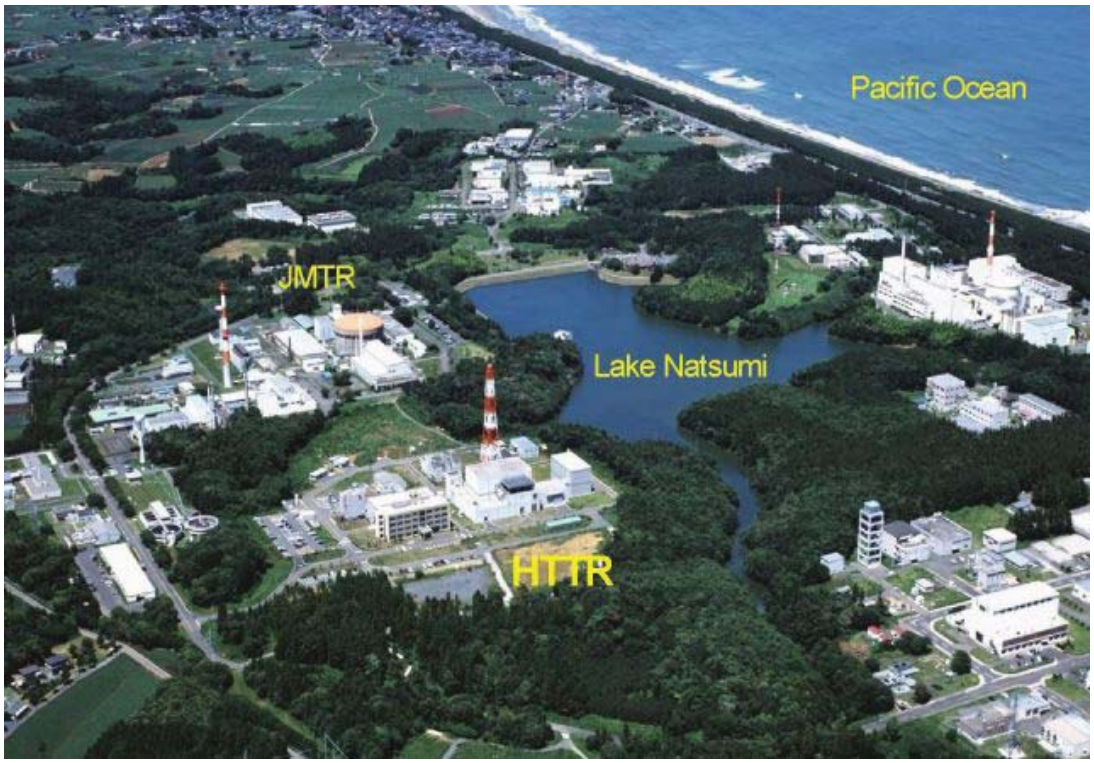


Figure 1.5. Aerial View of the HTTR Facility (http://httr.jaea.go.jp).

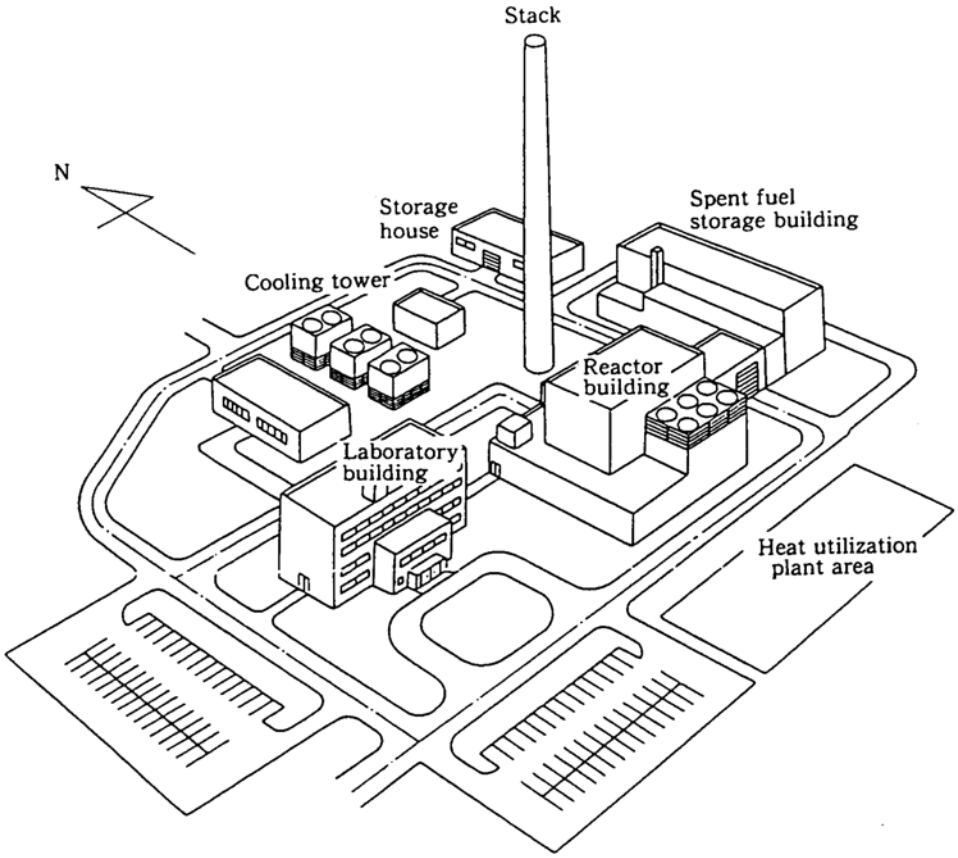


Figure 1.6. Isomeric View of HTTR Plant (Ref. 15, p. 10).


Figure 1.7. HTTR Building Exterior (http://httr.jaea.go.jp).

| ITEM / FY*1 | 1990 | 1991 | 1992 | 1993 | 1994 | 1995 | 1996 | 1997 | 1998 |
|---|---|---|---|---|---|---|---|---|---|
| MILESTONE | Construction start ▽ | | | | Electricity receive ▽ | | | Fueling ▽ ▽ Criticality | |
| Safety review | | | | | | | | | |
| Approval of design and construction method | | | | | | | | | |
| Site renovation | | | | | | | | | |
| Excavation of reactor building | | | | | | | | | |
| Reactor building | | | | | | | | | |
| Containment vessel | | | | | | | | | |
| Cooling system | | | | | | | | | |
| Reactor pressure vessel and core internals | | | | | | | | | |
| Fuel fabrication | | | | | | | | | |

*1 Fiscal year of Japan starts in April and ends in next March

Figure 1.8. Construction Schedule of the HTTR (Ref. 15, p. 6).

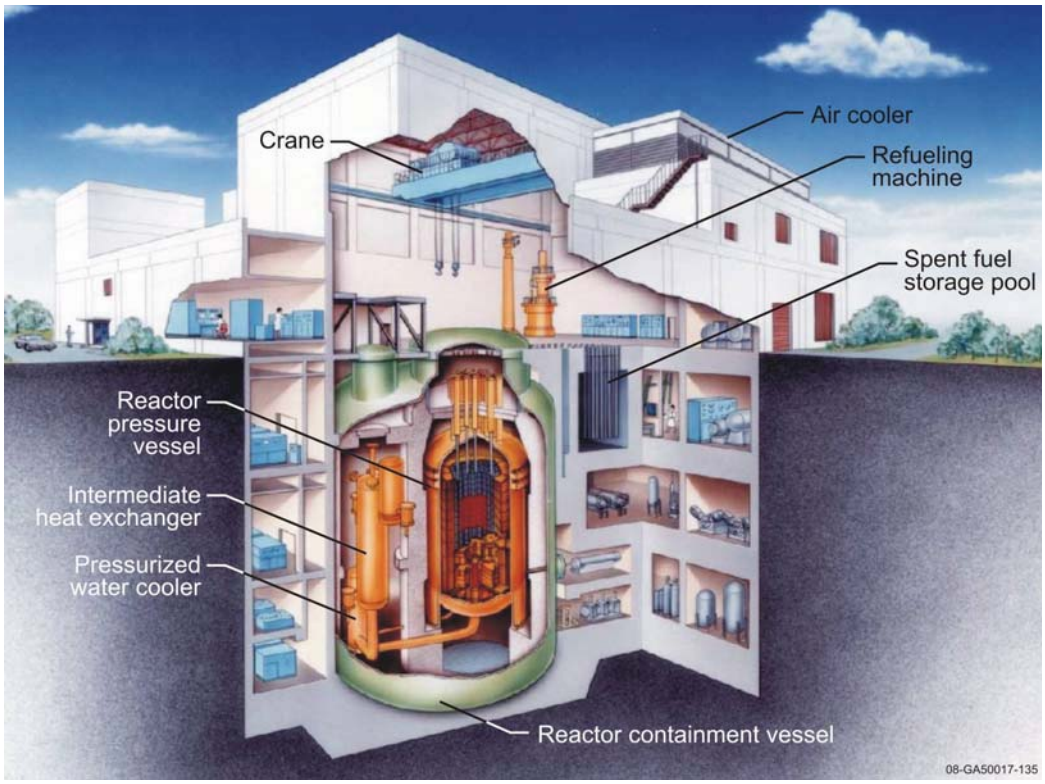


Figure 1.9. HTTR Building Interior.

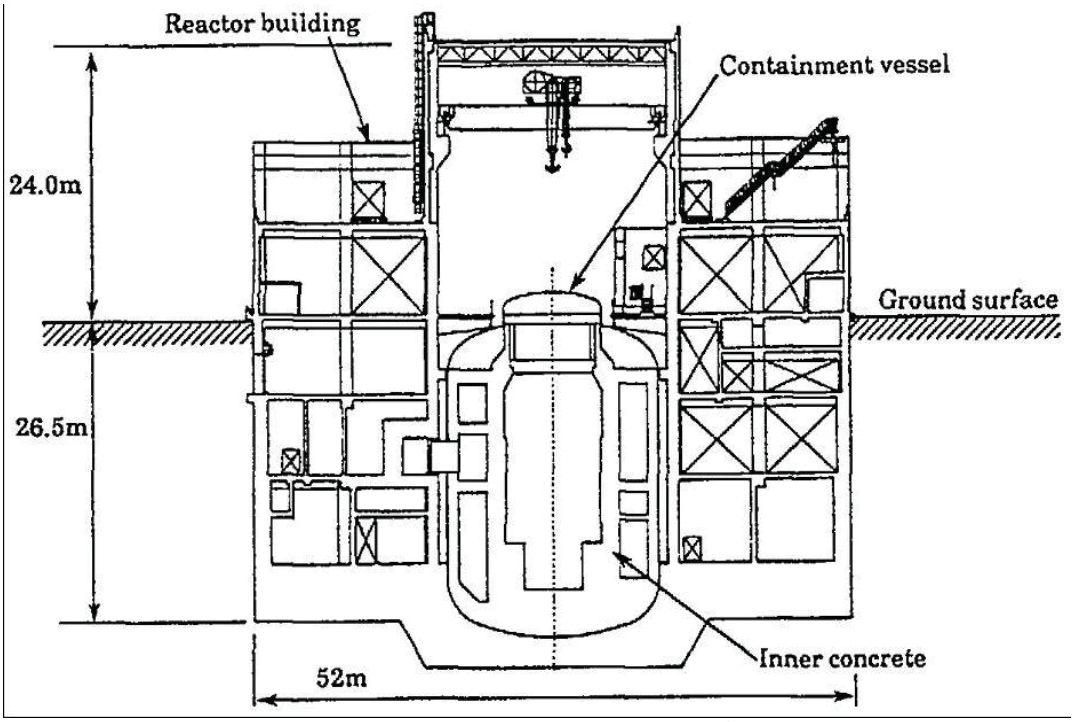


Figure 1.10. The HTTR Structure.[a]

[a] F. Yagishita, H. Suzuki, and Y. Yamagishi, "Soil-Structure Interaction Analysis of HTTR Building by a Simplified Model," *Proc. Int. Working Group on Gas-Cooled Reactors (IWGGCR-22)*, Gif-sur-Yvette, France (November 14-16, 1989).

Table 1.2. Major Design Specifications of the HTTR (Ref. 1, p. 311, and Ref. 2, p. 9).

| | |
|---|---|
| Thermal Power | 30 MW |
| Outlet Coolant Temperature | 850/950 ºC |
| Inlet Coolant Temperature | 395 ºC |
| Primary Coolant Pressure | 4 MPa |
| Core Structure | Graphite |
| Equivalent Core Diameter | 2.3 m |
| Effective Core Height | 2.9 m |
| Average Power Density | 2.5 $W/cm^3$ |
| Fuel | $UO_2$ |
| Enrichment | 3 to 10 wt.% |
| | 6 wt.% (average) |
| Fuel Type | Pin-in-Block Type |
| | Coated Fuel Particles |
| Burn-Up Period (EFPD) | 660 days |
| Fuel Block | Graphite Block |
| Coolant Material | Helium Gas |
| Flow of Direction in Core | Downward |
| Reflector Thickness | |
| Top | 1.16 m |
| Side | 0.99 m |
| Bottom | 1.16 m |
| Number of Fuel Assemblies | 150 |
| Number of Fuel Columns | 30 |
| Number of Pairs of Control Rods | |
| In Core | 7 |
| In Reflector | 9 |
| Plant Lifetime | 20 years |

## Containment Structure

The containment structures of the HTTR consist of the reactor containment vessel (C/V), the service area, and the emergency air purification system. The reactor containment vessel is relatively small, so as to minimize air ingress and reactivity with graphite in the event of a rupture of the primary pressure boundary. The carbon steel vessel has 2800 $m^3$ of free volume, with a height of 30.3 m and a diameter of 18.5 m. It has a personnel air lock, maintenance hatch, and refueling hatch, as shown in Figure 1.11. Elastic plugging material is installed between the reactor containment vessel and the base mat of the reactor building so as to absorb any thermal expansion in the event of an accident. Other penetrations in the C/V are shown in Figure 1.12. The C/V is designed to be leak tight with a leakage rate of less than 0.1 % of the total free volume per day at room temperature, air atmosphere, and 0.9 times its maximum pressure. Specifications of the C/V are tabulated in Table 1.3 (Ref. 10, pp. 135-137).

The containment vessel is installed in the center of the reactor building. Although the containment vessel is not needed for retention of an accidental release of fission products, it was required to meet Japanese safety design guidelines for light water nuclear power plants, as HTGR safety features had yet to be developed. Above the reactor pressure vessel (RPV) is a fueling hatch attached to the C/V. Some of the compartments surrounding the C/V function as confinement or serve areas. Major components such as the primary cooling system and RPV are contained within the C/V (Ref. 2, p. 6).

Mitsubishi Heavy Industries was in charge of the design, manufacture, and installation of the main HTTR equipment, such as the reactor containment vessel and the main cooling system (Ref. 14, p. 386).

A service area is provided (Figure 1.13) that surrounds the reactor C/V and includes the fuel handling and storage systems and the primary helium purification system. The service area is kept at a negative pressure during accidents by an emergency air purification system, which operates under the isolated reactor containment vessel condition. During normal operations, the service area is kept at a negative pressure by the ventilation and air conditioning systems (Ref. 10, pp. 140-141).

Because helium gas is employed as the coolant in the HTTR, a shielding effect is not expected as would be in a conventional LWR. Therefore, a thick shielding structure is necessary for the HTTR. A schematic of the shielding arrangement is shown in Figure 1.14.

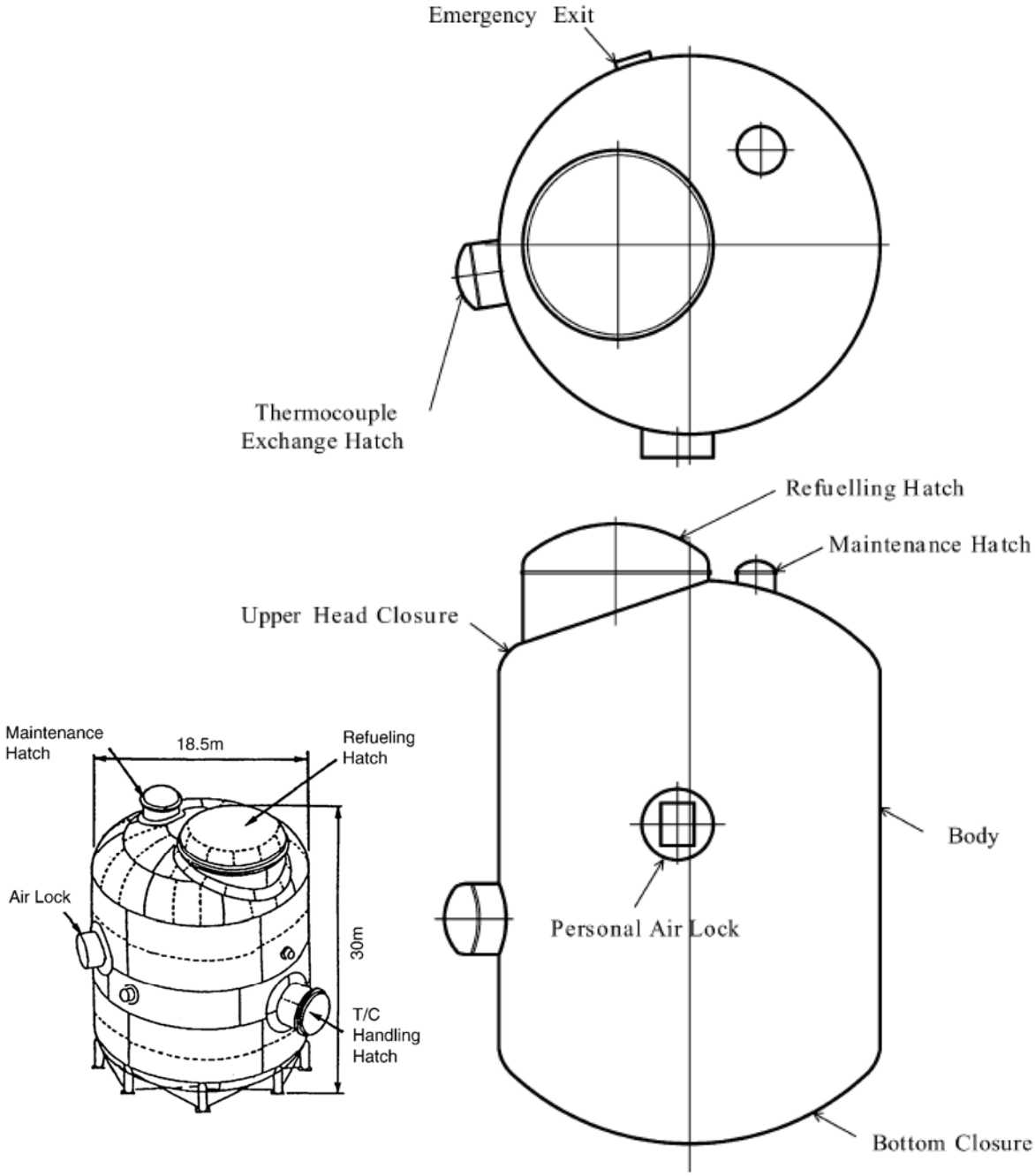


Figure 1.11. Reactor Containment Vessel Major Penetrations (Ref. 10, p. 136, and Ref. 14, p. 387).

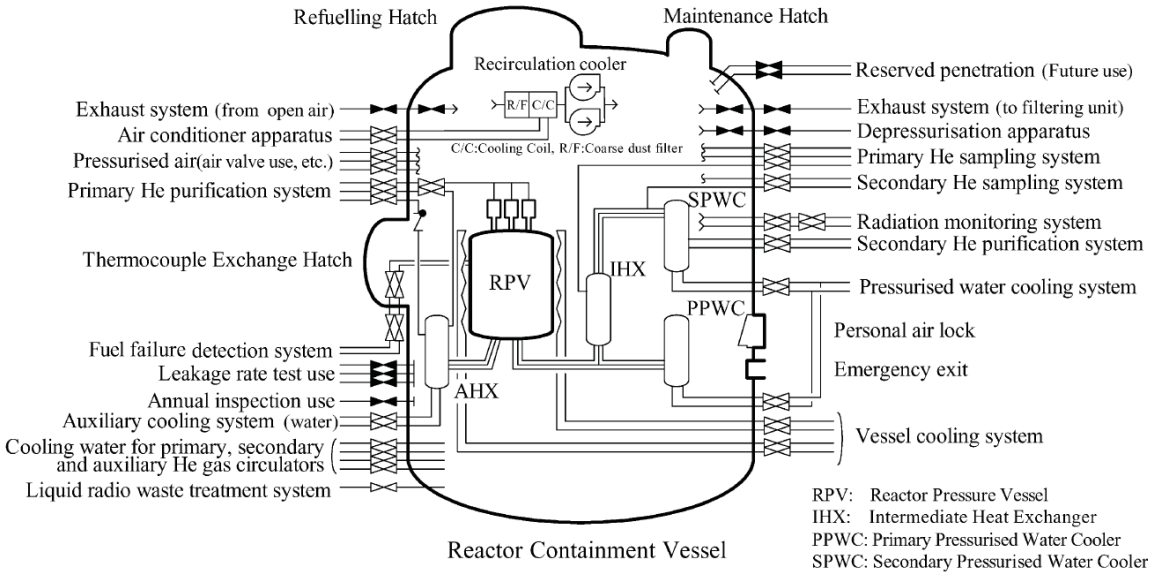


Figure 1.12. Reactor Containment Vessel Penetrations (Ref. 10, p. 137).

Table 1.3. Specifications of the Reactor Containment Vessel (Ref. 10, p. 137).

| | |
|---|---|
| Containment Type | Steel |
| Maximum Pressure in Service (MPa) | 0.4 |
| Maximum Temperature in Service (ºC) | 150 |
| Major Size | |
| Inner Diameter (m) | 18.5 |
| Overall Height (m) | 30.3 |
| Body Thickness (mm) | 30 |
| Upper Head Closure Thickness (mm) | 38 |
| Refueling Hatch Diameter (m) | 8.5 |
| Maintenance Hatch Diameter (m) | 2.4 |
| Personal Air Lock Diameter (m) | 2.5 |
| Free Volume ($m^3$) | 2800 |
| Material | Carbon Steel |
| Leakage Rate | Less than 0.1 %/d at the room temperature and 0.9 times the maximum pressure of 0.4 MPa |

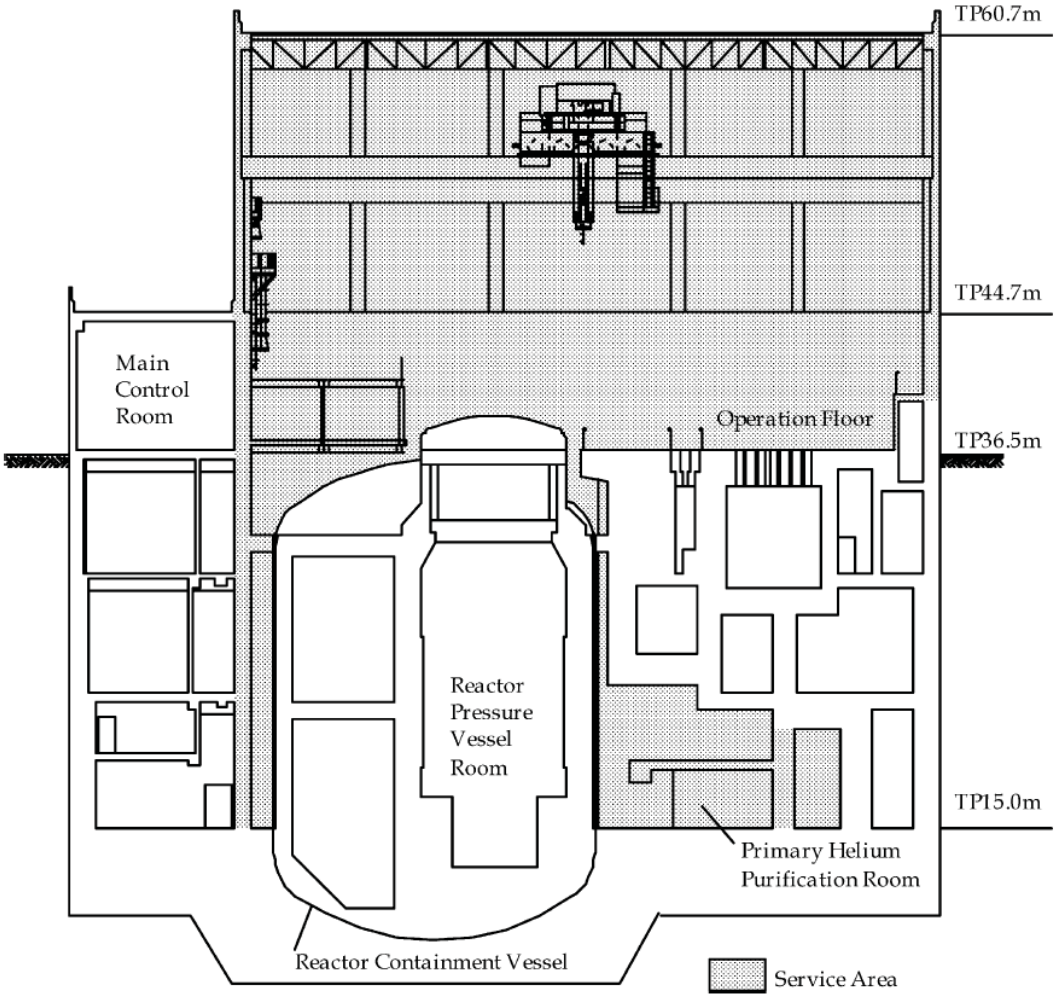


Figure 1.13. HTTR Service Area (Ref. 10, p. 142).

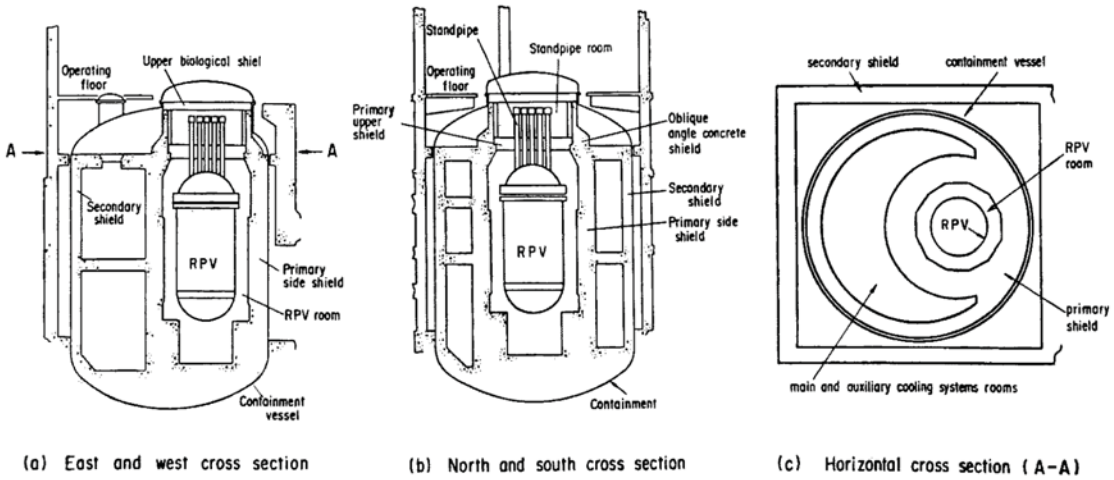


Figure 1.14. Schematic Arrangement of Shields in HTTR.[a]

[a] I. Murata, R. Shindo, and S. Shozawa, "Importance Determination Method for Geometry Splitting with Russian Roulette in Monte Carlo Calculations of Thick and Complicated Core Shielding Structure," *J. Nucl. Sci. Tech.*, **32**(10): 971-980 (October 1995).

## Reactor Pressure Vessel

The reactor pressure vessel is formed as a vertical cylinder with hemispherical top and bottom head closures, and 31 standpipes. The top head closure is bolted to a flange of the vessel cylinder. The standpipes are used for manipulation of control rods, irradiation experiments, and instrumentation. A diagram of the RPV and various reactor internals is shown in Figure 1.15 (Ref. 2, p. 6). The RPV is 13.2 m in height and 5.5 m in diameter (Ref. 3, p. 17).

A schematic of just the RPV is shown in Figure 1.16, with a close-up view of the upper structure in Figure 1.17. The RPV contains thirty-one standpipes that are welded to the top head dome. A thermal shield is installed on the inner surface of the top head closure to prevent high temperature exposure in accidents. The RPV is supported by a skirt, stabilizers, and a standpipe support beam. The skirt is welded to the outside of the bottom dome. The stabilizers surround the outside of the RPV cylinder and are supported by the side concrete. The standpipe support beam is located near the top of the standpipes. A special standpipe-fixing device is located at the top of some of the standpipes to prevent the standpipe internal structure from being ejected in the event of a standpipe break (Ref. 8, pp. 103-104).

Major specifications of the RPV are shown in Table 1.4. The RPV has a top head which includes standpipes, a top head dome, a top head flange, thermal shields, etc., and a RPV body comprised of a shell flange, shell, three standpipes, a bottom head petal, skirt, a bottom head dome, a support ring, and radial keys. The RPV top head is bolted to the RPV body by 72 stud bolts. There are 31 standpipes: 16 for control rods, five for irradiation tests, three for surveillance tests, three for neutron detection, two for in-service inspection of reactor internals, and two for measurement of temperatures and core differential pressure. These are welded to nozzles on the top head dome. The control standpipes constrain the control rod drive mechanism. The irradiation standpipes are used to install specimens and experimental equipment into the core. Figure 1.18 shows the arrangement of the standpipes on the top head dome and Table 1.5 provides the diameter of the standpipes and penetrating holes. The largest seven standpipes, N1-N7, are also used for refueling. Three other standpipes for hot plenum temperature measurement and fuel failure detection are welded to nozzles on the shell. The skirt supports weight and seismic load of the reactor. Horizontal seismic load is sustained by six stabilizers and a standpipe support beam, as well as the skirt. The support ring supports the vertical load of the core, and the radial keys hold horizontal movement of the core through a core restraint mechanism (Ref. 8, p. 105-106).

The standpipe closure, which can be handled with the control rod handling machine, is plugged into the standpipe with double rubber D-rings to provide leak tightness. Latches prevent the closure from being pushed out by the coolant pressure. The standpipe-fixing device is made up of snubbers, a support plate, and other devices. If a standpipe breaks off in an accident, the fixing device limits displacement of the top of the standpipe by the snubbers, to prevent the internal structures from being pulled out and to limit the outflow of primary coolant. In normal operation, a standpipe support beam is not in contact with the standpipes, and is free of thermal expansion of the RPV. It restrains an excessive displacement of standpipes induced by an earthquake (Ref. 8. p. 107).

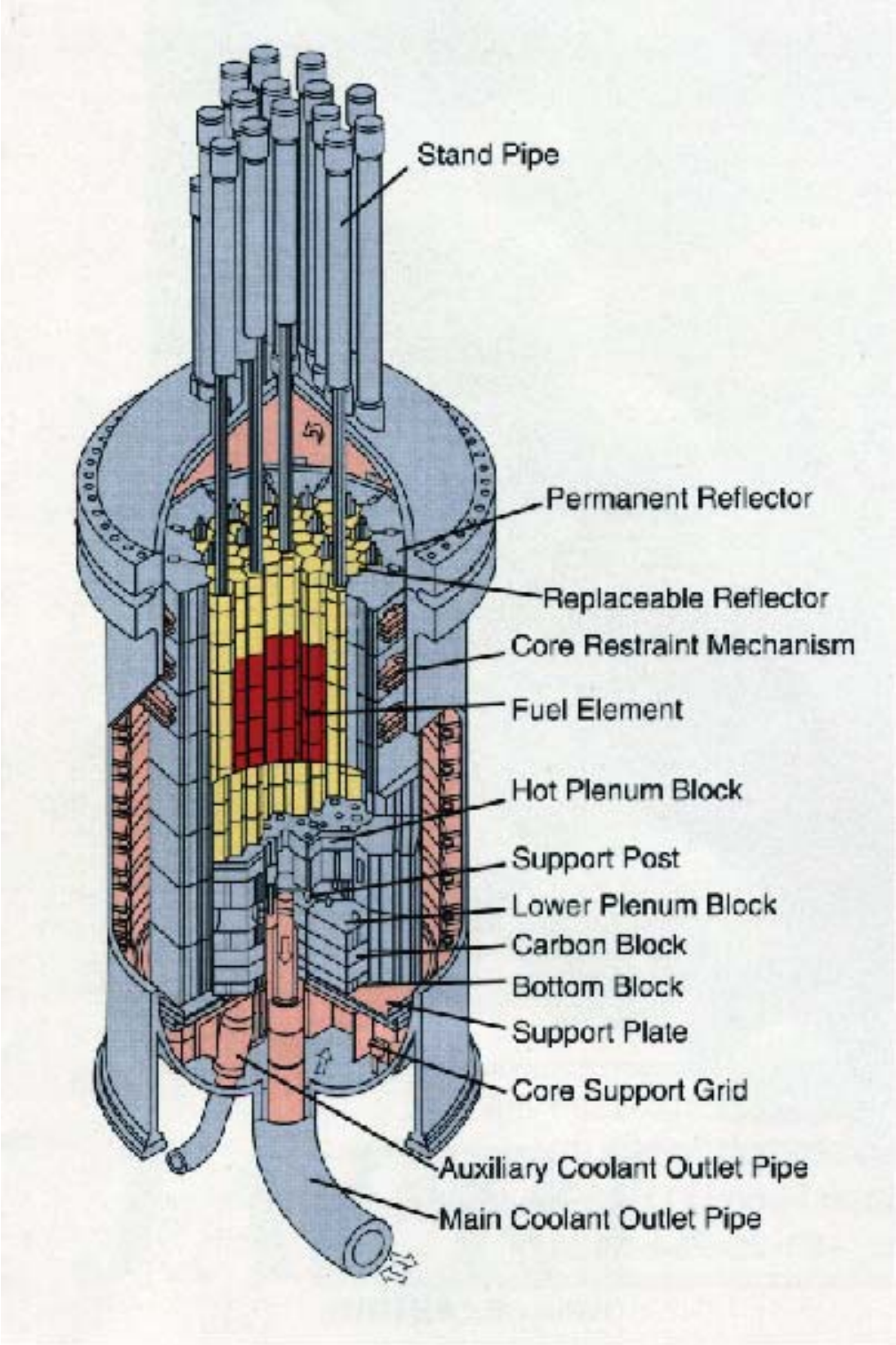


Figure 1.15. HTTR Pressure Vessel and Internals (http://httr.jaea.go.jp).

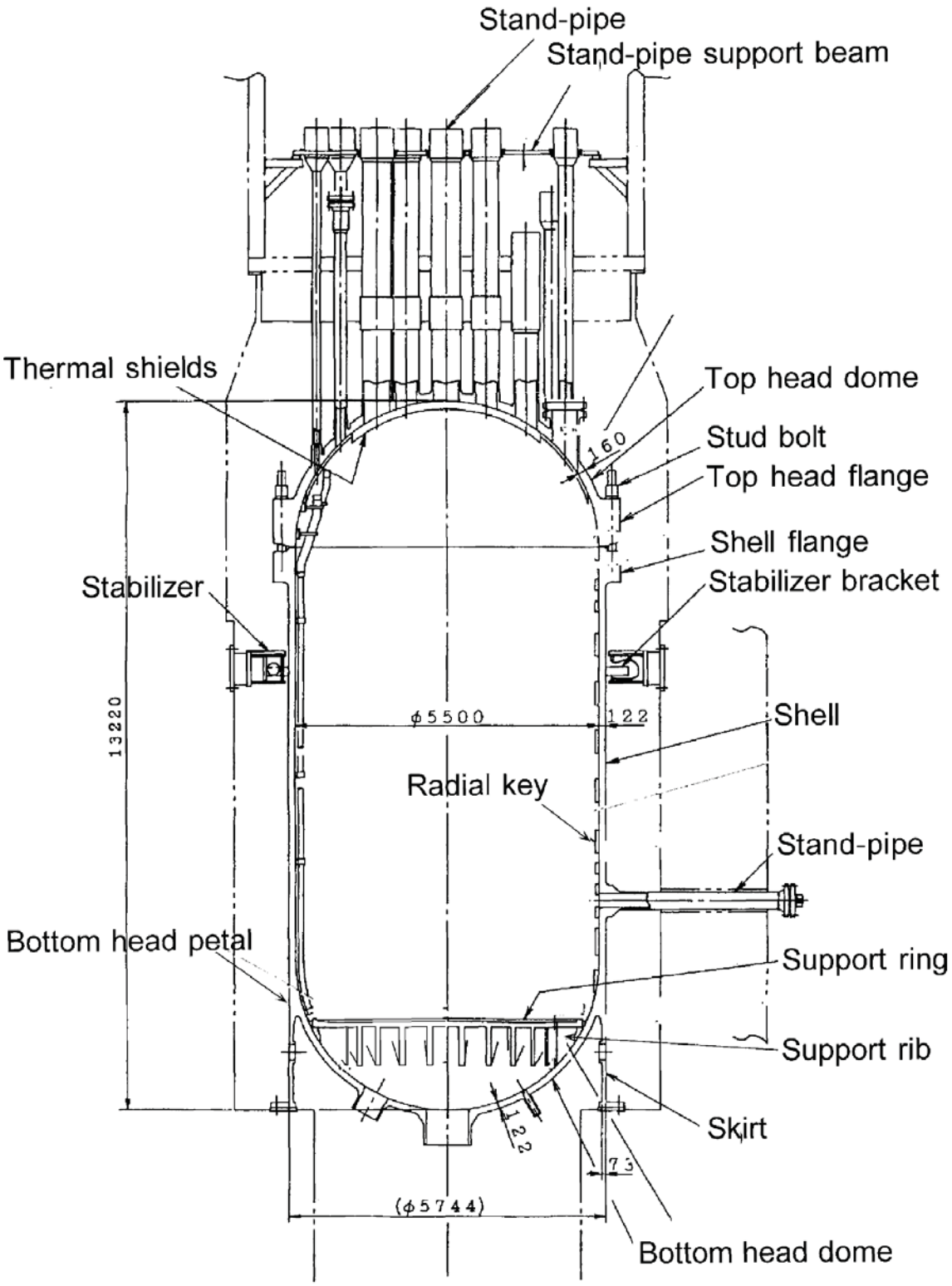


Figure 1.16. Schematic Design of the Reactor Pressure Vessel (Ref. 8, p. 104).

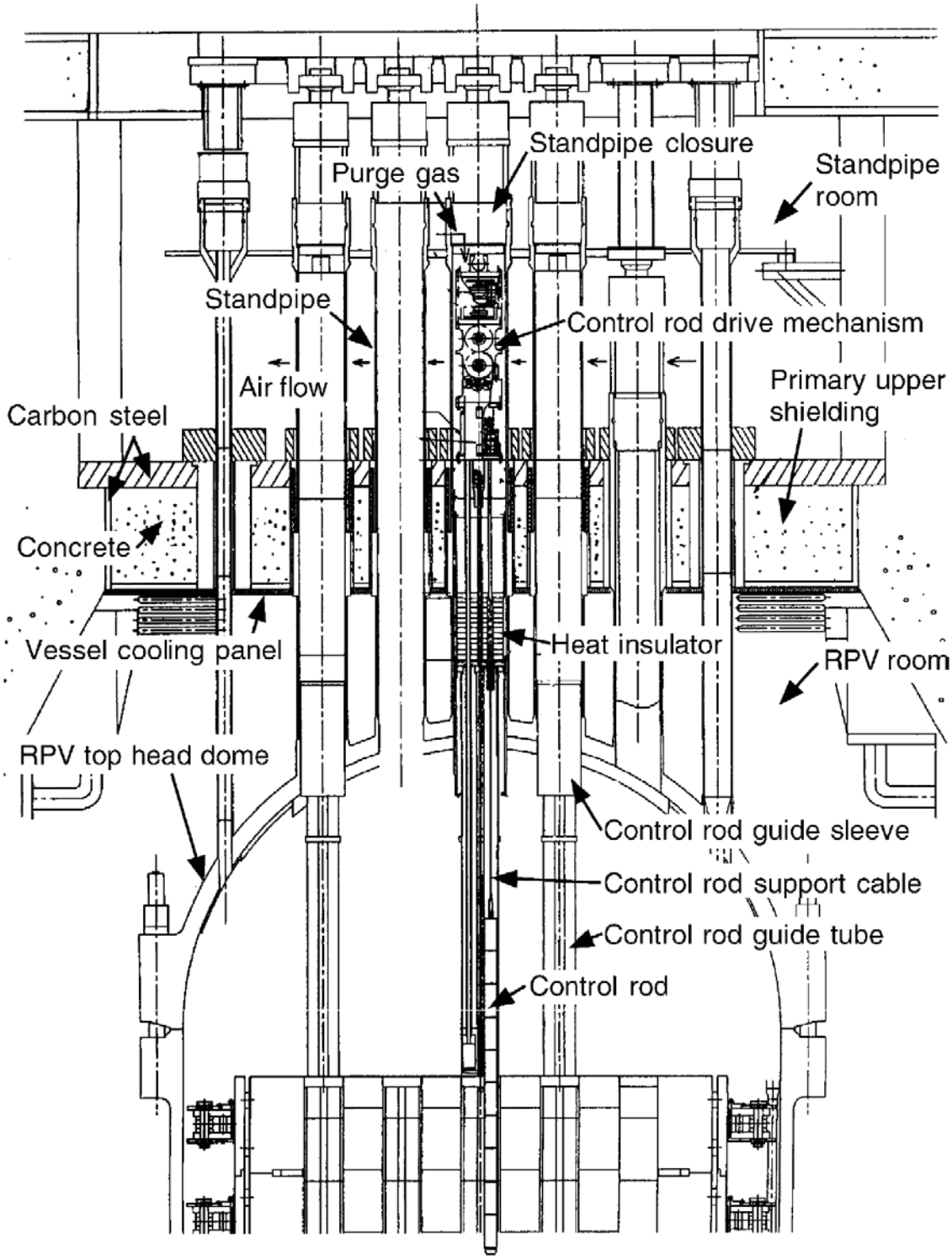


Figure 1.17. Upper HTTR Structure.[a]

[a] N. Fujimoto, Y. Tachibana, A. Saikusa, M. Shinozaki, M. Isozaki, and T. Iyoku, "Experience of HTTR Construction and Operation – Unexpected Incidents," *Nucl. Eng. Des.*, **233**: 273-281 (2004).

Table 1.4. Major Specifications of the HTTR RPV (Ref. 8, p. 105).

| | |
|---|---|
| Design Pressure (MPa) | 4.7 [gauge] |
| Design Temperature (ºC) | 440 |
| Normal Operating Pressure (MPa) | 3.9 [gauge] |
| Inlet Coolant Temperature (ºC) | 395 |
| Inside Diameter (m) | 5.5 |
| Height (m) | 13.2 |
| Thickness of Cylindrical Shell and Bottom Head Dome (mm) | 122 (minimum) |
| Thickness of Top Head Dome (mm) | 160 (minimum) |
| Number of Standpipes | 34 |
| Material | 2-1/4Cr-1Mo steel (normalized and tempered) |

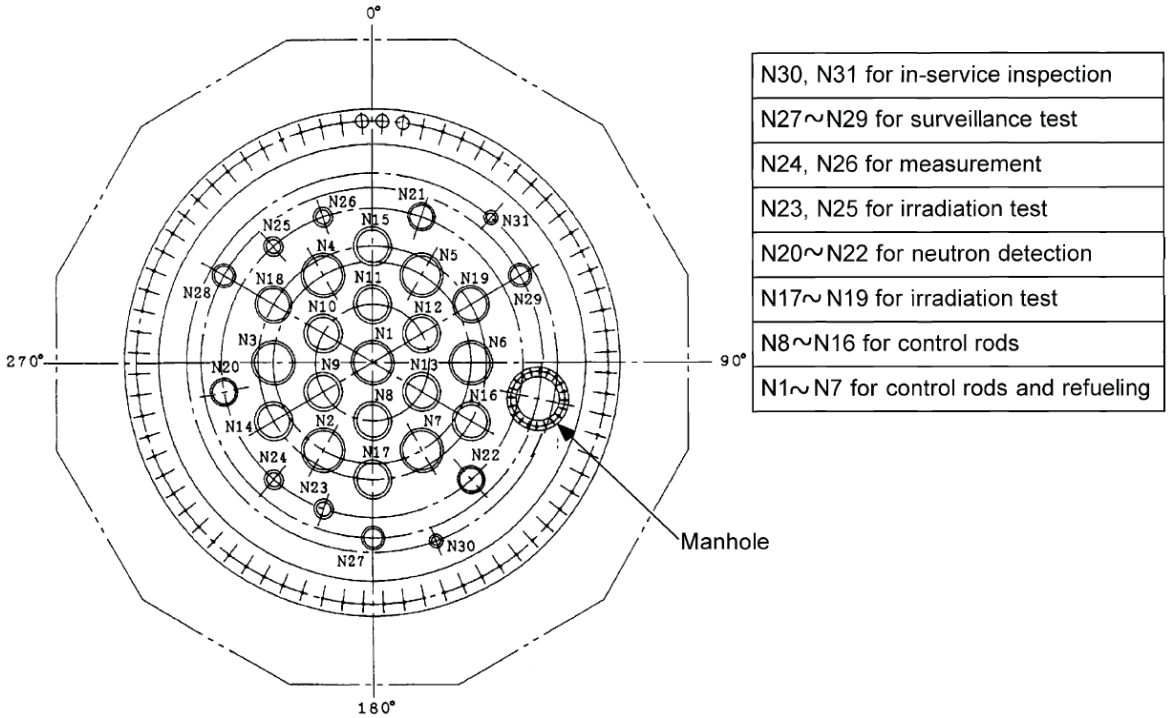


Figure 1.18. Arrangement of Standpipes of the HTTR (Ref. 8, p. 105).

Table 1.5. Diameter of Standpipes and Penetrating Holes in Support Plate.[(a)]

| Standpipe No. | Use | Outer Diameter of Standpipe (mm) | Inner Diameter of Standpipe (mm) | Diameter of Penetrating Hole (mm) |
|---|---|---|---|---|
| 1-7 | Control Rods | 525 | 485 | 525 |
| 8-16 | Control Rods | 460 | 425 | 460 |
| 17-19 | Irradiation Test | 512[a] | 405 | 640 |
| 20-22 | Neutron Detection | 319[a] | 298 | 614 |
| 23, 25 | Irradiation Test | 216 | 200 | 216 |
| 24, 26 | Reactor Instrumentation | 216[a] | 200 | 271 |
| 27-29 | Surveillance Test | 267 | 249 | 267 |
| 30, 31 | In-Service Inspection | 140 | 121 | 140 |

(a) Diameter of the standpipe fixing device.

## Reactor Cooling System

Hitachi was responsible for the design, manufacture, and installation of key HTTR components such as the reactor pressure vessel, the vessel cooling system, and the auxiliary cooling water system (Ref. 14, p. 380).

The reactor cooling system is comprised of a main cooling system (MCS), an auxiliary cooling system (ACS) and two reactor vessel cooling systems (VCSs), as shown in Figure 1.19. The MCS removes the heat energy from the reactor core during normal operations, while the ACS and VCSs function as engineered safety features to remove residual heat after a reactor scram. The ACS provides force-cooling of the core restraint mechanism to protect it against thermal damage from reactor heat during anticipated operational occurrences (AOOs) and normal operation (Ref. 2, p. 7).

Approximately 97 % of the reactor thermal power is removed by the MCS with a helium flow rate of 12.4 kg/s at rated operation and 10.2 kg/s at the high-temperature test operation. The remaining heat is removed mostly by the VCS. After a reactor scram, the residual core heat is removed by the ACS and/or the VCS.[a]

[a] E. Takada, S. Nakagawa, N. Fujimoto, and D. Tochio, "Core Thermal-Hydraulic Design," *Nucl. Eng. Des.*, **233**: 37-43 (2004).

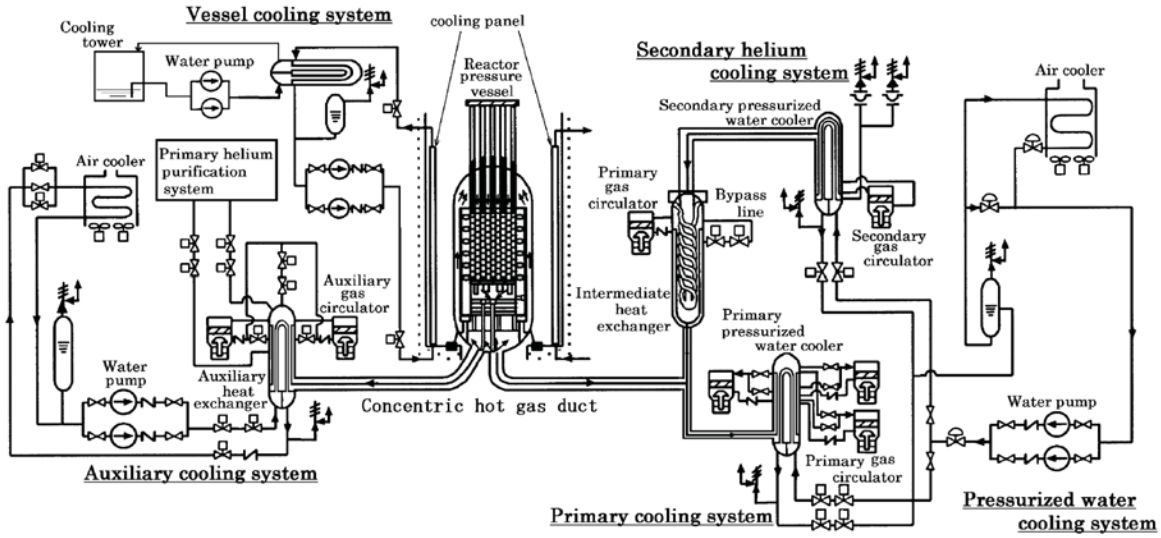


Figure 1.19. Schematic Diagram of HTTR Cooling System (Ref. 9 p. 114).

The MCS consists of an intermediate heat exchanger (IHX), a primary pressurized water cooler (PPWC), a secondary pressurized water cooler (SPWC), and a pressurized water/air cooler. The MCS has two operational modes: single-loaded operation and parallel-loaded operation. The PPWC functions to remove the reactor heat of 30 MW during the single-loaded operation, while during parallel-loaded operation the IHX removes 10 MW and the PPWC removes the other 20 MW. The SPWC serves the function of removing the heat from the IHX. The heat removed by the PPWC and the SPWC is transported through the pressurized water at 2.5 MPa. The pressurized water is then cooled down by the air cooler. In the HTTR reactor plant, the reactor heat is eventually transferred to the atmosphere by the pressurized water/air cooler. During normal operation, the pressure of the secondary helium is controlled to always by 0.1 MPa higher than that of the primary helium at the IHX heat transfer tubes in order to reduce the pressure load on the tubes and to protect against accidental leakage of radioactive materials into the secondary coolant. The water pressure is controlled so that a large amount of water cannot ingress into the core (Ref. 2, p. 8).

The IHX development was led by Toshiba and Ishikawahima-Harima Heavy Industries. Fabrication of the IHX was competed in September 1994 and installed at the HTTR site in February 1995 (Ref. 14, pp. 380-382).

The IHX is a vertical helically-coiled counter-flow type heat exchanger in which primary helium gas flows on the shell side and secondary helium gas in the tube side as shown in Figure 1.20. Table 1.6 has the major specifications of the IHX. Primary helium gas enters the IHX through the inner pipe of the primary concentric hot gas duct. It is deflected under a hot header and discharged around the heat transfer tubes to transfer the heat to the secondary helium cooling system. It flows to the primary gas circulator via the upper outlet nozzle and flows back to the annular space between the inner and outer shells. Secondary helium gas flows downwards in the heat transfer tubes and upwards in the central hot gas duct through the hot header. The inner insulation is installed inside the inner shell to maintain its temperature below 440 ºC. The insulation outside and inside the central gas duct restrain the heat transfer so that high efficiency can be obtained. In addition, it also keeps the temperature of the central duct below 940 ºC. Primary helium gas is contained only in the primary cooling system because the pressure in the secondary helium cooling system is adjusted somewhat higher than that in the primary cooling system (Ref. 9, pp. 116-117).

A floating hot header with a combination of a central hot gas duct passes through the central space inside the helix bundle so as to minimize constraints of axial and radial thermal expansion of the helically-

coiled heat transfer tubes. An assembled tube support allows free thermal expansion of a helix in the radial direction. The primary helium enters the IHX through the inner pipe of the primary concentric hot gas duct attached to the bottom of the IHX. It flows up outside the tubes, transferring 10 MW of nuclear heat to the secondary helium, and then flows back to the annular space between the inner and outer shells. A double-walled shell with thermal insulation attached to the inside surface of the inner shell provides reliable separation of the heat resisting and pressure retaining functions. Cold helium flowing through the annulus brings uniform temperature distribution throughout the outer shell, which serves the function of being the pressure retaining member (Ref .2, pp. 8-9).

The tube support assemblies hold the heat transfer tubes. Both the central hot gas duct and the heat transfer tube support assemblies are hung from the vessel top so that the thermal expansion is not constrained (Ref. 9, p. 117). A photograph of the IHX tube bundles is shown in Figure 1.21.

The IHX has a bypass line, which prevents natural circulation from the reactor core from entering IHX during the single-loaded operation. The forced circulation from the PPWC through the bypass line occurs and keeps the temperature of the outer shell below 430 ºC. Primary helium gas flows from the PPWC and enters into the annulus space between the inner and outer shells before flowing inside the inner shell through the bypass line. It then returns to the PPWC through the IHX and the primary concentric hot gas duct. The shutoff valve stops this forced circulation during the parallel-loaded operation and when the ACS is activated for a scram. The inner structures, such as the heat transfer tubes, central hot gas duct, and the hot header, are operated beyond 900 ºC (Ref. 9, pp. 117-118).

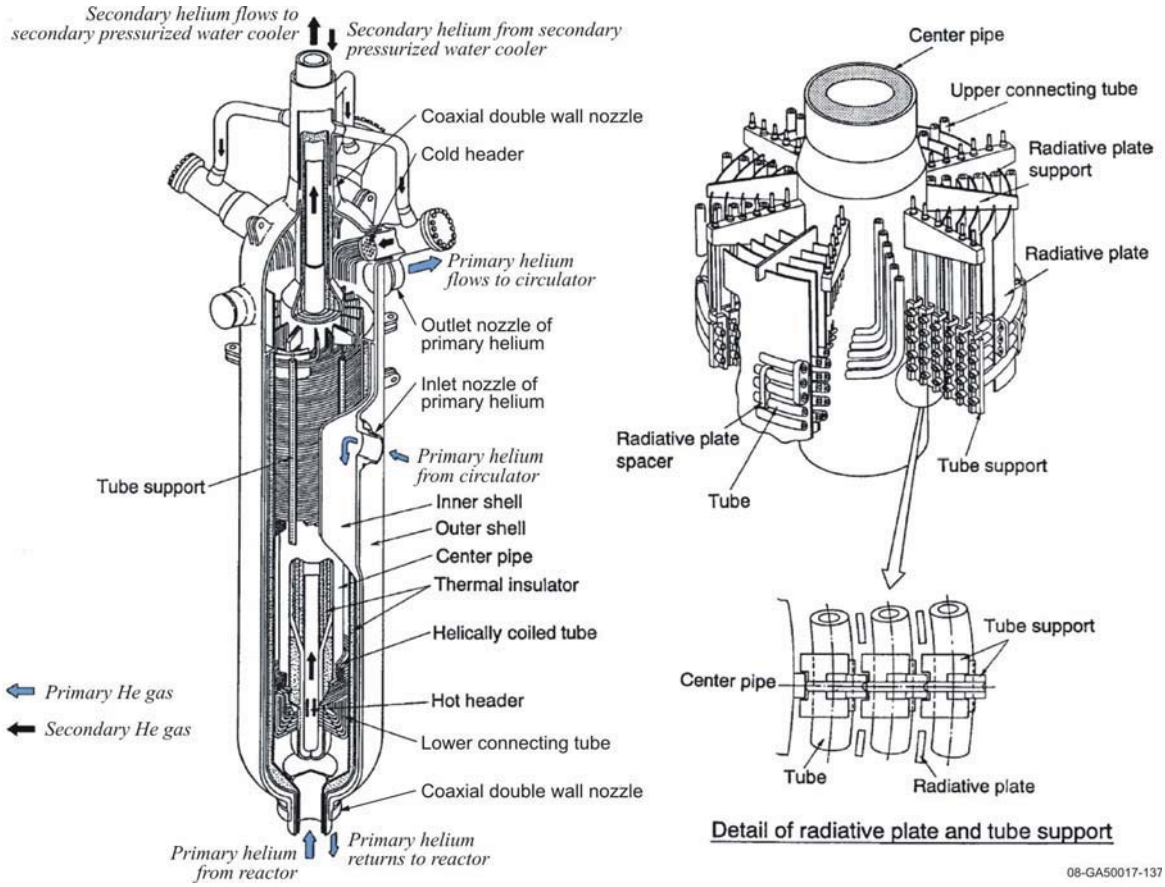


Figure 1.20. The Intermediate Heat Exchanger.

Table 1.6. Major Specifications of the Intermediate Heat Exchanger (Ref 9 p. 118 and Ref 14, p. 382).

| Type | Vertical Helically-Coiled Counter Flow | |
|---|---|---|
| Design Pressure | | |
| Outer Shell (MPa) | 4.7 | |
| Heat Transfer Tube (MPa) | 0.29 (differential pressure) | |
| Design Temperature | | |
| Outer Shell (ºC) | 430 | |
| Heat Transfer Tube (ºC) | 955 | |
| Operating Condition | Rated Operation | High Temperature |
| Flow Rate of Primary Helium Gas (t/h) | 14.9 (max) | 12.2 (max) |
| Inlet Temperature of Primary Helium Gas (ºC) | 850 | 950 |
| Outlet Temperature of Primary Helium Gas (ºC) | 395 | 395 |
| Flow Rate of Secondary Helium Gas (t/h) | 12.8 | 10.8 |
| Inlet Temperature of Secondary Helium Gas (ºC) | 244 | 237 |
| Outlet Temperature of Secondary Helium Gas (ºC) | 175 | 174 |
| Heat Capacity (MW) | 10 | |
| Heat Transfer Tube | | |
| Number | 96 | |
| Number of Coil Layers | 6 | |
| Pitch (mm) | 47 | |
| Outer Diameter (mm) | 31.8 | |
| Thickness (mm) | 3.5 | |
| Length (m) | 30 | |
| Outer Diameter of Shell (m) | 1.9 | |
| Total Height (m) | 10 | |
| Radiation Plate Thickness (mm) | 5 | |
| Material | | |
| Outer and Inner Shell | SCMV4-2NT(2-1/4Cr-1Mo Steel) | |
| Heat Transfer Tube | Hastelloy XR | |
| Hot Header and Center Pipe | Hastelloy XR | |


Figure 1.21. Completed Tube Bundles of the IHX (Ref. 14 p. 383).

The PPWC is a vertical U-tube heat exchanger (Figure 1.22 and Table 1.7). Hot primary helium gas from the inlet nozzle flows horizontally between the baffle plates, and cools the outside surface of the heat transfer tubes. It flows upwards and turns backwards several times. Then it flows out via the upper or lower outlet nozzles to the primary gas circulators and flows back to the annular space between the inner and outer shell to cool them. Pressurized water of 3.5 MPa is led to each heat transfer tube and heated up by the primary helium gas. Thermal insulation is installed inside the inner shell to maintain its temperature lower than 440 ºC. A tubesheet supports the heat transfer tubes (Ref. 9, p. 115).

The heat capacity of the PPWC can be changed from 30 to 20 MW by changing the helium gas flow paths according to the loop operational modes. Primary helium gas flows out through three lower outlet nozzles during parallel-loaded operation and the three upper nozzles during single-loaded operation (Ref. 9, p. 115).

The maximum temperature difference between the helium gas and pressurized water is approximately 800 ºC. To prevent burn out, the flow velocity of the primary helium gas in the high temperature region is maintained lower than the average flow velocity in the PPWC. The flow velocity in the lower temperature region is maintained higher than the average to promote heat transfer. The size of the PPWC thus remains compact (Ref. 9, pp. 115-116).

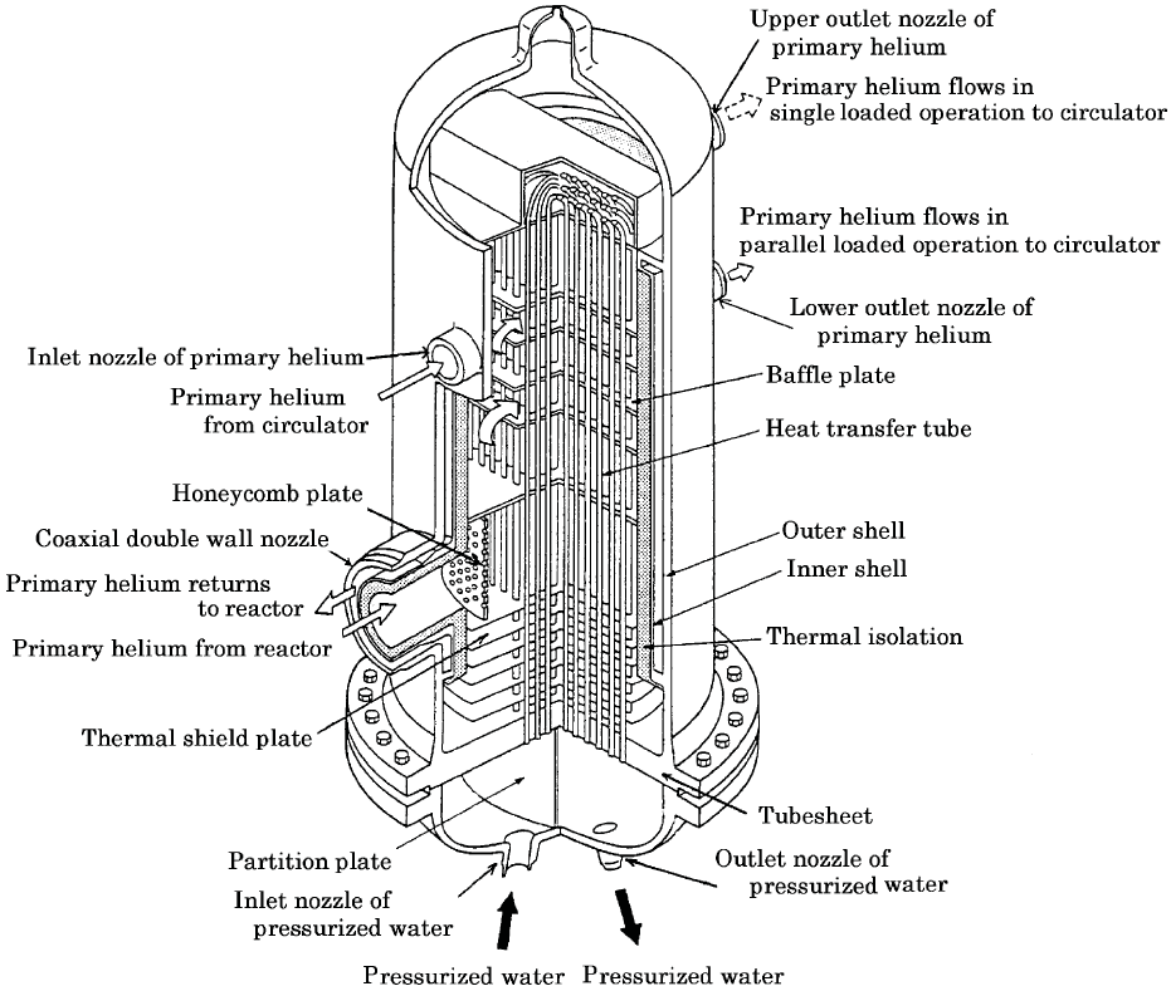


Figure 1.22. The Primary Pressurized Water Cooler (Ref. 9 p. 115).

Table 1.7. Major Specifications of the Primary Pressurized Water Cooler (Ref. 9 p. 116).

| Type | Vertical U-Bent Tube | |
|---|---|---|
| Design Pressure | | |
| Outer Shell (MPa) | 4.7 | |
| Heat Transfer Tube (MPa) | 4.7 | |
| Design Temperature | | |
| Outer Shell (ºC) | 430 | |
| Heat Transfer Tube (ºC) | 380 | |
| Operating Condition | Rated Operation | High Temperature |
| Flow Rate of Primary Helium Gas (t/h) | | |
| Single Loaded Operation (max) | 45.2 | 37.0 |
| Parallel Loaded Operation (max) | 29.7 | 24.3 |
| Inlet Temperature of Primary Helium Gas (ºC) | 850 | 950 |
| Outlet Temperature of Primary Helium Gas (ºC) | 395 | 395 |
| Flow Rate of Pressurized Water (t/h) | | |
| Single Loaded Operation | 625 | 618 |
| Parallel Loaded Operation | 413 | 410 |
| Inlet Temperature of Pressurized Water (ºC) | 135 | 134 |
| Outlet Temperature of Pressurized Water (ºC) | 175 | 174 |
| Heat Capacity (MW) | | |
| Single Loaded Operation | 30 | |
| Parallel Loaded Operation | 20 | |
| Heat Transfer Tube | | |
| Number | 136 | |
| Outer Diameter (mm) | 25.4 | |
| Thickness (mm) | 2.6 | |
| Length (m) | 10 | |
| Outer Diameter of Shell (m) | 2.1 | |
| Total Height (m) | 7.5 | |
| Material | | |
| Outer and Inner Shell | SCMV4-2NT(2-1/4Cr-1Mo Steel) | |
| Heat Transfer Tube | SUS321TB | |
| Tubesheet | SFVA F22B(2-1/4Cr-1Mo Steel) | |

The primary gas circulator is a centrifugal, dynamics gas bearing type circulator (Figure 1.23). Table 1.8 contains the major specifications of the circulator. There are three circulators for the PPWC and one for the IHX in the primary cooling system. The former circulators are operated during both parallel-loaded operation and single-loaded operation while the latter is only operated during parallel-loaded operation.

During operation the rotating assembly is fully floating on a dynamic gas bearing system. The circulator consists of the following components: electric stator and rotor assembly, internal structure supports, thrust bearings and journal bearings, impeller unit, and a filter unit. These internal structures are contained within a casing that is cooled by a water jacket. The casing prevents primary helium gas from leaking into the atmosphere. The flow rate of the gas is controlled by a variable speed motor using a frequency converter. The filter unit, which is on the top of the circulator, protects the impeller and rotating shaft from dust (Ref. 9, p. 118).

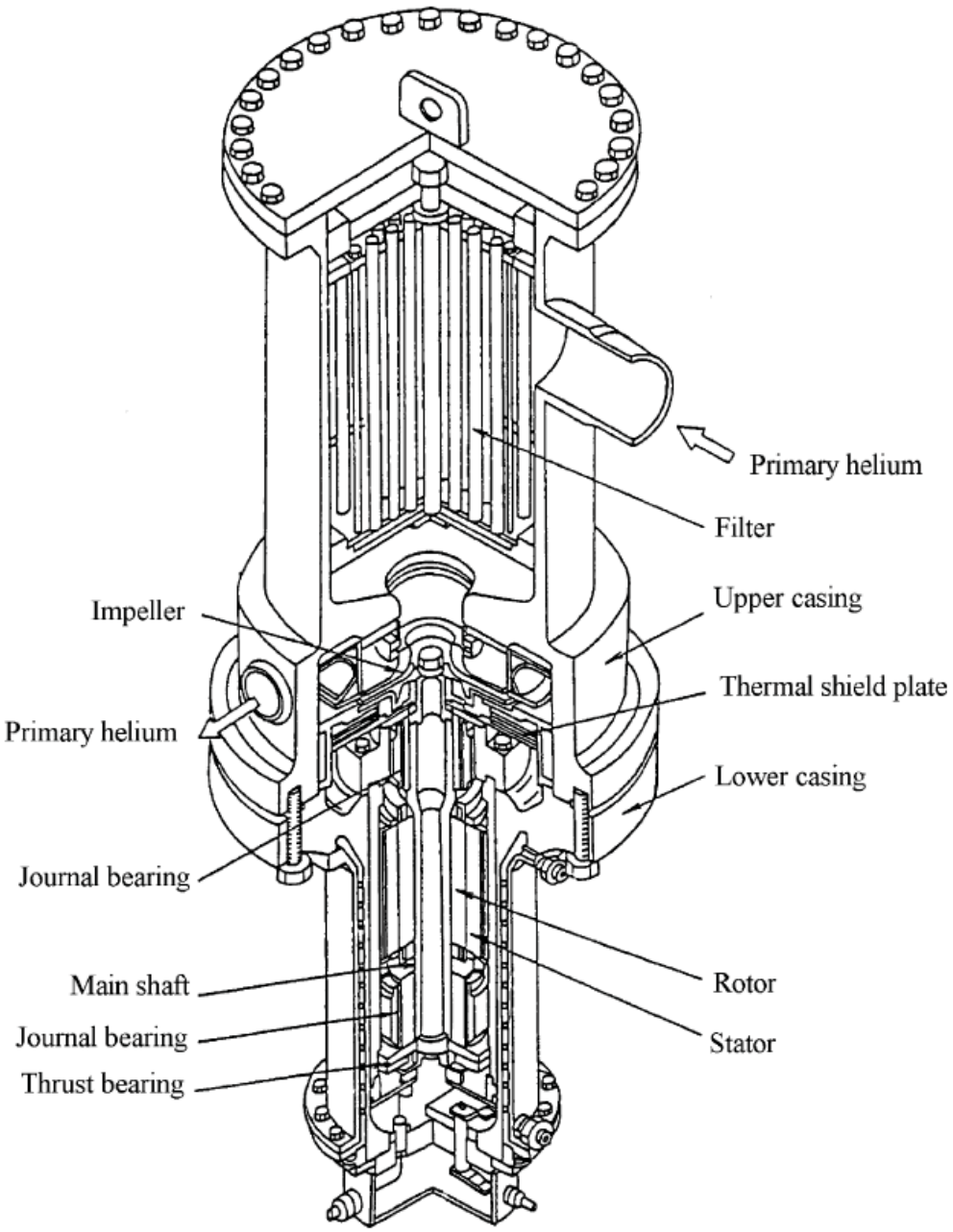


Figure 1.23. The Primary Gas Circulator (Ref. 9 p. 120).

Table 1.8. Major Specifications of the Primary Gas Circulator (Ref. 9 p. 119).

| Type | For the IHX | For the PPWC |
|---|---|---|
| | Centrifugal Gas Bearing | |
| Flow Rate (t/h) | 14.9 (max) | 15.1 (max) |
| Head (kPa) | 79.4 (max) | 107.9 (max) |
| Design Pressure (MPa) | 4.7 | 4.7 |
| Design Temperature (ºC) | 430 | 430 |
| Material | | |
| Casing | SCMV4-2NT SFVA F22B (2-1/4Cr-1Mo Steel) | |
| Motor | | |
| Type | Cage-Type Induction Motor | |
| Power (kW) | 260 | |
| Number of Revolutions (rpm) | 3000 – 12000 | |
| Type of Frequency Converter | Thyristor-Converter | |
| Filter | | |
| Type | Sintering Metal | |
| Material | SUS316 | |

The primary concentric hot gas duct consists of an outer pipe, an inner pipe, and a thermal insulator (Figure 1.24 and Table 1.9). The cold helium gas of 400 ºC flows in an annular path inside the inner pipe, which has a temperature of 950 ºC. The outer pipe can contain high pressure helium gas of 4.0 MPa. The inner pipe, which separates the high and low temperature helium gas paths, supports the pressure difference between the high and low gas. The pressure difference is about 0.1 MPa. The liner forms a high temperature helium gas boundary and reinforces the ceramic fiber insulator. The internal insulator between the liner and inner pipe minimizes heat loss from the high to low temperature helium gases and maintains the temperature of the inner pipe below 440 ºC (Ref. 9, p.119).

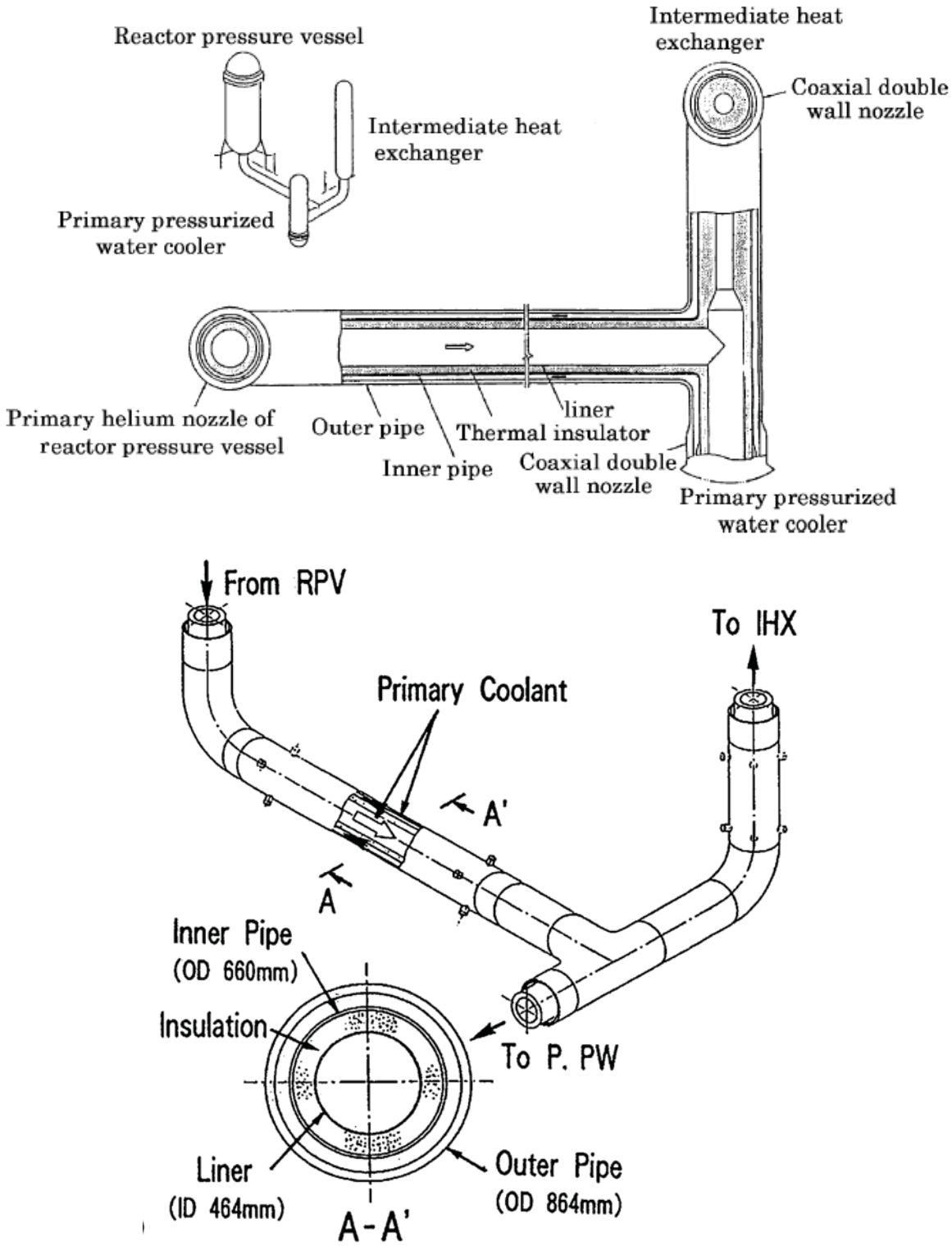


Figure 1.24. The Primary Concentric Hot Gas Duct (Ref. 9 p. 120 and Ref. 14, p. 387).

Table 1.9. Major Specifications of the Primary Concentric Hot Gas Duct (Ref. 9 p. 119).

| | |
|---|---|
| Design Pressure (MPa) | |
| Outer Pipe | 4.7 |
| Design Temperature (ºC) | |
| Outer Pipe | 430 |
| Dimension of Outer Pipe (mm) | |
| Outer Diameter | 863.6 |
| Thickness | 42 |
| Dimension of Inner Pipe (mm) | |
| Outer Diameter | 660.4 |
| Thickness | 15 |
| Thickness of Thermal Insulator (mm) | 90 |
| Material | |
| Outer Pipe | SCMV4-2NT (2-1/4Cr-1Mo Steel)<br>SFVA F22B (2-1/4Cr-1Mo Steel) |
| Inner Pipe | SCMV4-2NT (2-1/4Cr-1Mo Steel) |
| Liner | Hastelloy XR |

The secondary helium cooling system consists of a secondary gas circulator, the secondary pressurized water cooler, and a secondary helium piping. This system is operated during the parallel-loaded operation. The heat is transferred from the primary to the secondary helium gas through the IHX. This heat is sent to the pressurized water cooling system through the secondary pressurized water cooler. In the future, the hydrogen production system will be connected to the secondary helium cooling system (Ref. 9, p. 119).

The structure of the secondary pressurized water cooler is fundamentally the same as of the PPWC. The secondary pressurized water cooler is a vertical U-bent type heat exchanger with double shells. The inner shell is thermally insulated on the inside. The structure of the secondary gas circulator is nearly the same as that of the primary gas circulator. The secondary gas circulator has one vertical centrifugal type gas circulator that is composed of the casing, an impeller, a rotor, bearings, and a motor. The secondary helium piping consists of a concentric hot gas duct connecting the IHX and the secondary pressurized water cooler, and a single wall piping connecting the secondary pressurized water cooler and the secondary gas circulator. Thermal insulation is attached on the inside of the inner pipe of the concentric hot gas duct. The hot helium gas from the IHX flows inside the inner pipe. The helium gas flows in the annular space between the inner and outer pipes (Ref. 9, pp. 120-121).

The pressurized water-cooling system is installed to cool primary and secondary helium gas in the PPWC and secondary pressured water cooler, respectively. The heat is finally released to the atmosphere via an air cooler. This system consists of a pressurized water pump, an air cooler, and piping. The pressure of the water is controlled to be lower than that of the primary cooling system so as to minimize the amount of water ingress into the primary cooling system in the event of a tube rupture accident, but the pressure is still high enough to prevent boiling. Two pressurized water pumps (including a spare) of horizontal centrifugal type are installed. They have a capacity of 640 t/h flow rate at 90 m delivery head. The air cooler consists of finned heat transfer tubes and blowers. It has a 30 MW cooling capacity and an air flow rate of 2600 t/h (Ref. 9, p. 121).

The main cooling system is also used to remove decay heat of the core at normal reactor shutdown conditions. Besides the main cooling system, the HTTR has two other residual heat removal systems, which are the auxiliary cooling system and the vessel cooling system. The auxiliary cooling system removes the residual heat during anticipated operational occurrences and for accidents such as reactivity insertion or pipe rupture in the secondary cooling system. The vessel cooling system removes the residual heat during a loss of coolant accident in the primary cooling system (Ref. 9, p. 121).

The ACS consists of an auxiliary heat exchanger (AHX), two auxiliary helium circulators and an air cooler. At the AHX, the auxiliary helium is cooled by water. During normal operation, a small flow of auxiliary helium (~200 kg/h) passes through the AHX to the primary helium purification system so as to remove impurities contained within the reactor coolant. With a reactor scram, while the reactor coolant pressure boundary remains intact, the auxiliary helium cooling system automatically starts and transfers the residual heat from the core to the auxiliary air cooler. The AHX has heat transfer capacity of approximately 3.5 MW (Ref. 2, p. 8 and Ref. 9, p. 121).

The two VCSs (Figure 1.25) provide protection of the reactor core and RPV against thermal damage by residual heat after a scram when the ACS fails to cool the core. Each of these systems is capable of controlling temperatures of the core and RPV within safe limits and consists of water-cooled panels surrounding the RPV with two cooling water systems. Cooling tubes with fins form the panels and are arranged so that adjacent tubes do not belong to the same system, such that a tube failure will not endanger the RPV and core. The heat removal rate from the RPV to the panels is designed as 0.6 MW. The VCS is also an engineered safety feature equipped with two independent complete sets which are backed up with an emergency power supply. It is operated during normal operation to cool the biological shielding concrete wall (Ref. 2, p.8 and Ref. 9, p. 121).

The structure of the VCS cooling water panel is designed based on heat distribution calculations of the concrete wall of the RPV cavity and the analysis of heat removal values. Four heat reflectors were added between the RPV and the cooling water panel in order to decrease the heat removal values below pre-established limits at higher thermal loads. Cooling water pipes were added to the innermost reflector to increase heat removal values for low thermal loads. The pitch between two cooling water pipes is 120 mm. After the VCS was manufactured and installed, it had component testing completed by 1997 (Ref. 14, p. 380).

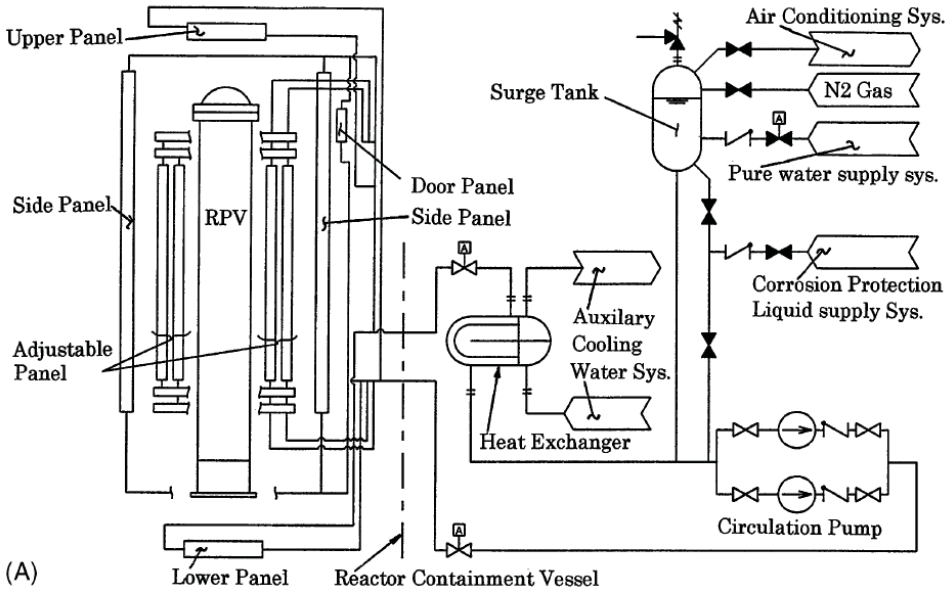


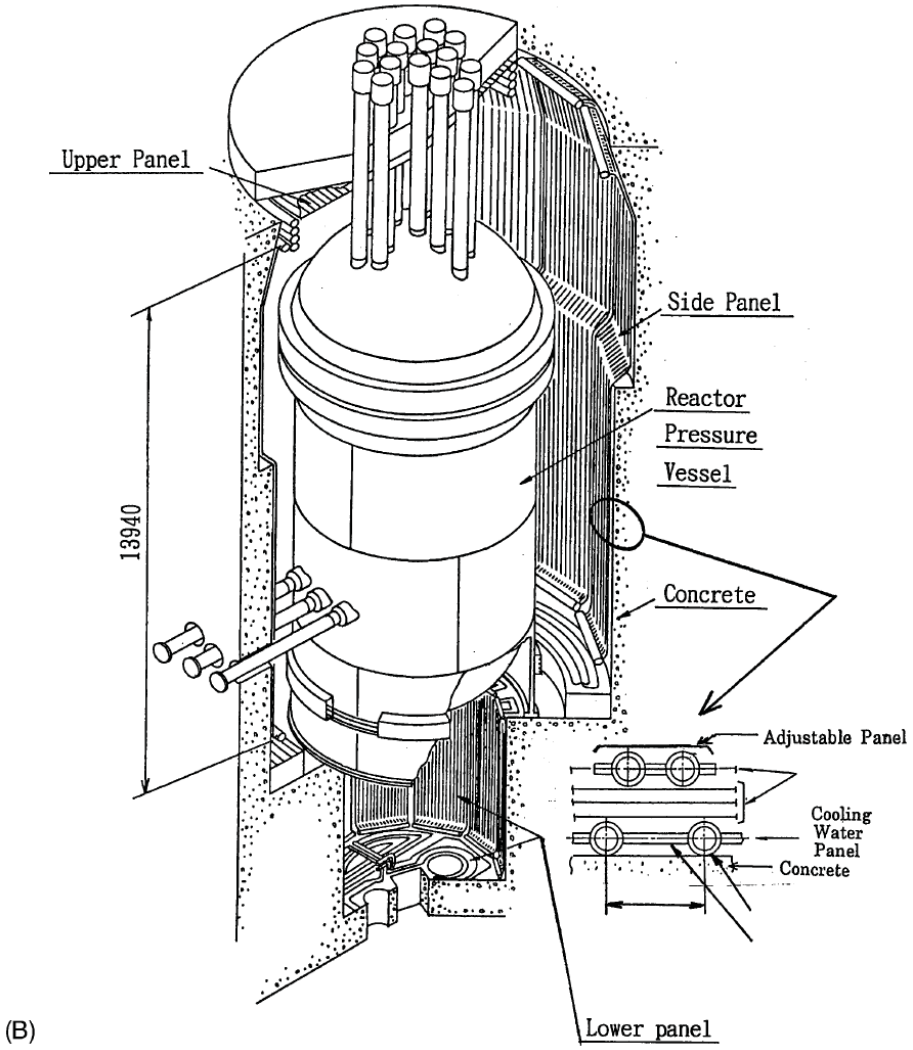


Figure 1.25. Structural View of the Water Cooling Panel of the Vessel Cooling System (Ref 14 p. 381).

## Utility Systems

The utility systems of the HTTR include the auxiliary helium systems (helium purification, helium sampling, and helium storage and supply) and fuel handling and storage. The helium purification system is installed in the primary and secondary helium cooling systems to reduce the quantity of chemical impurities that could induce corrosion of the reactor and its components. The helium sampling systems monitor the concentration of impurities and the helium storage and supply systems provide a steady pressure supply of helium during normal operation. The fuel handling and storage system is used to manage new and spent fuels. Refuelling occurs every three reactor years (Ref. 11, pp. 147-148).

The helium purification systems reduce the quantity of chemical impurities such as hydrogen, carbon monoxide, water vapor, carbon dioxide, methane, oxygen, and nitrogen to limits below those shown in Table 1.10. The primary helium purification system is mainly composed of a pre-charcoal trap, an inlet heater, two copper oxide fixed beds, coolers, two molecular sieve traps, two cold charcoal traps, and gas circulators. A flow diagram is shown in Figure 1.26. The secondary helium purification system is identical to the primary one, except that it does not have a pre-charcoal trap. The helium flow rate is 200 kg/h. The primary helium gas is introduced into the helium purification system through the auxiliary cooling system and the purified gas returns to the ACS and standpipes (Ref. 11, p. 148).

Table 1.10. Upper Impurity Limit in the Primary Coolant at 4 MPa and a Reactor Outlet Coolant Temperature between 800 to 950 ºC (Ref. 11 p. 148).

| Impurity | Concentration (ppm) |
|---|---|
| $H_2$ | 3.0 |
| CO | 3.0 |
| $H_2O$ | 0.2 |
| $CO_2$ | 0.6 |
| $CH_4$ | 0.5 |
| $N_2$ | 0.2 |
| $O_2$ | 0.04 |

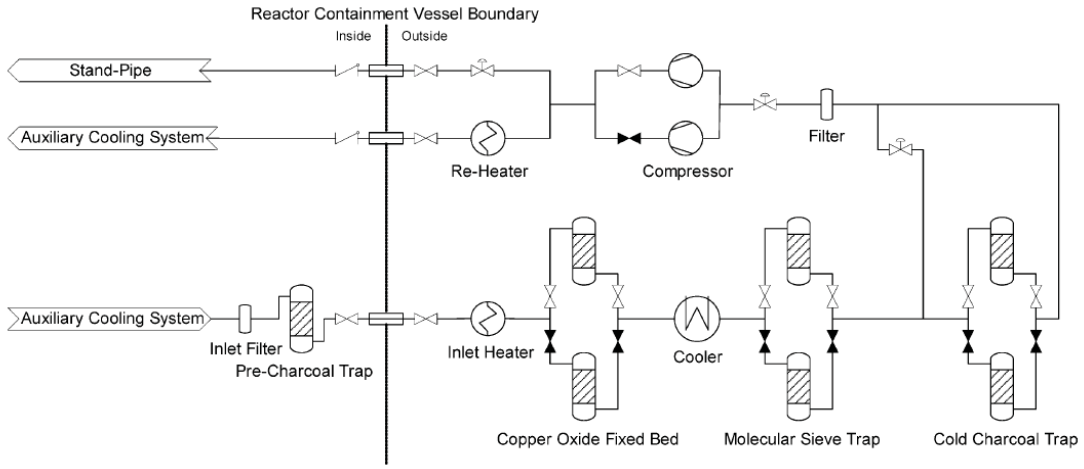


Figure 1.26. Flow Diagram of the Primary Helium Purification System (Ref. 11 p. 148).

The helium sampling system detects chemical and radioactive impurities in the primary cooling system and secondary helium cooling system using gas chromatograph mass spectrometers. Both systems transmit impurity concentration measurements to the main control room. The helium storage and supply systems are installed for the primary cooling system and the secondary helium cooling system. The primary helium storage and supply system is composed of storage tanks, a supply tank, and helium compressor. The primary coolant is kept at a fixed pressure of about 4.0 MPa during normal operation. The secondary helium storage and supply system stores helium gas at a pressure higher than that of the primary coolant. The primary helium system has six storage tanks with a capacity of 220 kg each and a supply tank with a capacity of 110 kg. Two helium gas compressors are installed with one compressor on stand-by. The supply valve for the primary coolant opens and closes at 3.92 to 3.99 MPa, respectively, and the exhaust valve opens and closes at a pressure of 4.00 and 3.96 MPa, respectively. The supply rate of the helium gas is used for detecting the leakage rate of primary coolant during operation. The secondary helium system has a storage tank capacity of 25 kg, a supply tank capacity of 10 kg, and two compressors. The supply valve for the secondary coolant opens and closes at a pressure difference of -29.4 and -9.8 kPa, respectively, and the exhaust valve opens and closes at a pressure difference of 29.4 and 19.5 kPa, respectively. The design pressure difference between the primary and the secondary coolant is 73.5 kPa (Ref. 11, pp. 149-150).

The fuel handling system, utilized to install and remove fuel elements, replaceable reflector blocks, top shielding blocks, control rod guide blocks, and control rods, consists of a fuel handling machine, attached equipment, and auxiliary equipment. The fuel handling machine consists mainly of a shielded cask, a gripper, a fuel handling unit drive system, a rotating rack, and a door valve. The machine has a shield sufficient to protect fuel handling personnel, has a gas-tight boundary, and maintains subcriticality when fully loaded. A diagram and photo of the fuel handling and storage systems are shown in Figures 1.27 and 1.28, respectively (Ref. 11, p 151).

The fuel handling machine (Figure 1.29) is 11 m in height and weighs 150 tons. It has a capacity to store 10 fuels blocks at a time. The fuel handling mechanism that grips the fuel block is hung down by wire rope and chain, and can access 13 columns through each standpipe. The fuel handling mechanism consists of a gripper that grips fuel blocks and a support link with a pantograph-type arm that guides the gripper movement. The gripper has latch pawls on the underside that are inserted into the fuel block and opened to hook and lift the block that weighs about 200 kg (Ref. 14, p. 385).

The HTTR has two fuel storage systems, one for new fuel and the other for spent fuel. The storage system for the fresh fuel consists of fuel assembly and testing equipment, a new-fuel storage cell, and inert gas replacement equipment. Up to 1.5 times the core inventory can be stored in new-fuel storage. A vertical, cylindrical vessel provides sufficient distance between storage racks to ensure subcriticality. The fuel elements are maintained in a dry, inert environment. The spent-fuel storage system is located inside the reactor building, and consists of a spent-fuel storage pool, water cooling and purification system, and irradiated material storage pits for spent fuel elements, control rod guide blocks, and replaceable reflector blocks (Figure 1.30). The spent-fuel storage has sufficient shielding and capacity to store about two core inventories. The inside of the pool is lined with stainless steel to prevent leakage of the pool water. After two years of cooling, the spent fuel is transferred to another spent-fuel storage system located in a neighboring building to the HTTR facility (Ref. 11, pp. 153-154).

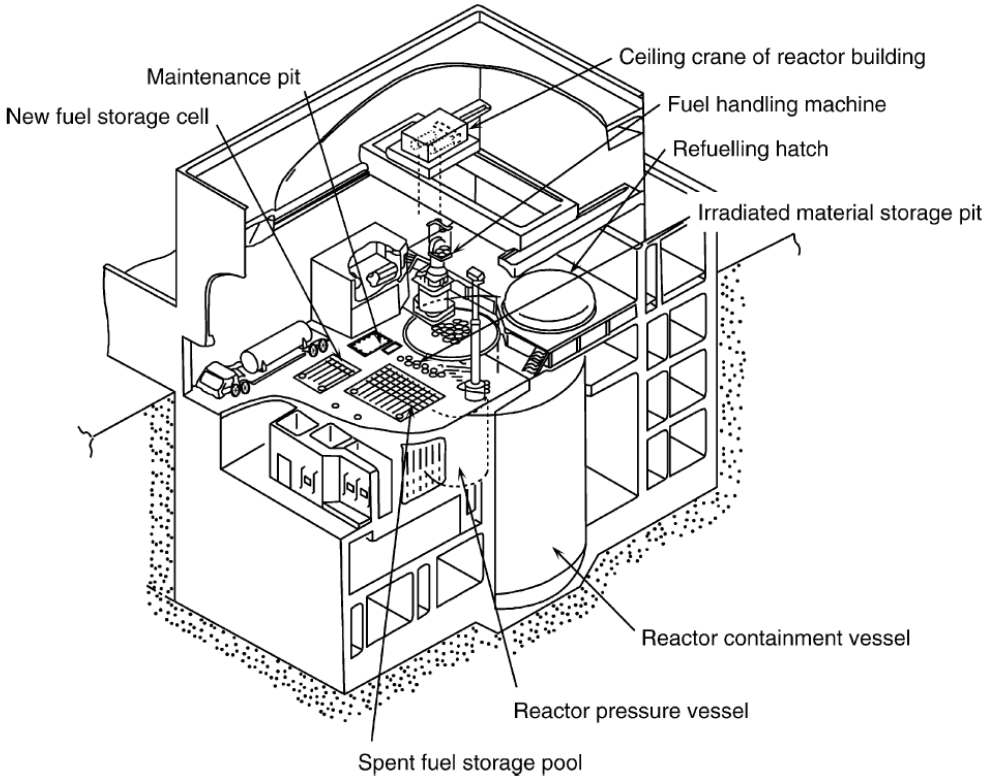


Figure 1.27. The Fuel Handling and Storage System in the Reactor Building (Ref. 11 p. 151).

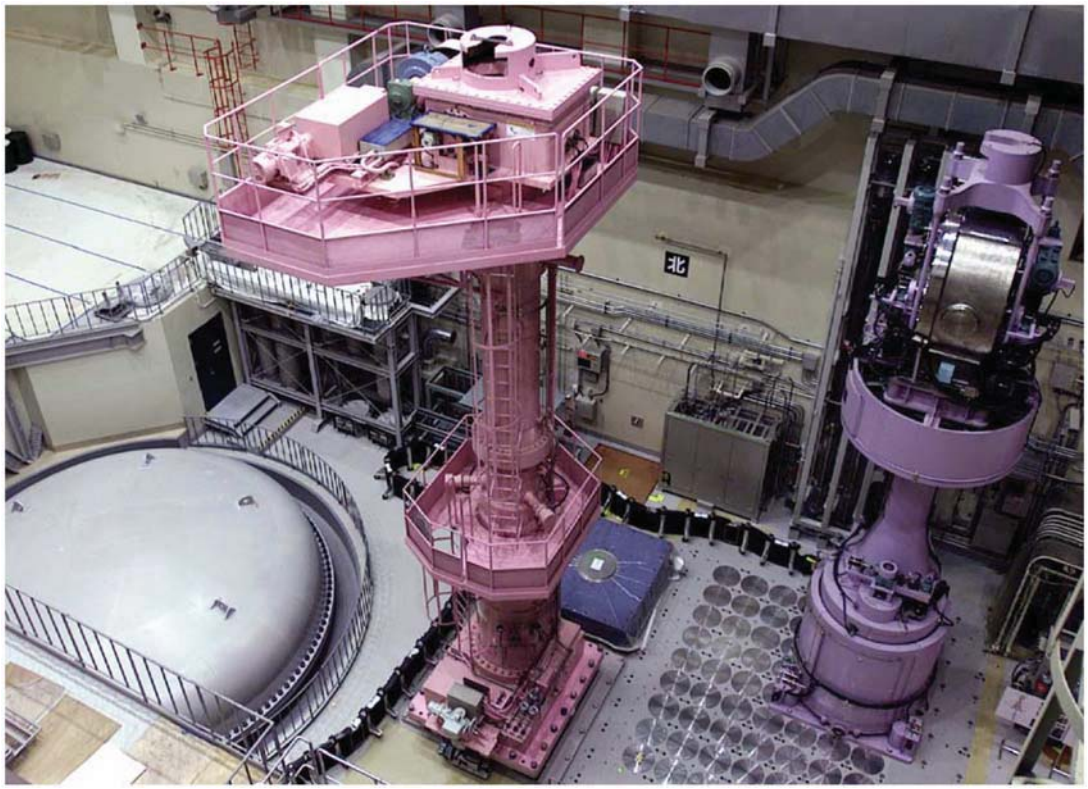

Figure 1.28. Photo of the Operation Floor in the Reactor Building (Ref. 11 p. 152). The fuel handling machine is above the spent-fuel storage pool on the right. The control-rod handling machine and refueling hatch of the reactor containment vessel are seen at the center and the left side, respectively.

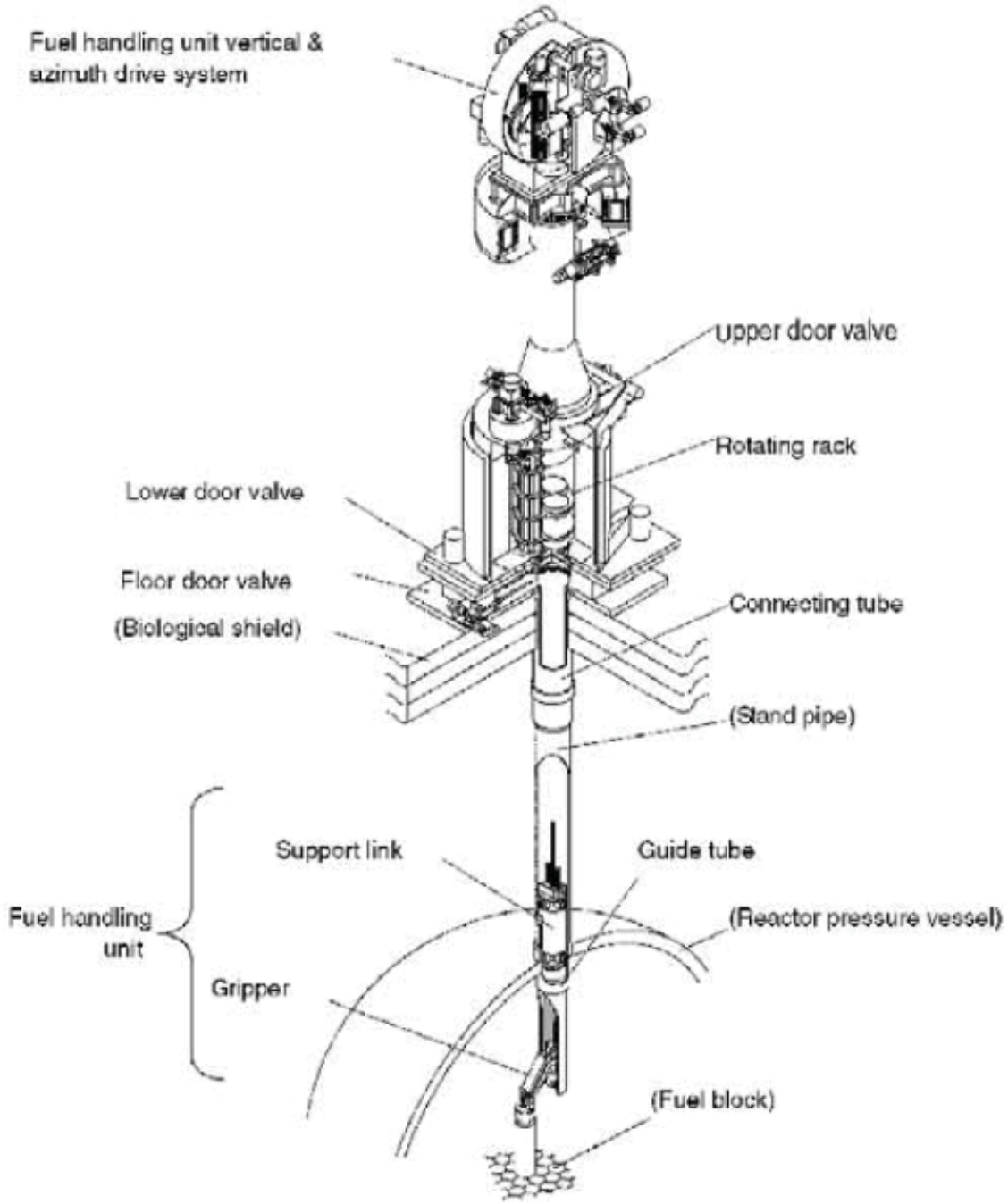


Figure 1.29. HTTR Fuel Handling Machine (Ref. 14, p. 384).

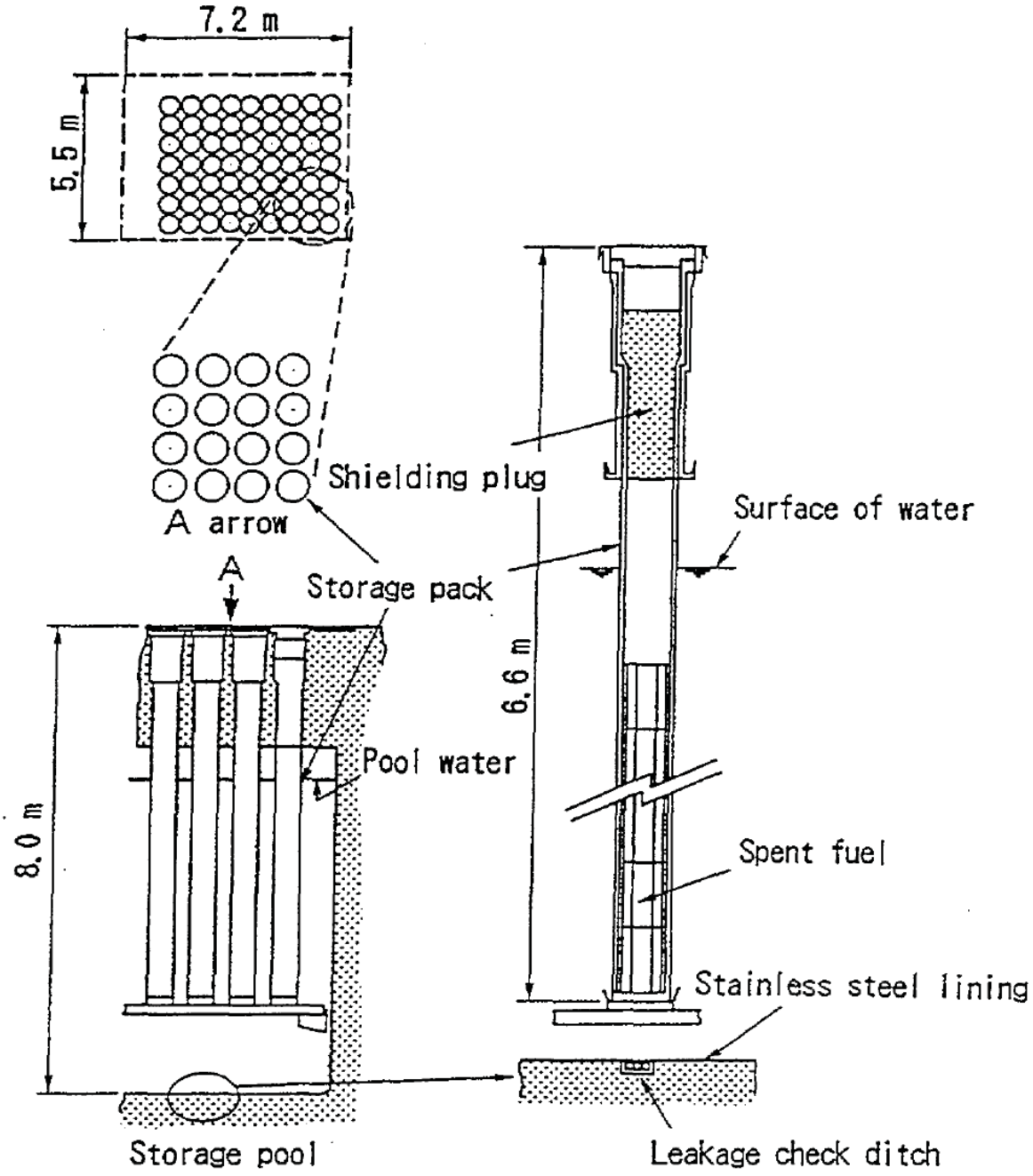


Figure 1.30. Spent Fuel Storage System in the HTTR Reactor Building.[a]

[a] K. Sawa, S. Yoshimuta, S. Shiozawa, S. Fujikawa, T. Tanaka, K. Watarumi, K. Deushi, and F. Koya, "Study on Storage and Reprocessing Concept of the High Temperature Engineering Test Reactor (HTTR) Fuel," IAEA-TECDOC-1043, International Atomic Energy Agency, Vienna, pp. 177-189 (September 1998).

### *1.1.2.2 Reactor Internals*

Fuji Electric collaborated with JAERI for much of the thermal-hydraulic, nuclear, and safety design analysis of the HTTR. They supplied major equipment such as the reactor internals, the fuel handling and storage facilities, and the radiation monitoring system (Ref. 14, p. 384).

The reactor internals consist of graphite core support structures, metallic core support structures, and the other components shown in Figure 1.31. The graphite support structures include hot plenum blocks, core bottom structures, and core support posts. The hot plenum blocks provide lateral and vertical positioning and support of the core array. The blocks contain flow paths that guide the primary coolant from the outlet of the fuel columns and distribute it into the hot plenum beneath the hot plenum blocks. The core support posts are designed such that they support the core and hot plenum block arrays, which form the hot plenum. The permanent reflector block is a graphite structure surrounding the replaceable reflector blocks and control rod guide blocks located in the circumference of the active core. The metallic core support structures are composed of core support plates, a core support grid and the core restraint mechanisms. The core support plate and the core support grid are placed below the thermal insulation layers. The core restraint mechanism surrounds the permanent reflector blocks (Ref. 3, pp. 15-16, and Ref. 6, p 82).

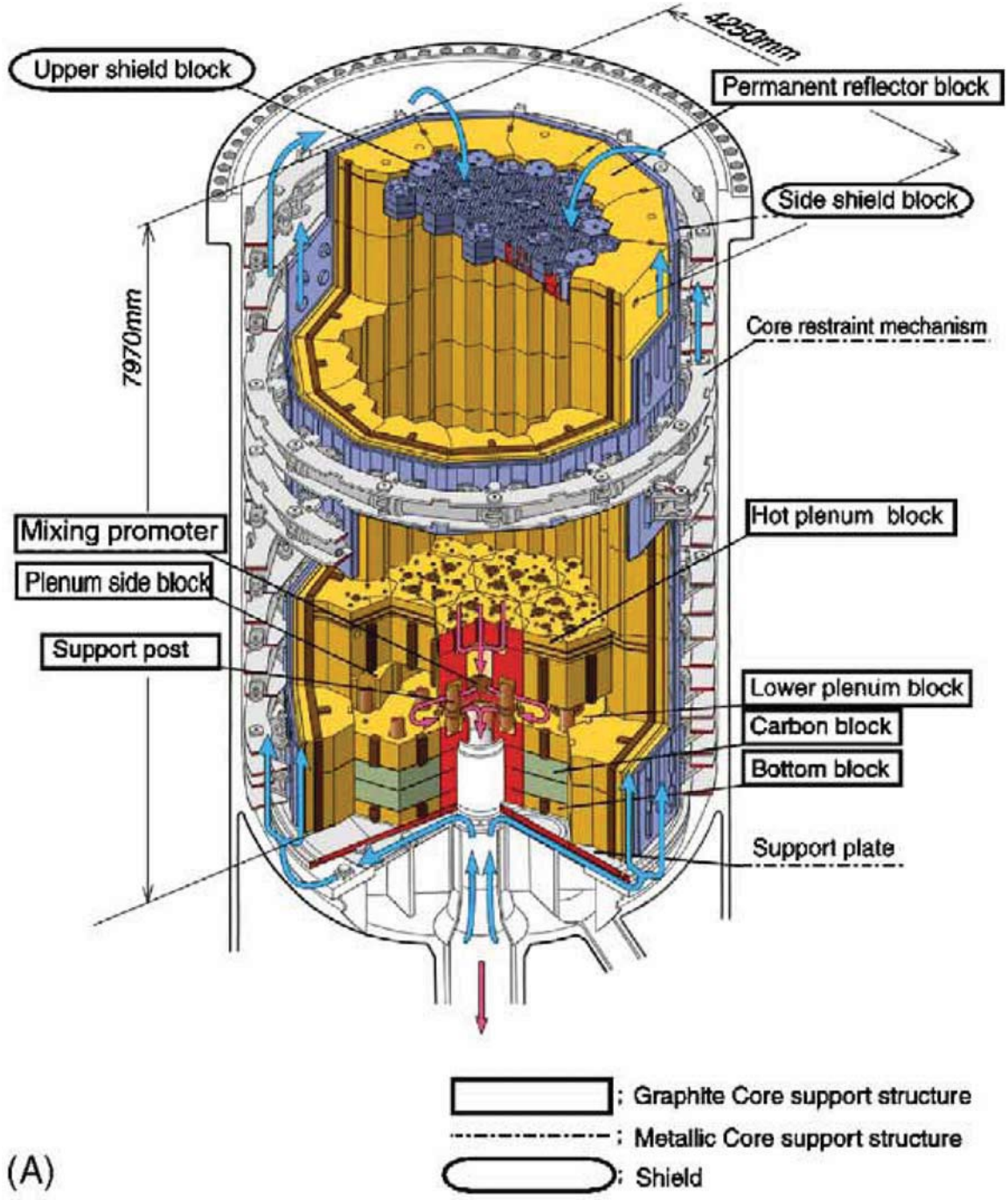


Figure 1.31. Reactor Core Internals of the HTTR (Ref. 14, p. 384).

## Graphite Support Structure

The structures at the core bottom consist of three types of blocks: lower plenum blocks, carbon blocks, and bottom blocks. These blocks function as thermal insulation between the hot plenum and metallic core support structure (Ref. 6, p. 83).

The hexagonal hot plenum block array is made up of two axial layers. The upper layers consist of sealed plenum blocks, in which leakage flow between these blocks is sealed by the triangular seal elements. The lower layer is composed of keyed plenum blocks, which provide lateral and vertical positioning and support of the core array. The hot plenum block assembly contains passages for the primary coolant flow from the columns in the core to the hot plenum (Ref. 6, p. 82).

The hot plenum block is 0.9 m in height and about 1 m across flats. They are combined with each other by key-keyway systems and are supported separately by core support posts that are 0.6 m in length and 0.15 m in diameter. Both ends of a core support post are spherical and fit into similarly shaped recesses in the post seats. The curvature radii of the ends of the core support post differ from those of the post seats to accommodate the relative motion between the hot plenum block and the lower plenum block.[a]

The support posts and seats are designed to support the core and hot plenum blocks while providing the hot plenum for the primary coolant flow. The hot plenum space is where the hot core outlet helium gas can be mixed uniformly (Ref. 6, pp. 82-83).

A diagram depicting the hot plenum blocks and support post is shown in Figure 1.32. A close-up of the reactor core internals at the bottom of the HTTR is shown in Figure 1.33. A diagram of the high-performance triangular shape seal used to minimize leakage in the hot plenum is depicted in Figure 1.34. These elements provide superior stability (Ref. 15, p. 41) and increase the effective core cooling by reducing gap-flow between the blocks.[b]

[a] T. Iyoku, J. Smita, M. Ishihara, and S. Ueta, "R&D on Core Seismic Design," *Nucl. Eng. Des.*, **233**: 225-234 (2004).

[b] S. Maruyama, A. Saikusa, S. Shiozawa, N. Tsuji, and T. Miki, "Results of Assembly Test of HTTR Reactor Internals," IAEA-TECDOC-901, International Atomic Energy Agency, Vienna, pp. 105-116 (August 1996).

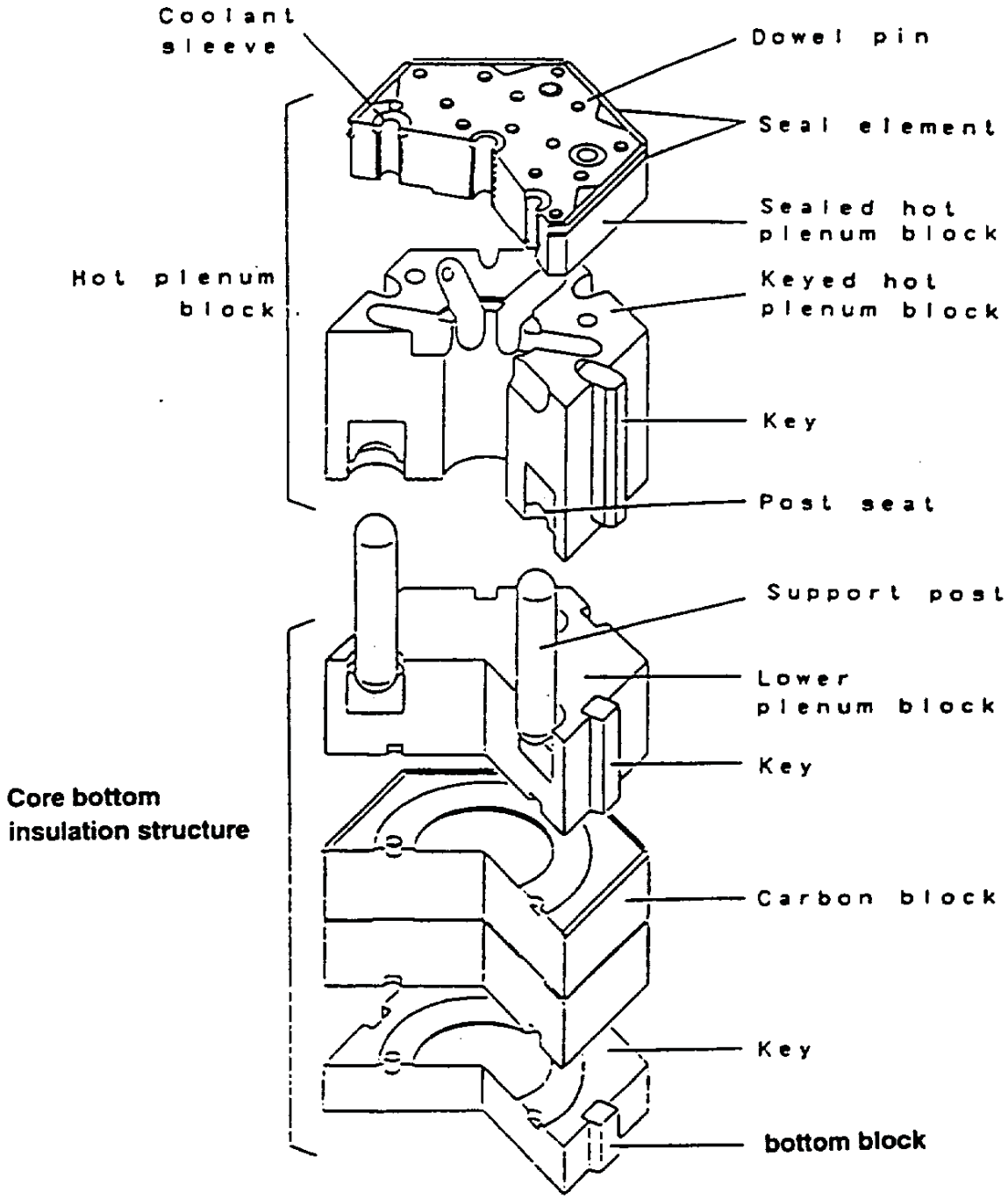


Figure 1.32. Keyed Plenum Block and Core Bottom Graphite Structure.[a]

[a] S. Maruyama, A. Saikusa, S. Shiozawa, N. Tsuji, and T. Miki, "Results of Assembly Test of HTTR Reactor Internals," IAEA-TECDOC-901, International Atomic Energy Agency, Vienna, pp. 105-116 (August 1996).

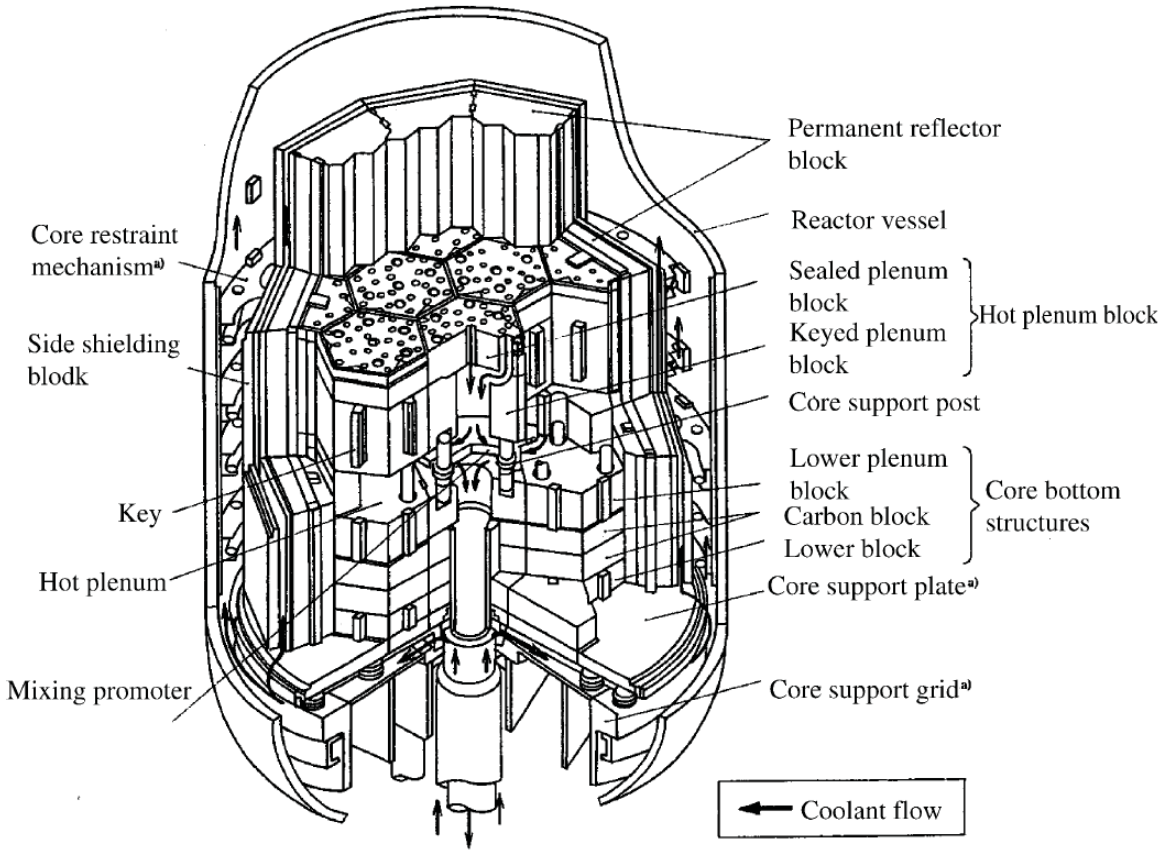


(a) metallic core support structures

Figure 1.33. Reactor Core Internals of the HTTR (Ref. 3, p. 17).

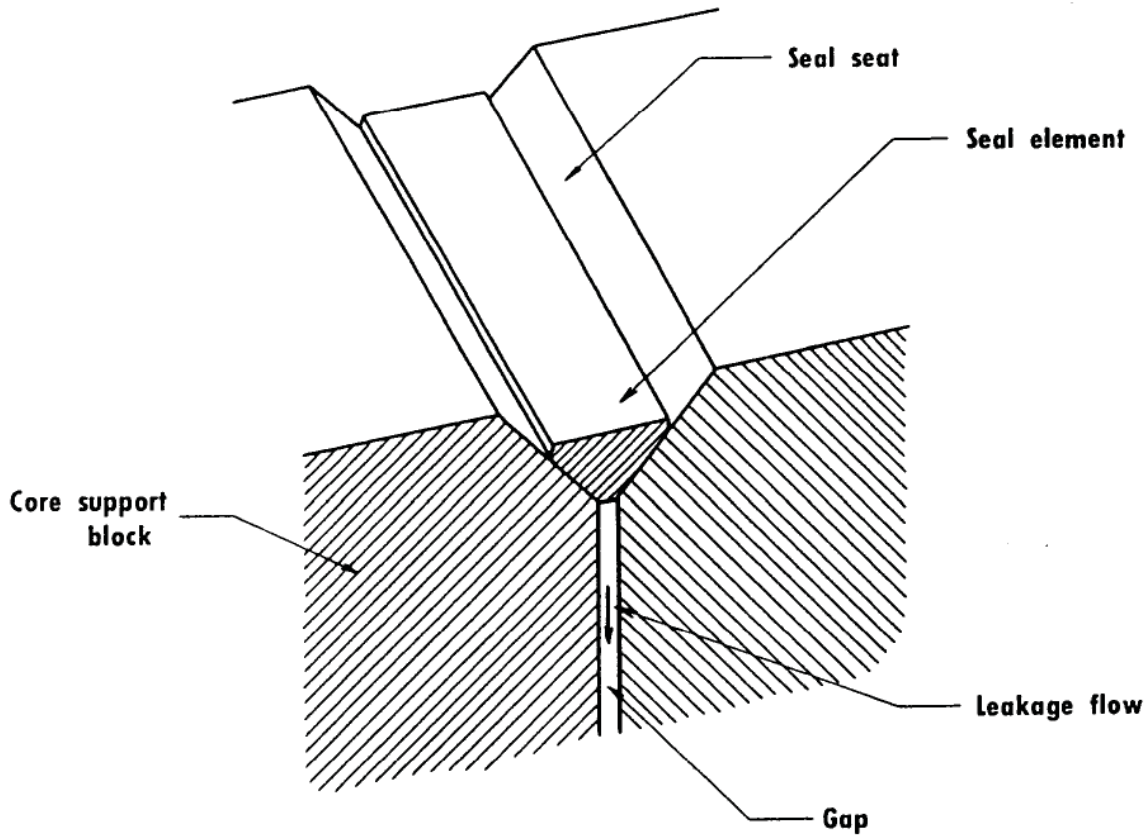


Figure 1.34. New Seal Mechanism for Hot Plenum Block (Ref. 15, p. 41).

## Metallic Support Structure

The metallic core support structures include a support plate, the core support grid, and the core restraint mechanism, as shown in Figure 1.33. The support plate and core support grid are located under the core-bottom insulation layer. The core restraint mechanism surrounds the permanent reflector blocks. The support plate and core support grid form a statically stable foundation for the core components and reactor internals under seismic loads and elevated temperatures (Ref. 6, p. 84).

The support plate forms a plain foundation surface for the core components and reactor internals, and is composed of steel plates with a thickness of 89 mm. The support plates are set on steel support posts, guiding the core weight to the core support grid below. The core support grid transfers the total weight of the core to the RPV through the support ribs welded onto the inner surface of the hemispherical bottom head closure. The grid is reinforced with welded diamond-shaped plate structures. The support plate and the core support grid are cooled by the primary coolant flowing into the RPV (Ref. 6, p. 85).

The core restraint mechanism surrounds and stresses the permanent reflector blocks with 10 axially distributed units. Each unit consists of 12 restraint bands, 12 band supports, and 2 restraint rings and radial keys, as shown in Figure 1.35. The restraint bands are stressed to produce radial force on the band supports that is transmitted to the permanent reflector blocks via the side shield blocks and support legs. The restraint rings, located above and below the restraint bands, are normally stress free. They limit radial displacement of the bands during seismic events. Normally there is no contact between the restraint rings and the radial keys. The radial keys are individually adjusted before being attached to the RPV and are provided to compensate for circumferential fabrication tolerances. The restraint bands are composed of a central rod and six concentric pipes, as shown in Figure 1.36, except for the 9$^{th}$ and 10$^{th}$

units. These latter units have eight concentric pipes each. The pipes are connected in series with the pipes mutually acting as compression and tensile elements. The whole arrangement forms a tensile spring with the bolt eyes connected to the central bar on one end and to the outer pipe on the other end of the band (Ref. 6, p. 85).

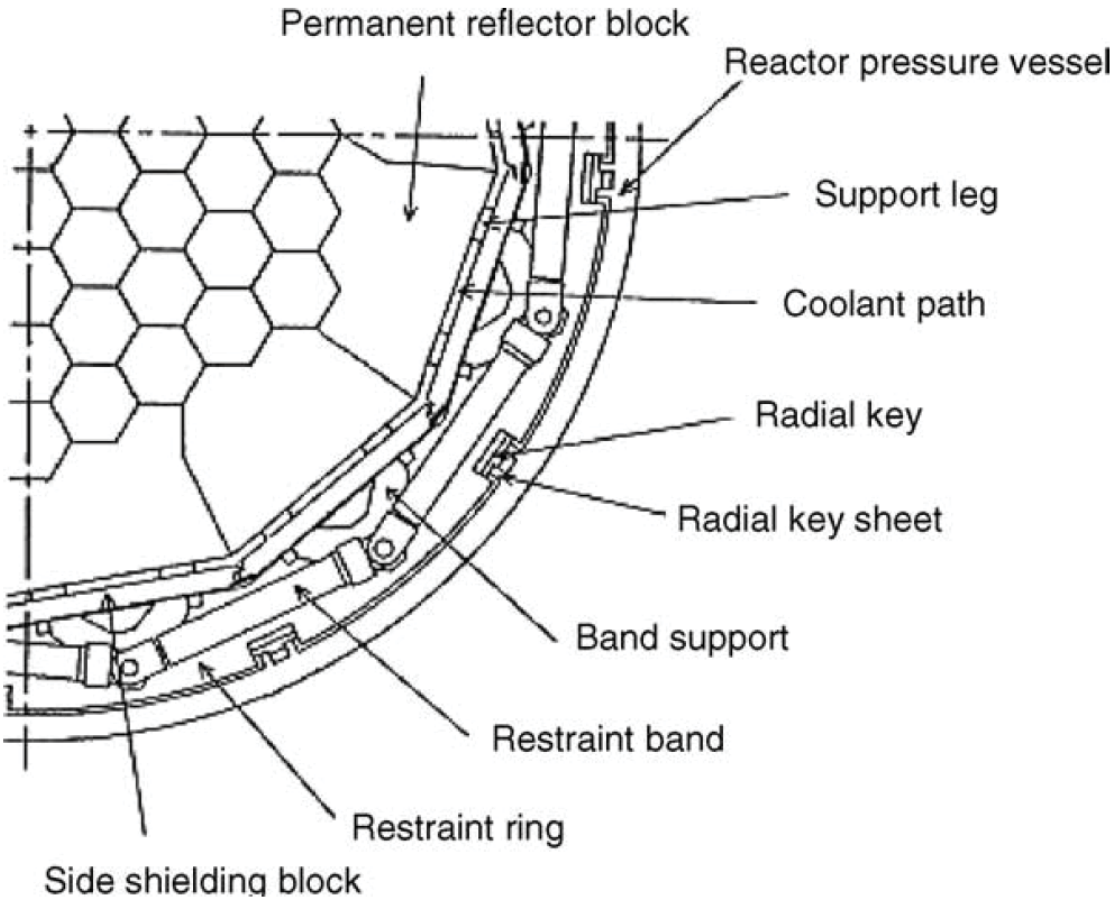


Figure 1.35. Core Restraint Mechanism (Ref. 6, p. 85).

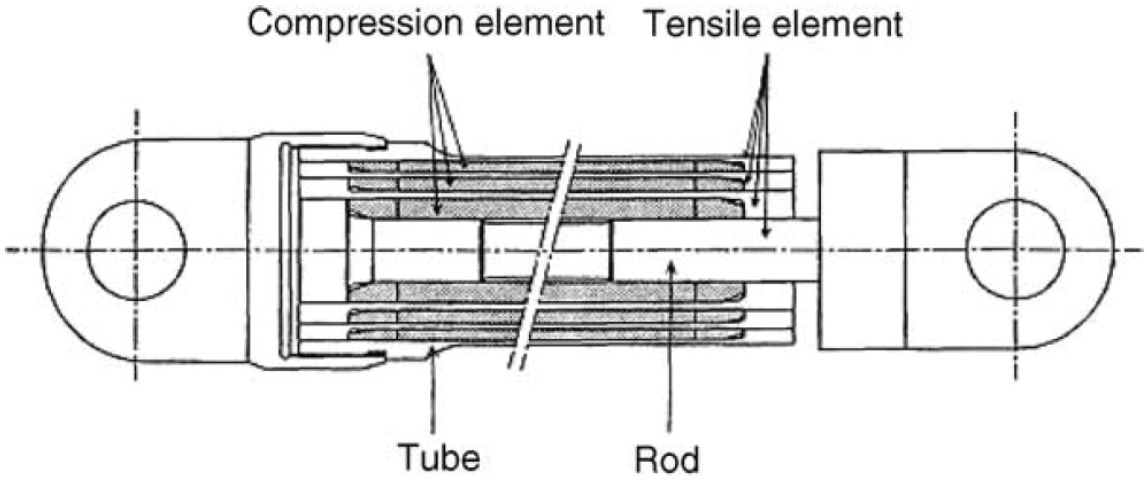


Figure 1.36. Core Restraint Band (Ref. 6, p. 85).

## Reactor Core Shielding

Shielding consists of top and side shielding blocks composed of neutron absorbing material and casing. The top shielding block is installed at the top of each column, and has coolant channels matching the channels in the column below. The side shielding blocks are installed outside of the permanent reflector blocks and are compressed inward by the core restraint mechanism. The top shielding block is hexagonal and composed of sintered $B_4C/C$, a casing of SUS316, and dowel pins. The top shielding blocks for the fuel columns have an internal cavity for coolant in order to prevent neutron streaming (Figure 1.37). Dowel pins on the top are used for positioning of the handling head of the fuel handling machine. The side shielding block is also composed of $B_4C/C$ and a SUS316 casing, as shown in Figure 1.38. Four support legs are connected directly to the thick SUS316 plate, which locates the RPV side of the blocks and transfers the compressive forces of the restraint band to the permanent reflector blocks (Ref. 6, p. 86).

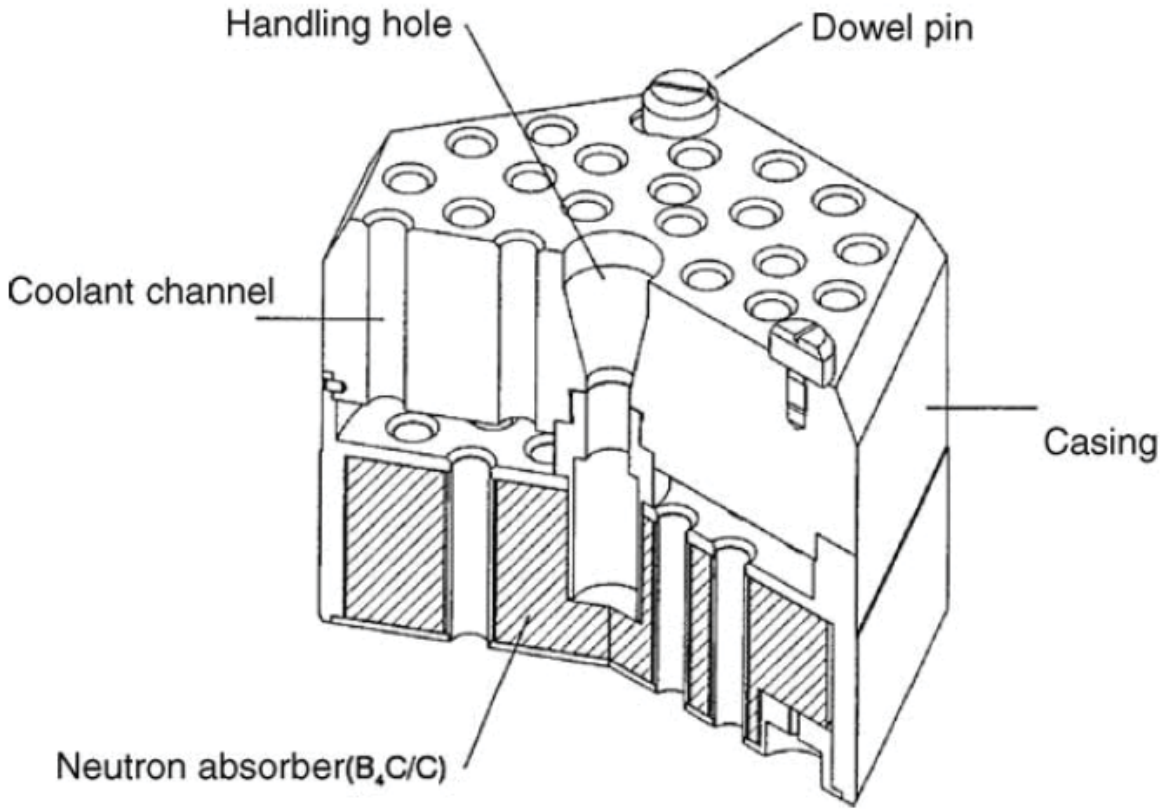


Figure 1.37. Top Shielding Block (Ref. 6, p. 86).

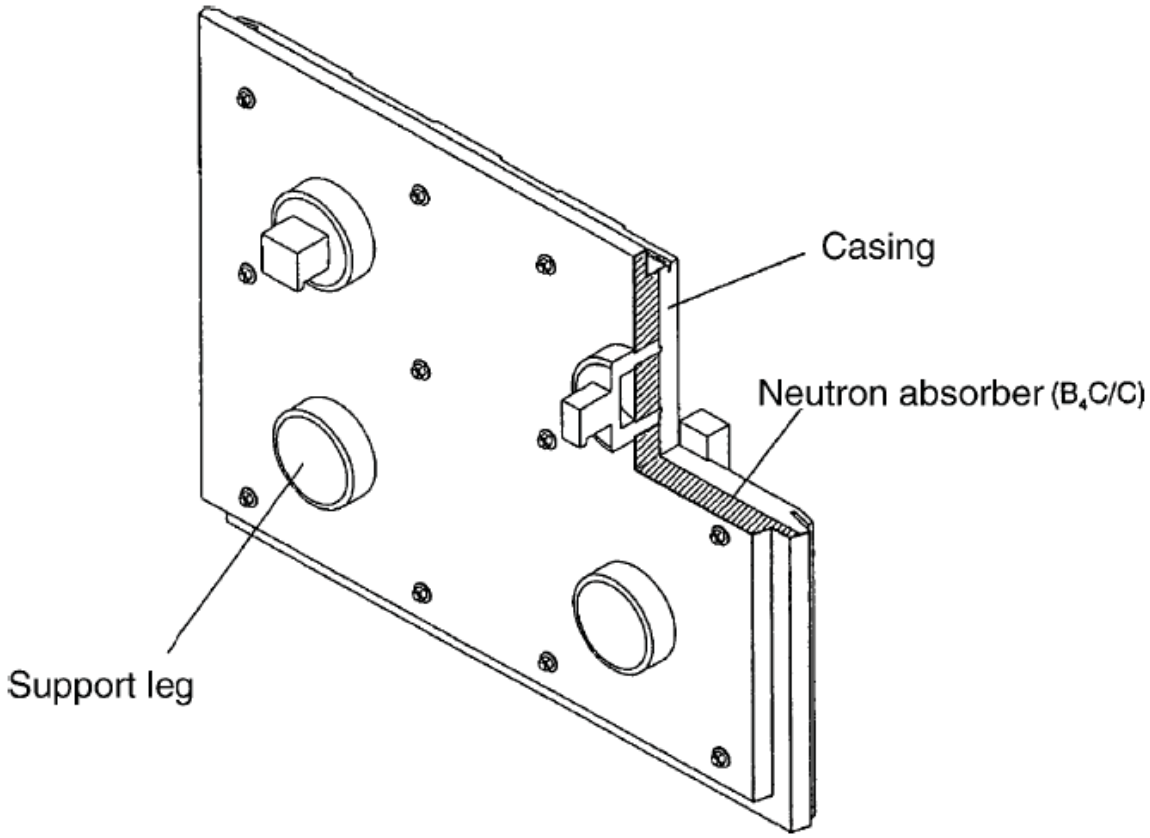


Figure 1.38. Side Shielding Block (Ref. 6, p. 86).

## General Instrumentation and Control Systems

The nuclear instrumentation for the HTTR is comprised of a wide range monitoring system (WRMSS) and a power range monitoring system (PRMS), shown in Figure 1.39. The wide range monitoring system is available as a post accident monitor under accident conditions such as rupture of the primary concentric hot gas duct. The wide range monitoring system is used to measure the neutron flux from $10^{-8}$ to 30% of rated power. Three fission chambers are installed in the permanent reflector blocks through the stand-pipes. The power range monitoring system is used to measure the neutron flux from 0.1 to 120% of rated power. The power range monitoring system is also used as the sensor for the reactor power control system. The detectors of the power range monitoring system are located outside the reactor pressure vessel. The detectors have high sensitivities so as to detect the neutron flux at very low levels. In order to monitor the core outlet temperature of the primary coolant, seven thermocouples are arranged in the hot plenum blocks below the reactor core. N-type thermocouples (Nicrosil-Nisil) are selected because the temperature of the primary coolant in the hot plenum reaches about 1000 ºC at rated power operation. The fuel failure detection system is composed of precipitators, a pre-amp, and a control box. The precipitator is used to detect β-rays radiated from short-lived gaseous fission products such as Kr-88, Kr-89, and Xe-138 (Ref. 3, p. 18). Additional details regarding the reactor instrumentation is summarized elsewhere.[a]

The maximum temperature of the blocks has also been reported of reaching about 1100 ºC during high temperature operation (Ref 7, p. 90).

[a] K. Saito, H. Sawahata, F. Homma, M. Kondo, and T. Mizushima, "Instrumentation and Control System Design," *Nucl. Eng. Des.*, **233**: 125-133 (2004).

The WRMS fission counter is used under a high temperature environment at the top of a permanent reflector. The PRMS uncompensated ionization chamber can detect a low neutron flux level outside the RPV. In the HTTR, the temperature around the wide range detector becomes about 600 ºC and the neutron flux level around the power range detector becomes about $10^7$ n/cm$^2$-s during the rated power operation of 30 MW (Ref. 15, pp. 111-112).

The control system of the HTTR consists of an operational mode selector, a reactor power control system, and a plant control system. Microcomputers are used for the plant control system and the reactor power control system. An operational mode selector supervises them. A schematic of the HTTR control system is shown in Figure 1.40. Additional information regarding reactor control design is summarized elsewhere.[a]

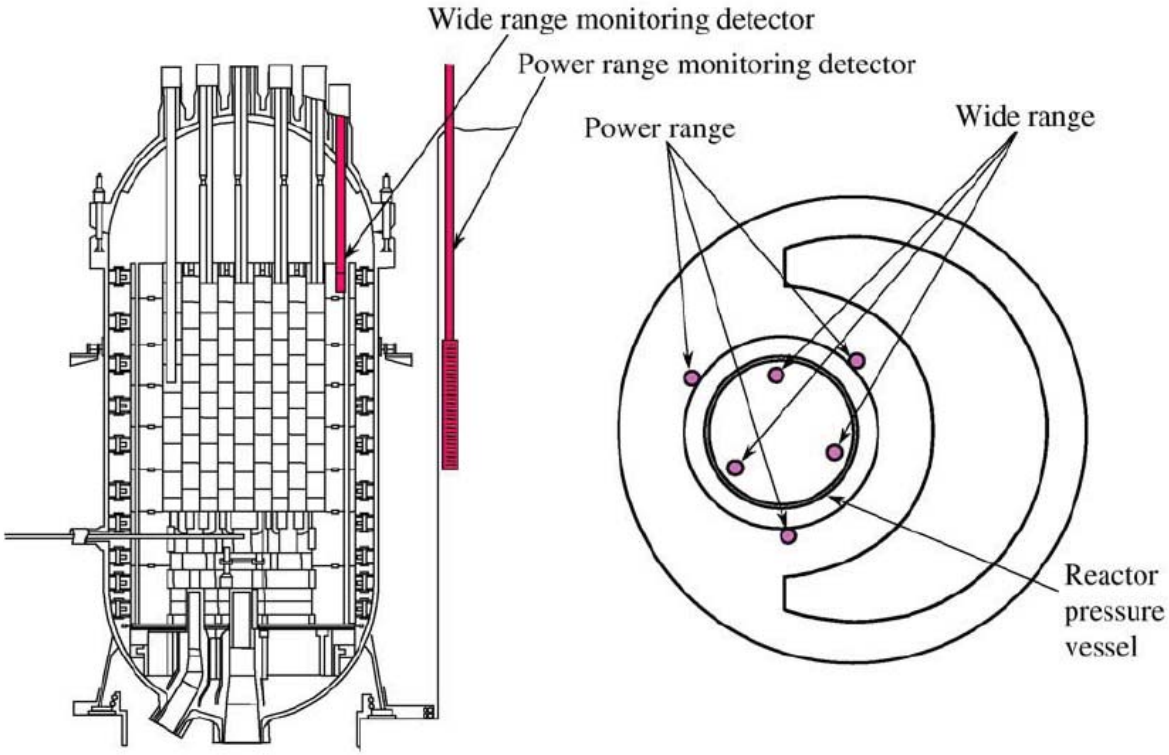


Figure 1.39. Neutron Detection Arrangement.[b]

[a] K. Saito, H. Sawahata, F. Homma, M. Kondo, and T. Mizushima, "Instrumentation and Control System Design," *Nucl. Eng. Des.*, **233**: 125-133 (2004).

[b] K. Saito, H. Sawahata, F. Homma, M. Kondo, and T. Mizushima, "Instrumentation and Control System Design," *Nucl. Eng. Des.*, **233**: 125-133 (2004).

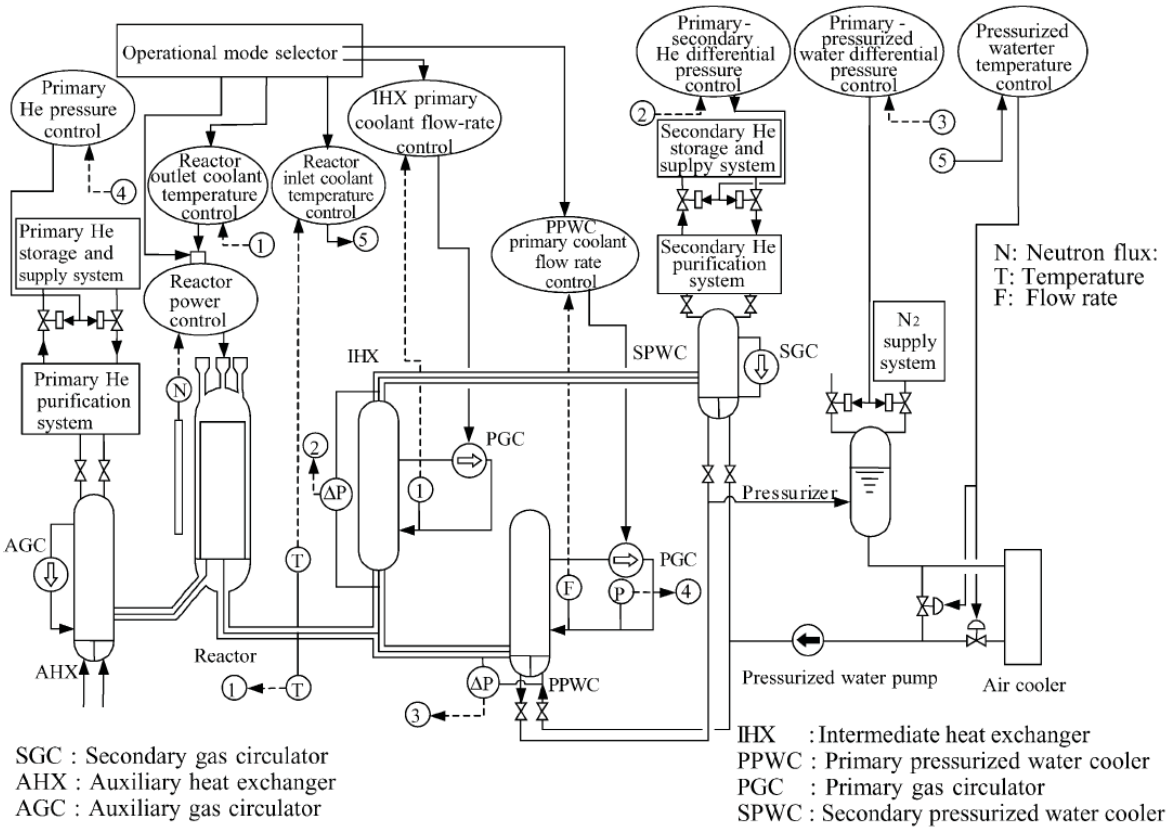


Figure 1.40. Schematic Diagram of the Control System of the HTTR.[a]

## Irradiation Equipment

The HTTR has a unique and superior capability to irradiate large-sized specimens at high temperatures with a uniform neutron flux in irradiation tests. The I-I type irradiation equipment (Figure 1.41) is the first irradiation rig in the HTTR and is served for an in-pile creep test for a metallic material. The equipment can have specimens up to 6 mm in diameter.[b]

[a] K. Saito, H. Sawahata, F. Homma, M. Kondo, and T. Mizushima, "Instrumentation and Control System Design," *Nucl. Eng. Des.*, **233**: 125-133 (2004).

[b] "Present Status of HTGR Research and Development," Japan Atomic Energy Research Institute, Tokaimura, March 2004.

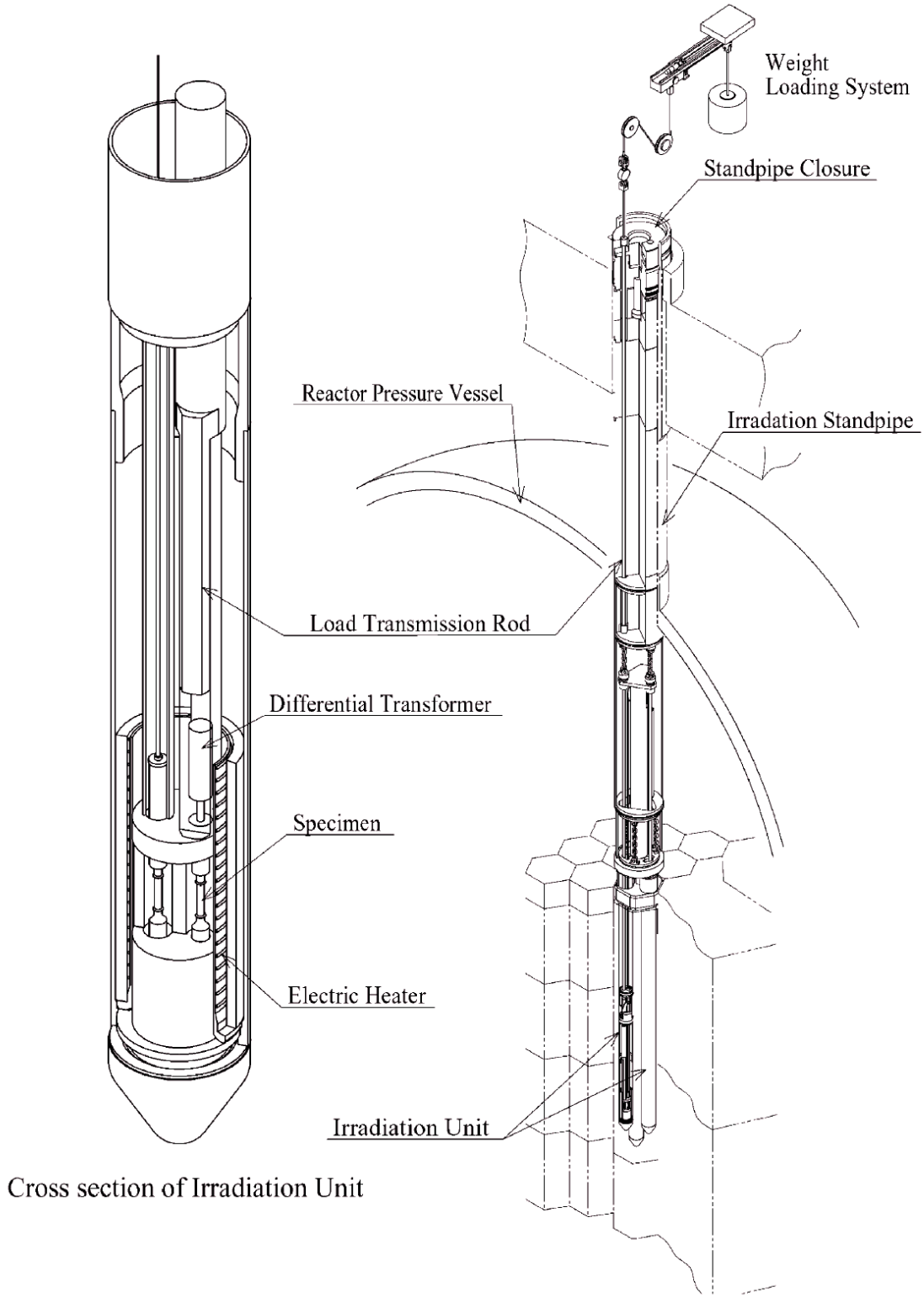


Figure 1.41. I-I Type Irradiation Equipment.[a]

[a] "Present Status of HTGR Research and Development," Japan Atomic Energy Research Institute, Tokaimura, March 2004.

*1.1.2.3 Reactor Core Components*

## Reactor Core

The active core has a height of 290 cm and effective diameter of 230 cm (Figures 1.42 and 1.43). The core consists of hexagonal graphite blocks 580 mm high and 360 mm across flats. These fuel blocks, control rod (CR) guide blocks, replaceable reflector blocks, and irradiation blocks are stacked vertically into columns. The active core contains 30 fuel columns. One column contains five fuel blocks. Each fuel block has 31 or 33 coolant channels, into which fuel rods are inserted. Fuel rods consist of a graphite sleeve containing 14 fuel compacts. Each fuel compact contains about 13,000 coated fuel particles (CFPs) randomly embedded in a graphite matrix (elsewhere is reported that each fuel compact contains about 13,500 particles[a]). Fuel-block assembly is depicted in Figure 1.44. A CFP is comprised of a spherical fuel kernel of low-enriched $UO_2$ with a coating of four layers. The core has 12 different uranium enrichments between 3.4 and 9.9 wt.% (as shown in Table 1.11), to reduce the maximum fuel temperature and increase the outlet temperature of the gas. Fuel blocks of more highly enriched uranium are placed in the upper- and outer-core regions. Burnable poisons (BPs), made of boron carbide and carbon, are inserted into two of three holes below the dowel pins in the fuel blocks. The coolant gas flow is downward through annular channels between the graphite blocks and fuel rods. Sixteen pairs of CRs are used for reactivity control. A pair of CRs is individually moved by a CR driving mechanism located in standpipes above the core. The CRs are inserted into two of three channels in the CR guide columns (Ref. 1, pp. 311-312).

The position of blocks in the core is described by a vertical position number and column number. The vertical number ranges from 1 through 9, where the top of the blocks is the 1st layer, and the bottom of the blocks is the 9th layer. The column number is named according to Figure 1.45. An example is position 4C05, which is the 4th block from the top, the 2nd ring of fuel from the center of the core, and the 5th block from the north in clockwise direction. All 30 fuel columns are grouped concentrically into 4 fuel zones (Ref. 2, p. 14).

The core consists of vertical columns of hexagonal blocks arranged on a uniform triangular pitch (Ref. 15, p. 52). The triangular pitch of the columns on each support block is 362 mm at cold conditions (Ref. 5, p. 75). The effective diameter of the core, including removable reflectors, is 3258 mm. The overall dimensions of the primary components of the core, including permanent reflectors, are a diameter of 4250 mm and a height of 5250 mm (Ref. 2, p. 10).

[a] K. Minato, H. Kikuchi, T. Tobita, K. Fukuda, M. Kaneko, N. Suzuki, S. Yoshimuta, and H. Tomimoto, "Improvements in Quality of As-Manufactured Fuels for High-Temperature Gas-Cooled Reactors," *J. Nucl. Sci. Tech.*, **34**(3): 325-333 (March 1997).

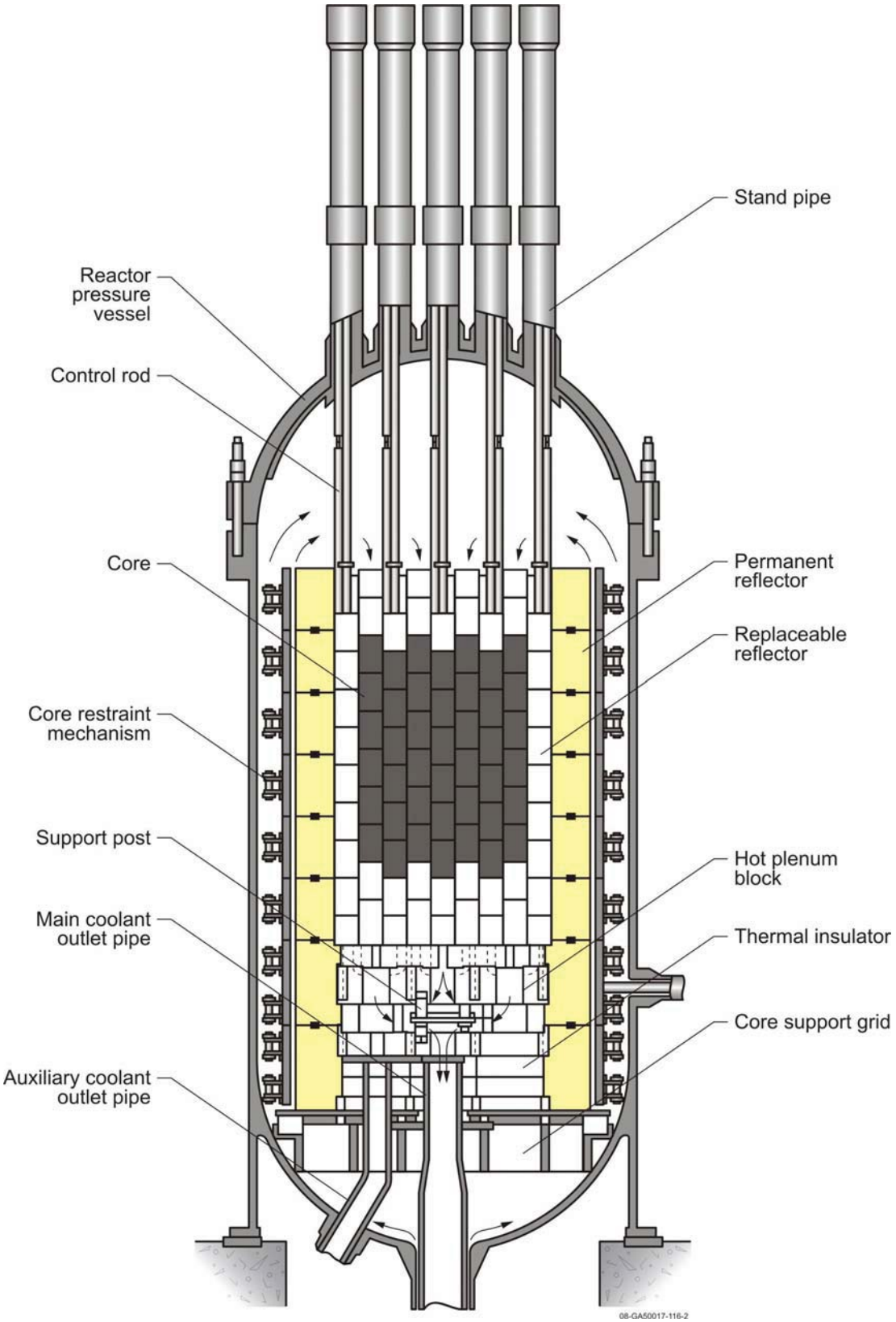


Figure 1.42. Vertical Cross Section of the HTTR (Redrawn from Ref. 1, p. 311).

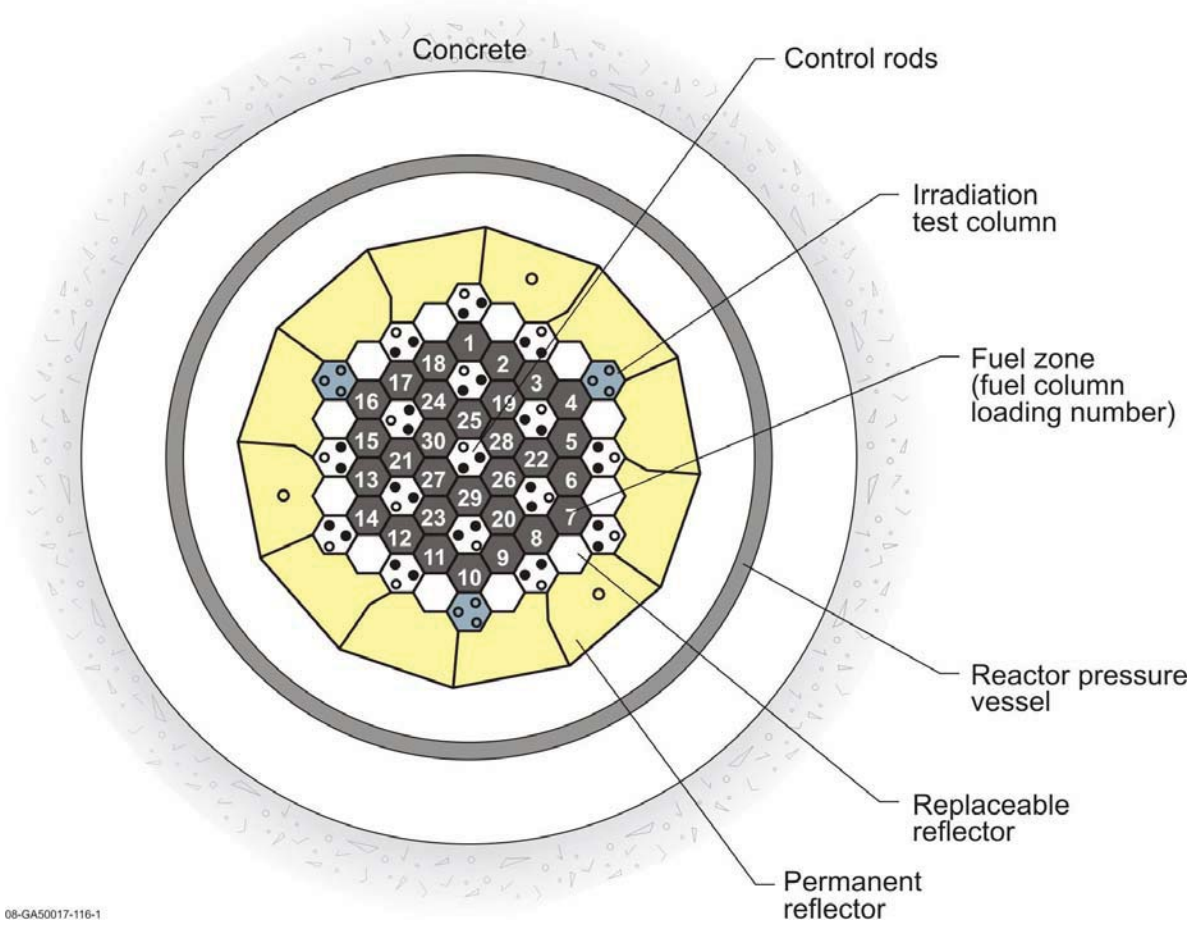


Figure 1.43. Horizontal Cross Section of the HTTR (Redrawn from Ref. 1, p. 313).

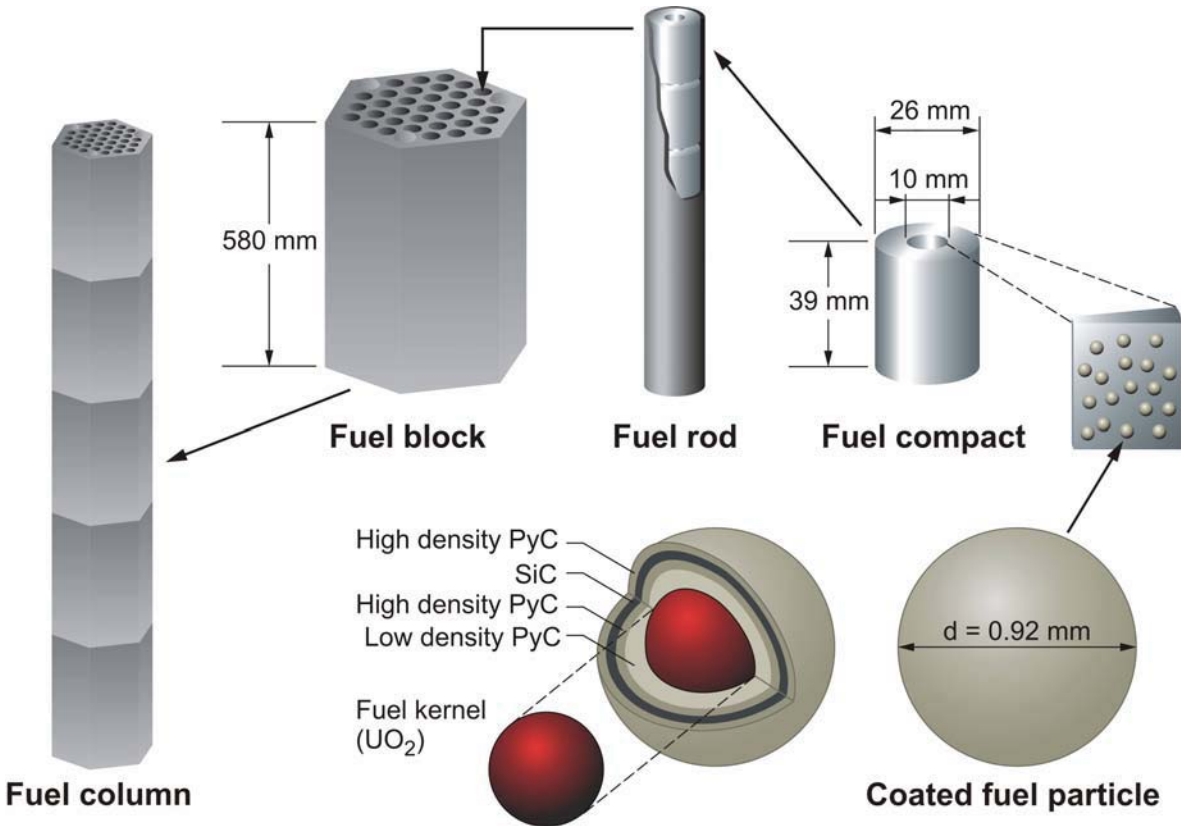


Figure 1.44. HTTR's Fuel Column, Fuel Block, Fuel Rod, Fuel Compact, and Coated Fuel Particle.[a]

[a] M. Goto, N. Nojiri, and S. Shimakawa, "Neutronics Calculations of HTTR with Several Nuclear Data Libraries," *J. Nucl. Sci. Tech.*, **43**(10): 1237-1244 (2006).

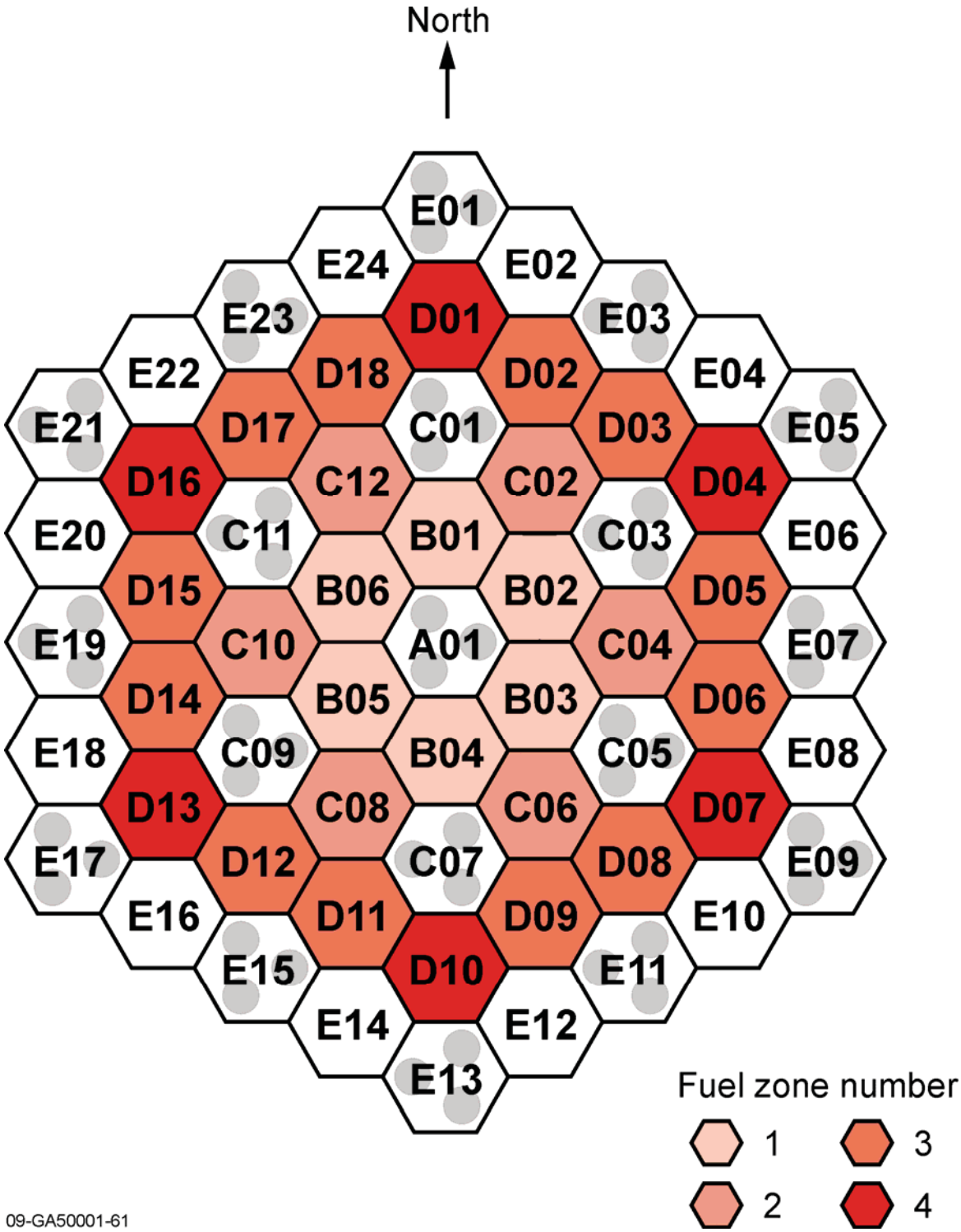


Figure 1.45. Fuel Column Name and Zone Number in the HTTR Core (adapted from Ref. 2, p. 12).

## Prismatic Fuel

The fuel element of the HTTR is a so-called pin-in-block type fuel element, which is composed of fuel rods in a hexagonal graphite block (Ref. 5, p. 72).

In 1992, Nuclear Fuel Industries Ltd. (NFI) started operating the HTR fuel plant in Tokai Works; based on established technologies, NFI successfully fabricated the first fuel loading of the HTTR from June 1995 to December 1997. The HTTR fuel fabrication consists mainly of the kernel, coated fuel particle, annular fuel compact, fuel rod, and fuel assembly process (Ref. 14, p. 378).

The fabrication of the first-core fuel started in June 1995 and took a total of 33 months. A total of 66,780 fuel compacts in 126 fabrication lots were produced, corresponding to 4770 fuel rods, containing 66,780 fuel compacts, using a total of 900 kg of uranium (Ref. 5, p. 75). In December 1997, 150 fuel assemblies were completely formed and stored in new-fuel storage cells of the HTTR.[a]

Approximately 900 million particles were fabricated for the first fuel loading of the HTTR. The average SiC defective fraction of the fuel compacts was as low as $8 \times 10^{-5}$ (Ref. 14, p. 378).

A fuel assembly consists of fuel rods, two BP rods, and a fuel graphite block. Each fuel rod (Figure 1.44) is comprised of a graphite sleeve with 14 fuel compacts containing CFPs. The fuel rods are inserted into vertical channels of 41-mm diameter in the fuel graphite block, to form annular coolant channels between the holes and rods. There are two types of fuel graphite blocks: 31- and 33-holed. There are twelve different uranium enrichments in the core (Figure 1.46 and Table 1.11). The enrichment of all compacts in a fuel assembly does not vary. The fuel assembly is classified by the uranium enrichment, number of fuel rods, and the type of BPs (Ref. 2, p. 14).

The core was divided axially into five layers to allow for optimization of the axial power distribution. A layer corresponds to a fuel block. The same uranium enrichments were loaded into the fourth and fifth layers because the power density decreases due to neutron leakage to the bottom reflector. It corresponds to the tail of the exponential form. Therefore the axial power distribution was optimized by decreasing the uranium enrichment ratios from the first layer to the fourth. The radial power distribution was optimized by adjusting the uranium enrichments so that the maximum radial power peaking in each fuel column could be brought close to unity. The uranium enrichment was increased from the core's center to the periphery to compensate for the decrease in the power production caused by neutron leakage into the side reflector.[b]

The fuel blocks were to be completely replaced by fresh fuel blocks after each burnup cycle (Ref. 4, p. 23). Each fuel element in the core will be discharged every three years. The fuel elements keep their original position during their lifetime in the core (Ref. 11, p. 151). However, the HTTR hadn't been refueled for at least the first 10 years of HTTR operation.

There are four types of HTTR fuel. The A-type fuel is the primary driver fuel for the HTTR. B-type fuel rods, namely B-1, B-2, and B-3, have different coating layer specifications for the CFPs, and are used in irradiation tests of advanced fuels. Fuel specifications are in Table 1.12 (Ref. 15, p. 46). The A-type fuel is currently the only fuel in use as the B-type fuel has yet to be fabricated.

Specifications for the fuel assemblies are compiled into Table 1.13.

---

[a] K. Sawa and S. Ueta, "Research and Development on HTGR Fuel in the HTTR Project," *Nucl. Eng. Des.*, **233**: 163-172 (2004).

[b] K. Yamashita, R. Shindo, I. Murata, S. Maruyama, N. Fujimoto, and T. Takeda, "Nuclear Design of the High-Temperature Engineering Test Reactor (HTTR)," *Nucl. Sci. Eng.*, **122**: 212-228 (1996).

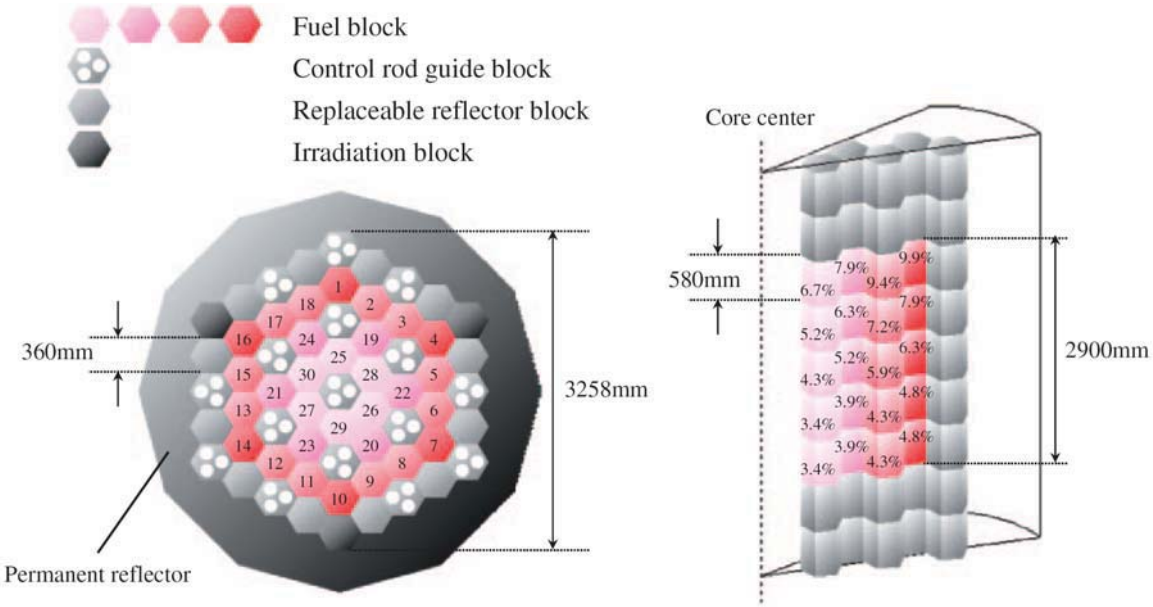


(a) Radial view and fuel loading order in critical approach

(b) Axial view and arrangement of fuel enrichment

Figure 1.46. Uranium Enrichments of the HTTR Core.[a]

Table 1.11. Uranium Enrichments of the HTTR Core (Ref. 4, p. 31).

| Layer[(c)] | Fuel Zone Number[(a)] | | | | BP[(b)] |
|---|---|---|---|---|---|
| | 1 | 2 | 3 | 4 | |
| 1 | 6.7 | 7.9 | 9.4 | 9.9 | 2.0 |
| 2 | 5.2 | 6.3 | 7.2 | 7.9 | 2.5 |
| 3 | 4.3 | 5.2 | 5.9 | 6.3 | 2.5 |
| 4 | 3.4 | 3.9 | 4.3 | 4.8 | 2.0 |
| 5 | 3.4 | 3.9 | 4.3 | 4.8 | 2.0 |

(a) $^{235}U$ enrichment (wt.%).
(b) Nat-B concentration (wt.%).
(c) Layer number from top fuel block.

[a] M. Goto, N. Nojiri, and S. Shimakawa, "Neutronics Calculations of HTTR with Several Nuclear Data Libraries," *J. Nucl. Sci. Tech.*, **43**(10): 1237-1244 (2006).

Table 1.12. Specification of Coated Fuel Particles (Ref. 5 p. 74, Ref. 15, p. 48). A-type fuel is the primary fuel for the HTTR with B-type fuel representing advanced fuel for irradiation tests.

| | A-Type | B-1/B-2 Type | B-3 Type |
|---|---|---|---|
| Fuel Type | Rod | Rod | Rod |
| Fuel Coating Type | TRISO | TRISO | TRISO |
| Diameter of Particle (μm) | 920 | 940 | 830 |
| Fuel Kernel | | | |
| Material | $UO_2$ | $UO_2$ | $(U,Th)O_2$ (Th/U=4) |
| Density (% of T.D.) | 95 | 95 | 95 |
| Diameter (μm) | 600 | 570 | 500 |
| Materials and Thickness (μm) of Coatings | | | |
| 1st Layer | Low Density PyC 60 | Low Density PyC 80 | Low Density PyC 60 |
| 2nd Layer | High Density PyC 30 | High Density PyC 30 | High Density PyC 30 |
| 3rd Layer | SiC 25 | SiC(B-1)/ZrC(B-2) 35 | SiC 30 |
| 4th Layer | High Density PyC 45 | High Density PyC 40 | High Density PyC 45 |
| Enrichment of $^{235}U$ (wt.%) | 3-10 (Ave. 6) | 5 | 20 |

Table 1.13. Main Specifications of HTTR Fuel (Ref. 5, p. 74 and Ref. 4, p. 25).

| | |
|---|---|
| Fuel Kernel | |
| Material | $UO_2$ |
| Diameter (μm) | 600 |
| Density ($g/cm^3$) | 10.41[(a)] |
| Coated Fuel Particle | |
| Type / Material | TRISO |
| Diameter (μm) | 920 |
| Impurity (ppm) | <3 (Boron Equivalent) |
| Fuel Compact | |
| Type | Hollow Cylinder |
| Material | CFPs, Binder, and Graphite |
| Outer / Inner Diameter (cm) | 2.6 / 1.0 |
| Length (cm) | 3.9 |
| Packing Fraction of CFPs (vol. %) | 30 (A and B-3)<br>35 (B-1 and B-2) |
| Density of Graphite Matrix ($g/cm^3$) | 1.7 |
| Impurity in Graphite Matrix (ppm) | <1.2 (Boron Equivalent) |

Table 1.13 (cont'd.). Main Specifications of HTTR Fuel (Ref. 5, p. 74 and Ref. 4, p. 25).

| | |
|---|---|
| Fuel Rod | |
| Outer Diameter (cm) | 3.4 |
| Sleeve Thickness (mm) | 3.75 |
| Length (cm) | 54.6 |
| Number of Fuel Compacts | 14 |
| Number of Rods in a Block | 31 / 33 |
| Graphite Sleeve | |
| Type | Cylinder |
| Material | IG-110 Graphite |
| Impurity (ppm) | <1 (Boron Equivalent) |
| Length (cm) | 58 |
| Gap Width between Compact and Sleeve (mm) | 0.25 |
| Graphite Block | |
| Type / Configuration | Pin-in-Block / Hexagonal |
| Material | IG-110 graphite |
| Width across Flats (cm) | 36 |
| Height (cm) | 58 |
| Fuel Hole Diameter (cm) | 4.1 |
| Density ($g/cm^3$) | 1.75 |
| Impurity (ppm) | <1 (Boron Equivalent) |

(a) The density reported in this reference is not the same as that reported in Table 1.14.

A CFP consists of a spherical fuel kernel of low enriched $UO_2$ (600 µm diameter at 95 % theoretical density, TD) with a tri-isotropic (TRISO) coating: low density, porous pyrolytic carbon (PyC) buffer layer (60 µm), high density inner isotropic PyC layer (30 µm), a SiC layer (25 µm), and a final outer PyC layer (45 µm), as shown in Figure 1.47 and Table 1.12. The CFPs are embedded in graphite matrix of the fuel compact, as shown in Figure 1.44. The fuel compact is a hollow cylinder with 10-mm inner diameter, 26-mm outer diameter, and a 39-mm height (Ref. 2, p. 14-16 and Ref. 5, p. 74).

Buffer and PyC layers are obtained from the thermal decomposition of $C_2H_2$ and $C_3H_6$, respectively, and the SiC layer from $SiCH_3Cl_3$. The defective fraction of SiC layers was minimized by reducing thermal and mechanical shocks during the process. The advanced fluidized bed for this process is able to coat about three million particles uniformly. The SiC defective fraction of CFPs is on the order of $10^{-7}$, less than three defective particles in one batch (Ref. 14, p. 378).

The porous PyC coating layer, called the buffer layer, attenuates fission recoils and provides void volume for gaseous fission products and carbon monoxide. The IPyC coating layer acts as a containment for the gases. The SiC coating layer provides mechanical strength for the particle and acts as a diffusion barrier to metallic fission products that diffuse easily through the IPyC layer. The OPyC coating layer protects the SiC coating layer mechanically.

Uncertainties in the fabrication of the first-loading fuel of the HTTR were assessed and characterized. Table 1.14 contains major specifications and uncertainties in the initial HTTR fuel. Figure 1.48 shows measured dimensions and distributions of as-fabricated coated fuel particles. The thickness of the coating layers was measured by optical microscopy. Further discussion of the uncertainties in fuel fabrication and uranium enrichment is discussed elsewhere.[ab]

The sphericity and deviation of kernel diameter has a profound effect on the strength and defective fraction of coated fuel particles. Therefore, much effort was focused on achieving high-quality mass-produced kernels using an ammonia diuranate dropping system capable of producing 4.3 kg of uranium per batch. The average sphericity was less than 1.05 and the standard deviation of the diameter was less than 3 % of the average diameter of the HTTR first loading fuel fabrication (Ref. 14, p. 378).

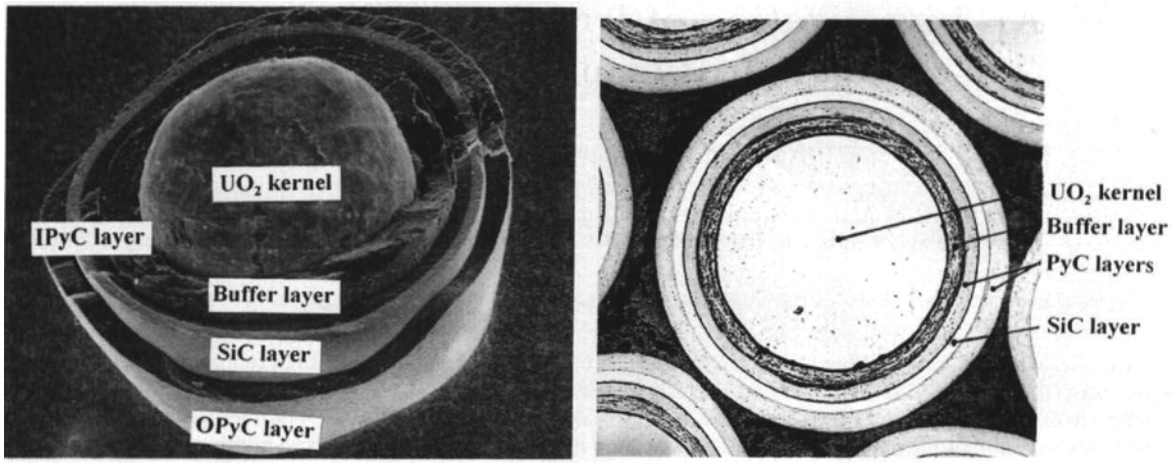


Figure 1.47. TRISO-Coated Fuel Particle.[a]

[a] K. Sawa and K. Minato, "An Investigation of Irradiation Performance of High Burnup HTGR Fuel," *J. Nucl. Sci. Tech.*, **36**(9): 781-791 (September 1999).

[b] S. Kato, S. Yoshimuta, T. Hasumi, K. Sato, K. Sawa, S. Suzuki, H. Mogi, S. Shiozawa, and T. Tanaka, "Fabrication of HTTR First Loading Fuel," IAEA-TECDOC-1210, International Atomic Energy Agency, Vienna, pp. 187-199 (April 2001).

Table 1.14. Major Specifications of the First-Loading Fuel of the HTTR. [a]

| | |
|---|---|
| Fuel Kernel | |
| Diameter (μm) | $600 \pm 55$ [b] |
| Density (g/cm$^3$) | $10.63 \pm 0.26$ |
| Impurity (ppm) | ≤3 EBC [c] |
| Coating Layer | |
| Buffer Thickness (μm) | $60 \pm 12$ |
| IPyC Thickness (μm) | $30 \pm 6$ |
| SiC Thickness (μm) | $25\ ^{+12}_{-0}$ |
| OPyC Thickness (μm) | $45 \pm 6$ |
| Buffer Density (g/cm$^3$) | $1.10 \pm 0.10$ |
| IPyC Density (g/cm$^3$) | $1.85\ ^{+0.10}_{-0.05}$ |
| SiC Density (g/cm$^3$) | ≥3.20 |
| OPyC Density (g/cm$^3$) | $1.85\ ^{+0.10}_{-0.05}$ |
| OPTAF [d] of PyC Layers | ≤1.03 |
| Coated Fuel Particle | |
| Diameter (μm) | $920\ ^{+50}_{-30}$ |
| Sphericity | ≤1.2 |
| Fuel Compact | |
| CFP Packing Fraction (vol. %) | $30 \pm 3$ |
| Impurity (ppm) | ≤5 EBC [c] |
| Exposed Uranium Fraction | $\leq 1.5 \times 10^{-4}$ |
| SiC-Failure Fraction | $\leq 1.5 \times 10^{-3}$ |
| Outer Diameter (mm) | $26.0 \pm 0.1$ |
| Inner Diameter (mm) | $10.0 \pm 0.1$ |
| Height (mm) | $39.0 \pm 0.5$ |
| Matrix Density (g/cm$^3$) | $1.70 \pm 0.05$ |
| Compressive Strength (N) | ≥4,900 |
| Fuel Rod | |
| Uranium Content (g) | $188.58 \pm 5.66$ |
| Total Length (mm) | $577 \pm 0.5$ |
| Fuel Compact Stack Length (mm) | ≥544 |

(a) K. Sawa, T. Tobita, H. Mogi, S. Shiozawa, S. Yoshimuta, S. Suzuki, and K. Deushi, "Fabrication of the First-Loading Fuel of the High Temperature Engineering Test Reactor," *J. Nucl. Sci. Tech.*, **36**(8): 683-690 (August 1999).
(b) The density reported in this reference is not the same as that reported in Table 1.13.
(c) EBC: Equivalent Boron Content
(d) OPTAF: Optical Anisotropy Factor

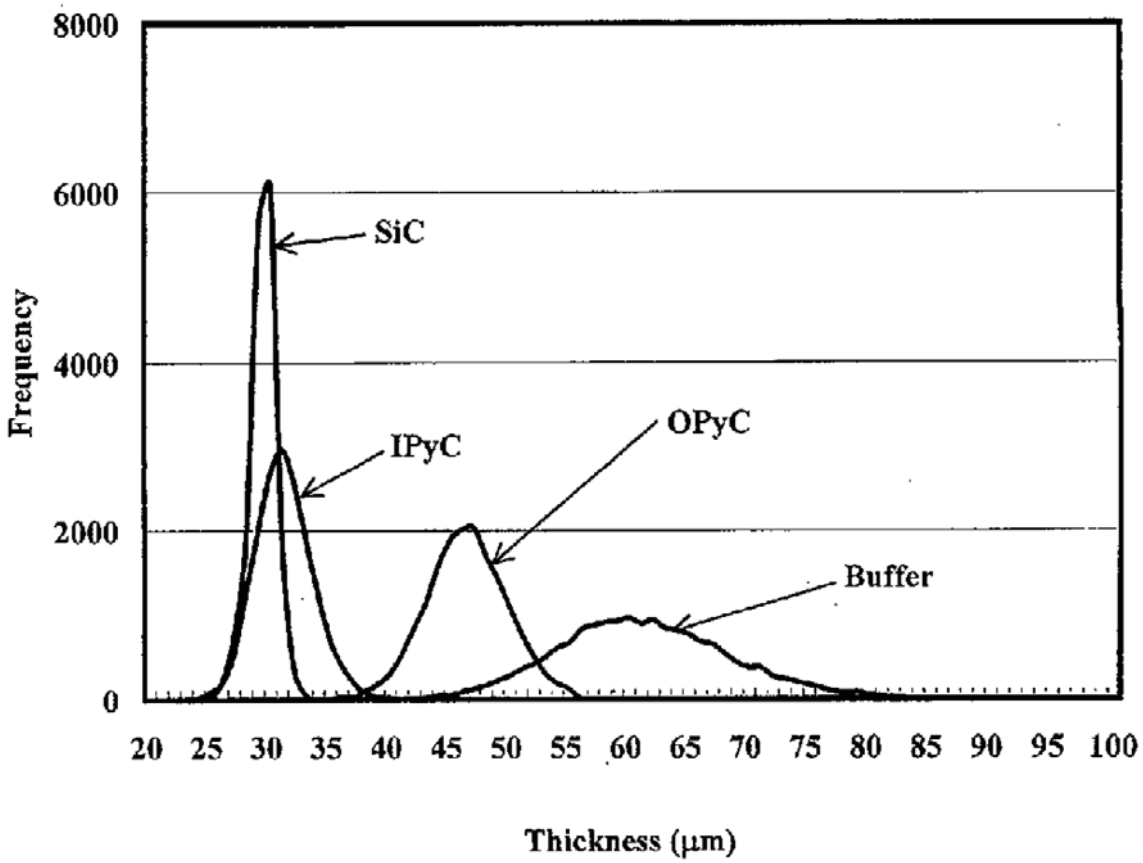


Figure 1.48. Measured Dimensions and Distributions of As-Fabricated Coating Layers.[a]

In order to create the fuel compact, the coated fuel particles are first overcoated with a graphite matrix. This process prevents close contact between the coated fuel particles. Hot pressing is utilized to obtain annular green compacts. The automatic hot pressing system weighs the overcoated particles, preheats the resin, charges the particles into dies, hot presses them, discharges the compacts, and then numbers each compact. This system can produce 230 green compacts in eight hours. The green compacts are carbonized in nitrogen gas and degassed in vacuum (Ref. 14, p. 378).

With about 13,000 fuel particles defined for each fuel compact, the corresponding packing density is about 30 % (Ref. 2, p. 136).

A black and white photo of some fuel compacts are shown in Figure 1.49. A horizontal cross-section view of a fuel compact with CFPs is shown in Figure 1.50.

[a] K. Sawa, T. Tobita, H. Mogi, S. Shiozawa, S. Yoshimuta, S. Suzuki, and K. Deushi, "Fabrication of the First-Loading Fuel of the High Temperature Engineering Test Reactor," *J. Nucl. Sci. Tech.*, **36**(8): 683-690 (August 1999).

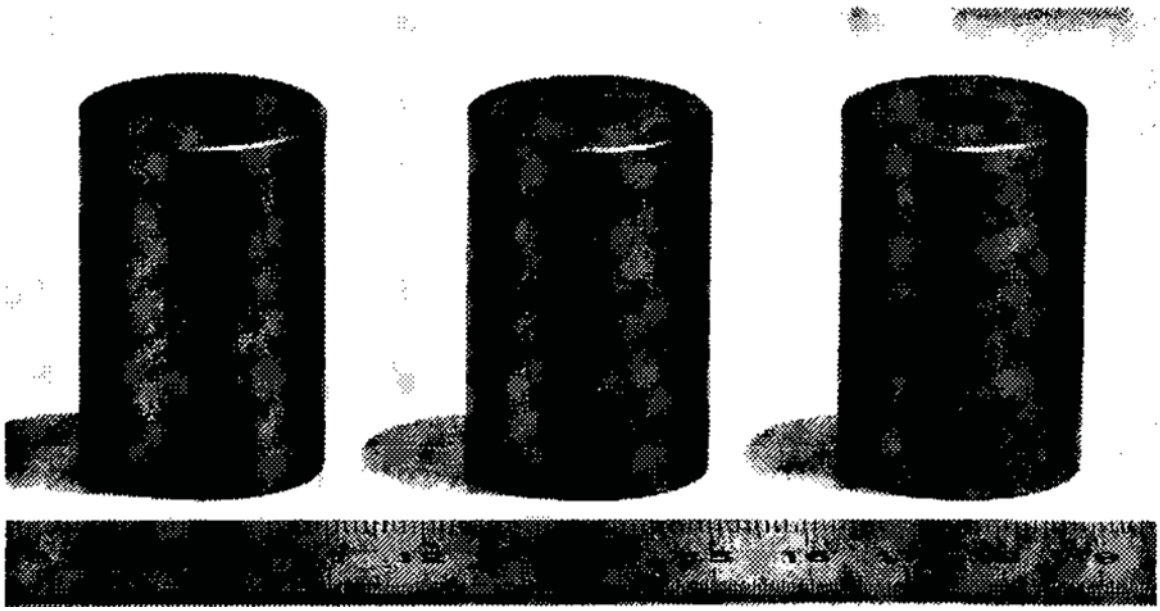

Figure 1.49. External View of Fuel Compacts.[a]

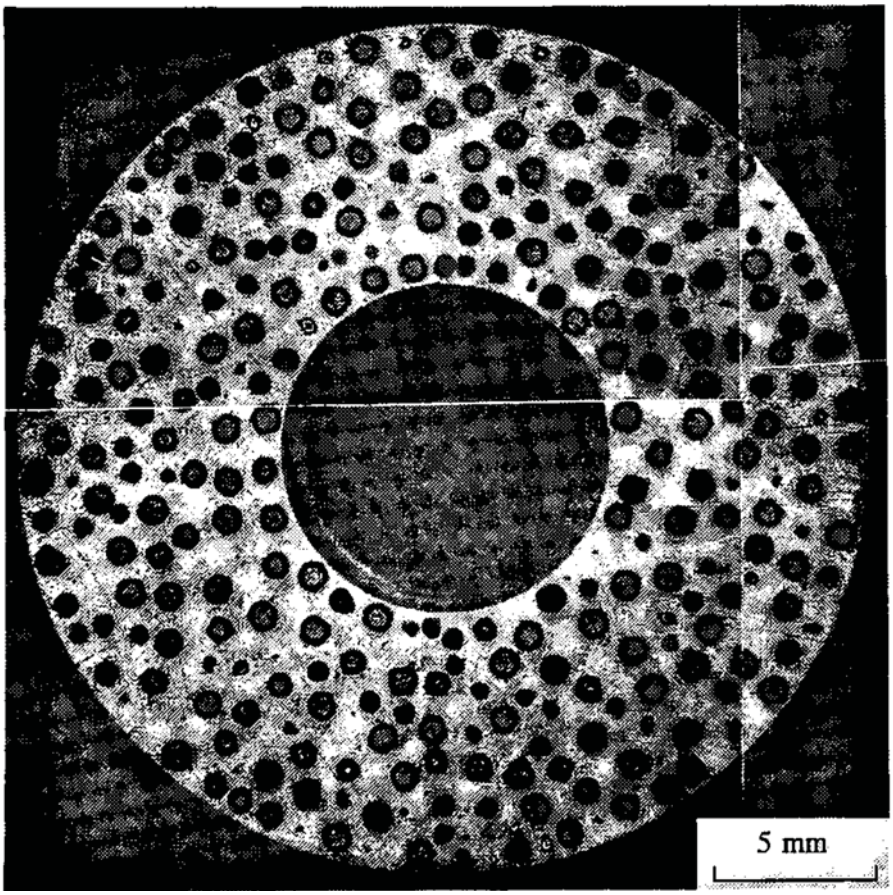


Figure 1.50. Horizontal Cross Section of a Fuel Compact.[a]

[a] K. Minato, H. Kikuchi, T. Tobita, K. Fukuda, M. Kaneko, N. Suzuki, S. Yoshimuta, and H. Tomimoto, "Improvements in Quality of As-Manufactured Fuels for High-Temperature Gas-Cooled Reactors," *J. Nucl. Sci. Tech.*, **34**(3): 325-333 (March 1997).

The sintered fuel compacts are contained in a fuel rod that is 34 mm in outer diameter and 577 mm in length (Ref. 3, p. 15). The form of the fuel rod (graphite sleeve containing 14 fuel compacts) is shown in Figure 1.51 (Ref. 2, p. 16). The annular fuel pin has an inner diameter of 26.25 mm.[a] The helium gas flows downward through the 3.5 mm annular gap between the hole and the fuel rod (Ref. 5, pp. 74-75).

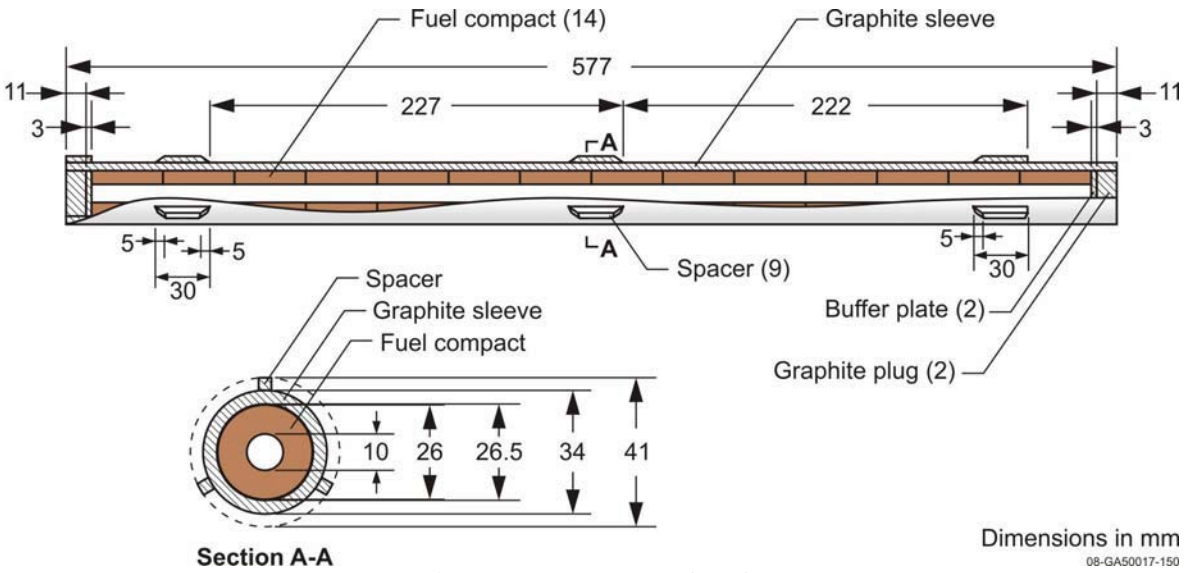


Figure 1.51. HTTR Fuel Rod.

The graphite block is a prismatic hexagonal block with a 580-mm height and 360-mm across the flats. Blocks in fuel zones 1 and 2 have 33 fuel holes, and blocks in fuel zones 3 and 4 have 31 fuel zones. The form of the block is given in Figures 1.52 and 1.53, respectively (Ref. 2, p. 18 and 19).

Ninety-nine percent of the total power is produced in the active core and the residual 1 % in the reflector region (Ref. 15, p. 14). Approximately 95 % of the thermal power in the active core is generated in the fuel elements and the rest in the graphite moderator. Thermal and irradiation conditions thus become severe for the blocks at the outermost region of the core. For this reason, the fuel blocks only contain 31 fuel rods instead of 33, maintaining their structural integrity.[b]

Three threaded dowels are installed on the top face of the fuel blocks that are coupled with sockets in the bottom face of the block located above it. A hole at the center of each fuel block is provided for fuel handling. The hole profile is shaped so that a lifting ledge is machined at the lower end. The grapple head of the fuel handling machine withstands against this ledge when lifting the block. Additional holes are provided in the corners of the blocks for the insertion of the BP rods (Ref. 5, p. 76 and Ref. 15, p. 53).

The arrangement pattern of the fuel blocks in the core is shown in Figure 1.54, and a photo depicting fuel loading of a graphite block is shown in Figure 1.55. There is a slight key slot in the holes of the fuel blocks to align and hold in the fuel rods (Figure 1.56).

[a] "Fuel Performance and Fission Product Behaviour in Gas Cooled Reactors," IAEA-TECDOC-978, International Atomic Energy Agency, Vienna (November 1997).

[b] E. Takada, S. Nakagawa, N. Fujimoto, and D. Tochio, "Core Thermal-Hydraulic Design," *Nucl. Eng. Des.*, **233**: 37-43 (2004).

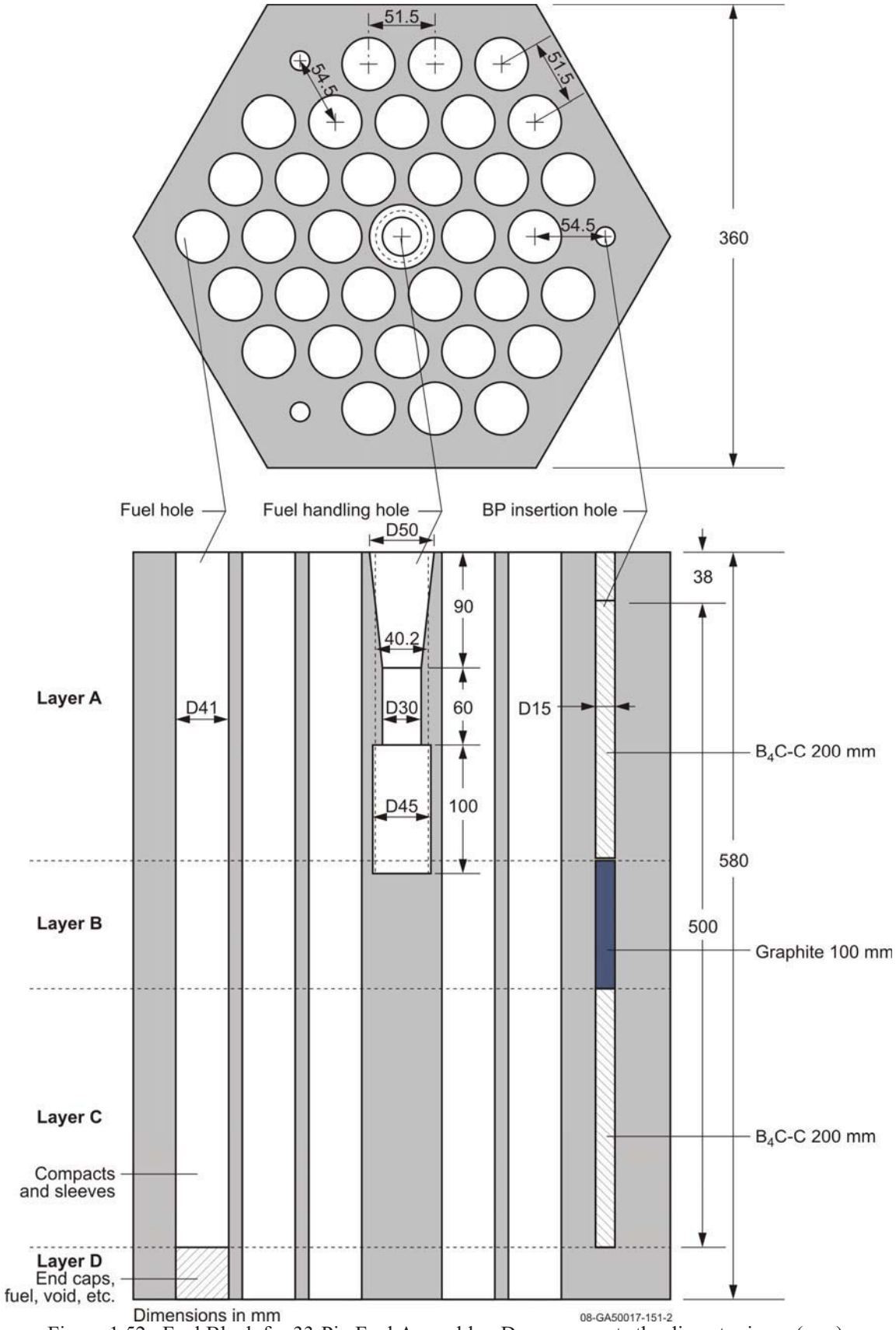


Figure 1.52. Fuel Block for 33-Pin Fuel Assembly. Dxx represents the diameter in xx (mm).

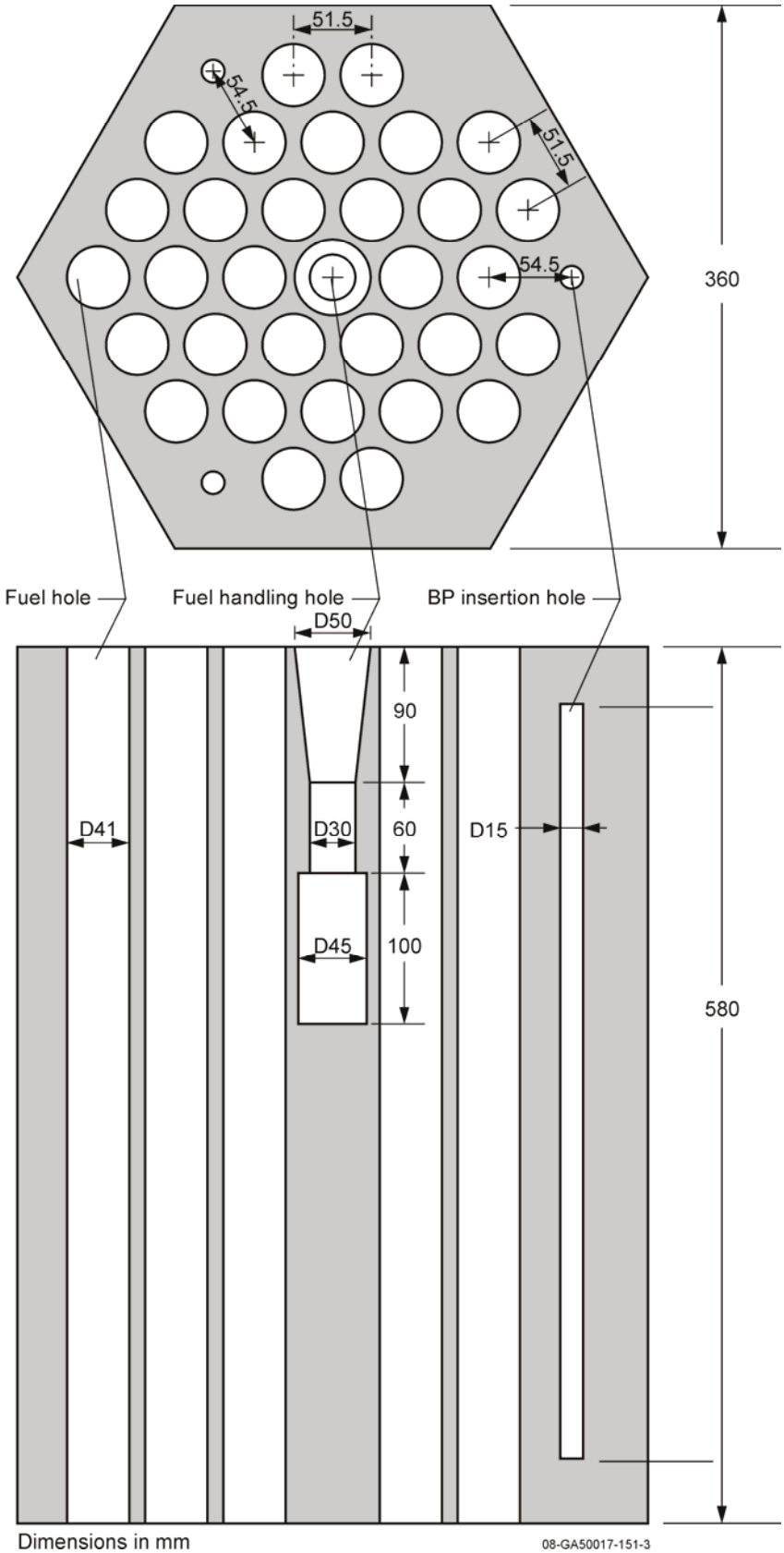


Figure 1.53. Fuel Block for 31-Pin Fuel Assembly. Dxx represents the diameter in xx (mm).

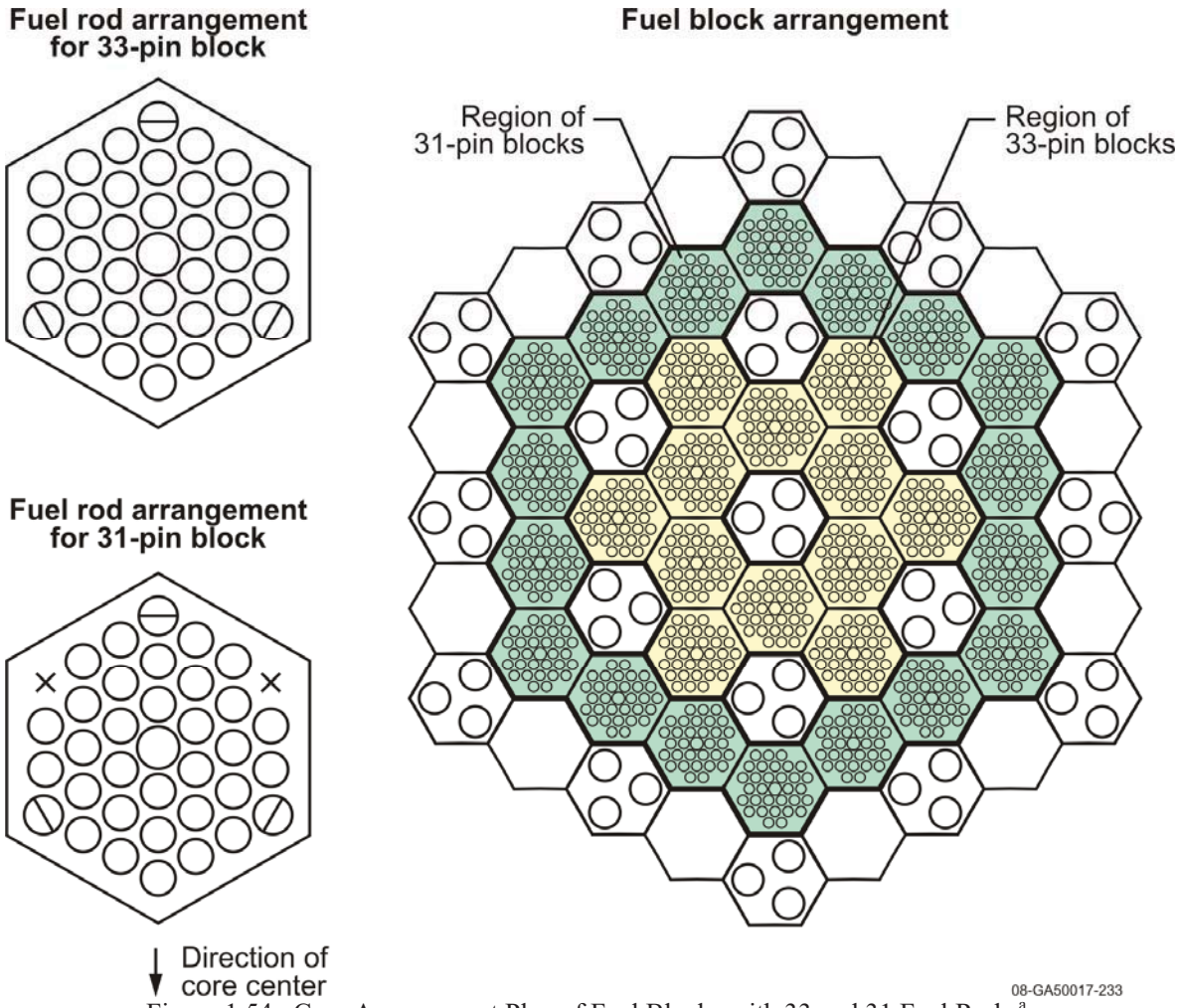


Figure 1.54. Core Arrangement Plan of Fuel Blocks with 33 and 31 Fuel Rods.[a]

[a] Y. Sudo, S. Saito, M. Yamada, M. Uno, and T. Ohno, "Design Considerations and Improvements of the High Temperature Engineering Test Reactor (HTTR) for a Reactor Outlet Coolant Temperature of 950 ºC," *Proc. Int. Working Group on Gas-Cooled Reactors (IWGGCR-19)*, San Diego, California (September 21-23, 1988).

Figure 1.55. Assembly of a Fuel Element Block.[a]


Figure 1.56. Close-Up View of a Fuel Assembly Block.[a]

[a] "Present Status of HTGR Research and Development," Japan Atomic Energy Research Institute, Tokaimura, March 2004.

## Burnable Poisons

BP rods are inserted into two of the three BP insertion holes in the fuel graphite blocks (Figure 1.57). The BP insertion holes are under the 3 dowel pins of the fuel graphite block and are 15 mm in diameter and 500 mm long. One hole is empty, without the BP rod. Figures 1.52 and 1.53 show the fuel block positions of the holes that are filled with BPs. The BP rod has a diameter of 14 mm. The rod contains BP pellets and graphite disks, as shown in Figure 1.58. The graphite disks are placed between the BP pellets. The BP cylindrical pellets are each 20 mm in height (Ref. 2, p. 21).

The large initial excess reactivity from fresh fuel is counteracted through the use of BPs. Optimization of the specifications for the BPs reduces deviation from the optimum power distribution due to burnup effects. This is done by changing the poison atom density and radius throughout the core. It then becomes possible to operate the reactor during full power operation at 950 ºC without changing the insertion position of the control rods (Ref. 3, p. 24).

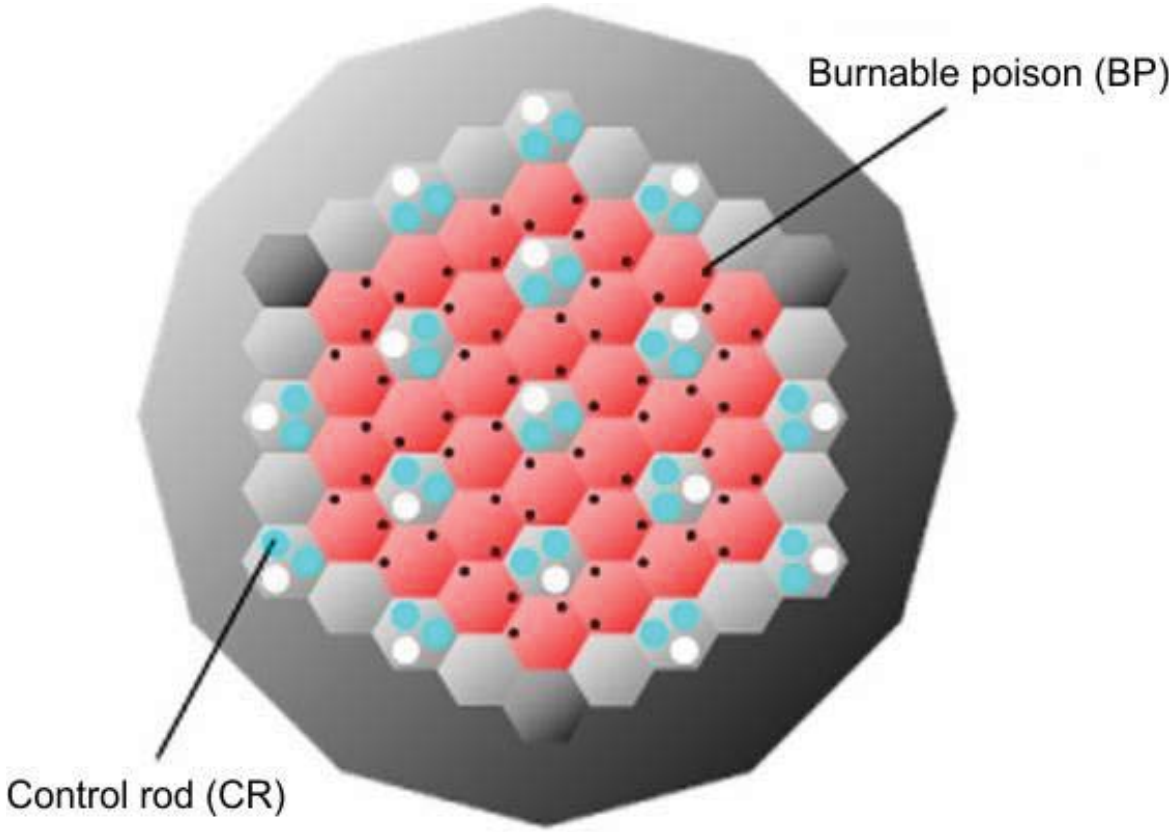


Figure 1.57. Location of BP Pellets in the HTTR.[b]

[a] S. Shiozawa, "Status of Japan's HTR Program," *Key Note Presentation at the 2007 Int. Congress on Advances in Nuclear Power Plants (ICAPP 2007)*, Nice, France (May 13-18, 2007).

[b] S. Shimakawa and K. Kunitomi, "Validation of Reactor Physics Codes used for HTTR and Design-Phase HTGRs at JAEA," *1st Int. Verification and Validation for Nuclear Systems Analysis Workshop*, Idaho Falls, Idaho, July 21-25, 2008.

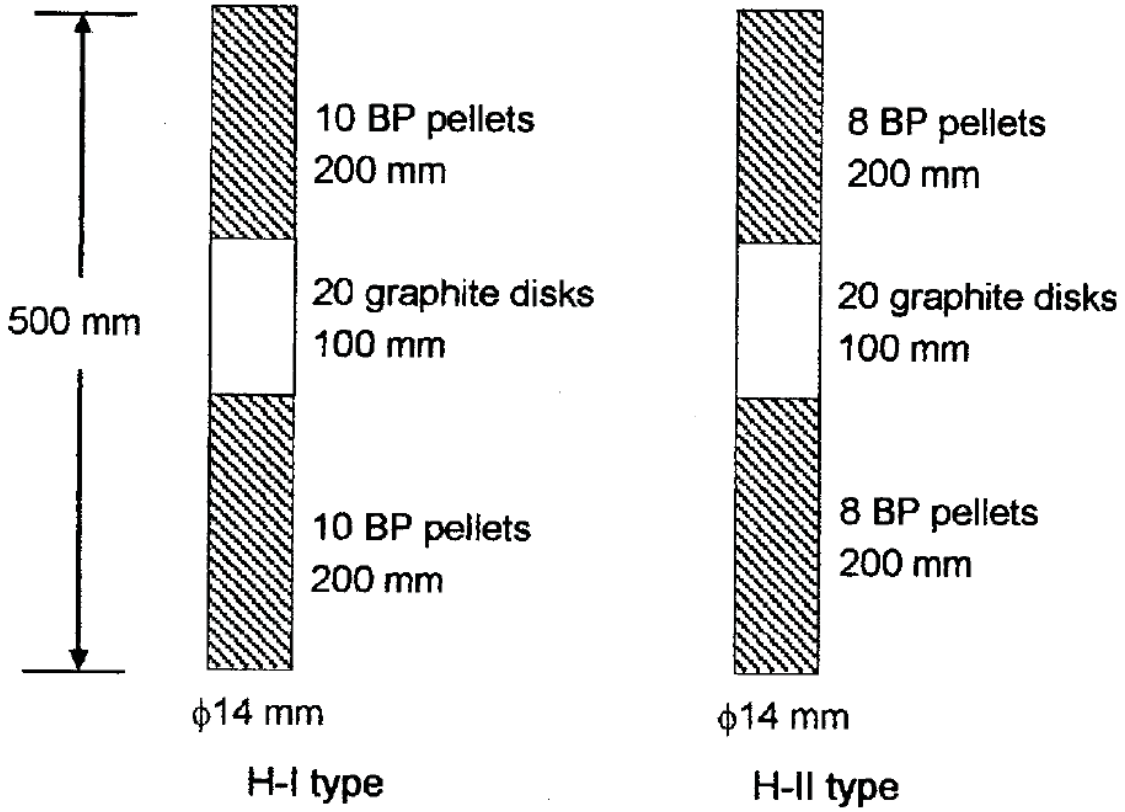


Figure 1.58. Configuration of BP Pellets and Graphite Disks in a BP Rod (Ref. 2, p. 17).

## Control Rods and Reserve Shutdown System

Toshiba and Ishikawajima-Harima Heavy Industries led development of the reactivity control instrumentation: the control rod drive mechanism and the reserve shutdown system (Ref. 14, p. 380).

There are 16 pairs of CRs: seven in the fuel region and nine in the replaceable reflector region. They are inserted into the holes of the CR guide columns. The control rod guide blocks have three holes: two for control rod insertion, and one for the emergency reserve shutdown system (RSS). Figure 1.43 shows the position of the CR insertion holes and RSS holes in the core and replaceable reflector region (Ref. 2, p. 21).

The center control rod can be removed such that the center column of the core could be used for an irradiation test. The control rod system can achieve subriticality from any operation state and maintain subcriticality in the cold core even when a pair of control rods sticks into an operational position. In case of a scram during normal operations, the control rods in the replaceable reflector region are inserted at first, and the rest of the control rods are inserted after the core has cooled down. This prevents the control rod cladding from being exposed to temperatures above 900 ºC. A pair of control rods is driven by one drive mechanism and released from the mechanism to be inserted by gravity in the event of a reactor scram.[a]

A pair of control rods is individually moved by a control rod drive mechanism located in stand-pipes connected to the hemispherical top head closure of the RPV (Ref. 2, p. 13).

[a] K. Kunitomi and S. Shiozawa, "Safety Design," *Nucl. Eng. Des.*, **233**: 45-58 (2004).

The control rod drive mechanism (Figure 1.59) consists of an AC motor, a decelerator, an electromagnetic clutch, a velocity-limiting brake, a shock absorbing mechanism, position indicators, manual control mechanisms, gears, and a control rod support cable. The drive motor is coupled to the cable drum through the decelerator, the electromagnetic clutch, and the gears. During normal operation, the position of the control rod is sustained by the torque of the motor. The maximum withdrawal velocity is limited to a value below 70 mm/s by the decelerator even when the motor is running at the maximum speed. When the electric current through the electromagnetic clutch is cut off by a scram signal, the clutch is separated to insert the control rod by gravity into the core. To protect the control rod support cable from overloading, the velocity-limiting brake maintains the insertion speed constant during a reactor scram by applying the braking torque in proportion to the speed. The shock absorbing mechanism reduces the speed of the control rods at the last stage of the insertion by using a gas damper to absorb any impact when the control rods are inserted for more than 80 % of their full stroke. The position indicator has three independent systems using synchro-mesh transmitters, as a built-in safety factor (Ref. 7, pp. 91-92).

The control rods were designed to provide a shutdown margin of more than 0.01 $\Delta k/k$, even when one pair of rods with the maximum reactivity worth is completely withdrawn and cannot be inserted. The reserve shutdown system also is designed to provide more than 0.01 $\Delta k/k$, even when the control rod system is unavailable. The maximum reactivity addition rate is limited to control rod withdrawal of less than 50 mm per step and a reactivity addition rate limit of $2.4 \times 10^{-4}$ $\Delta k/k$-s. The maximum driving speed of the control rod is 60 cm/min (Ref. 3, p. 24 and 31).

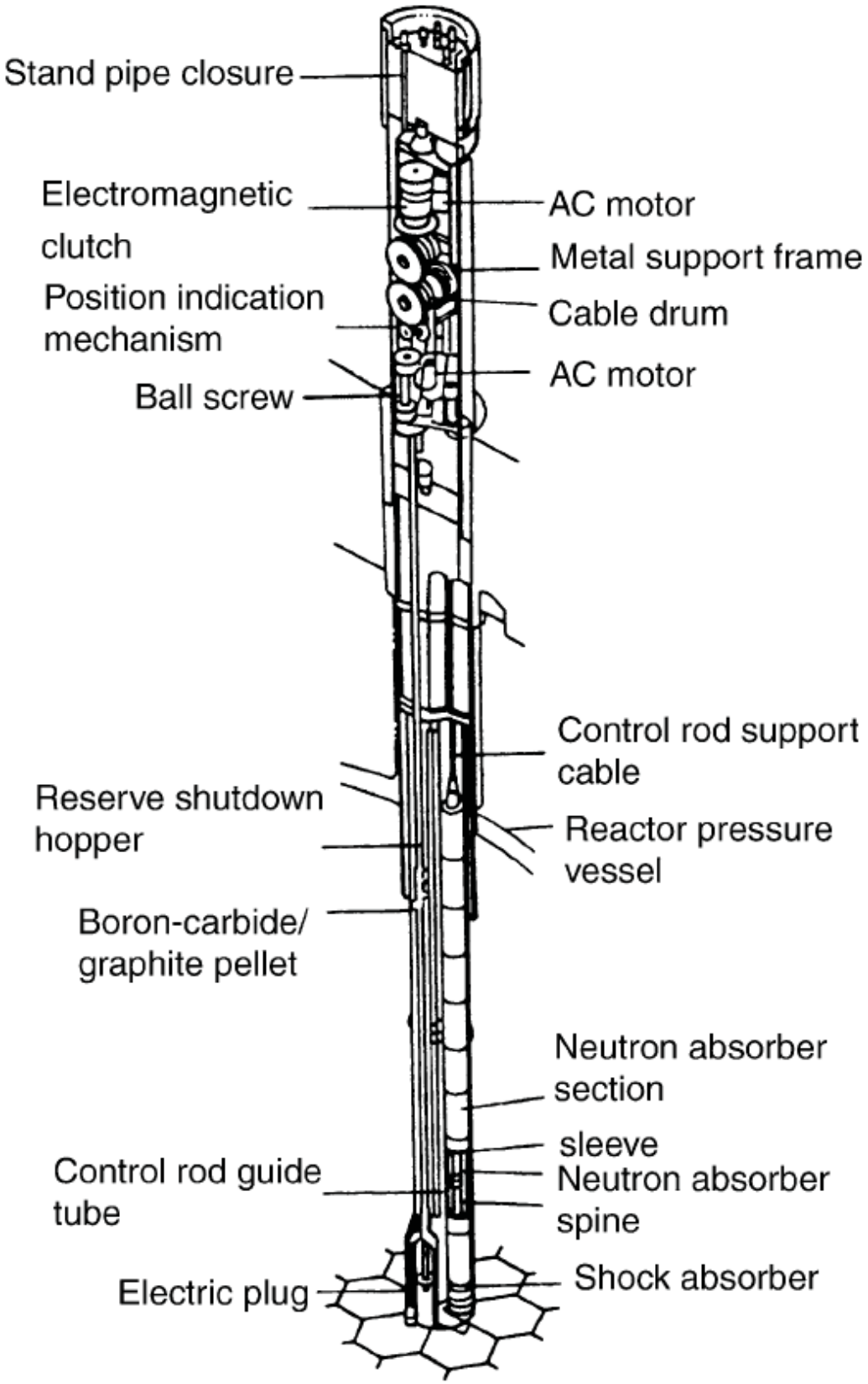


Figure 1.59. Control Rod System of the HTTR (Ref. 7, p. 91).

Each CR consists of 10 neutron absorber sections connected with metallic spines and support rings (Figure 1.60). Each section contains five sintered compacts of $B_4C$ and C as neutron absorbers in the annular space. The CR pairs were named center (C), ring 1 (R1), ring 2 (R2), and ring 3 (R3) from the center to the outside as shown in Figure 1.43. Both R2 and R3 CRs are in the replaceable reflector region surrounding the core, where the six CR pairs on the sides of the hexagonal loading pattern are R2 CRs and the three remaining CR pairs at corners of the hex are R3 CRs. The CR positions at critical conditions were measured to evaluate the calculation accuracy. They were inserted from top to bottom. The bottoms of the inserted CRs were kept almost at the same level at critical conditions. The CR positions were defined with distance from the bottom of the fifth fuel layer. The R3 CRs were fully withdrawn at critical conditions (Ref. 1 p. 317).

To reduce thermal stresses in the sleeves, the neutron absorber sections and spine are separated from each other and each section is sustained by a support ring. The absorber section is assembled from parts with gaps between them, and all parts are mechanically connected without welds. Each absorber section contains a guide ring to restrain them from rolling too much. The lower end of the spine is attached to a tubular shock absorber. At the bottom of the core are graphite dishes, also called shock absorbers, which absorb the impact of a control rod. The annular space of each absorber section contains the sintered compacts with a density of 1.9 $g/cm^3$ (Ref. 7, p. 90-91).

The total height of the control rods is 3094 mm. The pellets are surrounded by a 3.5 mm thick sleeve of Alloy 800H. Inner and outer diameters of the CRs are 65 and 113 mm, respectively. The height of the pellet stack in a single absorber section is 29 cm (Ref. 2, pp. 22 and 131).

Table 1.15 lists the specifications of the CR and RSS systems.

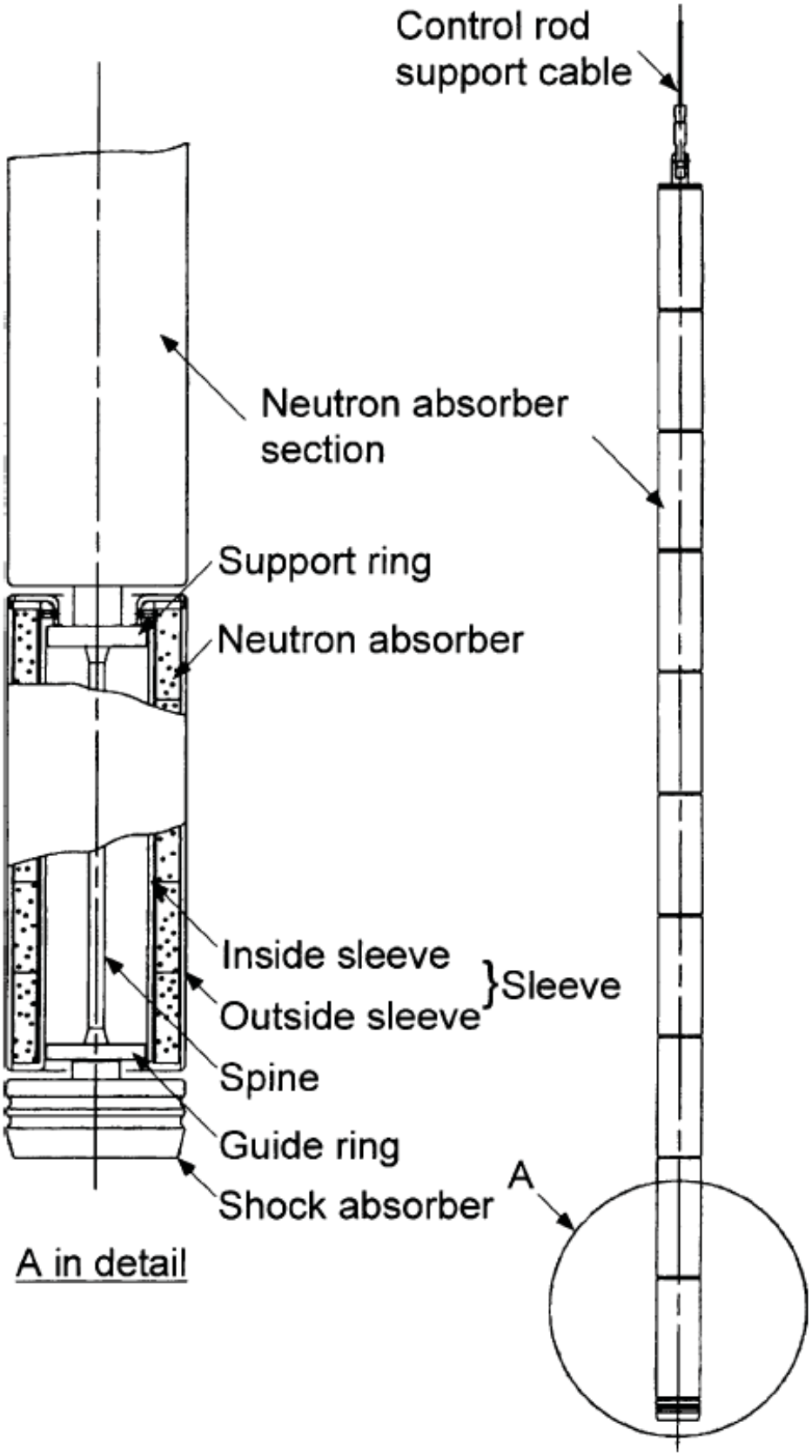


Figure 1.60. Control Rod of HTTR (Ref. 7, p. 92).

Table 1.15. Specifications of the CR System and the RSS (Ref. 4, p. 25 and Ref. 7, p. 91).

| | |
|---|---|
| CR System | |
| Type | Double Cylinders with Lid and Vent |
| Number | 16 Pairs (32 Rods)<br>15 Pairs when Irradiation Test is in Center Column |
| Total Length (m) | 3.1 |
| Outer Diameter (mm) | 113 |
| Inner Diameter (mm) | 65 |
| Sleeve | |
| Thickness (mm) | 3.5[(a)] |
| Material | Alloy 800H |
| Neutron Absorber | |
| Density (g/cm$^3$) | 1.9 |
| Outer Diameter (mm) | 105[(b)] |
| Inner Diameter (mm) | 75 |
| Material | Sintered Compact of $B_4C$/C |
| Natural Boron Concentration (wt.%) | 30 |
| Spine | |
| Diameter (mm) | 10 |
| Material | Alloy 800H |
| RSS | |
| Drive Mechanism | Drop $B_4C$/C Pellets by Gravity |
| Number | 16 |
| Effective Length (m) | 3.1 |
| Hole | |
| Packing Fraction (vol. %) | 55 |
| $B_4C$/C Graphite Pellets | |
| Density (g/cm$^3$) | 1.9 |
| Diameter (mm) | 13 |
| Length (mm) | 13 |
| Material | Sintered Compact of $B_4C$/C |
| Natural Boron Concentration (wt.%) | 30 |

(a) Mathematically, the clad thickness does not match up with the other dimensions provided for the control rod. It is unclear whether gaps exist between absorber and clad material or the cladding is thicker.

(b) Reference 4 lists this value as 115, which cannot fit within the designated cladding dimension. All other values reported in Reference 4 match values in Reference 7.

The RSS absorbers are a system of pellets produced by sintering $B_4C$ powder and graphite. These pellets can be released from the storage hoppers into holes in the control rod guide columns, to act as a backup system for the control rod system (Ref. 4, p. 31). In an accident when the control rods cannot be inserted, an electric plug is pulled out by a drive motor, and the neutron-absorbing pellets falls into the core by gravity. A schematic of the RSS is shown in Figure 1.61 and specifications are listed in Table 1.15 (Ref. 7, p. 99).

A cross-section depiction of the head of the reactor vessel with both CR and RSS configurations is shown in Figure 1.62.

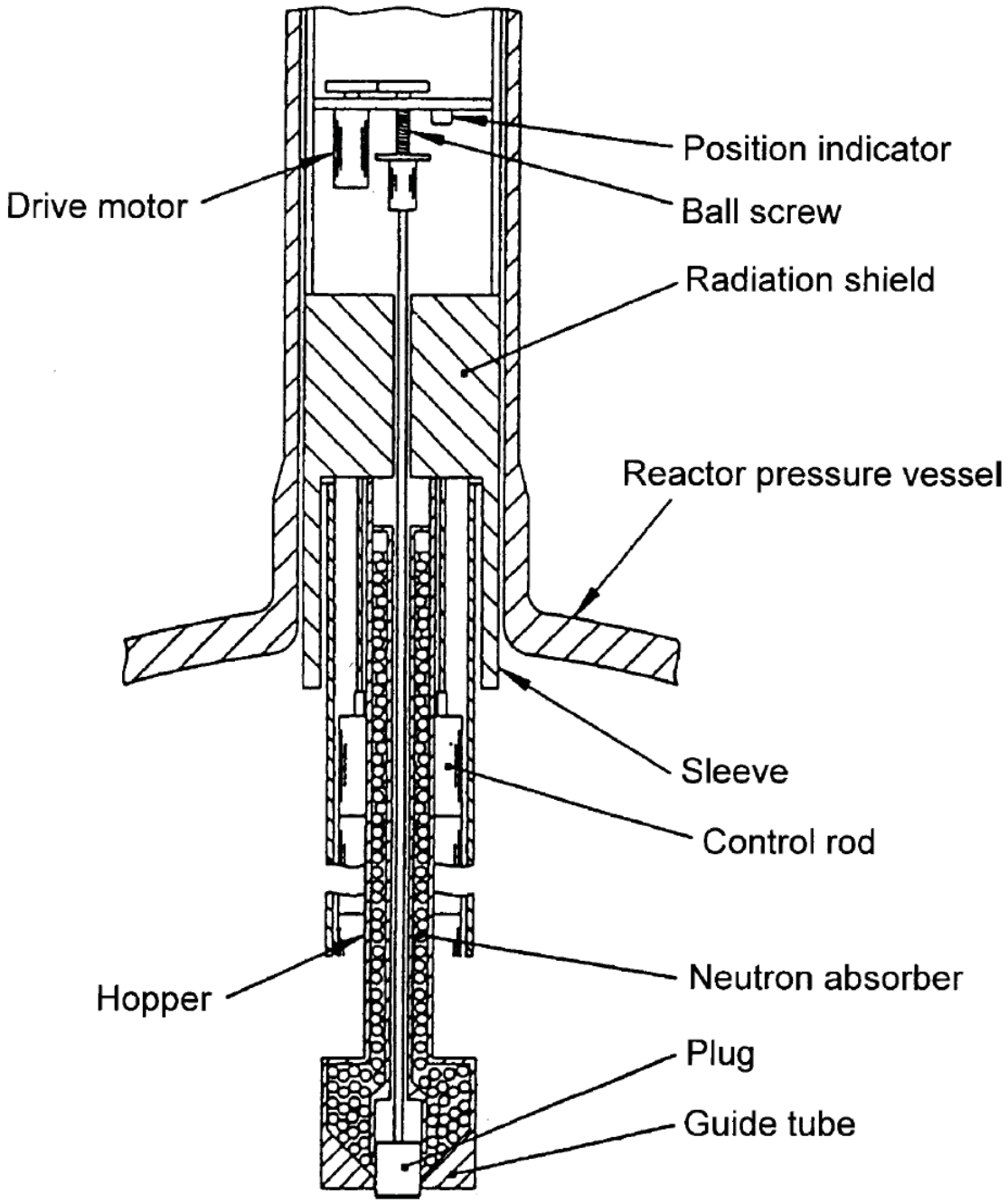


Figure 1.61. Reserved Shutdown System (Ref. 7, p. 99).

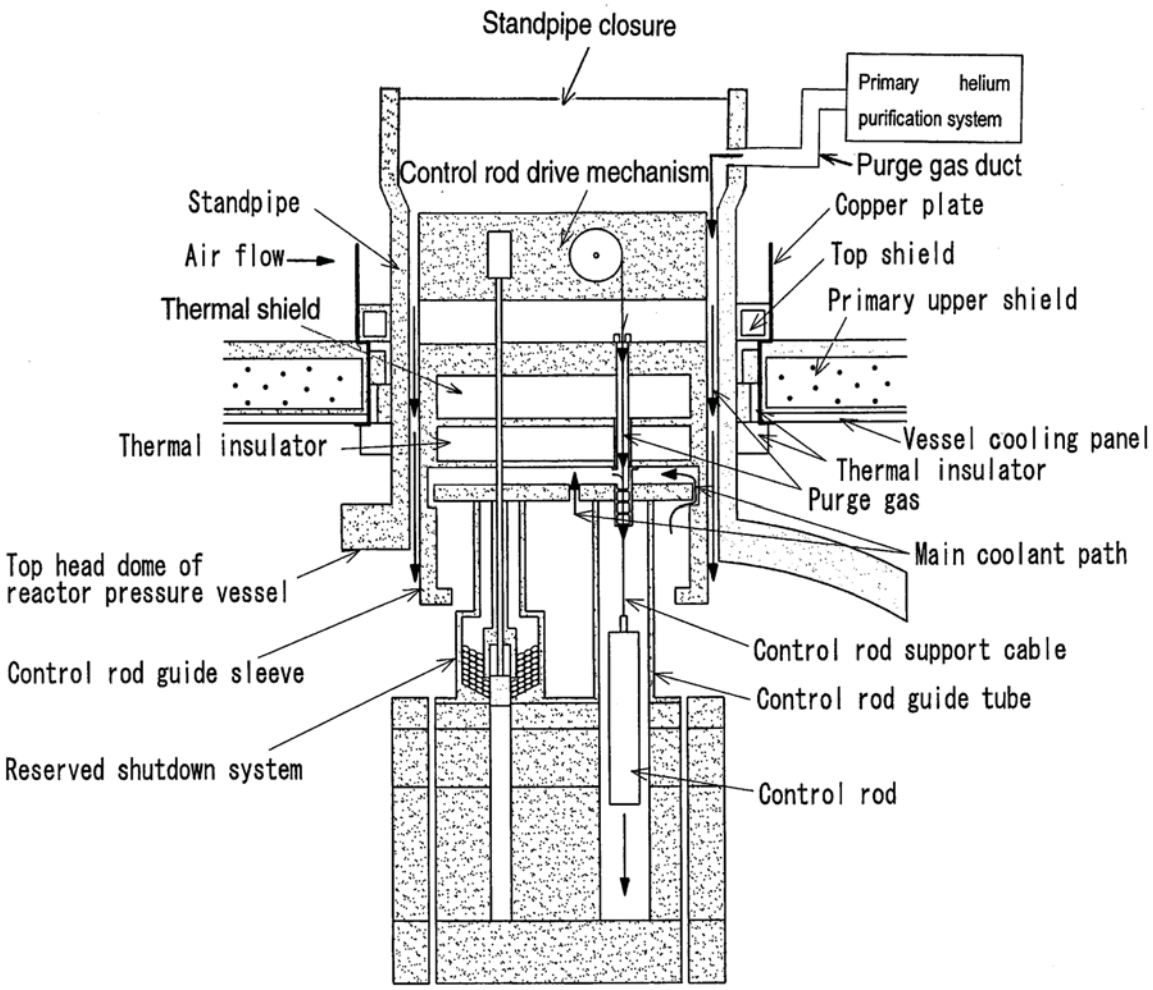


Figure 1.62. Vertical Cross-Section of Inside of Control Rod Standpipe.[a]

[a] T. Takeda and Y. Tachibana, "Indirect Air Cooling Techniques for Control Rod Drives in the High Temperature Engineering Test Reactor," *Nucl. Eng. Des.*, **223**: 25-40 (2003).

Control rod guide blocks have the same envelope dimensions as the fuel blocks and use the same dowel/socket connections as shown in Figures 1.63 and 1.64. The control rod and RSS insertion holes have a diameter of 123 mm. The bottom block of the CR guide column contains $B_4C$/C pins for thermal neutron shield (Ref. 5, p. 76). Specifications for CR blocks are found in Table 1.16.

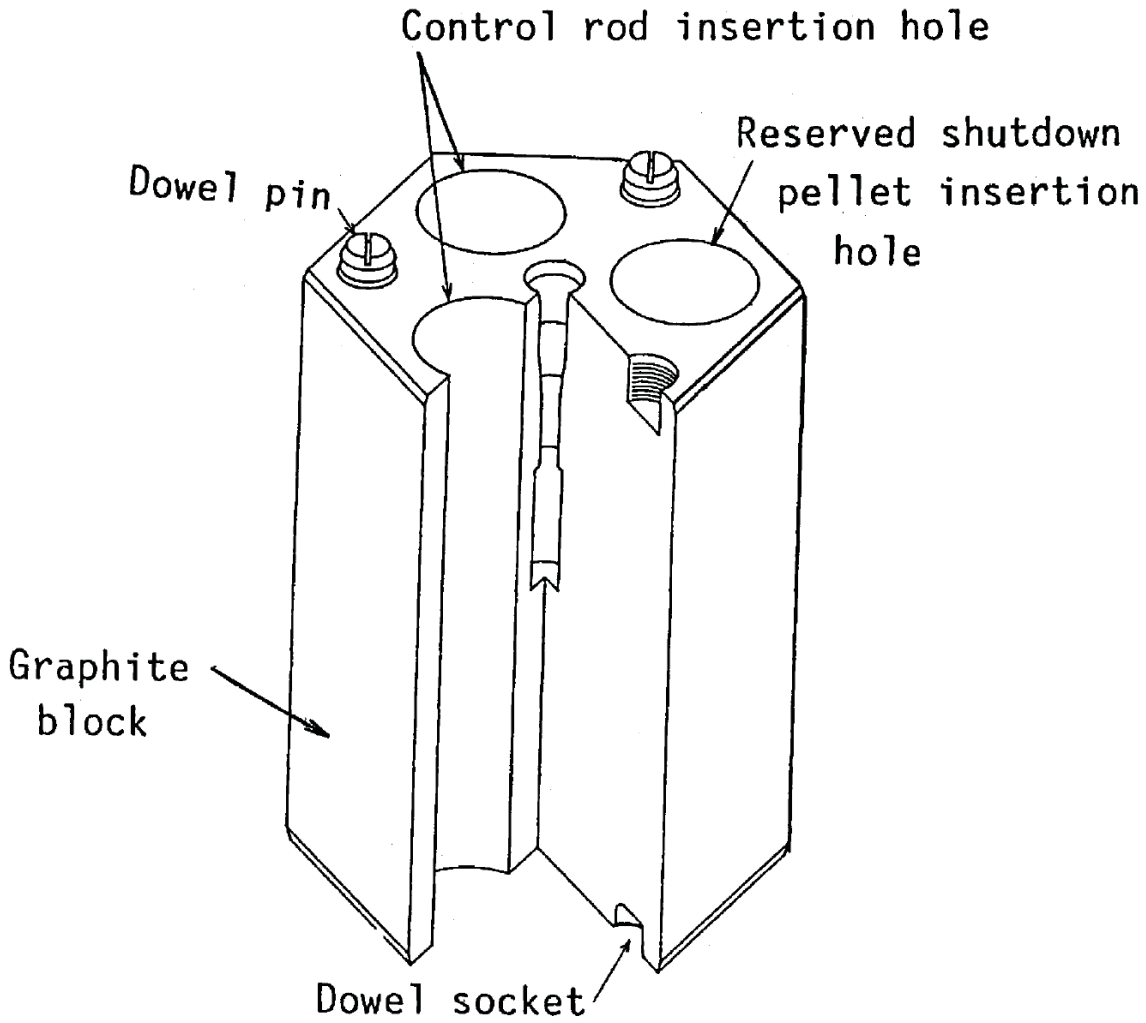


Figure 1.63. Control Rod Guide Block (Ref. 5, p. 76).

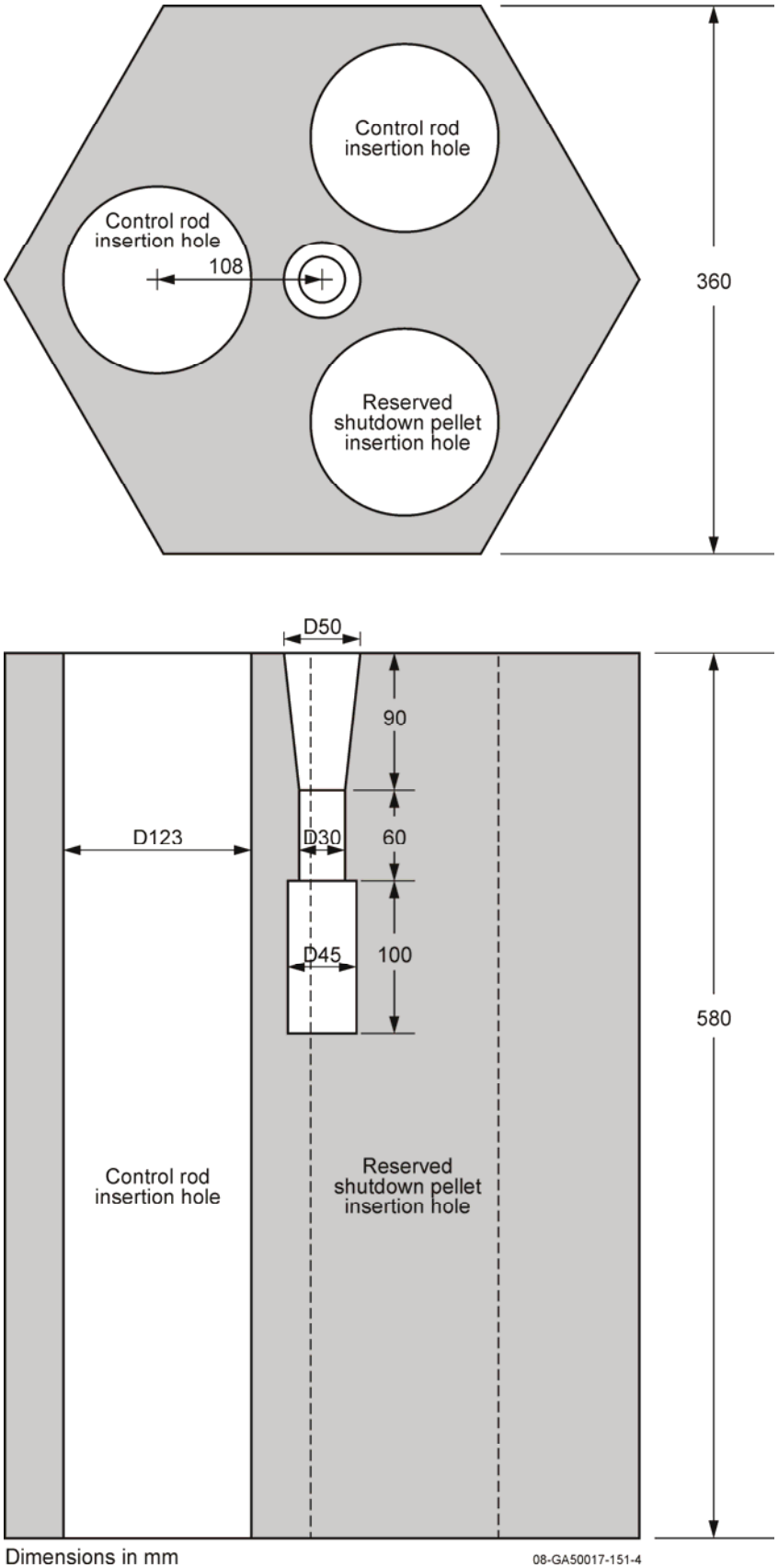


Figure 1.64. Control Rod Guide Block (Ref. 2, p. 19). Dxx represents the diameter in xx (mm).

Table 1.16. Specifications of Reflector Blocks and CR Guide Blocks (Ref. 4, p. 25).[(a)]

| | |
|---|---|
| Replaceable Reflector Blocks | |
| Material | IG-110 graphite |
| Width across Flats (cm) | 36 |
| Height (cm) | 58 |
| Density (g/cm$^3$) | 1.75 |
| Impurity (ppm) | <1 (boron equivalent) |
| Control Rod Guide Blocks | |
| Material | IG-110 graphite |
| Width across Flats (cm) | 36 |
| Height (cm) | 58 |
| Density (g/cm$^3$) | 1.75 |
| Impurity (ppm) | <1 (boron equivalent) |
| Hole | |
| Diameter (cm) | 12.3 |
| Number | 3 |
| Permanent Reflector | |
| Material | PGX graphite |
| Density (g/cm$^3$) | 1.73 |
| Impurity (ppm) | <5 (boron equivalent) |

(a) K. Yamashita, R. Shindo, I. Murata, S. Maruyama, N. Fujimoto, and T. Takeda, "Nuclear Design of the High-Temperature Engineering Test Reactor (HTTR)," *Nucl. Sci. Eng.*, **122**: 212-228 (1996).

The position indicator of the control rod drive mechanism has an accuracy of ±5 mm.[a]

The top of the control rod guide columns and irradiation columns are 100 mm lower than that of the fuel columns because the 9th layer blocks of these columns are 480 mm in height. Each horizontal gap width between two columns is 2 mm on average (Ref. 2, p. 13).

When the control rods are fully inserted, the lower ends of all control rods are on the same plane with the bottom face of the 7th layer of the fuel column. When the control rods are fully withdrawn, their upper limit is the upper face of the 1st replaceable reflector block over the fuel region with exception of the R2 CRs, which have upper limits at 725 mm below the top of the 1st block. Axial control rod positions are shown in Figure 1.65 (Ref. 2, p. 23 and 24).

The fully withdrawn positions of R2 were different from those of C, R1, and R3; they were limited because it was used for the scrams at full-power operations. The C and R1 CRs would then be inserted into the core only after core temperatures decreased, so as to maintain shutdown conditions (Ref. 1, p. 317).

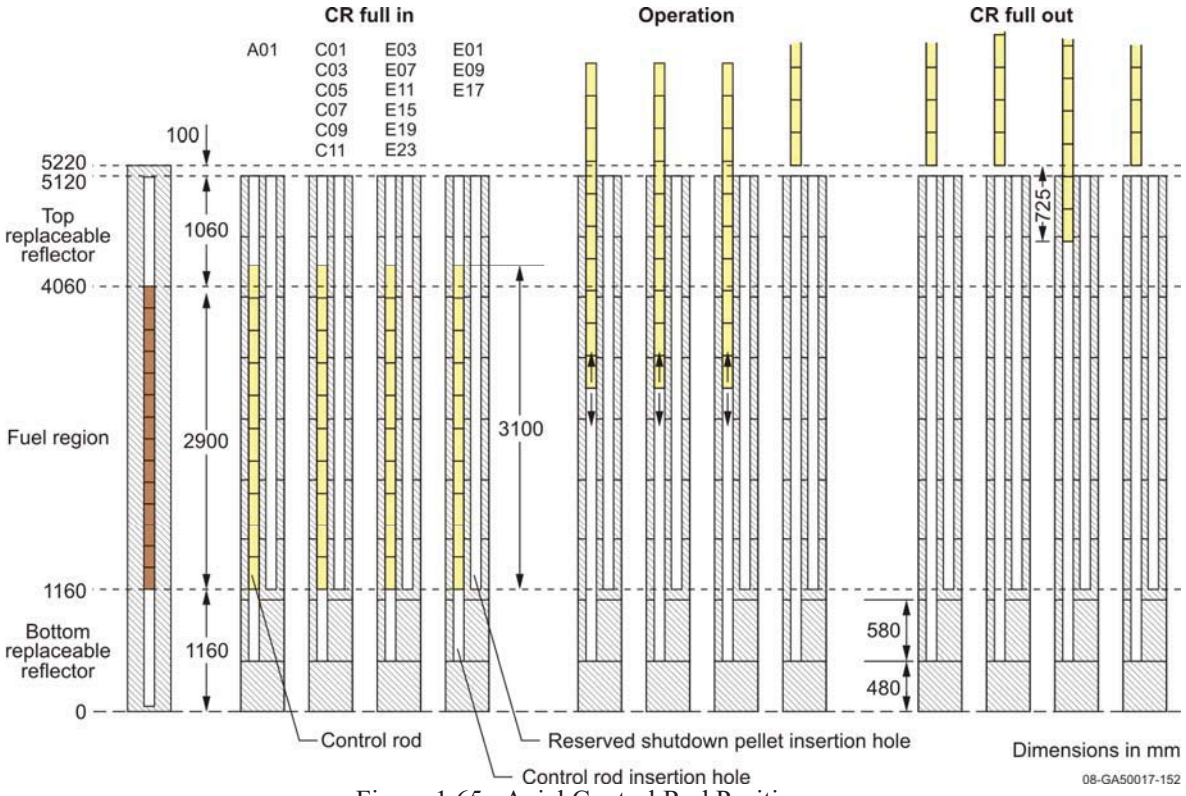


Figure 1.65. Axial Control Rod Positions.

[a] T. Takeda and Y. Tachibana, "Indirect Air Cooling Techniques for Control Rod Drives in the High Temperature Engineering Test Reactor," *Nucl. Eng. Des.*, **223**: 25-40 (2003).

## Instrumentation

Temporary neutron instrumentation was used for the start-up physics tests: three $BF_3$ counters, three micro-fission chambers (FCs), and two gamma-ray compensated ionization chambers (CICs). They were located in three irradiation test columns, as shown in Figure 1.66. The inverse multiplication factor was evaluated from the increase in neutron detection in the $BF_3$ counters. The FC was traversed in the irradiation test column for measurements of axial neutron flux distributions; they were 5 cm long and 0.6 cm in diameter and connected to the end of a long aluminum stick. The CIC was used for reactivity measurement using the inverse kinetic (IK) method. A temporary neutron source (Am-Be, $1.48 \times 10^4$ Bq) was inserted into one irradiation test column. The vertical position of equipment placed in each irradiation column is shown in Figure 1.67. An aluminum tube well was inserted into the holes of the irradiation test columns. The $BF_3$ counter in channel 1 was installed ~2 m apart from the neutron source to avoid effect of direct-flying neutrons from the source. The temporary neutron source was withdrawn from the core after establishment of critical conditions, to exclude the neutron source effect on reactivity measurements (Ref. 1, pp. 313 & 317).

The $BF_3$ counters and FCs in the same channel were located at the same vertical position for redundancy during the initial 1/M monitoring (Ref. 2, p. 25).

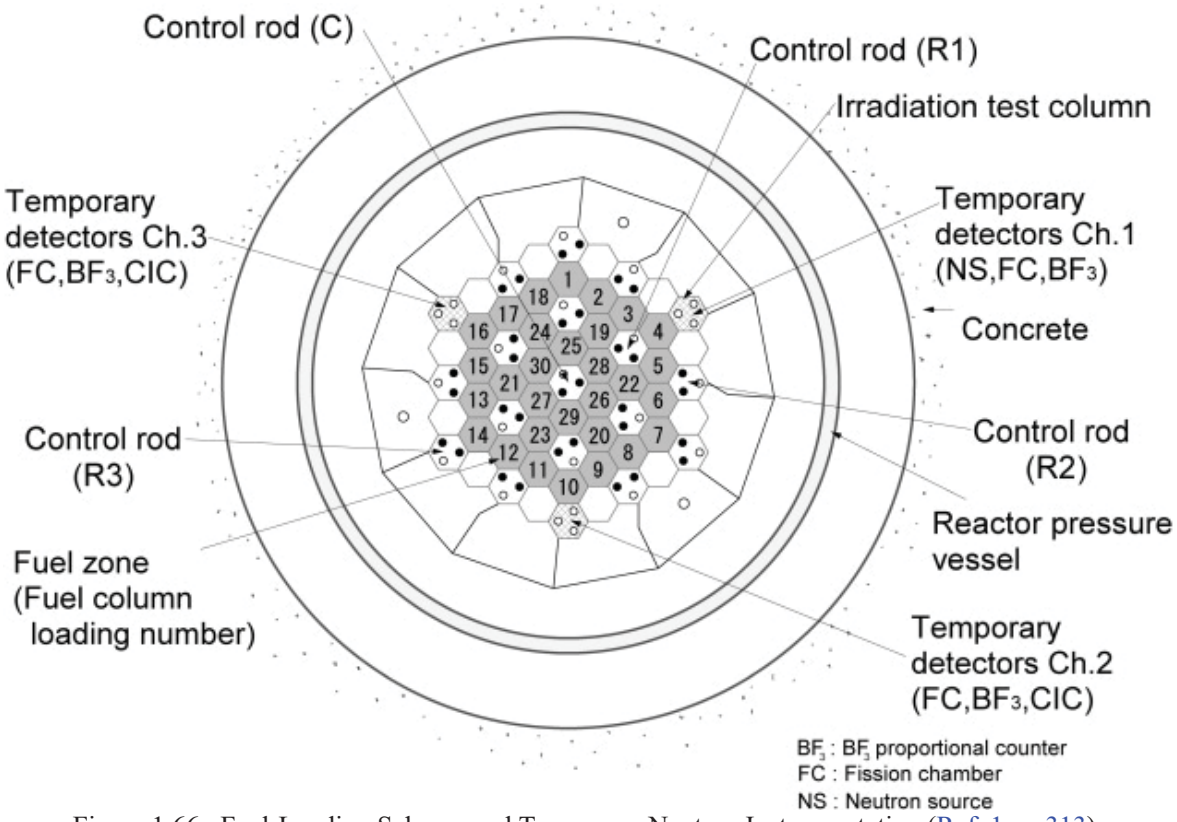


Figure 1.66. Fuel-Loading Scheme and Temporary Neutron Instrumentation (Ref. 1, p. 313).

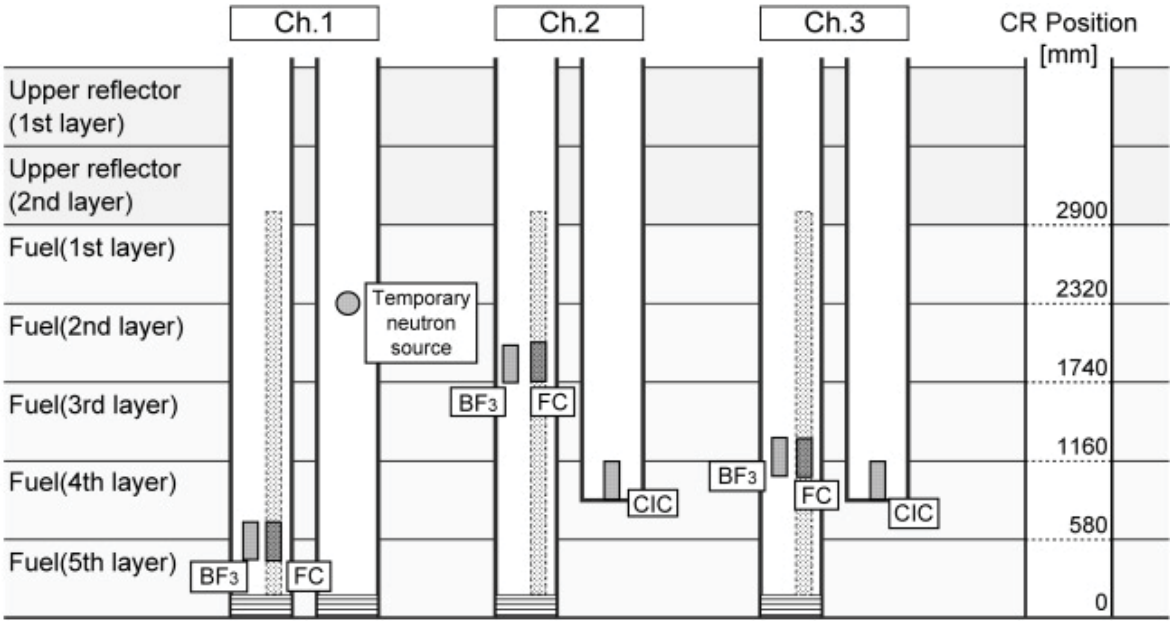


Figure 1.67. Vertical Position of the Temporary Neutron Detectors (Ref 1, p. 314).

## Graphite Blocks

The five fuel assembly blocks within a fuel column have two top reflector blocks and two bottom reflector blocks (Ref. 2, p. 12).

The top and bottom replaceable reflector blocks have the same basic configuration as the fuel blocks but do not contain fuel rods. These reflector blocks, above and below the active core, have the same arrangement of coolant channels as the fuel blocks within the same columns. The bottom replaceable reflector block below each fuel block column provides a transition of the many coolant channels to a single large channel which mates with the coolant channels within the hot plenum blocks. The alignment of the fuel, control rod guide, and replaceable reflector columns with the hot plenum blocks is maintained by dowel/socket connections in the bottom reflector blocks, which fit into the hot plenum blocks. The bottom layer of reflector blocks contains $B_4C$/C pins for the thermal neutron shield (Ref. 5, p. 76).

The arrangement of coolant channels (with 23-mm inner diameter) in the top replaceable reflector blocks (Figure 1.68) corresponds to that of coolant channels (with 41-mm inner diameter) in the fuel assemblies within the same column. The upper bottom replaceable reflector block ($8^{th}$ layer) has the same arrangement of coolant channels as the top replaceable reflector block. The lower bottom reflector block ($9^{th}$ layer) has six large coolant channels (Ref. 2, p. 21).

All blocks except the bottom block of the control rod guide column and the irradiation column are 58 cm in height and 36 cm in width across flats. Boron pins are installed into the lower parts of blocks in the $9^{th}$ layer for neutron shielding (Ref. 2, p. 23).

Consistent design of the dowel and socket system has a gap of ±0.3 mm between dowel and socket. Diameters of dowel are 45 mm and 55 mm for the fuel and control rod blocks, respectively. The socket diameters are 45.6 and 55.6 mm, respectively.[a]

[a] N. Takikawa, M. Ishihara, T. Iyoku, S. Shiozawa, M. Tokumitsu, S. Koe, and M. Uno, "Assessment of the Load Capacity of the Dowel and Socket System in the HTTR Hexagonal Block," IAEA-TECDOC-690, International Atomic Energy Agency, Vienna, pp. 105-112 (February 1993).

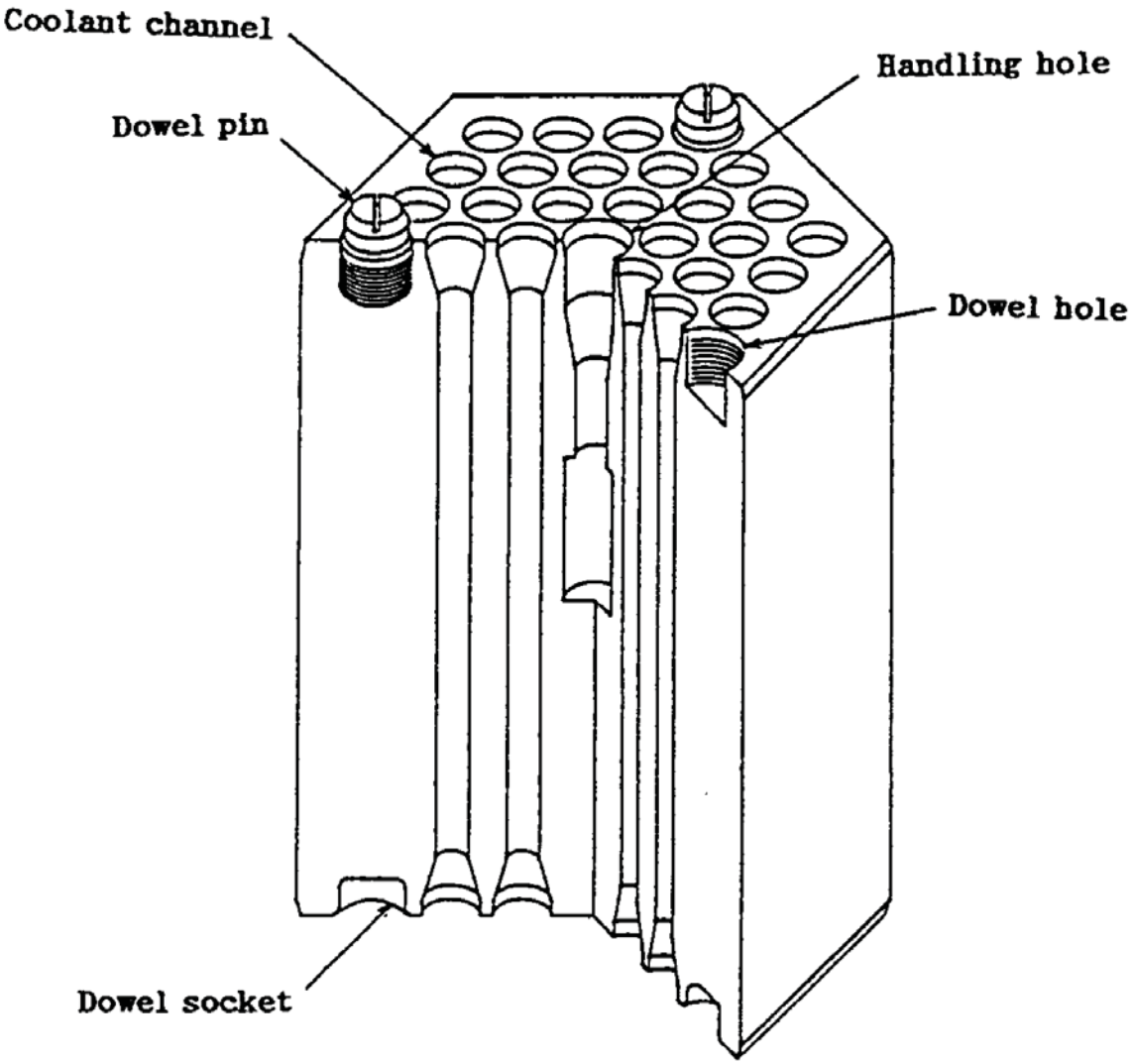


Figure 1.68. Axial Replaceable Reflector Block Used in Fuel Column Layers 1, 2, and 8 (Ref 15, p. 55).

## Dummy Blocks

Before fuel loading, the whole fuel region in the core was filled with graphite dummy blocks. There are two types of dummy blocks: graphite blocks with three large holes, and those with three small holes. The graphite blocks with three large holes were used as control rod guide columns for out-pile seismic tests of the core structure. The others with three small holes were newly produced as dummy fuel blocks (Ref. 2, p. 14).

The external form of the dummy fuel clock is the same as that of a fuel graphite block (Ref. 2, p. 23).

## Replaceable Reflectors

Twelve replaceable reflector columns are adjacent to the active core region and surrounded by permanent reflector blocks (Ref. 2, p. 12).

The side replaceable reflector blocks adjacent to the core have the same envelope dimensions as fuel blocks but are solid graphite and contain only a central handling hole for removal and insertion (Ref. 5, p. 76).

## Permanent Reflectors

A permanent graphite reflector region surrounds the core and holds it together (Figures 1.69 and 1.70). The 12 permanent reflector blocks are in the form of a large polygonal graphite block 4250 mm across flats. The permanent reflector blocks have holes for irradiation tests and neutron detectors, giving a void fraction of approximately 0.7 % (Ref. 2, p. 23).

The permanent reflector is an assembly of 12 circumferential segments in 8 axial layers (Ref. 6, p. 83).

The total height of the permanent reflectors is about 8 m. Each circumferential segment is keyed on the adjacent surface and bound to the core restraint mechanism. By-pass flow of the coolant is restricted between adjacent blocks by face contact and seal elements (see Figure 1.7).[a]

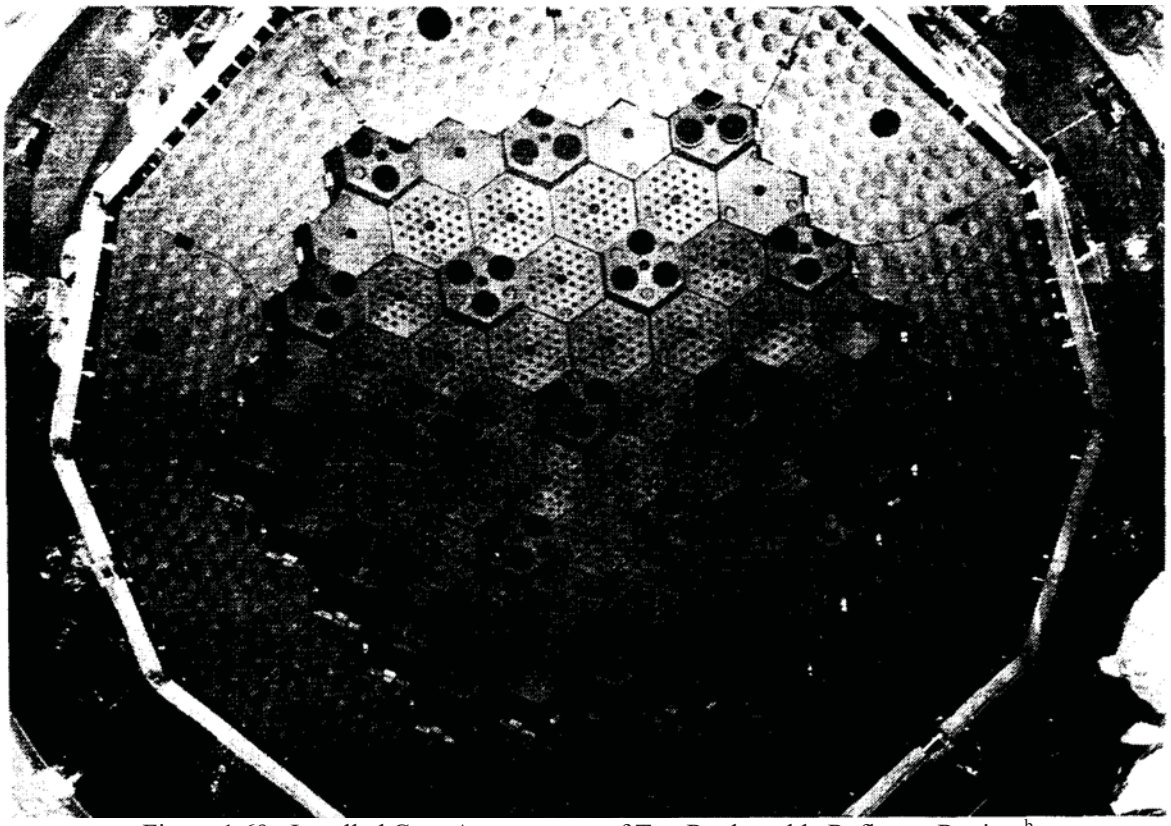

Figure 1.69. Installed Core Arrangement of Top Replaceable Reflector Region.[b]

[a] S. Maruyama, A. Saikusa, S. Shiozawa, N. Tsuji, and T. Miki, "Results of Assembly Test of HTTR Reactor Internals," IAEA-TECDOC-901, International Atomic Energy Agency, Vienna, pp. 105-116 (August 1996).

[b] T. Tanaka, O. Baba, S. Shiozawa, M. Okubo, and K. Kunitomi, "Construction of the HTTR and Its Testing Program for Advanced HTGR Development," IAEA-TECDOC-899, International Atomic Energy Agency, Vienna, pp. 15-23 (August 1996).

Figure 1.70. Inside of the Reactor Pressure Vessel. [a]

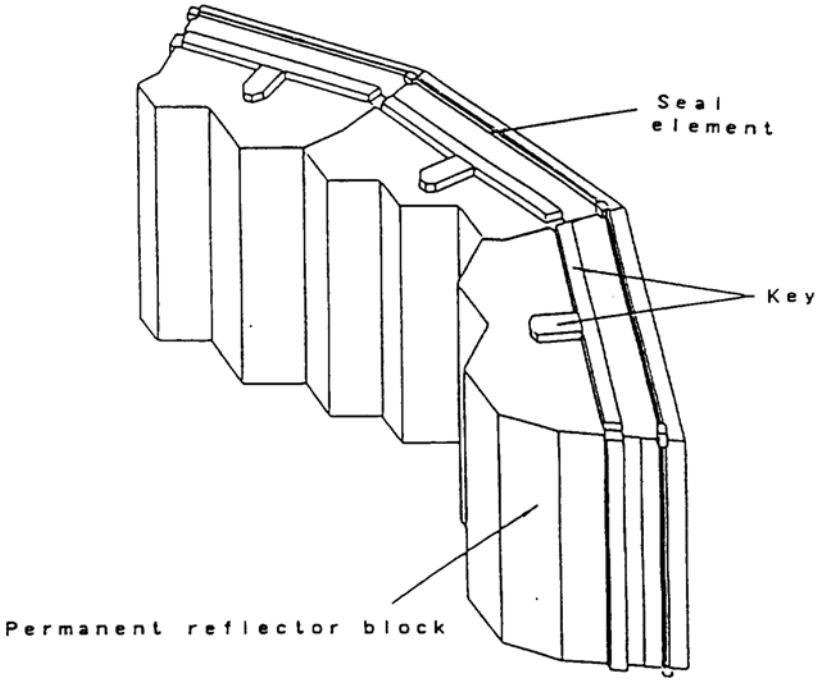


Figure 1.71. Schematic Diagram of the Permanent Reflector Blocks. [a]

[a] "Present Status of HTGR Research and Development," Japan Atomic Energy Research Institute, Tokaimura, March 2004.

**Helium Coolant**

The primary coolant system is filled with helium at normal atmospheric pressure and was not in operation during fuel loading (Ref. 2, p. 14). Impurity concentrations during initial physics tests were negligible

At power operation, the pressure in the primary circuit is about 4 MPa, and the impurity concentration is that shown in Table 1.10.

Helium gas enters the core after reversing at the upper plenum in the reactor vessel. The gas is heated as it flows downward through the fuel elements in each core region and leaves the reactor before passing through an inner tube of the outlet gas duct after mixing in the hot plenum.[b]

### *1.1.2.4 Description of Criticality Measurements*

Before fuel loading, the whole region in the core was filled with graphite dummy blocks. Helium gas was filled up to 1 atm at room temperature. Dummy blocks were replaced with fuel blocks, column by column, in the fuel loading, starting from the core periphery to the center, as shown in Figure 1.43.

In the first phase of fuel loading, six fuel columns were loaded consecutively. In the second phase, three fuel columns were loaded at a time, until a total of 15 columns were in the core. In the third phase of fuel loading, columns were loaded one at a time, so as to identify the number of fuel columns needed for the first criticality. In every loading phase, all control rods were withdrawn from the core after each fuel loading, and inverse multiplication factors were measured. Initial criticality was achieved with 19 fuel columns loaded. Symmetric annular cores were formed at 21-, 24-, and 27-fuel-column loaded cores. The fully-loaded core consists of 30 fuel columns. Figure 1.72 shows some of the fuel-loading steps during the initial core loading (Ref. 13, p. 285).

[a] S. Maruyama, A. Saikusa, S. Shiozawa, N. Tsuji, and T. Miki, "Results of Assembly Test of HTTR Reactor Internals," IAEA-TECDOC-901, International Atomic Energy Agency, Vienna, pp. 105-116 (August 1996).

[b] Y. Inagaki, R. Hino, K. Kunitomi, K. Takase, I. Ioka, and S. Maruyama, "R&D on Thermal Hydraulics of Core and Core-Bottom Structure," *Nucl. Eng. Des.*, **233**: 173-183.

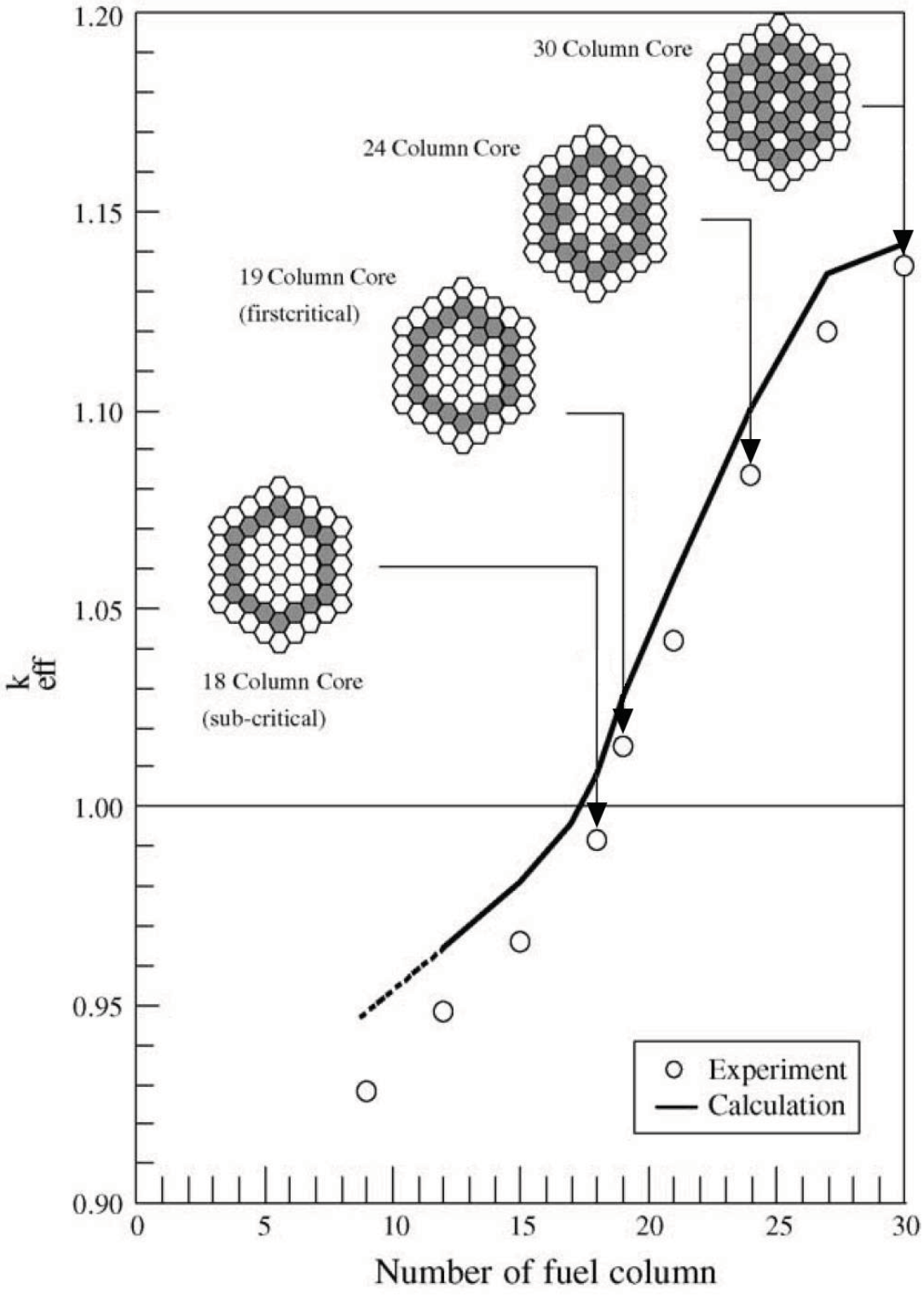


Figure 1.72. Change in $k_{eff}$ Value on Critical Approach at Room Temperature using the Fuel Addition Method (Ref. 13, p. 285).

The inverse neutron multiplication factor was monitored in order to observe the approach to criticality; the core was regarded as critical when the neutron flux was self-sustained after removing the temporary neutron source. After the initial criticality, reactivity increase was measured using the IK (Inverse Kinetics) method. The excess reactivity of the core was then obtained by adding all increments of the reactivity from the first criticality to the fully-loaded core (Ref. 2, p. 14).

Inverse multiplication factors were evaluated at 0, 6, 9, 12, 15, 16, 17, and 18 fuel-column-loaded cores to predict the first criticality (Ref. 2, p. 39). The inverse multiplication data were recorded and are shown in Figure 1.73.

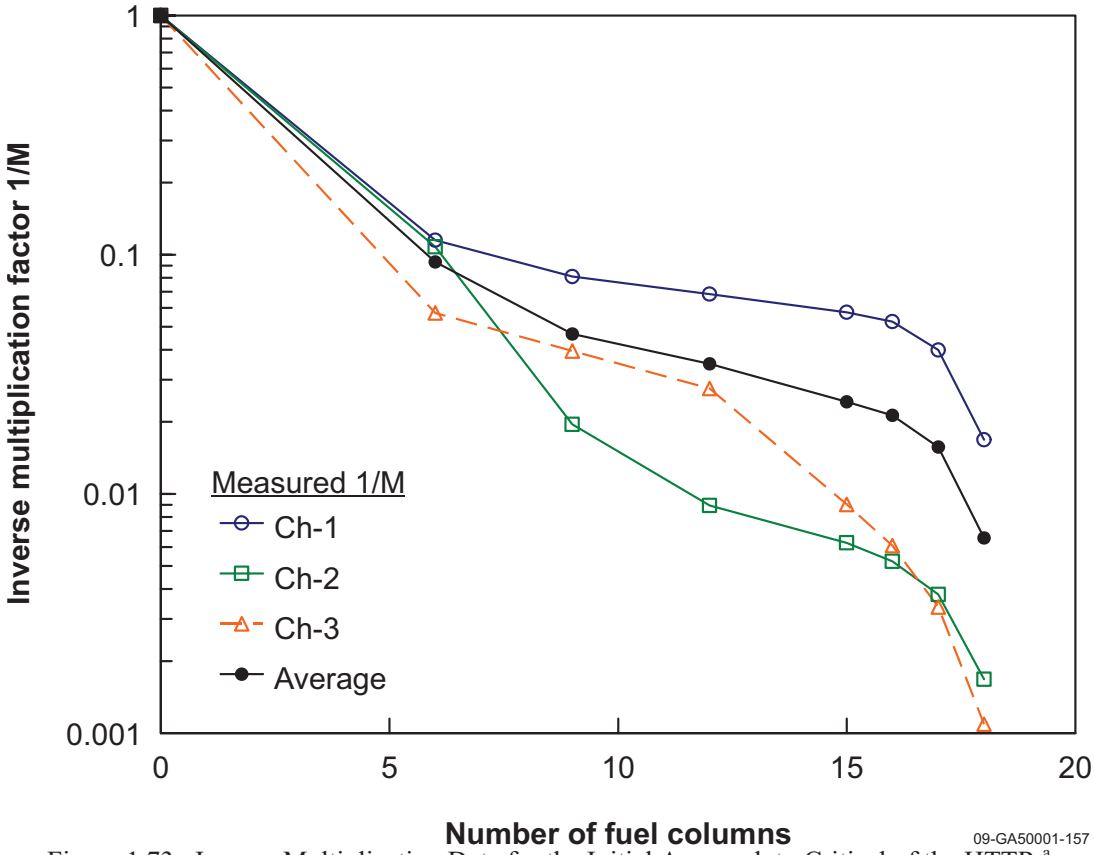


Figure 1.73. Inverse Multiplication Data for the Initial Approach to Critical of the HTTR.[a]

[a] "Present Status of HTGR Research and Development," Japan Atomic Energy Research Institute, Tokaimura, March 2004.

Measurements were carried out by using the signal processing system DSA-2 connected to the CICs, in real time. During the online reactivity experiments, the measured DC signals were digitized for use in the IK method. During the first approach to critical (after loading the 19th fuel assembly) the source criticality at very low power was achieved. Then the neutron source was removed and the central control rod moved to compensate for the change in reactivity. The first criticality of the reactor was attained on November 10, 1998. Figure 1.74 shows the result of the reactivity measurements during this approach to critical (Ref. 2, p. 113).

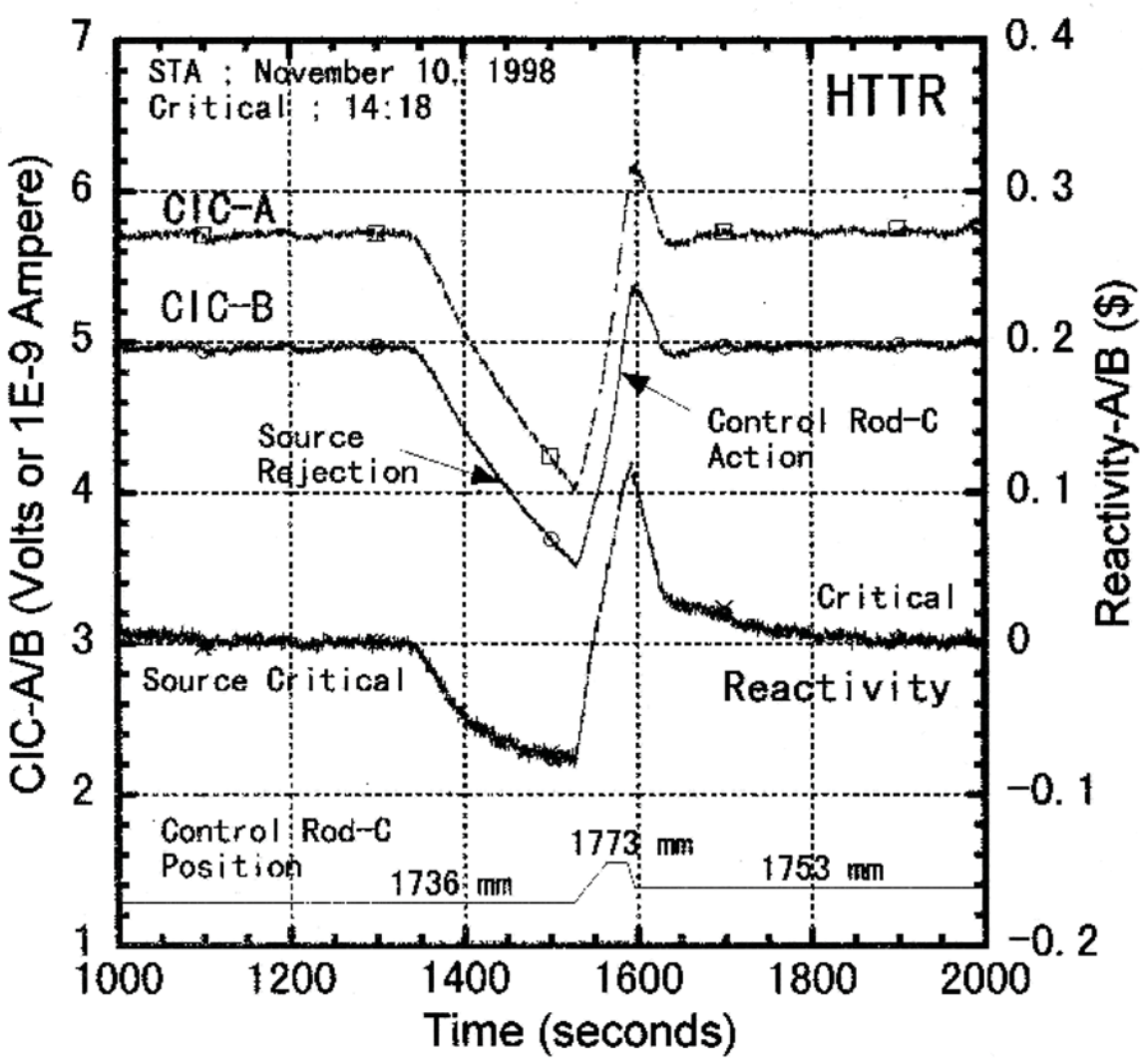


Figure 1.74. Initial Approach to Criticality (Ref 2, p. 114).

The CR positions are provided in Table 1.17 for the critical conditions of the annular and fully-loaded cores. The C-CR was inserted into the 19-column core to adjust initial criticality while the other CRs were fully withdrawn (Ref. 1, p. 317).

All control rod insertion levels are adjusted on the same level except for the three pairs of control rods in the most outer region in the side reflectors. These three pairs of CRs are usually fully withdrawn (Ref. 2, p. 40).

There were two CR patterns used for the 24-fuel-column core. The first was the flat standard (FS) pattern, where the C, R1, and R2 CRs were inserted into the core at the same height, and the R3 CRs were fully withdrawn. The second pattern was the F23 pattern, where the R2 and R3 CRs in the side reflector were inserted into the core at the same height and the C and R1 CRs were fully withdrawn. The F23 pattern was used to simulate the control of future HTGRs, where the reflector CRs would mainly be used for reactivity control. The effective multiplication factors for the measured CR positions at critical conditions were evaluated for different annular cores and temperatures. The results in Table 1.17 are adjusted such that the multiplication factors could be evaluated at 27 ºC, 300 K (Ref. 1, pp. 317-318).

Table 1.17. Measured Control Rod Positions for Critical Conditions (Ref. 1, p. 318).

| Case | Fuel Columns | Temperature (ºC) | $k_m$ [a] | Critical Rod Position (mm) [b] | | | | Remark [c] |
|---|---|---|---|---|---|---|---|---|
| | | | | C | R1 | R2 | R3 | |
| 1 | 19 | 23 | 1.00049 | 1739 | 4050 | 3325 | 4050 | C |
| 2 | 21 | 24 | 1.00037 | 2647 | 2645 | 2646 | 4049 | FS |
| 3 | 24 | 24 | 1.00037 | 2213 | 2215 | 2215 | 4049 | FS |
| 4 | 24 | 24 | 1.00037 | 4051 | 4050 | 1593 | 1592 | F23 |
| 5 | 27 | 24 | 1.00037 | 1901 | 1899 | 1899 | 4050 | FS |
| 6 | 30 | 25 | 1.00025 | 1775 | 1775 | 1775 | 4049 | FS |

(a) Measured $k_m$ has been corrected with the measured temperature coefficient (TC) for the 30-fuel-column core [$-1.23 \times 10^{-4}$ ($\Delta k/k/ºC$) to 27 ºC (300 K)]. It was assumed that use of the TC for the 30-fuel-column core was practically still useful for the other cores because of the small temperature difference of <4 ºC.

(b) Nominally fully withdrawn positions of C, R1, and R3 CRs are 4060 mm and that of the R2 CRs is 3335 mm.

(c) C = criticality obtained using central control rod only.
FS = flat standard pattern where C, R1, and R2 CRs were inserted into the core at the same levels while R3 CRs were fully withdrawn.
F23 = only R2 and R3 CRs were used for control while C and R1 CRs were fully withdrawn.

A simpler statement for control rod positions of four of the critical cases is shown in Table 1.18, representing the average for rods C, R1, and R2 (with R3 completely withdrawn).

Table 1.18. Average Control Rod Positions for Critical Conditions (Ref. 2, p. 40).

| Fuel Column | 21 (Case 2) | 24 (Case 3) | 27 (Case 5) | 30 (Case 6) |
|---|---|---|---|---|
| Rod Position (mm) | 2646 ± 5 | 2215 ± 5 | 1899 ± 5 | 1775 ± 5 |

Effective corrections to critical rod position in the core include a sinking effect from the CR driving mechanism of about -14 mm and a temperature expansion effect of about +2 mm from 25 to 27 ºC (Ref. 2, p. 46). Reported Japanese data typically had the sinking effect already accounted for in the reported rod heights.
Control rods positions were defined with distance from the bottom of the fifth fuel layer (Ref. 1, p. 317).

#### *1.1.2.5 Description of Subcriticality Measurements*

Additional information for the fully-loaded core reports a measured subcritical effective multiplication factor of 0.685 ± 0.010 when the control rods are completely inserted (Ref. 2, p. 111). The shutdown margin of the HTTR was measured by the inverse kinetics (IK) method during the criticality tests of the HTTR. The configuration of the fully-loaded subcritical core is identical to the fully-loaded critical configuration (Case 6) described in the previous section (see Figure 1.66), but with all the control rods fully inserted to rod positions of zero, which means the bottom of the control rods are level with the bottom of the bottommost fuel blocks in the core (see Figure 1.65).

Subcritical configurations were developed during the loading of the HTTR reactor and results were obtained using 1/M measurements. For the 9-, 12-, 15-, 16-, 17-, and 18-fuel-column-cores, the experimental $k_{eff}$ was 0.9282, 0.9481, 0.9652, 0.9701, 0.9785, and 0.9913, respectively. The reactivity worth for these configurations was -7.7, -5.5, -3.6, -3.1, -2.2, and -1.0 % Δk/k, respectively (Ref. 2, p. 89). The control rod positions were not reported for these configurations as they were most likely fully withdrawn.

#### *1.1.2.6 Description of Warm Criticality Measurements*

Control-rod positions for criticality were also recorded at 480 K during the evaluation of the core temperature coefficient. Control rod groups C, R1, and R2 were at the same level (1825 mm) and group R3 was fully withdrawn (Ref. 2, pp. 46, 48, and 331). The warm critical configuration is identical to that of the fully-loaded critical configuration (Case 6) described in the previous section (see Figure 1.66), but with the control rods withdrawn to the positions stated in this paragraph.

Unfortunately, this data does not represent a valid benchmark experiment (see Section 2.1.9).

### 1.1.3 Material Data

#### *1.1.3.1 Facility Description*

**Site and Facility**

Additional information is not available.

**Containment Structure**

The containment vessel is made of carbon steel (Ref. 10, pp. 135-137).

**Reactor Pressure Vessel**

The RPV is made of 2-1/4Cr-1Mo steel, normalized and tempered. There are three kinds of 2-1/4Cr-1Mo steel: forgings of Japan Industrial Standard (JIS) specification SFVAF22B, equivalent to ASTM A-336 Gr F22, Cl 3; plates of JIS SCMV4-2, equivalent to ASTM A-387 Gr 22, Cl2; and seamless pipes of JIS STPA24, equivalent to ASTM A-335 Gr P22. Material of components and weld lines are shown in Figure 1.75. The thickness of the RPV is determined so that general primary membrane stress is less than the allowable value for the design pressure of 4.7 MPa (Ref. 8, p. 106).

The fabrication procedure for the RPV is shown in Figure 1.76. There are two types of standpipes: ‘a’, a forging; and ‘b’, a forging and pipe welded together. The inner nineteen standpipes are for control rods and irradiation tests, which require dimensional accuracy in manufacturing, and are type ‘a’ standpipes. The heads on the outer 12 standpipes on the top head dome and the three standpipes on the shell are forgings that are welded to seamless pipes (Ref. 8, pp 107-108).

The top head dome is a very large forging, and the 19 nozzles for the inner standpipes are integrated into it (i.e., there are no weld lines between the dome and the nozzles). The other 13 nozzles, including a manhole nozzle, are welded to the top head dome. After welding the top head dome to the upper flange, stress relieving (SR) and final machining was performed. Then the standpipes were welded to the top head dome, followed by local stress relieving. The cylindrical shell of the RPV is made up of four plates formed and welded together. The shell was welded to the shell flange. The bottom head petal was welded to the bottom head dome, which consists of four formed plates, and the skirt. These were then welded together to build the RPV body for final stress relieving and machining. The welding of large components involved automatic narrow-gap (groove) MIG welding that was developed by Babcock-Hitachi, K.K (Ref. 8, p. 108).

Additional RPV manufacturing details can be found elsewhere.[a]

Irradiation embrittlement of the RPV is evaluated to be insignificant due to a lifetime fast fluence of less than $1 \times 10^{17}$ n/cm$^2$ (E > 1 MeV). Temper embrittlement is a concern. To reduce embrittlement, the content of Si, Mn, P, Sn, and As must be reduced according to a J-factor and X-bar parameter:

$$J - factor = \underset{(Si, Mn, P, Sn : wt.\%)}{(Si + Mn)(P + Sn) \cdot 10^4 \le 100},$$

and

$$\overline{X} = \underset{(P, Sb, Sn, As : ppm)}{\frac{10P + 5Sb + 4Sn + As}{100} \le 10}.$$

Figure 1.77 shows the J-factor and X-bar of 19 heats of manufactures 2-1/4Cr-1Mo steels for the RPV. The J-factor and X-bar ranges from 25 to 55 and from 4.1 to 8.4, respectively, which satisfies the HTTR specification. There is almost a linear relationship between the J-factor and X-bar. The embrittlement factors for the weld metal of the RPV range from 60 to 84 and 6.0 to 9.0, respectively. The silicon and manganese content of weld metal is higher than that of the base metal (Ref. 8, pp. 108-109).

The thermal shield is equipped to protect the top head closure and the standpipes from high temperature exposure, and is made up of layers of metallic heat reflecting plates (Ref. 8, p. 106).

[a] Y. Tachibana, K. Kunitomi, S. Shiozawa, T. Asami, and S. Yamaguchi, "Material and Fabrication of the HTTR Reactor Pressure Vessel," IAEA-TECDOC-988, International Atomic Energy Agency, Vienna, pp. 305-318 (December 1997).

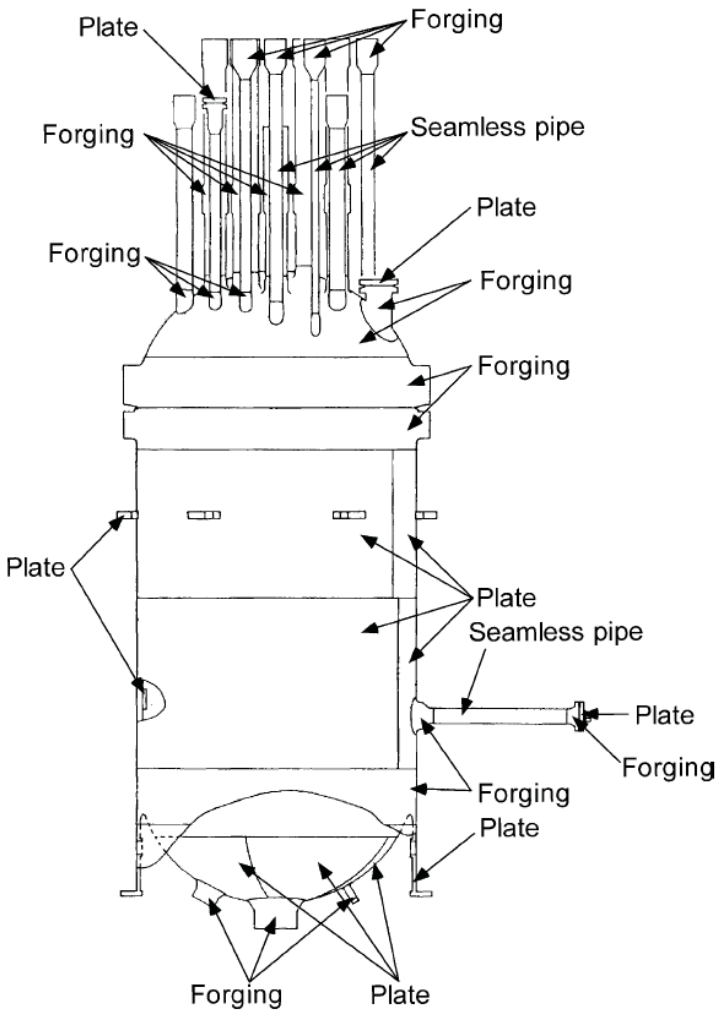


Figure 1.75. Material and Weld Lines of the RPV (Ref. 8, p. 106).

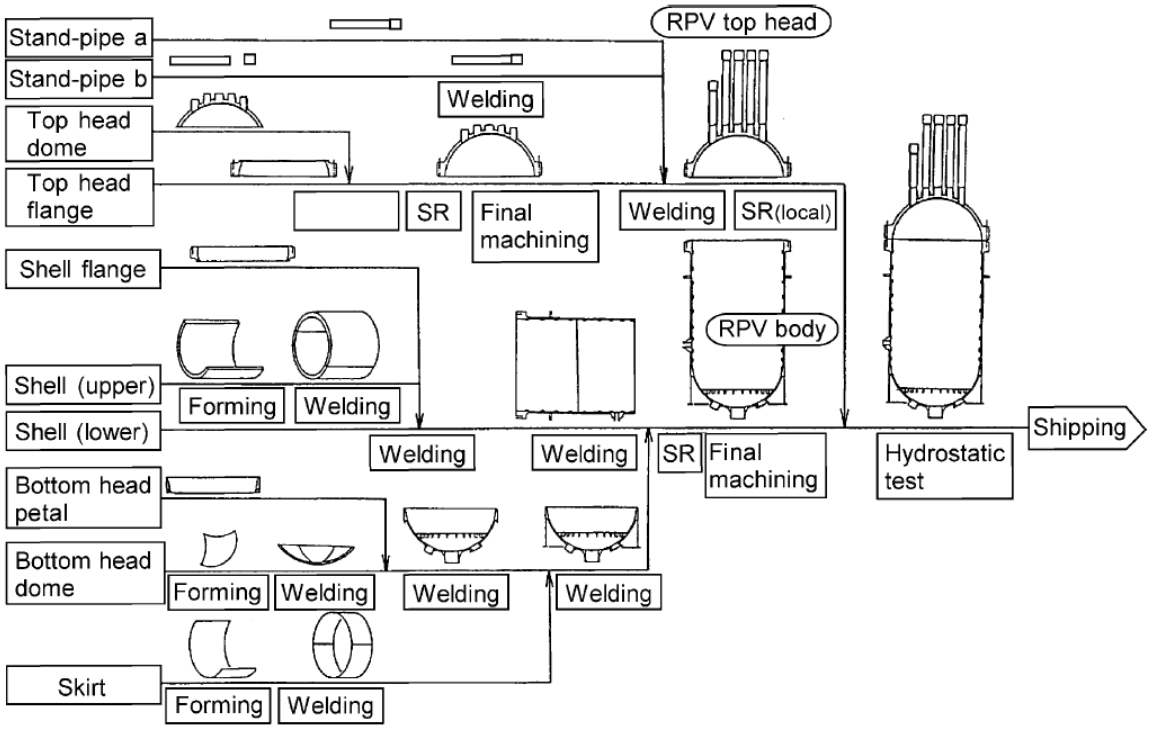


Figure 1.76. Fabrication Procedure of the RPV (Ref. 8, p. 107).

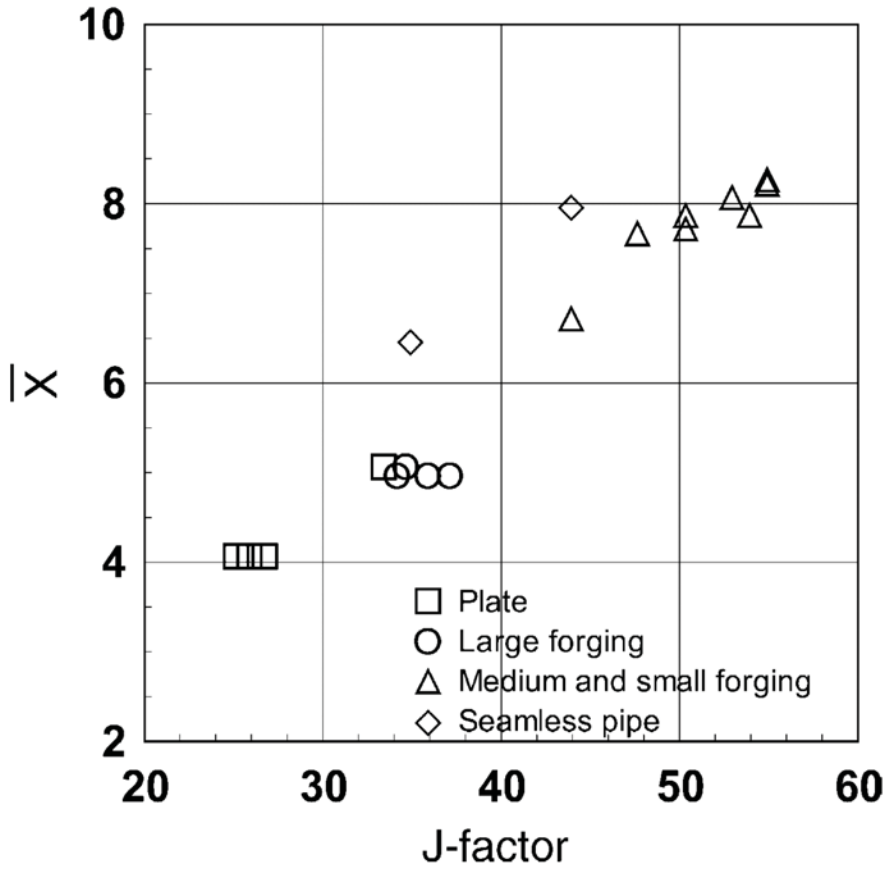


Figure 1.77. Distribution of X parameter and J-factor on 2-1/4Cr-1Mo Steel for the RPV (Ref. 8, p. 109).

**Reactor Cooling System**

The material of the heat transfer tubes and the hot header of the IHX is Hastelloy XR, and the inner and outer shells are made of 2-1/4Cr-1Mo steel (Ref. 9, p. 117).

The inner and outer shells of the PPWC are made of 2-1/4Cr-1Mo steel. Austenitic stainless steel SUS321TB is used for the heat transfer tubes because of its strength and anti-corrosion characteristics at high temperatures. The material of the baffle plates is Hastelloy XR because they will be exposed to high temperature helium gas (Ref. 9, p. 115). The casing of the primary gas circulators is made of 2-1/4Cr-1Mo steel (Ref. 9, p. 118).

The outer and inner pipes of the primary concentric gas duct are made of 2-1/4Cr-1Mo steel, the liner material is Hastelloy XR, and the insulation material is a ceramic fiber composed of $SiO_2$ and $Al_2O_3$ (Ref. 9, p.119).

For the secondary pressurized water cooler, 2-1/4Cr-1Mo steel of SCMV4-2T is used for the inner and outer shells, SUS321TB is used for the heat transfer tubes, and Hastelloy XR is used for the baffle plates and liner. 2-1/4Cr-1Mo steel is used in the pipes and Hastelloy XR is used for the liner (Ref. 9, pp. 120-121)

### *1.1.3.2 Reactor Internals*

**Graphite Support Structure**

Toyo Tanso supplied the core graphite components, fuel blocks, control rod guide blocks, replaceable reflector blocks, support posts, and post seats. They also manufactured the neutron absorber and boron-carbide/graphite (Ref. 14, p. 387).

The arrangement of graphite and carbon components in the HTTR are shown in Figure 1.78. Properties of the graphite and carbon materials are summarized in Table 1.19. Grade IG-110 graphite is isotropic fine-grained nuclear grade material. Grade PGX graphite is a structural grade with medium-to-fine grained mold. The carbon blocks at the bottom of the HTTR are fabricated from nuclear grade ASR-0RB carbon, so as to keep the metallic core support structures below 500 ºC.[a]

High-grade graphite IG-110 with high strength, corrosion, and irradiation resistance was developed with established graphite structural design guidelines (Ref. 3, p. 19). IG-110 graphite materials are highly oxidation resistant.[b] A comparison of the irradiation resistance of graphite used in the HTTR is shown in Figure 1.79. The production process for the IG-110 graphite is shown in Figure 1.80. Some photos from the fabrication and inspection processes are shown in Figures 1.81 and 1.82.

The required impurity limit in the HTTR is a boron equivalent of less than 1 ppm. Seven additional elements with requirements for reduced quantities (due to large activation cross sections, long half-lives for radioactive products, and large concentrations) are shown in Table 1.20. Cobalt impurity has a concentration on the order of 0.01 ppm or less, and is proportional to the iron impurity.[c]

---

[a] M. Ishihara, J. Sumita, T. Shibata, T. Iyoku, and T. Oku, "Principle Design and Data of Graphite Components," *Nucl. Eng. Des.*, **233**: 251-260 (2004).

[b] K. Kunitomi and S. Shiozawa, "Safety Design," *Nucl. Eng. Des.*, **233**: 45-58 (2004).

[c] N. Takikawa, T. Iyoku, S. Shiozawa, N. Ooka, M. Kambe, and A. Ide, "Non-Destructive Testing and Acceptance Test for HTTR Graphite Components," IAEA-TECDOC-690, International Atomic Energy Agency, Vienna, pp. 281-288 (February 1993).

Despite the large variance in the concentration of individual elements, the thermal-neutron absorption cross section of graphite does not exceed 4.5 – 4.8 mb.[a]

Thirteen elements such as Li, B, Na, Mg, Al, Ti, V, Cr, Fe, Mn, Ni, Co, and Zn were analyzed with ICP-MS (inductive coupled plasma-mass spectrometry) and three elements such as K, Ca, and Cu with MA-FLAAS (metal atomizer-flameless atomic absorption spectrophotometry). A quantitative analysis for the rare earths was also performed. The detection limits of the ICP-MS are shown in Figure 1.83. The determined impurities in IG-110 graphite are shown in Table 1.21. Existence of rare earth was trace in these analyses. Uranium and thorium impurity are possible but were not analyzed at the time. Because the graphite is halogen-gas purified, residual halides might be present, but are difficult to detect.[b]

The results from a later analysis of the impurity content are shown in Table 1.22.

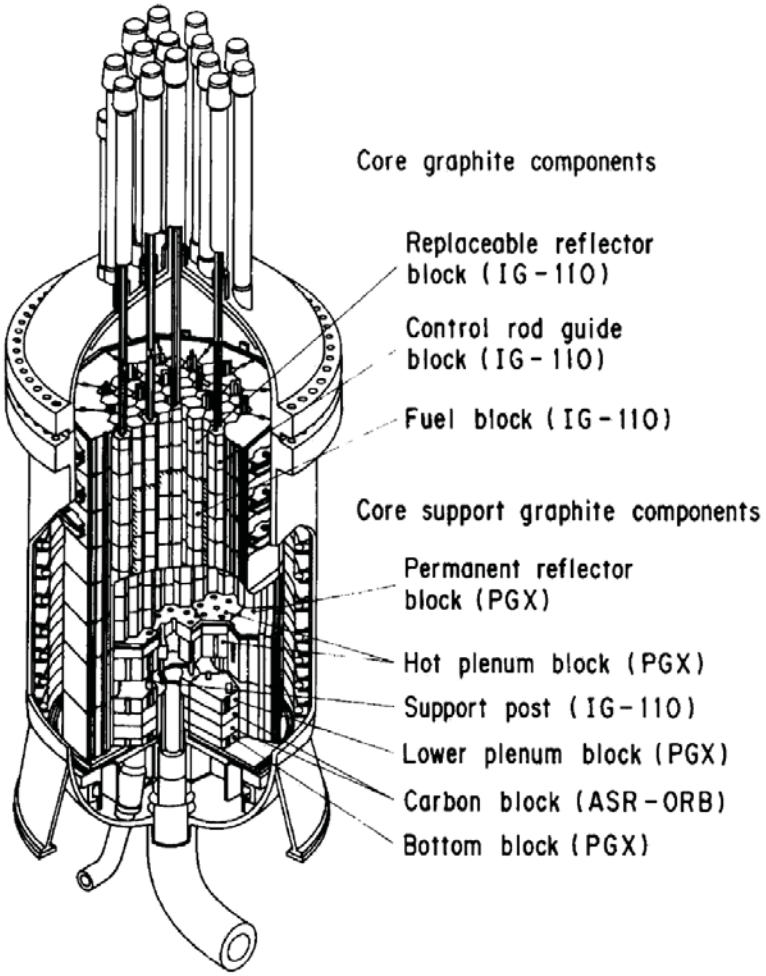


Figure 1.78. Arrangement of Graphite and Carbon Components in the HTTR.[c]

[a] Yu. S. Virgil'ev, "Impurities in and Serviceability of Reactor Graphite," *Atomic Energy*, **84**(1): 6-13 (1998).

[b] T. Miyatani, H. Suzuki, and O. Yoshimoto, "Quantitative Analysis of Trace Amounts of Impurities Contaminating Pure Graphite with ICP-MS and Metal Atomizer FLAAS," IAEA-TECDOC-690, International Atomic Energy Agency, Vienna, pp. 304-308 (February 1993).

[c] M. Ishihara, J. Sumita, T. Shibata, T. Iyoku, and T. Oku, "Principle Design and Data of Graphite Components," *Nucl. Eng. Des.*, **233**: 251-260 (2004).

Table 1.19. Typical Thermo-Mechanical Properties of Graphite and Carbon Materials in the HTTR at Unirradiated, Unoxidized, and Room Temperature Conditions (Ref. 6, p. 84).

| | IG-110 Graphite | PGX Graphite | ASR-0RB Carbon |
|---|---|---|---|
| Bulk Density ($mg/m^3$)[(a)] | 1.78 | 1.73 | 1.65 |
| Mean Tensile Strength (MPa) | 25.3 | 8.1 | 6.8 |
| Mean Compressive Strength (MPa) | 76.8 | 30.6 | 50.4 |
| Young's Modulus (GPa) | 7.9 | 6.5 | 8.7 |
| Mean Thermal Expansion Coefficient from 293-673 K ($10^{-6}$ K) | 4.06 | 2.34 | 4.40 |
| Thermal Conductivity (W/m-K at 673 K) | 80 | 75 | 10 |
| Ash (ppm) | 100 Max | 7000 Max | 5000 Max |
| Grain Size (μm) | Mean = 20 | 800 Max | 2000 Max |

(a) The units for the bulk density were correctly copied from the reference yet do not match up with other reported density units. The author most likely intended to write $mg/mm^3$, which is equal to $g/cm^3$, causing the reported densities to be more realistic.

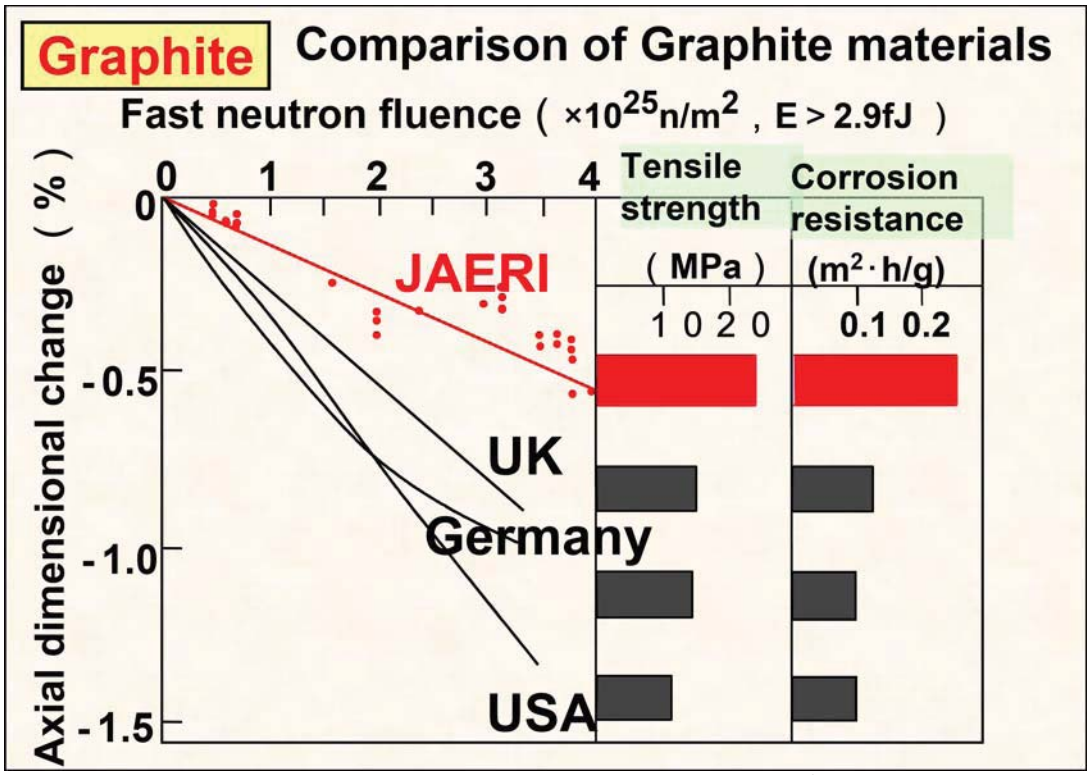


Figure 1.79. Comparison of Graphite Materials.[a]

[a] S. Shiozawa, "Status of Japan's HTR Program," *Key Note Presentation at the 2007 Int. Congress on Advances in Nuclear Power Plants (ICAPP 2007)*, Nice, France (May 13-18, 2007).

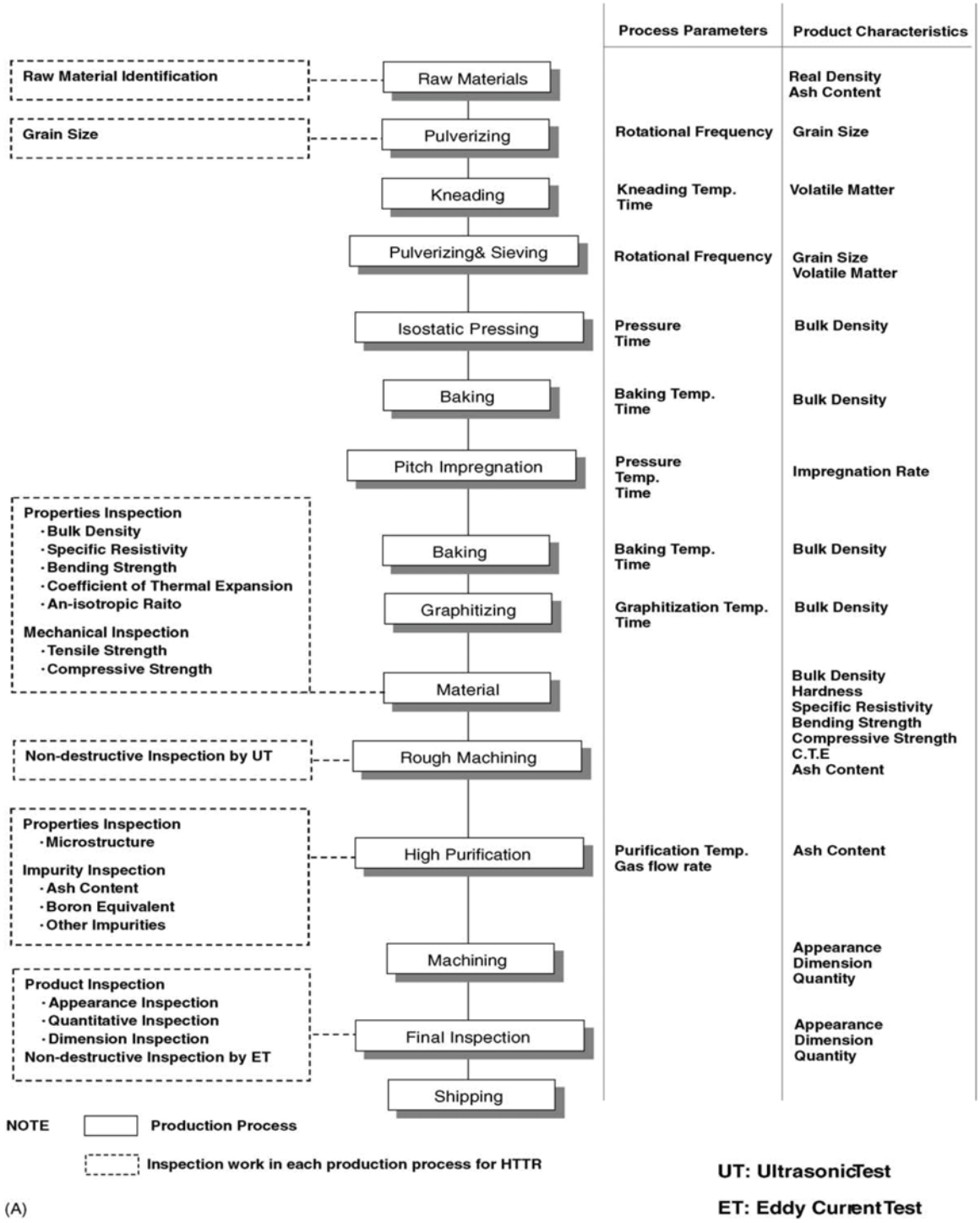


Figure 1.80. Production and Inspection Processes of IG-110 Graphite (Ref. 14, p. 388).

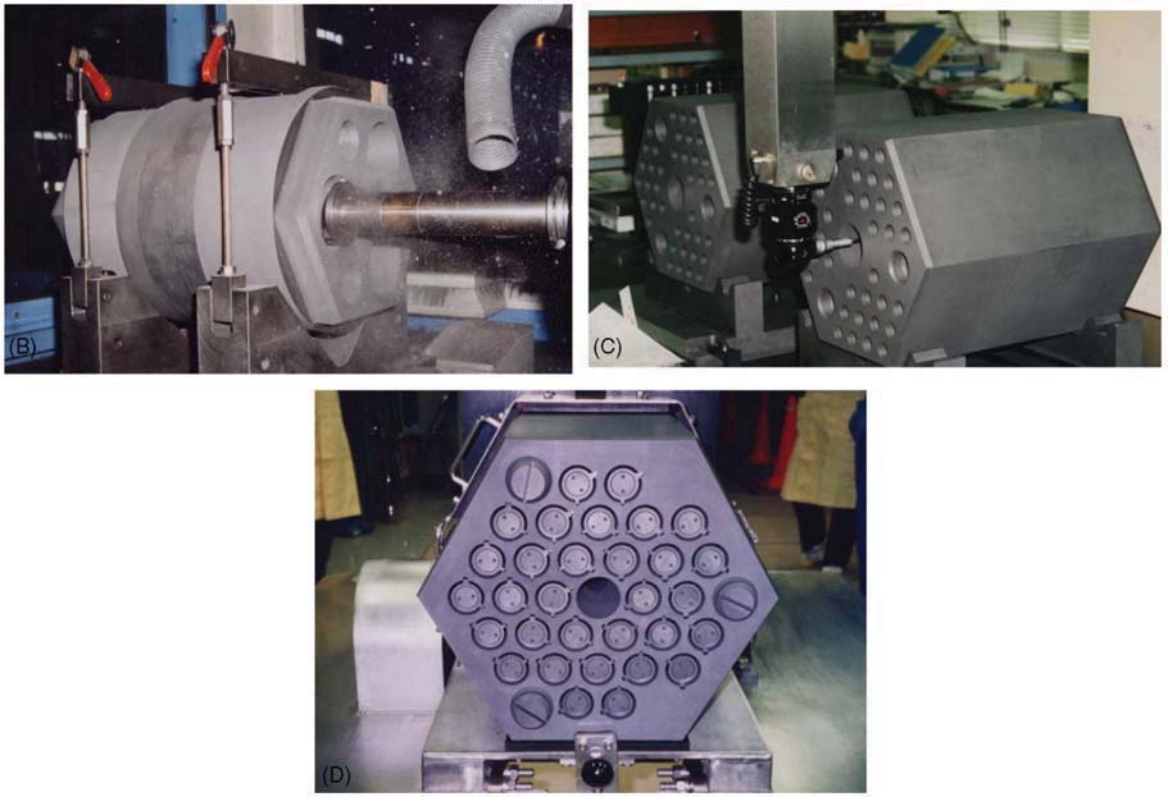


Figure 1.81. Production and Inspection Processes of IG-110 Graphite (Ref. 14, p. 388).

Figure 1.82. HTTR Graphite Block Undergoing Machining.[a]

[a] R. Bratton and T. Burchell, "NGNP Graphite Testing and Qualification Specimen Selection Strategy," INL/EXT-05-00269 (May 2005).

Table 1.20. Typical Graphite Impurities.[a]

| | Density ($g/cm^3$) | Ash (ppm) | Impurity (ppm) | | | | | |
|---|---|---|---|---|---|---|---|---|
| | | | Ca | Al | Fe | Ti | V | Si |
| IG-110 | 1.75 | <80 | 2 | ND | 2 | 0.2 | ND | <0.1 |
| IG-11 | 1.75 | 1450 | 490 | 30 | 84 | 53 | 180 | 78 |
| PGX | 1.74 | 1000 | 116 | 25 | 304 | 38 | 5 | 58 |
| ASR-0RB | 1.69 | 3000 | -- | -- | -- | -- | -- | -- |

(a) ND = Not Detectable.

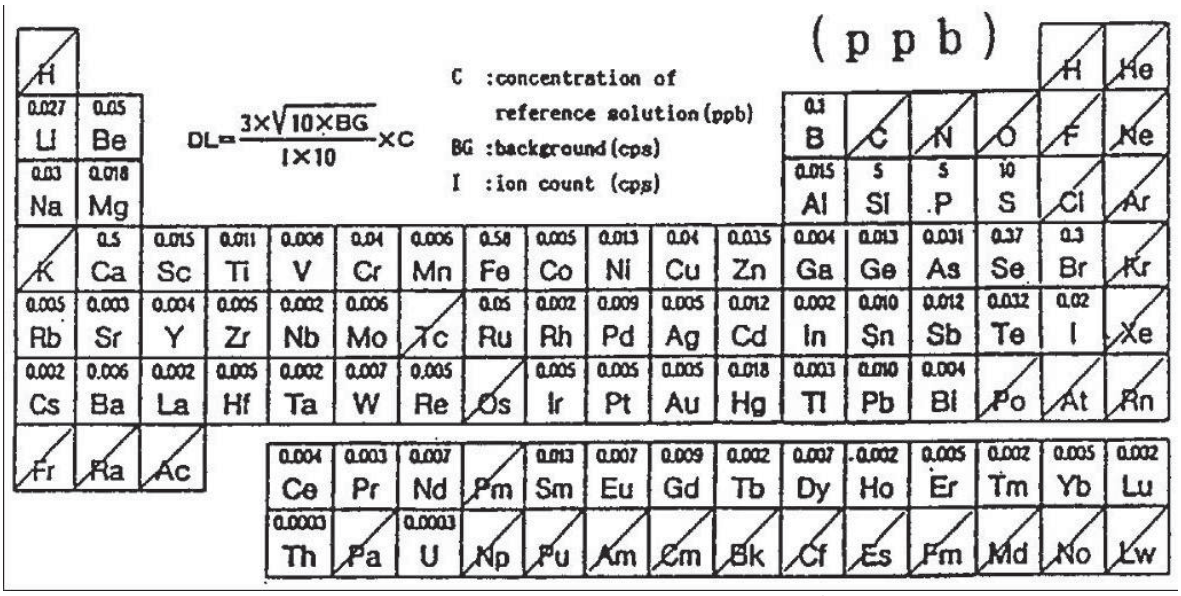


Figure 1.83. Detection Limits of ICP-MS.[a]

[a] T. Miyatani, H. Suzuki, and O. Yoshimoto, "Quantitative Analysis of Trace Amounts of Impurities Contaminating Pure Graphite with ICP-MS and Metal Atomizer FLAAS," IAEA-TECDOC-690, International Atomic Energy Agency, Vienna, pp. 304-308 (February 1993).

Table 1.21. Determined Value of Impurities in the Highly Purified Graphite (IG-110).[a]

| Element | Determined Value (ppm) | Lower Limit of Determination (ppm) |
|---|---|---|
| Li | 0.002 | 0.0004 |
| B | <0.02 | 0.02 |
| Na | 0.05 | 0.02 |
| Mg | <0.006 | 0.006 |
| Al | 0.06 | 0.02 |
| Ca | 0.08 | 0.07 |
| K | 0.03 | 0.03 |
| Ti | <0.006 | 0.006 |
| V | 0.018 | 0.002 |
| Cr | 0.006 | 0.006 |
| Fe | 0.06 | 0.01 |
| Mn | <0.004 | 0.004 |
| Co | 0.014 | 0.003 |
| Ni | 0.006 | 0.006 |
| Cu | <0.05 | 0.05 |
| Zn | 0.06 | 0.02 |

(a) T. Miyatani, H. Suzuki, and O. Yoshimoto, "Quantitative Analysis of Trace Amounts of Impurities Contaminating Pure Graphite with ICP-MS and Metal Atomizer FLAAS," IAEA-TECDOC-690, International Atomic Energy Agency, Vienna, pp. 304-308 (February 1993).

Table 1.22. Mass Fraction of Impurities and Ash in Masonry Graphite of the HTTR.[a]

| Graphite | B | Al | Ca | Ni | V | Fe | Cd | Ash |
|---|---|---|---|---|---|---|---|---|
| IG-110 | <0.1 | 0.6 | 2 | 0.2 | 0.2 | 2 | -- | 82 |
| PGX | -- | 25 | 116 | 38 | 5 | 304 | -- | 1000 |

(a) Yu. S. Virgil'ev, "Impurities in and Serviceability of Reactor Graphite," *Atomic Energy*, **84**(1): 6-13 (1998).

## Metallic Support Structure

High temperature structural materials were chosen for the high temperature components of the HTTR. The materials used include a nickel-based, corrosion and heat resistant superalloy, Hastelloy XR; normalized and tempered (NP) 2-1/4Cr-1Mo steel; two types of austenitic steels, SUS321TB and SUS316; and 1Cr-0.5Mo-V steel, which is an alloy steel bolting material for high temperature service. The components and service conditions for these materials is listed in Table 1.23 (Ref. 12, pp. 261-262).

Nuclear grade Hastelloy XR was developed by tightening the chemical composition specifications of Hastelloy X. Improvements include an optimization of the manganese and silicon contents, lowering of

aluminum and titanium contents, lowering of the cobalt content, and optimization of the boron content (addition of within 40-60 ppm). A comparison of Hastelloys X and XR is shown in Table 1.24 (Ref. 12, pp. 262-263). The average composition of the base and weld metals of Hastelloy XR is shown in Table 1.25. A separate study found the average composition of Hastelloy XR to be that reported in Table 1.26.

Although the chemical composition of Hastelloy XR is similar to that of Hastelloy X, the corrosion resistance of Hastelloy XR is much better in high-temperature helium surroundings (Figure 1.84).[a]

Hastelloy XR was developed by JAERI and Misubishi Material Co. (Ref .14, p.382).

The component materials of the restraint band are SNB16 steel for the tensile element and SUS316 for the compression element. Although the thermal expansion coefficients of the steels are different from those of graphite and the core structural materials, the coefficient of the band itself is adjusted to be equal to that of graphite (Ref. 6, p. 85).

2-1/4Cr-1Mo steel has a variety of applications to pressure-retaining components in service at elevated temperatures, in particular to boilers and liquid metal fast breeder nuclear reactors (LMFBRs) including the Japanese prototype LMFBR "Monju" (Ref. 12, p. 269).

SUS321TB and SUS316 steels are both well-experienced heat-resistant materials with superior mechanical strengths at temperatures up to about 700 ºC. In the HTTR, SUS321TB is applied to heat transfer tubes of the PPWC, secondary pressurized water cooler, and the AHX. The tube maximum temperature is about 400 ºC during normal operation. SUS316 is applied to reactor internal structures such as a core restraint mechanism and control rod guide tubes. The maximum temperature of these structures is also 400 ºC under normal operating conditions (Ref. 12, p. 270).

1Cr-0.5Mo-V steel has widespread application for bolts in chemical plant vessels, and is used as a bolting material for nuclear applications below 425 ºC. In the HTTR, 1Cr-0.5Mo-V steel (JIS SNB16) is applied not just in bolts for the RPV and gas circulator castings, but also for parts in the core restraint mechanism (Ref. 12, p. 270).

[a] T. Takeda, J. Iwatsuki, and Y. Inagaki, "Permeability of Hydrogen and Deuterium of Hastelloy XR," *J. Nucl. Mat.*, **326**: 47-58 (2004).

Table 1.23. Materials and Service Conditions of HTTR High Temperature Components (Ref. 12, p 262).

| Material | Product Form | Components | Service Conditions | | Maximum Allowable Temperature (°C) |
|---|---|---|---|---|---|
| | | | Design Temperature (°C) | Design Pressure (MPa) | |
| 9/4Cr-1Mo Steel | Plate, Forging, Pipe | Reactor Pressure Vessel | 440 | 4.8 | 550 |
| | | Shells of Intermediate Heat Exchanger, Primary Pressurized Water Cooler, etc. | 430 | | |
| | | Outside Pipe of Concentric Double Pipe | 430 | | |
| Hastelloy XR | Tube, Plate, Forging | Intermediate Heat Exchanger Heat Transfer Tubes | 955 | 0.29 | 1000 |
| | | Intermediate Heat Exchanger Hot Header | 940 | | |
| SUS321 | Tube | Primary Pressurized Water Cooler Heat Transfer Tubes | 380 | 4.8 | 650 |
| SUS315 | Bar | Core Restraint Mechanism | 450 | -- | 650 |
| 1Cr-0.5Mo-V Steel | Forging | Core Restraint Mechanism | 450 | -- | 450 |

Table 1.24. Chemical Compositions (wt.%) of Hastelloys XR and X (Ref. 12, p 263).

| Material | Range | C | Mn | Si | P | S | Cr | Co | Mo | W | Fe | Ni | B | Al | Ti | Ca |
|---|---|---|---|---|---|---|---|---|---|---|---|---|---|---|---|---|
| XR | Max | 0.15 | 1.00 | 0.50 | 0.040 | 0.030 | 23.00 | 2.50 | 10.00 | 1.00 | 20.00 | Rest | 0.010 | 0.05 | 0.03 | 0.50 |
| | Min | 0.05 | 0.75 | 0.25 | -- | -- | 20.50 | -- | 8.00 | 0.20 | 17.00 | Rest | -- | -- | -- | -- |
| X | Max | 0.15 | 1.00 | 1.00 | 0.040 | 0.030 | 23.00 | 2.50 | 10.00 | 1.00 | 20.00 | Rest | 0.010 | 0.50 | 0.15 | 0.50 |
| | Min | 0.05 | -- | -- | -- | -- | 20.50 | 0.50 | 8.00 | 0.20 | 17.00 | Rest | -- | -- | -- | -- |

Table 1.25. Chemical Composition (wt.%) of Hastelloys XR base and weld material.[(a)]

| Material | C | Mn | Si | Cr | Co | Mo | W | Fe | Ni | B | Al | Ti |
|---|---|---|---|---|---|---|---|---|---|---|---|---|
| Base | 0.060 | 0.89 | 0.33 | 21.6 | 0.03 | 9.06 | 0.49 | 17.99 | Rest | 0.0037 | <0.01 | 0.01 |
| Weld | 0.051 | 0.80 | 0.39 | 21.3 | 0.001 | 9.20 | 0.53 | 18.2 | Rest | 0.0033 | 0.05 | 0.002 |

(a) Y. Kurata, T. Tanabe, I. Mutoh, H. Tsuji, K. Hiraga, M. Shindo, and T. Suzuki, "Creep Properties of Base Metal and Welded Joint of Hastelloy XR Produced for High-Temperature Engineering Test Reactor in Simulated Primary Coolant Helium," *J. Nucl. Sci. Tech.*, **36**(12): 1160-1166 (December 1999).

Table 1.26. Chemical Composition (wt.%) of Hastelloys XR.[(a)]

| C | Mn | Si | P | S | Cr | Co | Mo | W | Fe | Ni | B | Al | Ti | Cu | N |
|---|---|---|---|---|---|---|---|---|---|---|---|---|---|---|---|
| 0.08 | 0.94 | 0.36 | <0.001 | 0.001 | 21.18 | 0.01 | 9.07 | 0.49 | 18.02 | Rest | 0.0021 | 0.02 | <0.01 | <0.01 | 0.009 |

(a) Y. Kaji, H. Tsuji, H. Nishi, Y. Muto, H-J. Penkalla, and F. Schubert, "Multiaxial Creep Behavior of Nickel-Base Heat-Resistant Alloys Hastelloy XR and Ni-Cr-W Superalloy at Elevated Temperature," *J. Nucl. Sci. Tech.*, **39**(8): 923-928 (August 2002).

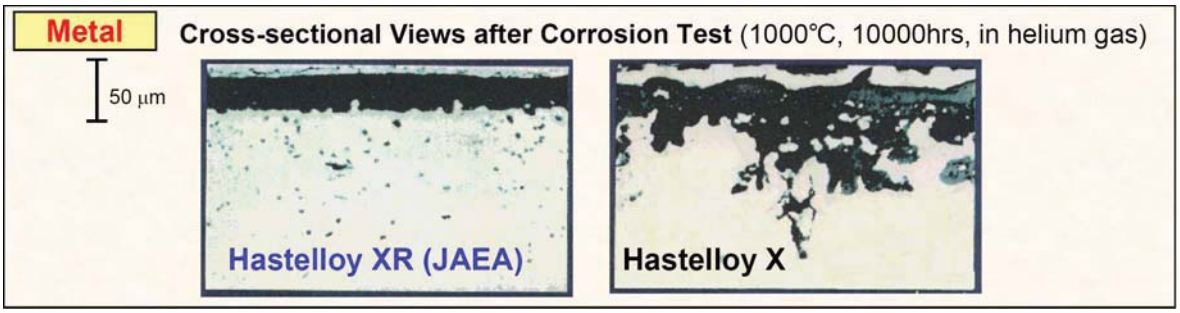


Figure 1.84. Demonstration of Improved Corrosion Resistance of Hastelloy XR.[a]

## Reactor Core Shielding

The top shielding block is hexagonal and composed of sintered $B_4C/C$, a casing of SUS316, and dowel pins. The side shielding block is also composed of $B_4C/C$ and a SUS316 casing. The support plate is composed of SUS316 (Ref. 6, p. 86).

## General Instrumentation and Control Systems

Hastelloy XR was implemented in the instrumentation and control systems of the HTTR due to the high temperature environment. Heat and corrosion resistant superalloy Hastelloy XR can be used at temperatures as high as 950 ºC at normal operation and 1000 ºC in accidents. High temperature structural design guidelines for high temperature metallic components were established (Ref. 3, p. 19).

### *1.1.3.3 Reactor Core Components*

## Reactor Core

The core consists of nine block layers with 30 columns in the active core surrounded by removable and permanent reflectors, the composition of which is described below.

## Prismatic Fuel

Some fuel material properties are contained within Tables 1.13 and 1.14. Uranium enrichment details are provided in Table 1.11.

Figure 1.85 shows a flow diagram of the HTTR fuel production process. The $UO_2$ kernels were fabricated in a gel-precipitation process, where a uranyl nitrate solution containing methocel and an additive was dropped into concentrated ammonia solution. Gel-particles formed in the ammonia solution were then dried, calcinated, and sintered. The coating layers were deposited on the kernels in a CVD

[a] S. Shiozawa, "Status of Japan's HTR Program," *Key Note Presentation at the 2007 Int. Congress on Advances in Nuclear Power Plants (ICAPP 2007)*, Nice, France (May 13-18, 2007).

process using a fluidized coater. The buffer and high density PyC coating layers were derived from $C_2H_2$ and $C_3H_6$, respectively, and the SiC layer from $CH_3SiCl_3$. In the fabrication process of the fuel compacts, the coated particles were overcoated in advance with phenol-resinated graphite powder, and these particles were formed into green compacts by warm-press. The green compacts were carbonized by a heat treatment at 800 ºC, followed be degassing at 1800 ºC.

In the process of the fuel compact fabrication, the overcoat of the graphite matrix powder was affixed on the coated particles aimed to protect the coating layer from mechanical damage by pressing in metal dies and by graphite-matrix shrinkage during heat treatments of the green compacts. Dual-layered overcoat of about 200 μm thickness was applied, providing 30 vol. % packing fraction of the coated particles in the fuel compacts. The first layer of overcoat was 80 μm thick, followed by curing at about 180 ºC. Then the second layer was added to achieve the desired packing fraction.

The resinated graphite powder is prepared by mixing electrographite powder, natural graphite powder, and phenol resin as a binder in the ratio 16:64:20, followed by grinding the mixture to powder.[a]

The final heat-treatment of the green fuel compacts is at 1073 K in flowing $N_2$ to carbonize the binder. Then the compacts are degassed in vacuum at 2073 K.[b]

The fabrication schedule for the first HTTR fuel loading is shown in Figure 1.86.

[a] K. Minato, H. Kikuchi, T. Tobita, K. Fukuda, M. Kaneko, N. Suzuki, S. Yoshimuta, and H. Tomimoto, "Improvements in Quality of As-Manufactured Fuels for High-Temperature Gas-Cooled Reactors," *J. Nucl. Sci. Tech.*, **34**(3): 325-333 (March 1997).

[b] K. Minato, H. Kikuchi, T. Tobita, K. Fukuda, M. Kaneko, N. Suzuki, S. Yoshimuta, and H. Tomimoto, "Improvements in Quality of As-Manufactured Fuels for High-Temperature Gas-Cooled Reactors," *J. Nucl. Sci. Tech.*, **34**(3): 325-333 (March 1997).

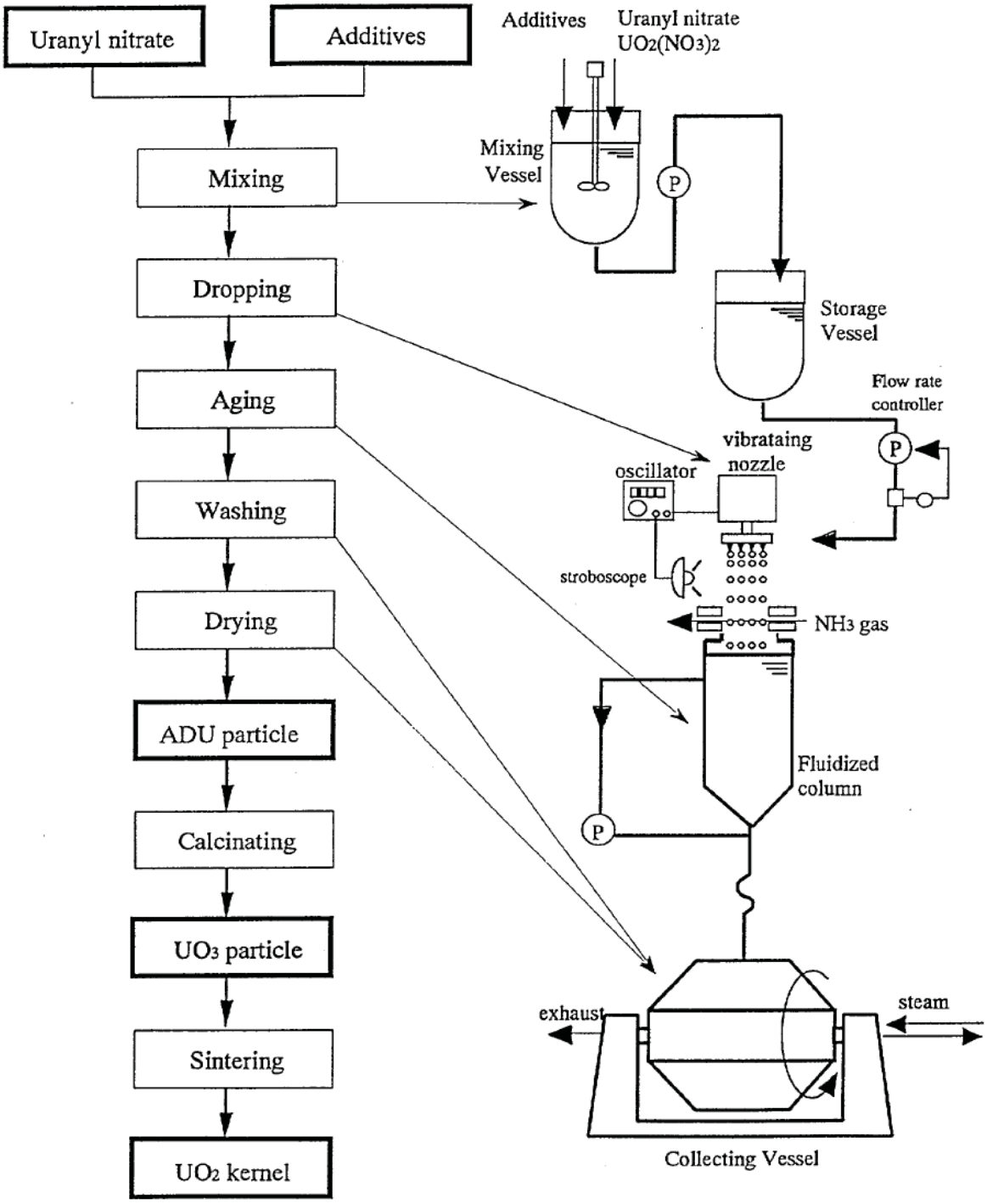


Figure 1.85. Flow Diagram of HTTR Fuel Fabrication Process.[a]

[a] S. Kato, S. Yoshimuta, T. Hasumi, K. Sato, K. Sawa, S. Suzuki, H. Mogi, S. Shiozawa, and T. Tanaka, "Fabrication of HTTR First Loading Fuel," IAEA-TECDOC-1210, International Atomic Energy Agency, Vienna, pp. 187-199 (April 2001).

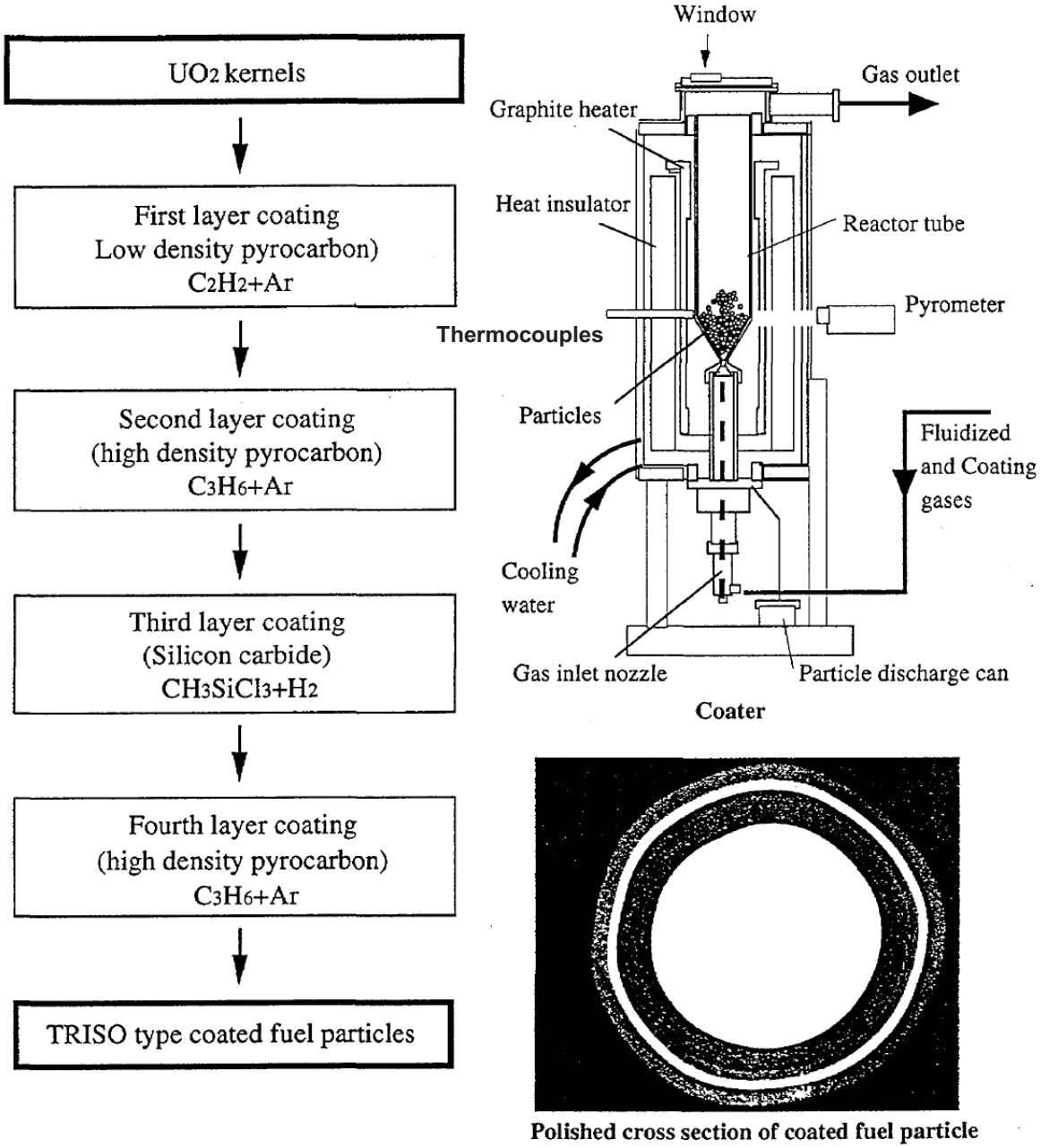


Figure 1.85 (cont'd.). Flow Diagram of HTTR Fuel Fabrication Process.[a]

[a] S. Kato, S. Yoshimuta, T. Hasumi, K. Sato, K. Sawa, S. Suzuki, H. Mogi, S. Shiozawa, and T. Tanaka, "Fabrication of HTTR First Loading Fuel," IAEA-TECDOC-1210, International Atomic Energy Agency, Vienna, pp. 187-199 (April 2001).

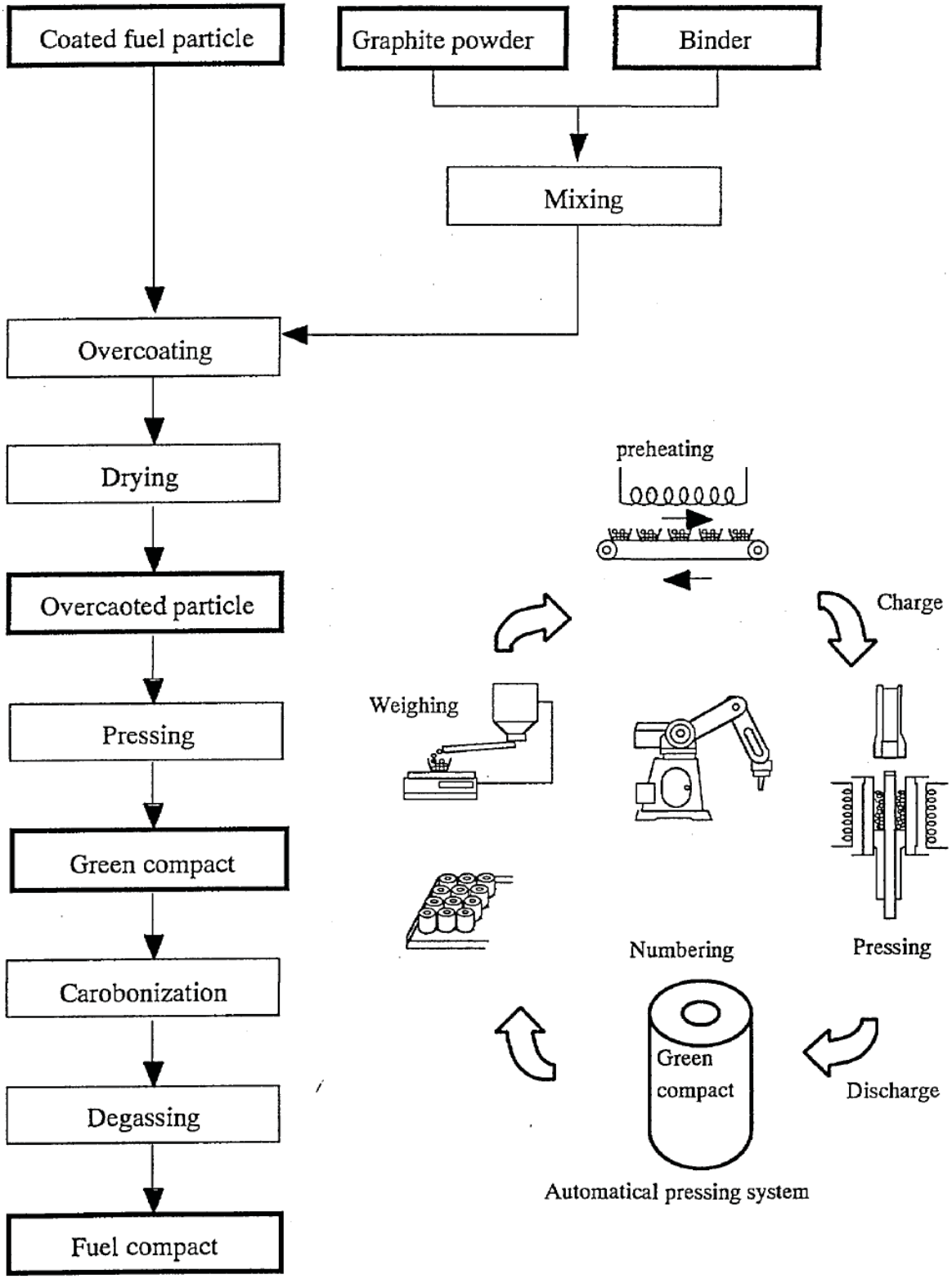


Figure 1.85 (cont'd.). Flow Diagram of HTTR Fuel Fabrication Process.[a]

[a] S. Kato, S. Yoshimuta, T. Hasumi, K. Sato, K. Sawa, S. Suzuki, H. Mogi, S. Shiozawa, and T. Tanaka, "Fabrication of HTTR First Loading Fuel," IAEA-TECDOC-1210, International Atomic Energy Agency, Vienna, pp. 187-199 (April 2001).

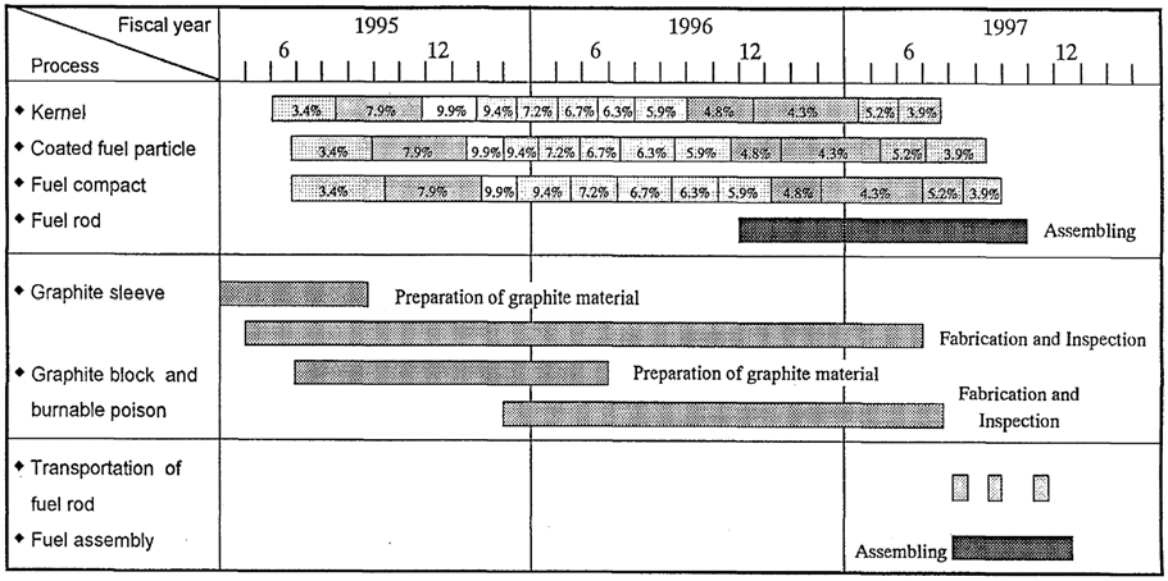


Figure 1.86. Fabrication Schedule of the First-Loading Fuel of the HTTR.[a]

Various mandatory fuel inspection standards were employed. The sphericity of the fuel kernel and coated fuel particles should be less than 1.2 within a 95 % confidence limit to prevent locally high stress during irradiation. The O/U ratio in the fuel kernel should be almost 2.0 to assure irradiation performance. The coating layer density and thickness must confirm integrity of coated fuel particles during irradiation. The OPTAF in high-density PyC layers should be less than 1.04 to prevent excessive deformation by fast neutron irradiation. The failure fractions (exposed uranium and SiC-failure) must be sufficiently low so as to provide fission product retention.

The enrichment of $^{235}U$ and uranium content in the fuel compact were measured by γ-ray spectro analysis. Diameter and sphericity of fuel kernels and the coated fuel particles were measured by optical particle size analysis. Density of the fuel kernel was measured by mercury substitution method. The O/U ratio was measured by oxidation and weighing. Impurities were measured by emission spectro analysis. Coating layer thickness and density were measured by X-ray radiograph and solvent substitution or sink-float methods, respectively. The OPTAF of the PyC layers was measured by polarization photometry. Appearance and ceramographed cross sections of the coated fuel particles and the fuel compacts were visually inspected. Strength of the coated fuel particles was measured by point crushing.

Density, impurities, grain size, water content in graphite powder, ash, melting point, and impurities in binder are inspected. Exposed uranium fraction and SiC-failure fraction are measured by deconsolidation/acid leaching and burn/acid leaching, respectively. Packing fraction of coated fuel particles and matrix density in a fuel compact is measured by weighing and calculation. Dimensions of the fuel compacts were measured by micrometer. Marking on the fuel compact was inspected by visual observation. Compressive strength of the fuel compact was also measured.

Uranium content in the fuel rods is confirmed by calculation of measured fuel compacts. Total length of the fuel rod was measured. The number of fuel compacts in a fuel rod is checked by assembling record. The Stack length of the fuel compacts is checked by calculation. Surface contamination of the fuel rod is measured by smear method. Appearance of the fuel rod and the fuel assembly is visually observed. The

[a] S. Kato, S. Yoshimuta, T. Hasumi, K. Sato, K. Sawa, S. Suzuki, H. Mogi, S. Shiozawa, and T. Tanaka, "Fabrication of HTTR First Loading Fuel," IAEA-TECDOC-1210, International Atomic Energy Agency, Vienna, pp. 187-199 (April 2001).

$^{235}$U enrichment is checked by fuel compacts and graphite sleeve markings. Components in the fuel rod and the fuel assembly are checked by assembling record. The uranium content in the fuel assembly was calculated. Weight of the fuel assembly was also measured.[a]

The total number of particles with a through-coating failure in the active core has been estimated to be 2500, which translates into a fraction of about $2.5 \times 10^{-6}$. The contamination of the fuel element matrix graphite has been estimated to be approximately 2.5 g of uranium. According to the total loading of 900 kg of U in the core, the respective contamination fraction is about $2.5 \times 10^{-6}$. Free uranium is considered to exist as heavy metal contamination of the fuel graphite, as particles with a through-coating failure, and those with a defective SiC layer. The irradiation performance of fuel particles in the HTTR is shown in Figure 1.86; the expected fuel quality for the first-core fuel in the HTTR is shown in Table 1.26.[b]

The free uranium fractions of the fuel compacts were measured by the deconsolidation followed by the acid leaching on four fuel compacts for each fuel compact fabrication lot (containing up to about 700 fuel compacts). The HTTR first-loading fuel compacts were fabricated from 126 fuel compact lots.[c]

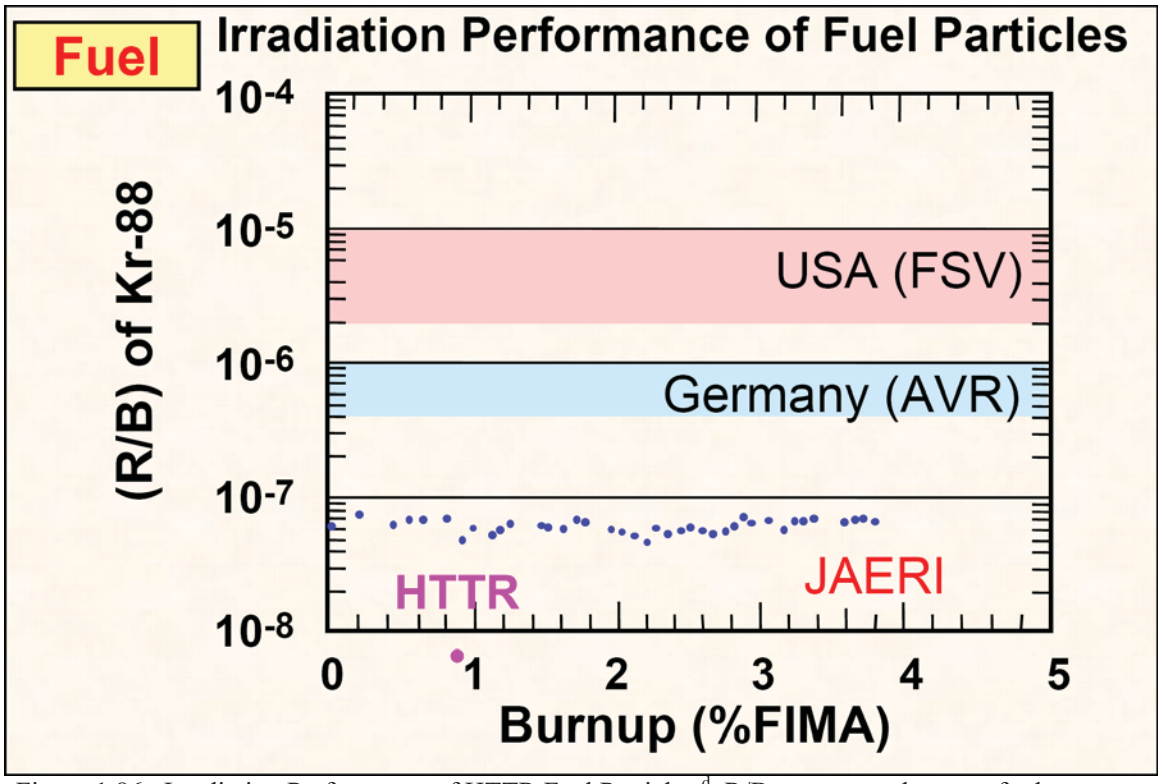


Figure 1.86. Irradiation Performance of HTTR Fuel Particles.[d] R/B represents the rate of release over the rate of fuel burnup.

---

[a] K. Sawa, S. Suzuki, and S. Shiozawa, "Safety Criteria and Quality Control of HTTR Fuel," *Nucl. Eng. Des.*, **208**: 305-313 (2001).

[b] K. Verfondern, J. Sumita, S. Ueta, and K. Sawa, "Modeling of Fuel Performance and Metallic Fission Product Release Behavior During HTTR Normal Operating Conditions," *Nucl. Eng. Des.*, **210**: 225-238 (2001).

[c] K. Sawa, T. Tobita, H. Mogi, S. Shiozawa, S. Yoshimuta, S. Suzuki, and K. Deushi, "Fabrication of the First-Loading Fuel of the High Temperature Engineering Test Reactor," *J. Nucl. Sci. Tech.*, **36**(8): 683-690 (August 1999).

[d] S. Shiozawa, "Status of Japan's HTR Program," *Key Note Presentation at the 2007 Int. Congress on Advances in Nuclear Power Plants (ICAPP 2007)*, Nice, France (May 13-18, 2007).

Table 1.26. Fuel Quality of the HTTR First Core Fuel Production.[a]

| Contribution | Defect Fraction | | |
|---|---|---|---|
| | Expected | Regulatory | Safety Design |
| Heavy Metal Contamination | $2.5 \times 10^{-6}$ | $1.5 \times 10^{-4}$ | $2.0 \times 10^{-3}$ |
| Initial Through-Coating Defects | $2.5 \times 10^{-6}$ | -- | -- |
| Initial SiC Defects | $8.0 \times 10^{-5}$ | $1.5 \times 10^{-3}$ | -- |
| Irradiation-Induced Failures | 0 | $2.0 \times 10^{-3}$ | $8.0 \times 10^{-3}$ |
| Total at EOL | $8.5 \times 10^{-5}$ | $3.7 \times 10^{-3}$ | $1.0 \times 10^{-2}$ |

(a) K. Verfondern, J. Sumita, S. Ueta, and K. Sawa, "Modeling of Fuel Performance and Metallic Fission Product Release Behavior During HTTR Normal Operating Conditions," *Nucl. Eng. Des.*, **210**: 225-238 (2001).

Additional specified impurity parameters for some of the graphite components in the active core of the HTTR are listed in Table 1.27.

Table 1.27. Parameters for Graphites (Ref. 2, p. 105).

| Component | Density (g/cm$^3$) | Impurity (ppm $B_{nat}$) |
|---|---|---|
| Matrix | 1.690 | 0.82 |
| Sleeve | 1.770 | 0.37 |
| Fuel / Control Block | 1.770 | 0.40 |
| Replaceable Reflector | 1.760 | 0.37 |
| Permanent Reflector | 1.732 | 1.91 |

## Burnable Poisons

The compositions of the BP pellets are $B_4C$ and C. There are two types of BP pellets: H-I with 2.22 at.% natural boron concentration and H-II with 2.74 at.%, with material properties shown in Table 1.28 (Ref. 2, p. 21).

Table 1.28. Material Properties of BP and Graphite Disks (Ref. 2, p. 17).

| | | |
|---|---|---|
| Burnable Poison Pellet | | |
| Material | $B_4C$-C Composite | |
| Type | H-I | H-II |
| Density ($g/cm^3$) | 1.79 | 1.82 |
| Natural Boron Concentration (at.%) | 2.22 | 2.74 |
| Diameter (mm) | 13.9 | 13.9 |
| $^{10}B$ Abundance Ratio (wt.%) | 18.7[(a)] | 18.7[(a)] |
| Graphite Disk | | |
| Material | Graphite | |
| Diameter (mm) | 14.0 | |
| Density ($g/cm^3$) | 1.77 | |
| Impurity (ppm, natural B equivalent) | 0.37 | |

(a) These may be typographical errors or listed in atomic percent since natural boron has an abundance between 19.1 and 20.3 wt.% (see Section 2.1.3.4).

## Control Rods and Reserve Shutdown System

Some control rod material properties are contained within Table 1.15.

Typical impurities in sintered $B_4C$ pellets are shown in Table 1.29. Information is provided as a comparison of manufacturing results.

Ferritic superalloy Alloy 800H is selected for material of metallic parts of the control rod. Alloy 800H is selected for the metal parts of the control rods mainly because iron-based alloys are superior to nickel-rich alloys in both post-irradiation tensile and creep properties (Ref. 7, pp. 91 and 93).

Table 1.29. Typical Impurities in Sintered $B_4C/C$ Pellets.[(a)]

| | | $B_4C/C$ (30 %) | $B_4C/C$ (40 %) | $B_4C/C$ (50 %) | $B_4C$ |
|---|---|---|---|---|---|
| Pellet Density ($g/cm^3$) | | 2.04 ± 0.03 | 2.06 ± 0.03 | 2.25 ± 0.03 | 2.31 |
| Boron Content (wt.%) | | 30 ± 3 | 40 ± 3 | 50 ± 3 | 78 |
| Impurity (ppm) | Na | ~100 | ~100 | ~10 | ~10 |
| | Al | ~1000 | ~1000 | ~1000 | ~1000 |
| | Si | ~1000 | ~1000 | ~1000 | ~1000 |
| | Ca | ~1000 | ~1000 | ~100 | ~100 |
| | Ti | ~100 | ~1000 | ~1000 | ~1000 |
| | Mn | ~10 | ~10 | ~10 | ~10 |

(a) K. Fujii, S. Nomura, H. Imai, and M. Shindo, "Corrosion Behavior of Sintered Pellet of Graphite and Boron Carbide in Helium Containing Water Vapor," IAEA-TECDOC-690, International Atomic Energy Agency, Vienna, pp. 169-176 (February 2003).

Some control rod guide block material properties are contained within Table 1.16.

## Instrumentation

No material information is available regarding the $BF_3$ counters, micro-fission chambers, or the gamma-ray compensated ionization chambers.

## Graphite Blocks

Graphite composition is discussed in the section associated with Tables 1.19 through 1.22.

## Dummy Blocks

Dummy fuel blocks contain higher impurity than the fuel graphite blocks (Ref. 2, p. 23).

While the material of blocks and dowels in the HTTR is IG-110, typically IG-11 was used for research studies of various components. IG-11 is the same as IG-110 except without purity and economy.[a]

Some of the graphite used for the dummy blocks was originally manufactured for out-of-pile seismic tests, and there was an uncertain amount of impurity in them. The impurity in the boron equivalent was 3.1 ppm (Ref. 1, p. 314).[b]

[a] N. Takikawa, M. Ishihara, T. Iyoku, S. Shiozawa, M. Tokumitsu, S. Koe, and M. Uno, "Assessment of the Load Capacity of the Dowel and Socket System in the HTTR Hexagonal Block," IAEA-TECDOC-690, International Atomic Energy Agency, Vienna, pp. 105-112 (February 1993).

[b] Fujimoto, N., Nakano, M., Takeuchi, M., Fujisaki, S., and Yamashita, K., "Start-Up Core Physics Tests of High Temperature Engineering Test Reactor (HTTR), (II): First Criticality by an Annular Form Fuel Loading and Its Criticality Prediction Method," *J. Atomic Energy Society Japan*, **42**(5), 458-464 (2000).

**Replaceable Reflectors**

Some replaceable reflector block material properties are contained within Table 1.16. Additional information is provided in the section associated with Tables 1.19 through 1.22.

**Permanent Reflectors**

Some permanent reflector material properties are contained within Table 1.16. Additional information is provided in the section associated with Tables 1.19 through 1.22.

The permanent reflectors are fabricated from grade PGX graphite (Ref. 6, p. 83).

Around the permanent reflector blocks are side shielding blocks consisting of $B_4C$/C (Ref. 2, p. 23).

**Helium Coolant**

See Table 1.10 for the upper impurity limit concentration in the primary helium coolant.

The primary helium purification system of the HTTR is designed to have hydrogen concentration limited to less than 3 ppm.[a]

The impurity limits provided are for full power operation. During the cold critical tests, the helium coolant impurity concentrations would be negligible.

### 1.1.4 Temperature Data

The core is at room temperature (Ref. 2, p. 14). Table 1.17 provided the temperature of the experiment for each of the six critical cases, ranging between 23 and 25ºC.

### 1.1.5 Additional Information Relevant to Critical and Subcritical Measurements

Additional information is not available.

## 1.2 Description of Buckling and Extrapolation Length Measurements

Buckling and extrapolation length measurements were not made.

## 1.3 Description of Spectral Characteristics Measurements

Spectral characteristics measurements were not made.

## 1.4 Description of Reactivity Effects Measurements

### 1.4.1 Overview of Experiment

Excess reactivity and shutdown margin measurements have been evaluated for this benchmark configuration. Benchmark values for the control rod worths have not been completely evaluated. Further

[a] T. Takeda, J. Iwatsuki, and Y. Inagaki, "Permeability of Hydrogen and Deuterium of Hastelloy XR," *J. Nucl. Mat.*, **326**: 47-58 (2004).

analysis is necessary to assess the current discrepancies between the computational and experimental data.

### 1.4.2 Geometry of the Experiment Configuration and Measurement Procedure

The geometry of the core is that of the fully-loaded core configuration in Section 1.1.2 with modifications as stated below.

#### *1.4.2.1 Excess Reactivity*

After the initial criticality, reactivity increase was measured using the inverse kinetic (IK) method. The excess reactivity of the core was then obtained by adding all increments of the reactivity from the first criticality to the fully-loaded core (Ref. 2, p. 14).

A fuel addition method was applied for the measurement of the excess reactivity. The CR position at criticality became deeper after fuel loading, allowing for measurement of the change in reactivity. The reactivity of the inserted part of each CR was measured via the IK method after every addition of three fuel columns. The measurement was performed for the 21-, 24-, 27-, and 30-fuel-column cores. It was expected that the excess reactivity could be obtained by summation of the reactivity of each CR; however, the measurement was strongly affected by the negative shadowing effect between neighboring CRs. The measured excess reactivity was then revised with the following equations to correct for the shadowing effects:

$$\rho_{exm} = \sum_{step}^{n} \Delta\rho_{exm} ,$$

$$\Delta\rho_{exm} = R \cdot \Delta\rho_{ikm} ,$$

and

$$\Delta\rho_{ikm} = \sum_{CR}^{m} \Delta\rho_{ikRod} ,$$

where n is the number of fuel addition steps, m is the number of CRs, $\rho_{exm}$ is the revised excess reactivity (% Δk/k), $\Delta\rho_{exm}$ is the revised increase in excess reactivity (% Δk/k), $\Delta\rho_{ikm}$ is the increase in excess reactivity measured with IK method after fuel addition (% Δk/k), and $\Delta\rho_{ikRod}$ is the measured reactivity of inserted part of CR after fuel addition (% Δk/k). The revising factor, R, was estimated with diffusion calculation using the nuclear design code system of the HTTR with the following relation:

$$R = \frac{\Delta\rho_{excal}}{\Delta\rho_{ikcal}},$$

where $\Delta\rho_{ikcal}$ is the increase in excess calculated according the IK measurement procedure (%Δk/k), and $\Delta\rho_{excal}$ is the increase in excess reactivity calculated by withdrawing all CRs together (%Δk/k). The theoretical excess reactivity was calculated with the following relation:

$$\rho_{exMVP} = \frac{k-1}{k},$$

where k was obtained with the Japanese Monte Carlo MVP code (150 batches × 20000 histories/batch). The revised and calculated excess reactivity is shown in Table 1.30; they agree within the experimental

errors for each core, and the difference between the measured and calculated mean values was reduced from 3.5 to 1 % Δk/k by introducing the revising factor (Ref. 1, pp. 318-319).

The excess reactivity for core configurations containing 18 and 19 fuel columns are reported as -0.9 and 1.5 % Δk/k, respectively. The required limits for 660 effective full power days of operation is between 11.1 and 16.5 % Δk/k (Ref. 13, p. 286).

Table 1.30. Revised and Calculated Excess Reactivity (Ref. 1, p. 319).[(a)]

| Fuel Columns | Measurement $\rho_{ikm}$ (% Δk/k) | Measurement $\Delta\rho_{ikm}$ (% Δk/k) | Revising Factor R[(b)] | Revised Excess Reactivity $\Delta\rho_{exm}$ (% Δk/k) | Revised Excess Reactivity $\rho_{exm}$ (% Δk/k) | Calculation $\rho_{exMVP}$ (% Δk/k) | Difference ($\rho_{exMVP}$-$\rho_{exm}$) (% Δk/k) |
|---|---|---|---|---|---|---|---|
| 21 | 2.3±0.23 | 2.3±0.23 | 1.69±0.12 | 4.0±1.1 | 4.0±1.1 | 5.0±0.15 | 1.0 |
| 24 | 5.0±0.50 | 2.7±0.27 | 1.40±0.11 | 3.7±1.0 | 7.7±2.1[(c)] | 8.6±0.15 | 0.9 |
| 27 | 7.4±0.74 | 2.4±0.24 | 1.26±0.15 | 3.0±0.9 | 10.7±3.0[(c)] | 11.3±0.15 | 0.6 |
| 30 | 8.5±0.85 | 1.1±0.11 | 1.19±0.04 | 1.3±0.3 | 12.0±3.3[(c)] | 12.0±0.15 | 0.0 |

(a) Based upon a reported $\beta_{eff}$ of 0.0065 (Ref. 2, p. 42).
(b) The error of R is evaluated from errors of calculated CR worth $\Delta\rho_{ikcal}$ and $\Delta\rho_{excal}$. The errors of CR worth were determined in analyses of the critical assembly VHTRC experiments.
(c) Cumulative reactivity values confirmed in Ref. 13, p. 286.

### *1.4.2.2 Shutdown Margin*

The scram reactivity, or shutdown margin, was evaluated for two cases: 1) all reflector CRs inserted at critical condition, and 2) all CRs in reflector and core inserted at critical condition. The core was fully loaded with fresh fuel.

The scram reactivity for Case 1 was evaluated as follows:

$$\rho_R = \frac{k_{Crit} - k_{RCR-in}}{k_{Crit} \cdot k_{RCR-in}},$$

where $\rho_R$ is the scram reactivity of the reflector CRs (Δk/k), $k_{Crit}$ is the effective multiplication factor at critical CR position, and $k_{RCR-in}$ is the effective multiplication factor at CR position after scram.

The temperature of the core and reflector is 300 K. Critical rod positions for Case 1 are provided in Table 1.31 (Ref. 2, pp. 26 and 42).

Table 1.31. Control Rod Position (mm) for Case 1 (Ref. 2, p. 42).

| CR Group | Critical Position | Position after Scram |
|---|---|---|
| C | 1775 | 1775 |
| R1 | 1775 | 1775 |
| R2 | 1775 | -55[(a)] |
| R3 | Full Out | -55[(a)] |

(a) Control rods are inserted slightly into the top of the bottom reflector.

The scram reactivity of all control rods (Case 2) was evaluated as follows:

$$\rho_A = \frac{k_{Crit} - k_{ACR-in}}{k_{Crit} \cdot k_{ACR-in}},$$

where $\rho_A$ is the scram reactivity of all CRs ($\Delta k/k$), $k_{Crit}$ is the effective multiplication factor at critical CR position, and $k_{ACR-in}$ is the effective multiplication factor at CR position after scram.

The temperature for core and reflector is 300 K. Critical rod positions for Case 2 are provided in Table 1.32 (Ref. 2, pp. 26 and 43).

Table 1.32. Control Rod Position (mm) for Case 2 (Ref. 2, p. 43).

| CR Group | Critical Position | Position after Scram |
|---|---|---|
| C | 1775 | -55[(a)] |
| R1 | 1775 | -55[(a)] |
| R2 | 1775 | -55[(a)] |
| R3 | Full Out | -55[(a)] |

(a) Control rods are inserted slightly into the top of the bottom reflector.

The measured scram reactivity for Cases 1 and 2 were 12.1 and 46.3 %$\Delta k/k$, respectively (Ref. 2, p. 44). These values were then later reported (in the same document) as 12.0 and 46.0 %$\Delta k/k$, respectively (Ref. 2, p. 331).

Elsewhere, the shutdown margins, which were determined via the IK and rod drop methods, were reported as shown in Table 1.33. Generally the rod-drop method is used for shutdown margin measurement. However, as it takes about 10 seconds for the CR insertion of the HTTR, the rod-drop method was not directly applicable. The measured shutdown margin becomes smaller than the real value when it takes a few seconds for CR insertion. Therefore the IK method was tried for measurement of the shutdown margin and the reactivity was evaluated continuously by computer from the neutron density signals of the CIC detectors using the IK method.[a]

[a] "Present Status of HTGR Research and Development," Japan Atomic Energy Research Institute, Tokaimura, March 2004.

Table 1.33. Shutdown Margins of the HTTR (Ref. 12, p. 287).

| | Experiment (% Δk/k) | | Calculation (% Δk/k) |
|---|---|---|---|
| | IK Method | Rod Drop Method | |
| One-Step Scram | | | |
| All Control Rods | -46.7 | -43.7 | -42.9 |
| Two-Step Scram | | | |
| 1st: Control Rods in Reflector Region | -12.1 | -- | -8.6 |
| 2nd: Control Rods in Fuel Region | -34.2 | -- | -34.3 |
| All Control Rods (Total) | -46.3 | -49.0 | -42.9 |

#### *1.4.2.3 Control Rod Worth*

The reactivity worth of each control rod was continuously measured by the IK method from full insertion to full withdrawal. The differential control rod worth for the center control rod is shown in Figure 1.87. The full insertion and withdrawal levels correspond to 0 and 4060 mm, respectively, in axial distance from the bottom of the fuel region. The reactivity addition rate is below the limit of $2.4 \times 10^{-4}$ Δk/k-s (Ref. 13, p. 287).

### 1.4.3 Material Data

The materials in the core were those described in the fully-loaded core configuration in Section 1.1.3 with modifications as stated below.

### 1.4.4 Temperature Data

Experiments were essentially performed at room temperature.

### 1.4.5 Additional Information Relevant to Reactivity Effects Measurements

Additional information is not available.

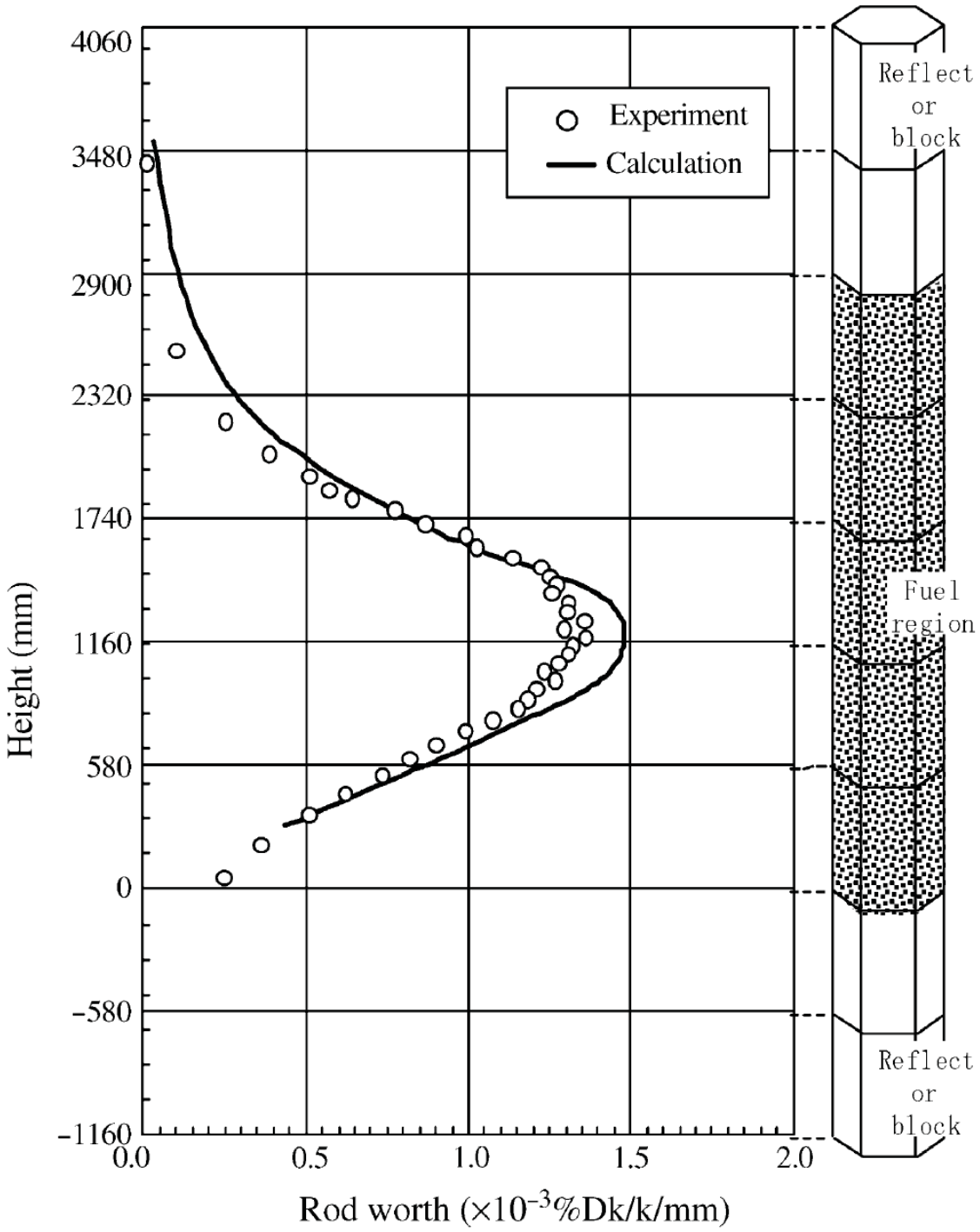


Figure 1.87. Differential Control Rod Worth for Zero Power Operation (Ref. 13, p. 286).

## 1.5 Description of Reactivity Coefficient Measurements

### 1.5.1 Overview of Experiment

The reactor physics experiments described in this section pertain to the data available for the isothermal temperature coefficient.

### 1.5.2 Geometry of the Experiment Configuration and Measurement Procedure

The geometry of the core is that of the fully-loaded core configuration in Section 1.1.2 with modifications as stated below.

#### *1.5.2.1 Isothermal Temperature Coefficient*

Reference 2 contains calculations regarding evaluation of the isothermal temperature coefficients in the HTTR but does not actually represent experimental data. Reference 13 contains information pertinent to the actual determination of the isothermal temperature coefficient in the HTTR.

The reactivity coefficient of the HTTR is dominated by the temperature coefficient of the fuel and reflector. The temperature coefficient was determined by the reactivity difference incurred by changes in the core temperature. The reactor power was maintained constant and the coolant temperature was changed by adjusting the heat removal rate from the secondary coolant system. The reactivity was then estimated from the control rod worth curve. Figure 1.88 shows the results for calculating the isothermal temperature coefficient. The absolute value of the coefficient decreases as the average core temperature increases; however, all values remain negative. Previous calculation results show a discrepancy between calculated and actual coefficient values for temperatures below 400 ºC (Ref 13, pp. 287-288).

The isothermal temperature coefficients of the fully-loaded core can be evaluated from the effective multiplication factors, using the following relationship:

$$\rho_n = \frac{k_{n+1} - k_n}{k_{n+1} \cdot k_n} \cdot \frac{1}{\left(T_{n+1} - T_n\right)},$$

where $\rho_n$ is the temperature coefficient between $T_n$ and $T_{n+1}$ $(\Delta k/k)/K$, $T_n$ is the core temperature of the $n^{th}$ measurement (K), $T_{n+1}$ is the core temperature of the $(n+1)^{th}$ measurement (K), $k_n$ is the effective multiplication factor at $T_n$, and $k_{n+1}$ is the effective multiplication factor $T_{n+1}$. The critical control rod positions were changed with temperature elevation during reactor operation but typically not during the calculation of the reactivity difference.

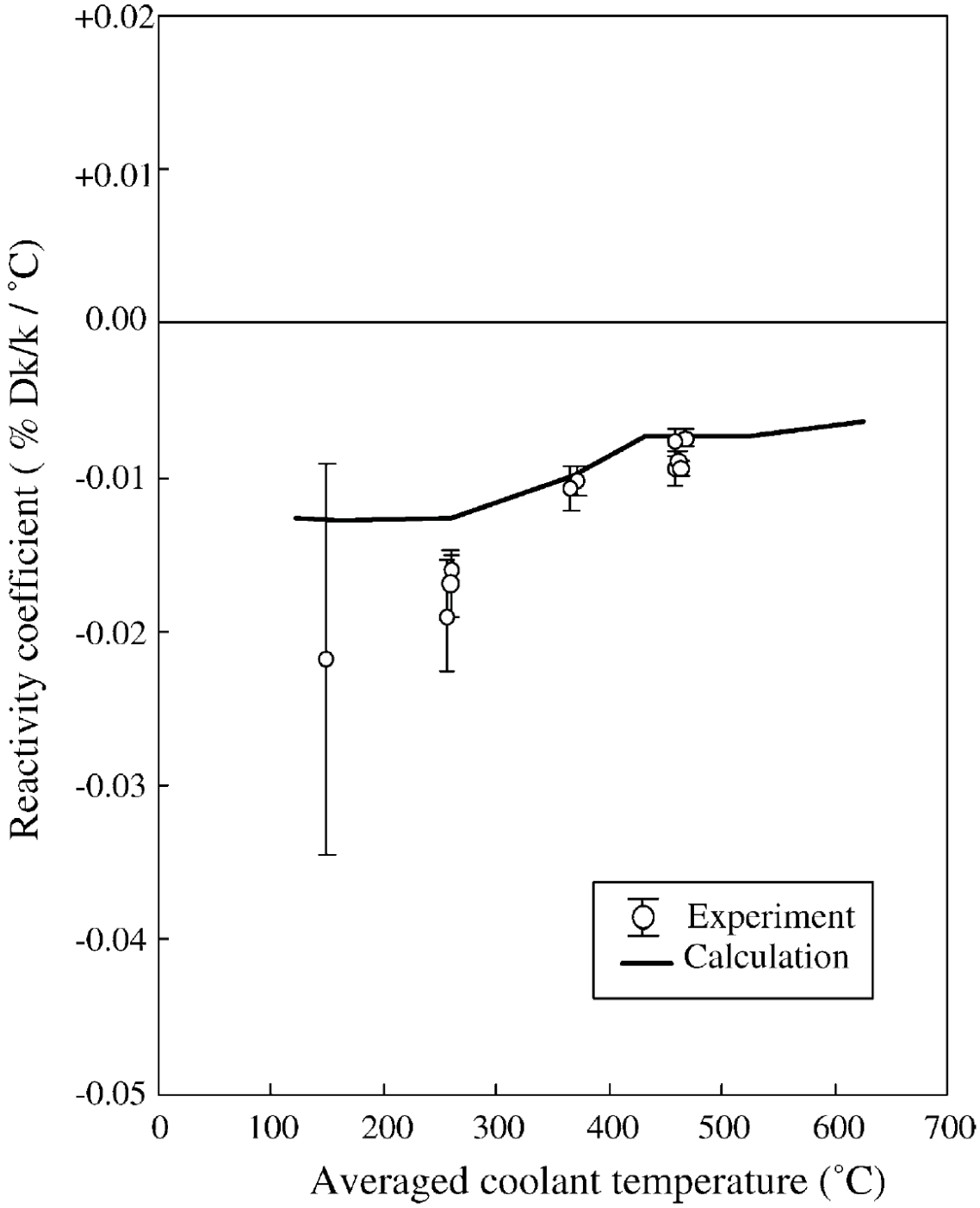


Figure 1.88. Temperature Coefficients vs. Average Coolant Temperature (Ref. 13, p. 288).

### 1.5.3 Material Data

The materials in the core were those described in the fully-loaded core configuration in Section 1.1.3 with modifications as stated below.

### 1.5.4 Temperature Data

See Figure 1.88 for information regarding the core temperatures.

### 1.5.5 Additional Information Relevant to Reactivity Coefficient Measurements

Additional information is not available.

## 1.6 Description of Kinetics Measurements

### 1.6.1 Overview of Experiment

Experimental information gathered from the references regarding the neutron generation time is provided in this section, but not currently evaluated.

### 1.6.2 Geometry of the Experiment Configuration and Measurement Procedure

The geometry of the core is that of the fully-loaded core configuration in Section 1.1.2 with modifications as stated below.

"Inherent to this type of reactor, the neutron generation time is long and was calculated to be: 1.173±0.001 ms. The prompt neutron decay constant is quite close to the decay of the fastest delayed neutrons, therefore no intermediate plateau can be recognized in the measured spectral function" (Ref. 2, p. 115).

### 1.6.3 Material Data

The materials in the core were those described in the fully-loaded core configuration in Section 1.1.3 with modifications as stated below.

### 1.6.4 Temperature Data

Experiments were essentially performed at room temperature.

### 1.6.5 Additional Information Relevant to Kinetics Measurements

Additional information is not available.

## 1.7 Description of Reaction-Rate Distribution Measurements

### 1.7.1 Overview of Experiment

The axial reaction rate profile in the instrumentation columns has been evaluated for this benchmark configuration.

### 1.7.2 Geometry of the Experiment Configuration and Measurement Procedure

The geometry of the core is that of the fully-loaded core configuration in Section 1.1.2 with modifications as stated below.

#### *1.7.2.1 Axial Reaction Rate Distribution*

The fission reaction rate of $^{235}U$ was regarded as a neutron flux distribution because the neutron flux distribution could not be directly measured in the HTTR core. The three micro fission chambers (FCs) placed in the irradiation test columns were used to measure the axial reaction rate. The FCs are 5 cm long with a diameter of 0.6 cm. A FC was connected to the end of a long aluminum stick such that it could be axially traversed by moving the stick in the aluminum tube well inserted into the holes of the irradiation test columns. The temporary neutron source was withdrawn from the core during measurements. The reaction rates were then measured at several points around the peak of the reaction rate distribution to search for the peak. The reactor power was changed by the movement of the FC because reactivity was added by movement of the attached stick and cable, which caused a change in the reaction rates of the FCs. The reaction rate of the traversing FC was then normalized with the reaction rate of the FC fixed in another irradiation test column. The axial fission reaction rate distributions were measured for the 24- and 30-fuel-column cores. Both FS and F23 patterns were formed in the 24-fuel-column core. The experimental error of the neutron flux was ~0.2 %, and was evaluated from the number of FC pulse counts. Measured distributions are shown (compared with some of Japan's calculated results) in Figure 1.89 (Ref. 1, pp. 317-318).

The two 24-fuel-column configurations in Figure 1.89 are evaluated in HTTR-GCR-RESR-002, as these represent measurements performed using annular core configurations of the HTTR.

Figure 1.90 shows the measured and calculated axial neutron flux distribution for a reactor power of 27 W. The control rod position at the measurement was about 1780 mm. From the comparison of experimental to calculation results, it was confirmed that the neutron flux in the reflector region could be accurately calculated for the provision of fundamental data in irradiation tests (Ref. 13, pp. 288-289).

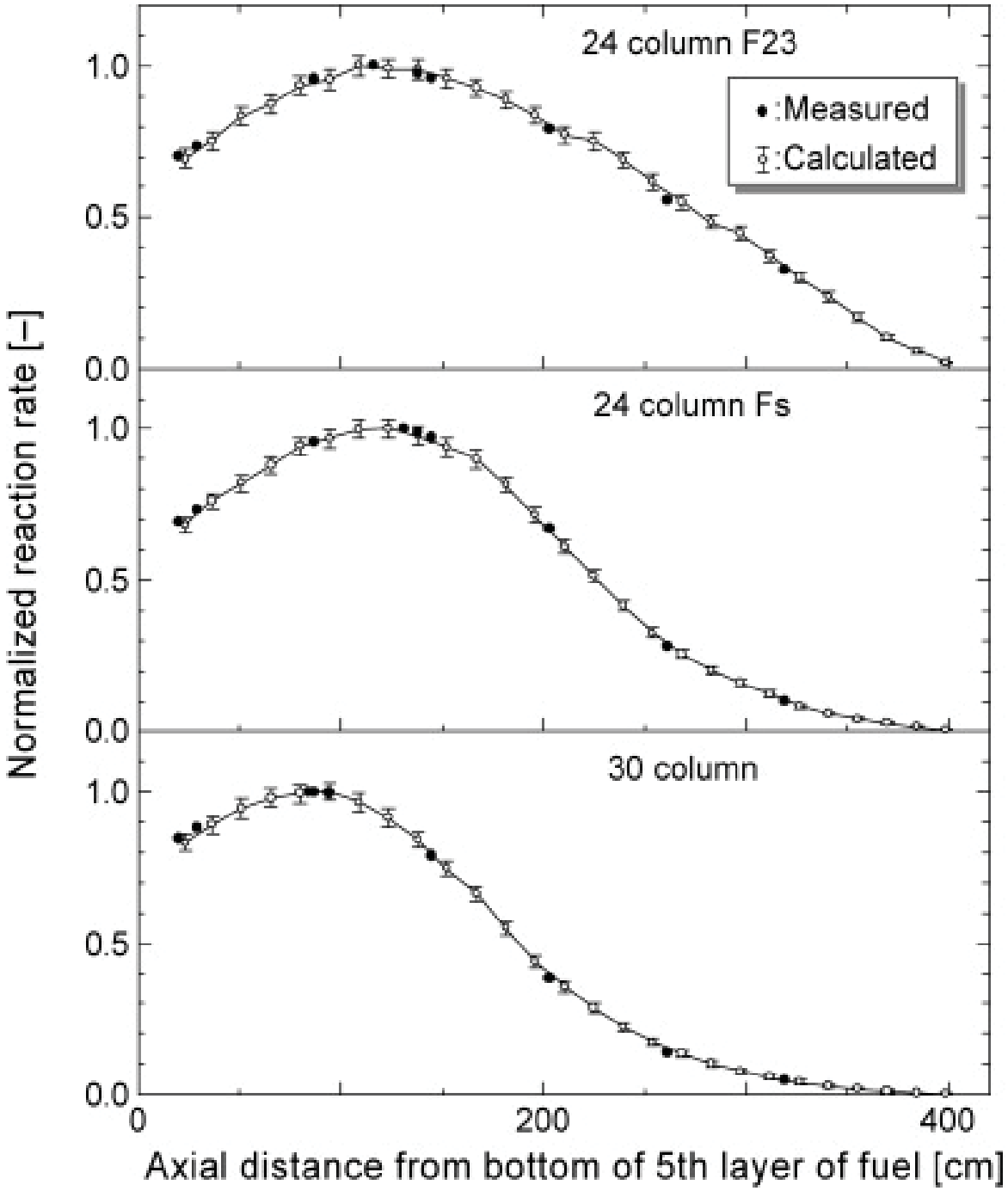


Figure 1.89. Axial Reaction Rate Distribution in Irradiation Column for 24- and 30-Fuel-Column Cores (Ref. 1, p. 318). F23 and FS are defined in the footnote of Table 1.17. The 24-fuel-column core reaction-rate measurements are evaluated in HTTR-GCR-RESR-002.

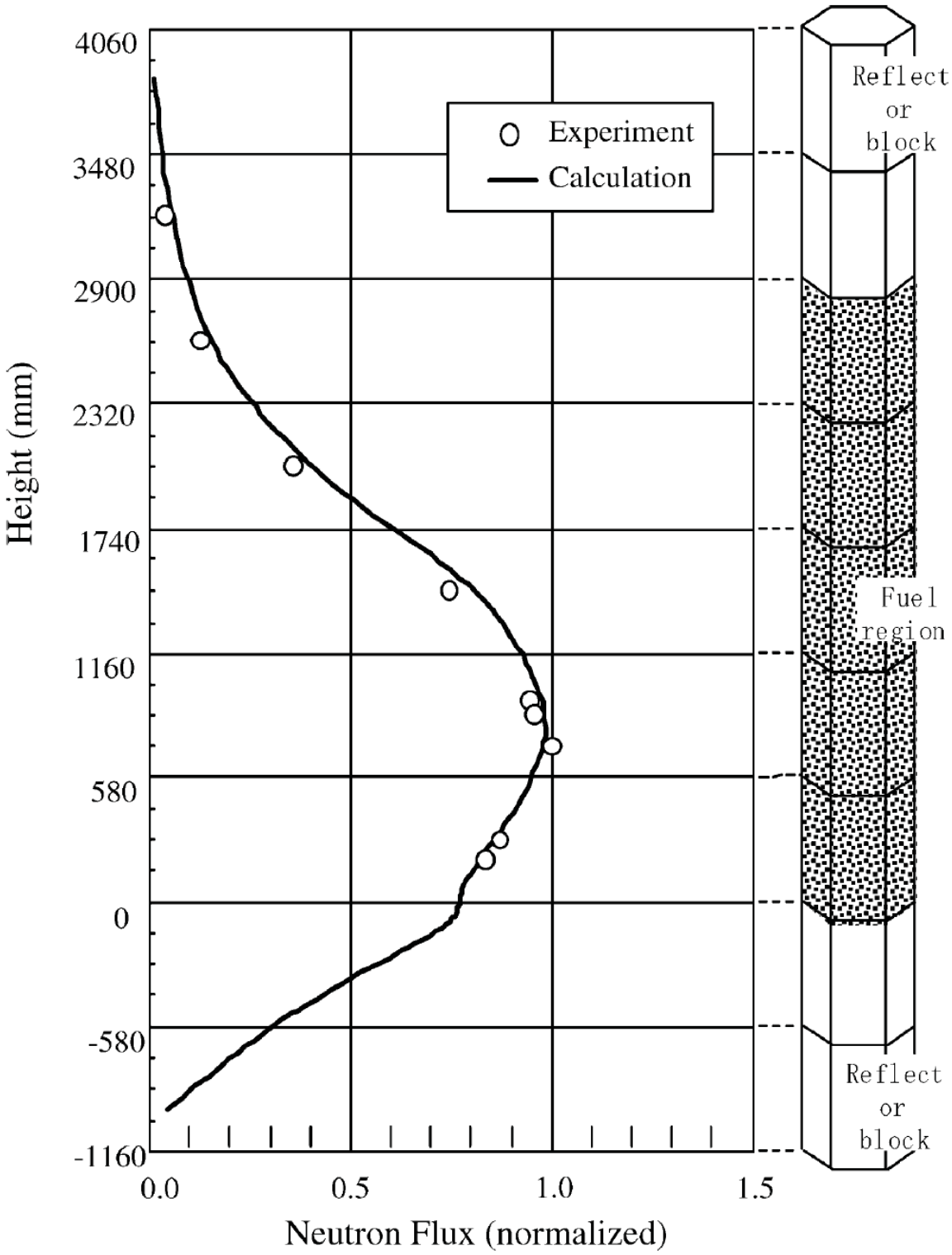


Figure 1.90. Axial Neutron Flux Distribution for Zero Power Operation (Ref. 13, p. 289).

### 1.7.3 Material Data

The materials in the core were those described in the fully-loaded core configuration in Section 1.1.3 with modifications as stated below.

### 1.7.4 Temperature Data

Experiments were essentially performed at room temperature.

### 1.7.5 Additional Information Relevant to Reaction-Rate Distribution Measurements

Additional information is not available.

## 1.8 Description of Power Distribution Measurements

Power distribution measurements were not made.

## 1.9 Description of Isotopic Measurements

Isotopic measurements were not made.

## 1.10 Description of Other Miscellaneous Types of Measurements

Other miscellaneous types of measurements were not made.

## 2.0 EVALUATION OF EXPERIMENTAL DATA

The overall uncertainty in the calculated value of $k_{eff}$, which is a function of multiple input parameters, is given by[a]

$$u_c^2(k_{eff}) = \sum_{i=1}^{N} (\Delta k_i)^2 + 2\sum_{i=1}^{N-1} \sum_{j=i+1}^{N} (\Delta k_i)(\Delta k_j) r_{i,j} \,. \qquad (2.1)$$

In Equation 2.1, $\Delta k_i$ is the change in $k_{eff}$ when parameter $i$ is changed by the standard deviation in the parameter, and $r_{i,j}$ is the correlation coefficient for parameters $i$ and $j$.

Where standard deviations are available, they are used for calculating the effects these uncertainties might have on $k_{eff}$, in terms of $\Delta k_i$. Where observed ranges are given, but not standard deviations, the limiting values of the observed ranges are usually applied, and plausible distribution functions are assumed for finding $\Delta k_i$. Where only tolerances are given, their limiting values are used, along with plausible distribution functions. Where no guidance is given on the variability of a parameter, engineering judgement is used to select a range of variation that will produce the largest reasonable uncertainty in $k_{eff}$. The bounding values in this range are then applied in the uncertainty analysis. If the overall uncertainty in $k_{eff}$ predicted by this approach is small enough that the experiment can be judged an acceptable benchmark, one can be confident that the real experiment is actually even better. All uncertainties are adjusted to values of one standard deviation ($1\sigma$). No information is available on correlations among parameters, so all parameters and their uncertainties are assumed to be uncorrelated.

Usually, no information is publicly available about the distribution function of the deviation of a parameter from its nominal value. In most cases, it is reasonably assumed that the most relevant quantity is uniformly distributed. For example, if the change in $k_{eff}$ from its nominal value is dependent on the change in the volume of a spatial region, then it is assumed that the deviation of the volume of that region from its nominal value is uniformly distributed.

The uncertainty analyses were performed in accordance with guidance provided in the ICSBEP Handbook.

It should be noted that assuming a uniform distribution of a parameter between its limits leads to overprediction of the effect on $k_{eff}$.

These observations are used repeatedly in the following analysis.

The following sections discuss the calculation of the effects of uncertainties in the parameters listed in tables in each section. The values of the tabulated parameters are computed in the benchmark critical configuration and in the configuration with each parameter assigned its maximum variation (or its standard deviation when available), one parameter at a time. The bases for the choices of the parameter values are discussed.

In all cases where tolerances or observed variations apply to large numbers of objects, such as TRISO fuel particles, both deterministic (or systematic) uncertainties (applying to all the objects equally) and random uncertainties (different from one object to the next) will occur. For the fuel particles and their subregions especially, the random uncertainties are extremely small (the tolerance limit for the random uncertainty divided by the square root of the number of fuel particles in the core. In all cases, division by such large numbers would make the random component of the uncertainty negligible. Positional

[a] *International Handbook of Evaluated Criticality Safety Benchmark Experiments,* NEA/NSC/DOC(95)03/I-VIII, OECD-NEA, "ICSBEP Guide to the Expression of Uncertainties," Revision 1, p. 29, September 30, 2004.

dependence of objects within the assembly also influences the effective proportional effect on the resultant uncertainty and bias calculations. However, since no information is available about how the uncertainties are divided between the systematic and random components, it is assumed throughout that the uncertainties are 25 % systematic and 75 % random for all uncertainties that exhibit a random component.

This assumption provides a basic prediction of the effect on $k_{eff}$ until additional information regarding systematic uncertainties can be better evaluated. The 25 % systematic uncertainty is bound by the fact that most systematic uncertainties would be below 50 % of the total uncertainty and above the historic approach of ignoring the unknown systematic components (i.e., treat it with a 0 % probability). In actuality, careful experimenters may have an unknown systematic uncertainty that is approximately 10-15 % of their total reported uncertainty. Evaluated uncertainties are listed as calculated, such that the readers may adjust results according to some desired systematic to random uncertainty ratio. The summary in Section 2.1.7 does list the systematic and random components of the uncertainty as separate entities based on the assumption that uncertainties with random components have 25 % systematic uncertainty.

It is important to note that most parameters regarding the TRISO particles are normally distributed.

## 2.1 Evaluation of Critical and / or Subcritical Configuration Data

In the preliminary Japanese computational evaluation, the predicted number of fuel columns to achieve criticality was 16±1, much less than the experimental result of 19. It was regarded that the neglect of nitrogen in the porous graphite led to this discrepancy. Two reevaluations were carried out after the initial criticality experiment (Ref. 1, pp. 313-314). The first reevaluation examined the air content in the graphite, simplification of graphite geometry, and impurity concentration in the dummy blocks. The predicted number of fuel columns for initial criticality was changed to 18±1.[a] The second reevaluation wasn't performed until after the full power tests at 30 MW and 850 ºC. Heterogeneity effects and air composition in the graphite was analyzed; the reevaluation also predicted 18±1 fuel columns for initial criticality.[b]

Monte Carlo n-Particle (MCNP) version 5.1.40 calculations were utilized to estimate the biases and uncertainties associated with the experimental results for HTTR critical configurations in this evaluation. MCNP is a general-purpose, continuous-energy, generalized-geometry, time-dependent, coupled n-particle Monte Carlo transport code.[c] The Evaluated Neutron Data File library, ENDF/B-VI.8,[d] was utilized in analysis of the experiment and benchmark model biases and uncertainties.

Elemental data such as molecular weights and isotopic abundances were taken from the 16th edition of the Chart of the Nuclides.[e] These values are summarized in Appendix C.

---

[a] Fujimoto, N., Nakano, M., Takeuchi, M., Fujisaki, S., and Yamashita, K., "Start-Up Core Physics Tests of High Temperature Engineering Test Reactor (HTTR), (II): First Criticality by an Annular Form Fuel Loading and Its Criticality Prediction Method," *J. Atomic Energy Society Japan*, **42**(5), 458-464 (2000).

[b] Yamashita, K., Fujimoto, N., Takeuchi, M., Fujisaki, S., Nakano, M., Umeda, M., Takeda, T., Mogi, H., and Tanaka, T., "Startup Core Physics Tests of High Temperature Engineering Test Reactor (HTTR), (I): Test Plan, Fuel Loading and Nuclear Characteristics Tests," *J. Atomic Energy Society Japan*, **42**(1), 30-42 (2000).

[c] X-5 Monte Carlo Team, "MCNP – a General Monte Carlo n-Particle Transport Code, version 5," LA-UR-03-1987, Los Alamos National Laboratory (2003).

[d] H. D. Lemmel, P. K. McLaughlin, and V. G. Pronyaev, "ENDF/B-VI Release 8 (Last Release of ENDF/B-VI) the U.S. Evaluated Nuclear Data Library for Neutron Reaction Data," IAEA-NDS-100 Rev. 11, International Atomic Energy Agency, Vienna (November 2001).

[e] Nuclides and Isotopes: Chart of the Nuclides, 16th edition, (2002).

Only the primary components of the HTTR active core and surrounding reflector region were included in the analysis of uncertainties in this evaluation. Currently only the 30-fuel-column start-up core critical test was evaluated. The uncertainty analysis was performed using a model temperature of approximately 300 K.

For all impurity assessments, only the equivalent natural-boron content is utilized in the evaluation. In the compositions used in the evaluation models, the natural-boron content is adjusted to include only the primary absorber $^{10}B$, according to the isotopic abundance of 19.9 at.%.

All MCNP calculations of $k_{eff}$ have statistical uncertainties between 0.00013 and 0.00014, resulting in $\Delta k$ statistical uncertainties of approximately 0.00020, assuming no correlation between the individual MCNP results.

Some of the calculated uncertainties are poorly estimated because they are very small and on the order of the statistical uncertainty of the analysis method. However, these uncertainties are insignificant in magnitude compared to the total benchmark uncertainty. Reanalysis of most of these parameters with larger variations would not significantly reduce their uncertainties below the statistical uncertainty of the Monte Carlo calculations.

Uncertainties less than 0.00001 are reported as negligible (neg). When calculated uncertainties in $\Delta k_{eff}$ are less than their statistical uncertainties, the statistical uncertainties are used in the calculation of the total uncertainty.

The term "Scaling Factor" denotes the necessary correction to adjust the evaluated uncertainty in $k_{eff}$ to a $1\sigma$ value. Often a larger uncertainty is evaluated such that the calculated $\Delta k$ value is greater than the statistical uncertainty in the analysis method.

### 2.1.1 Experimental Uncertainties

#### *2.1.1.1 Temperature*

Various temperature coefficients of reactivity are reported, ranging from $-1.23 \times 10^{-4}$ $\Delta k/k$-ºC (Table 1.17) to -14.2 pcm/ºC (Ref. 2, p. 113 and 132). An average of -13.25 pcm/ºC with a deviation of ±0.95 ($1\sigma$) was selected to represent the effective change in reactivity with temperature adjustment. The experiments were performed near room temperature, and an uncertainty of ±1 ºC ($1\sigma$) was selected to represent the uncertainty in the temperature of the experiment. Results are shown in Table 2.1.

The uncertainty in the temperature is considered all systematic with no random component.

Table 2.1. Effect of Uncertainty in Temperature.

| Deviation | $\Delta k$ | ± | $\sigma_{\Delta k}$ | Scaling Factor | $\Delta k_{eff}$ ($1\sigma$) | ± | $\sigma_{\Delta keff}$ |
|---|---|---|---|---|---|---|---|
| -1 ºC | 0.00013 | ± | 0.00001 | 1 | 0.00013 | ± | 0.00001 |
| +1 ºC | -0.00013 | ± | 0.00001 | 1 | -0.00013 | ± | 0.00001 |

#### *2.1.1.2 Control Rod Position*

Control rod positions were varied ±5 mm (1σ), as shown in Table 1.18, to determine the effective change in $k_{eff}$. The sinking effect of -14 mm had already been applied to the rod position shown in Tables 1.17 and 1.18. It is unconfirmed whether temperature expansion effect of ±2 mm (reported at the end of Section 1.1.2.4) applies uniformly to all control rods, how it was obtained, or that is was even applied to the reported experimental positions. Therefore it is applied with the ±5 mm in a root mean square approach, the overall uncertainty in the height remains approximately ±5 mm. No additional bias or bias uncertainty was evaluated for the sinking effect of the control rods. Results are shown in Table 2.2.

The total number of control rods used in the core is 32. For determining the random component of the uncertainty in Section 2.1.7, the results in Table 2.2 are divided by √16.

Table 2.2. Effect of Uncertainty in Control Rod Position.

| Deviation | Δk | ± | $\sigma_{\Delta k}$ | Scaling Factor | $\Delta k_{eff}$ (1σ) | ± | $\sigma_{\Delta keff}$ |
|---|---|---|---|---|---|---|---|
| -5 mm (1σ) | -0.00053 | ± | 0.00020 | 1 | -0.00053 | ± | 0.00020 |
| +5 mm (1σ) | 0.00065 | ± | 0.00020 | 1 | 0.00065 | ± | 0.00020 |

#### *2.1.1.3 Measured Value of $k_{eff}$*

There is no additional information regarding the accuracy of the $k_{eff}$ measurements for the critical core conditions reported in Table 1.17.

### 2.1.2 Geometrical Properties

#### *2.1.2.1 Coated Fuel Particles*

**Kernel Diameter**

The kernel diameter was varied ±55 μm from the nominal value of 600 μm (Tables 1.12 through 1.14) to determine the effective uncertainty in $k_{eff}$. It is a bounding limit. All other thicknesses in the TRISO particle were maintained the same. The packing fraction (i.e., the ratio of the TRISO particle volume to the volume of a unit cell of fuel containing the TRISO particle) of the TRISO particles in the fuel was not conserved but remained within 2σ of the nominal value of 30 vol. % (±3 % in Table 1.14). Results are shown in Table 2.3.

The uncertainty in the kernel diameter causes a large uncertainty in $k_{eff}$. It may likely that the uncertainty reported for the diameter 3σ value. Figure 4 in the IAEA TECDOC-1210[a] displays standard deviations of fuel kernel diameters between 15 and 20 μm, which corresponds with treatment of the ±55 μm as a 3σ uncertainty with a 1σ value of ±18.33 μm. Even reduced from a 3σ to 1σ uncertainty, the uncertainty in kernel diameter, which would provide uncertainty in the total uranium mass in the core, is still quite large before accounting for the statistical reduction of random particles.

The total number of TRISO particles used in the core is approximately 861,140,000. For determining the random component of the uncertainty, the results in Table 2.3 would be divided by √861,140,000.

[a] S. Kato, S. Yoshimuta, T. Hasumi, K. Sato, K. Sawa, S. Suzuki, H. Mogi, S. Shiozawa, and T. Tanaka, "Fabrication of HTTR First Loading Fuel," IAEA-TECDOC-1210, International Atomic Energy Agency, Vienna, pp. 187-199 (April 2001).

Because of the overspecification (i.e., provision of four parameters of which only two can be independent) of the TRISO particles in Table 1.14 and the correlation of uranium kernel diameter, density, TRISO packing fraction and mass, the effect of the uncertainty in the kernel diameter is not included in the total uncertainty (See Section 2.1.6).

Table 2.3. Effect of Uncertainty in Kernel Diameter.

| Deviation | $\Delta k$ | $\pm$ | $\sigma_{\Delta k}$ | Scaling Factor | $\Delta k_{eff}$ (1$\sigma$) | $\pm$ | $\sigma_{\Delta keff}$ |
|---|---|---|---|---|---|---|---|
| -55 μm | -0.04785 | ± | 0.00020 | 3 | -0.01595 | ± | 0.00007 |
| +55 μm | 0.03174 | ± | 0.00019 | 3 | 0.01058 | ± | 0.00006 |

## Buffer Diameter

The buffer thickness was varied ±12 μm (3σ) from the nominal value of 60 μm (Tables 1.12 and 1.14, and Figure 1.48) to determine the effective change in $k_{eff}$. All other thicknesses in the TRISO particle were maintained the same. The packing fraction of the TRISO particles in the fuel was not conserved, so as to conserve fuel mass, but remained within 1σ of the nominal value of 30 vol. % (±3 % in Table 1.14). Results are shown in Table 2.4.

The total number of TRISO particles used in the core is approximately 861,140,000. For determining the random component of the uncertainty, the results in Table 2.4 would be divided by √861,140,000.

Table 2.4. Effect of Uncertainty in Buffer Diameter.

| Deviation | $\Delta k$ | $\pm$ | $\sigma_{\Delta k}$ | Scaling Factor | $\Delta k_{eff}$ (1$\sigma$) | $\pm$ | $\sigma_{\Delta keff}$ |
|---|---|---|---|---|---|---|---|
| -12 μm (3σ) | 0.00040 | ± | 0.00019 | 3 | 0.00013 | ± | 0.0.0006 |
| +12 μm (3σ) | -0.00002 | ± | 0.00020 | 3 | -0.00001 | ± | 0.00007 |

## IPyC Diameter

The IPyC thickness was varied ±6 μm (3σ) from the nominal value of 30 μm (Tables 1.12 and 1.14, and Figure 1.48) to determine the effective uncertainty in $k_{eff}$. All other thicknesses in the TRISO particle were maintained the same. The packing fraction of the TRISO particles in the fuel was not conserved but remained within 1σ of the nominal value of 30 vol. % (±3 % in Table 1.14). Results are shown in Table 2.5.

The total number of TRISO particles used in the core is approximately 861,140,000. For determining the random component of the uncertainty, the results in Table 2.5 would be divided by √861,140,000.

Table 2.5. Effect of Uncertainty in IPyC Diameter.

| Deviation | Δk | ± | $\sigma_{\Delta k}$ | Scaling Factor | $\Delta k_{eff}$ (1σ) | ± | $\sigma_{\Delta keff}$ |
|---|---|---|---|---|---|---|---|
| -6 μm (3σ) | -0.00005 | ± | 0.00019 | 3 | -0.00002 | ± | 0.00006 |
| +6 μm (3σ) | -0.00004 | ± | 0.00019 | 3 | -0.00001 | ± | 0.00006 |

## SiC Diameter

The SiC thickness was varied ±12 μm (3σ) from the nominal value of 30 μm (Tables 1.12 and 1.14, and Figure 1.48) to determine the effective uncertainty in $k_{eff}$. Although there is a negative component to the deviation in the thickness (Figure 1.48), TRISO particles with SiC thicknesses less than 25 μm are not acceptable for use as a final product. The thickness of 25 μm for the thickness appears to be a manufacturing limit while the thickness of 30 μm is more likely to be the actual thickness of the SiC layer. All other thicknesses in the TRISO particle were maintained the same. The packing fraction of the TRISO particles in the fuel was not conserved but remained within 1σ of the nominal value of 30 vol. % (±3 % in Table 1.14). Results are shown in Table 2.6.

The total number of TRISO particles used in the core is approximately 861,140,000. For determining the random component of the uncertainty, the results in Table 2.6 would be divided by √861,140,000.

Table 2.6. Effect of Uncertainty in SiC Diameter.

| Deviation | Δk | ± | $\sigma_{\Delta k}$ | Scaling Factor | $\Delta k_{eff}$ (1σ) | ± | $\sigma_{\Delta keff}$ |
|---|---|---|---|---|---|---|---|
| -12 μm (3σ) | 0.00153 | ± | 0.00020 | 3 | 0.00051 | ± | 0.00007 |
| +12 μm (3σ) | -0.00112 | ± | 0.00019 | 3 | -0.00037 | ± | 0.00006 |

## OPyC Diameter

The OPyC thickness was varied ±6 μm (3σ) from the nominal value of 45 μm (Tables 1.12 and 1.14, and Figure 1.48) to determine the effective uncertainty in $k_{eff}$. All other thicknesses in the TRISO particle were maintained the same. The packing fraction of the TRISO particles in the fuel was not conserved but remained within 1σ of the nominal value of 30 vol. % (±3 % in Table 1.14). Results are shown in Table 2.7.

The total number of TRISO particles used in the core is approximately 861,140,000. For determining the random component of the uncertainty, the results in Table 2.7 would be divided by √861,140,000.

Table 2.7. Effect of Uncertainty in OPyC Diameter.

| Deviation | Δk | ± | $\sigma_{\Delta k}$ | Scaling Factor | $\Delta k_{eff}$ (1σ) | ± | $\sigma_{\Delta keff}$ |
|---|---|---|---|---|---|---|---|
| -6 μm (3σ) | -0.00002 | ± | 0.00020 | 3 | -0.00001 | ± | 0.00006 |
| +6 μm (3σ) | -0.00001 | ± | 0.00020 | 3 | 0.00000 | ± | 0.00007 |

**Overcoat Diameter**

Because insufficient data is available for the final composition and density of the graphite overcoat, this layer is being treated with equal properties to that of the surrounding compact graphite matrix (Table 1.14). Therefore modification of the overcoat diameter would not generate an effective uncertainty in $k_{eff}$ beyond statistical uncertainty.

*2.1.2.2 Prismatic Fuel Compact*

**Dimensions**

The inner and outer diameters (ID and OD) of a fuel compact were each individually varied ±0.1 mm and the height (H) was varied ±0.5 mm to determine the effective uncertainty in $k_{eff}$. For the effective change in height, the fuel stack height was adjusted by ±7.0 mm and the effect from a height change in a single fuel compact was then determined by dividing by 14 for the number of compacts in a fuel rod. The nominal values for the inner diameter, outer diameter, and height of the fuel compacts are 10.0, 26.0, and 39.0 mm, respectively (Table 1.14). Results are shown in Table 2.8. In essence, changing the dimensions of the fuel compact without changing the number of TRISO particles would adjust the packing fraction.

Later information was obtained regarding manufacturing tolerances for the fuel compacts. The ±0.1 mm of the ID and OD represents a bounding limit (with assumed uniform probability) and the effective stack height has a bounding limit (with assumed uniform probability) of ±1.0 mm.[a] The appropriate corrections to the scaling factors have been incorporated into the uncertainty analysis of these parameters.

The total number of fuel compacts used in the core is 66,780. For determining the random component of the uncertainty, the results in Table 2.8 would be divided by √66,780.

Table 2.8. Effect of Uncertainty in Compact Dimensions.

| Deviation | $\Delta k$ | ± | $\sigma_{\Delta k}$ | Scaling Factor | $\Delta k_{eff}$ (1σ) | ± | $\sigma_{\Delta keff}$ |
|---|---|---|---|---|---|---|---|
| -0.1 mm ID | 0.00025 | ± | 0.00020 | √3 | 0.00014 | ± | 0.00011 |
| +0.1 mm ID | 0.00028 | ± | 0.00019 | √3 | 0.00016 | ± | 0.00011 |
| -0.1 mm OD | -0.00020 | ± | 0.00020 | √3 | -0.00012 | ± | 0.00011 |
| +0.1 mm OD | 0.00058 | ± | 0.00020 | √3 | 0.00033 | ± | 0.00011 |
| -7.0 mm (7 × limit) H | -0.00002 | ± | 0.00020 | 7√3 | 0.00000 | ± | 0.00002 |
| +7.0 mm (7 × limit) H | 0.00041 | ± | 0.00020 | 7√3 | 0.00003 | ± | 0.00002 |

**Packing Fraction**

The packing fraction was varied ±3 vol. % from the nominal value of 30 % (Table 1.14) to determine the effective uncertainty in $k_{eff}$. It is a bounding limit. Results are shown in Table 2.9. This adjustment was performed by varying the number of TRISO particles packed into a single compact. Fuel mass is not

[a] S. Maruyama, K. Yamashita, N. Fujimoto, I. Murata, R. Shindo, and Y. Sudo, "Determination of Hot Spot Factors for Calculation of the Maximum Fuel Temperatures in the Core Thermal and Hydraulic Design of HTTR," JAERI-M 88-250, JAEA (November 18, 1988). [in Japanese].

conserved when adjusting the packing fraction, providing correlation between uncertainties in the fuel mass and packing fraction.

The total number of fuel compacts used in the core is 66,780. For determining the random component of the uncertainty, the results in Table 2.8 would be divided by √66,780.

Because of the overspecification of the TRISO particles in Table 1.14 and the correlation of uranium kernel diameter, density, TRISO packing fraction and mass, the effect of the uncertainty in the packing fraction is not included in the total uncertainty (See Section 2.1.6).

Table 2.9. Effect of Uncertainty in Compact Packing Fraction.

| Deviation | $\Delta k$ | ± | $\sigma_{\Delta k}$ | Scaling Factor | $\Delta k_{eff}$ (1σ) | ± | $\sigma_{\Delta keff}$ |
|---|---|---|---|---|---|---|---|
| -3 vol. % (+TRISO content) | 0.01301 | ± | 0.00019 | √3 | 0.00751 | ± | 0.00011 |
| +3 vol. % (-TRISO content) | -0.01580 | ± | 0.00020 | √3 | -0.00912 | ± | 0.00011 |

### *2.1.2.3 Graphite Sleeves*

The uncertainty in the sleeve thickness was unreported. An inner diameter uncertainty of ±0.5 mm, which is limited by the 0.25 mm gap width between the sleeve and fuel compacts (Table 1.13), and an outer diameter uncertainty of ±2 mm were assumed; their effects on the uncertainty of $k_{eff}$ were determined. Figure 1.51 shows an inner diameter of 26.25 mm for the graphite sleeves, which would only provide a gap space of 0.125 mm. The assumed uncertainty encompasses the discrepancy in this value. Results are shown in Table 2.10.

The fuel sleeve height was varied ±0.5 mm from the nominal value of 577 mm (Table 1.14 and Figure 1.51) and the effect on the uncertainty of $k_{eff}$ was determined. Results are shown in Table 2.10.

Later information was obtained regarding manufacturing tolerances for the fuel sleeves. The ±0.1 mm of the ID and OD represents a bounding limit (with assumed uniform probability) and the height is then assumed to have a bounding limit (with assumed uniform probability) also of ±0.1 mm.[a] The appropriate corrections to the scaling factors have been incorporated into the uncertainty analysis of these parameters.

The total number of graphite sleeves used in the core is 4,770. For determining the random component of the uncertainty, the results in Table 2.8 would be divided by √4,770.

[a] S. Maruyama, K. Yamashita, N. Fujimoto, I. Murata, R. Shindo, and Y. Sudo, "Determination of Hot Spot Factors for Calculation of the Maximum Fuel Temperatures in the Core Thermal and Hydraulic Design of HTTR," JAERI-M 88-250, JAEA (November 18, 1988). [in Japanese].

Table 2.10. Effect of Uncertainty in Graphite Sleeve Dimensions.

| Deviation | $\Delta k$ | ± | $\sigma_{\Delta k}$ | Scaling Factor | $\Delta k_{eff}$ (1σ) | ± | $\sigma_{\Delta keff}$ |
|---|---|---|---|---|---|---|---|
| -0.5 mm (5 × limit) ID | 0.00150 | ± | 0.00019 | 5√3 | 0.00017 | ± | 0.00002 |
| +0.5 mm (5 × limit) ID | -0.00157 | ± | 0.00019 | 5√3 | -0.00018 | ± | 0.00002 |
| -2 mm (20 × limit) OD | -0.00833 | ± | 0.00019 | 20√3 | -0.00024 | ± | 0.00001 |
| +2 mm (20 × limit) OD | 0.00857 | ± | 0.00019 | 20√3 | 0.00025 | ± | 0.00001 |
| -0.5 mm (5 × limit) H | 0.00040 | ± | 0.00019 | 5√3 | 0.00005 | ± | 0.00002 |
| -0.5 mm (5 × limit) H | 0.00015 | ± | 0.00020 | 5√3 | 0.00002 | ± | 0.00002 |

### *2.1.2.4 Burnable Poisons*

The uncertainty in the diameters of the BPs and BP insertion holes was unreported. A BP diameter uncertainty of ±1 mm from the nominal diameter (D) of 14 mm and a BP insertion hole diameter uncertainty of ±1 mm from the nominal diameter of 15 mm were assumed and their effects on the uncertainty of $k_{eff}$ were determined. Results are shown in Table 2.11.

The uncertainty in the height stack of the BPs was unreported. A stack height (H) uncertainty of ±1 mm from the nominal height of 200 mm was assumed (approximately ±0.1 mm per BP pellet) and the effective uncertainty in $k_{eff}$ was determined. The height of the BP insertion hole was adjusted to accommodate the change in BP stack height. Results are shown in Table 2.11.

The uncertainty in the dimensions of the graphite disks was unreported. A diameter uncertainty of ±1 mm from the nominal diameter of 14 mm and a height uncertainty of ±1 mm from the nominal stack height of 100 mm were assumed and their effects on the uncertainty of $k_{eff}$ were determined. The height of the BP insertion hole was adjusted to accommodate the change in graphite-disk stack height. Results are shown in Table 2.11.

Because of the tight manufacturing tolerances of the fuel compacts and graphite sleeves (Sections 2.1.2.2 and 2.1.2.3, respectively) it is believed that similar tolerances apply to other graphite and boron carbide components of the HTTR. Therefore, the BP and graphite disk diameters are treated with a tolerance (with uniform probability) of ±0.1 mm and a stack height tolerance (with uniform probability) of ±1.0 mm. The appropriate corrections to the scaling factors have been incorporated into the uncertainty analysis of these parameters.

The total number of burnable poison pellets used in the core is 5,520. For determining the random component of the uncertainty, the results in Table 2.11 would be divided by √5,520. The total number of BP stacks is 600, of pin holes is 450, and of graphite disk stacks is 300.

Table 2.11. Effect of Uncertainty in BP Pin Dimensions.

| Deviation | $\Delta k$ | ± | $\sigma_{\Delta k}$ | Scaling Factor | $\Delta k_{eff}$ (1$\sigma$) | ± | $\sigma_{\Delta keff}$ |
|---|---|---|---|---|---|---|---|
| -1 mm (10 × limit) BP D | 0.01362 | ± | 0.00020 | 10√3 | 0.00079 | ± | 0.00001 |
| +1 mm (10 × limit) BP D | -0.01271 | ± | 0.00020 | 10√3 | -0.00073 | ± | 0.00001 |
| -1 mm BP Stack H | 0.00076 | ± | 0.00020 | √3 | 0.00044 | ± | 0.00011 |
| +1 mm BP Stack H | -0.00064 | ± | 0.00019 | √3 | -0.00037 | ± | 0.00011 |
| -1 mm (10 × limit) Hole D | 0.00108 | ± | 0.00020 | 10√3 | 0.00006 | ± | 0.00001 |
| +1 mm (10 × limit) Hole D | -0.00101 | ± | 0.00020 | 10√3 | -0.00006 | ± | 0.00001 |
| -1 mm (10 × limit) Disk D | -0.00014 | ± | 0.00020 | 10√3 | -0.00001 | ± | 0.00001 |
| +1 mm (10 × limit) Disk D | 0.00003 | ± | 0.00020 | 10√3 | 0.00000 | ± | 0.00001 |
| -1 mm Disk H | 0.00002 | ± | 0.00020 | √3 | 0.00001 | ± | 0.00011 |
| +1 mm Disk H | -0.00009 | ± | 0.00020 | √3 | -0.00005 | ± | 0.00011 |

### *2.1.2.5 Control Rods*

**Absorber Dimensions**

The uncertainty in the absorber dimensions was unreported. Assumed inner and outer diameter (ID and OD) uncertainties are ±5 mm each from the nominal values of 75 and 105 mm (Table 1.15), respectively, and their effects on the uncertainty of $k_{eff}$ were determined. The uncertainty in the pellet height was assumed to be ±1 cm from the nominal stack height (H) of 29 cm. The alternate value of 115 mm provided for the outer diameter of the absorber material is believed to be a typographical error (see footnote of Table 1.15). Results are shown in Table 2.12.

Because of the tight manufacturing tolerances of the fuel compacts and graphite sleeves (Sections 2.1.2.2 and 2.1.2.3, respectively) it is believed that similar tolerances apply to other graphite and boron carbide components of the HTTR. Therefore, the absorber diameters are treated with a tolerance (with uniform probability) of ±0.1 mm and a stack height tolerance (with uniform probability) of ±1.0 mm. The appropriate corrections to the scaling factors have been incorporated into the uncertainty analysis of these parameters.

The total number of control rod absorber pellets used in the core is approximately 975. The assumption is based on that only 13 control positions are approximately 30% inserted into the core. For determining the random component of the uncertainty, the results in Table 2.12 would be divided by √975.

Table 2.12. Effect of Uncertainty in CR Absorber Dimensions.

| Deviation | $\Delta k$ | ± | $\sigma_{\Delta k}$ | Scaling Factor | $\Delta k_{eff}$ (1σ) | ± | $\sigma_{\Delta keff}$ |
|---|---|---|---|---|---|---|---|
| -5 mm (50 × limit) Absorber ID | -0.00020 | ± | 0.00020 | 50√3 | 0.00000 | ± | 0.00000 |
| +5 mm (50 × limit) Absorber ID | 0.00036 | ± | 0.00019 | 50√3 | 0.00000 | ± | 0.00000 |
| -5 mm (50 × limit) Absorber OD | 0.00175 | ± | 0.00020 | 50√3 | 0.00002 | ± | 0.00000 |
| +5 mm (50 × limit) Absorber OD | -0.00171 | ± | 0.00020 | 50√3 | -0.00002 | ± | 0.00000 |
| -1 cm (10 × limit) Absorber H | 0.00086 | ± | 0.00020 | 10√3 | 0.00005 | ± | 0.00001 |
| +1 cm (10 × limit) Absorber H | -0.00084 | ± | 0.00020 | 19√3 | -0.00005 | ± | 0.00001 |

## Clad Dimensions

The uncertainty in the clad dimensions was unreported, and detailed dimensions for anything similar to the diagram shown in Figure 1.60 were unavailable. Therefore a solid clad material encasing the control rod absorber was defined without detail for the end caps. Inner and outer thicknesses were varied ±5 mm (from the nominal values of 65 and 113 mm (Table 1.15), respectively, to determine their effects on the uncertainty of $k_{eff}$. The spine diameter was varied ±10 mm from the nominal value of 10 mm (Table 1.15) and its effect on the uncertainty of $k_{eff}$ was determined. The clad height of a single control rod section was varied ±1. The reported clad thickness of 3.5 mm does not appear to conform to the difference between reported diameters of the clad and absorber materials. It is unclear whether a gap exists or there is rounding of values in the original table. The uncertainties evaluated encompass the overall uncertainty in this discrepancy. The control rod diameters are chosen as the more appropriate dimensions for modeling, such that inner and outer clad thicknesses are approximately 5 and 4 mm, respectively.. Results are shown in Table 2.13.

Height change of clad also affects the effective height of each control rod segment.

Because of the tight manufacturing tolerances of the fuel compacts and graphite sleeves (Sections 2.1.2.2 and 2.1.2.3, respectively) it is believed that tighter tolerances apply to the absorber cladding. Therefore, the diameters are treated with a tolerance (with uniform probability) of ±0.5 mm and a height tolerance (with uniform probability) of ±1.0 mm. The appropriate corrections to the scaling factors have been incorporated into the uncertainty analysis of these parameters.

The total number of control rod sections used in the core is approximately 97.5. The assumption is based on that only 13 control positions are approximately 30% inserted into the core. For determining the random component of the uncertainty, the results in Table 2.13 would be divided by √97.5.

Table 2.13. Effect of Uncertainty in CR Clad Dimensions.

| Deviation | $\Delta k$ | ± | $\sigma_{\Delta k}$ | Scaling Factor | $\Delta k_{eff}$ (1$\sigma$) | ± | $\sigma_{\Delta keff}$ |
|---|---|---|---|---|---|---|---|
| -5 mm (10 × limit) Clad ID | -0.00002 | ± | 0.00020 | 10√3 | 0.00000 | ± | 0.00001 |
| +5 mm (10 × limit) Clad ID | -0.00019 | ± | 0.00020 | 10√3 | -0.00001 | ± | 0.00001 |
| -5 mm (10 × limit) Clad OD | -0.00110 | ± | 0.00020 | 10√3 | -0.00006 | ± | 0.00001 |
| +5 mm (10 × limit) Clad OD | 0.00089 | ± | 0.00019 | 10√3 | 0.00005 | ± | 0.00001 |
| -1 cm (10 × limit) Clad H | 0.00082 | ± | 0.00019 | 10√3 | 0.00005 | ± | 0.00001 |
| +1 cm (10 × limit) Clad H | -0.00102 | ± | 0.00020 | 10√3 | -0.00006 | ± | 0.00001 |
| -10 mm (20 × limit) Spine D | -0.00007 | ± | 0.00020 | 20√3 | 0.00000 | ± | 0.00001 |
| +10 mm (20 × limit) Spine D | 0.00005 | ± | 0.00020 | 20√3 | 0.00000 | ± | 0.00001 |

### *2.1.2.6 Instrumentation*

Insufficient information is available to comprehensively model and evaluate the uncertainties and biases related to the utility of instrumentation in the HTTR. Neglect of instrumentation inclusion in the model would be a bias; uncertainty in the dimensions and composition of the instrumentation would provide uncertainty in that bias or uncertainty in the model should it have been included in the benchmark model. An approximation of the instrumentation in the HTTR was modeled using information from Section 1.1.2.3 and approximate diagrams shown in a presentation at the IAEA CRP-5 Meeting.[a] The expected bias in the instrumentation, from the aforementioned reference, is ~0.2 % $\Delta$k/k.

Figures 2.1 through 2.4 provide basic geometric descriptions of the instrumentation utilized in the HTTR core. Figure 2.1 shows the respective heights. Figure 2.2, 2.3, and 2.4 provide additional information regarding channels 1, 2, and 3, respectively (columns E05, E13, and E21, respectively). The 5-cm long 0.6-cm diameter $BF_3$ counters were modeled containing gas at 1 atm with 100 at.% $^{10}B$ content. All metallic components were modeled as aluminum. Approximate dimensions were used based on scaling of the Figures 2.2 through 2.4 and the known hole diameter of 123 mm.

Approximate biases were calculated (Section 3.1.1.1). The bias for the fully-loaded core critical was calculated to be 0.254 ± 0.073 % $\Delta$k/k, which is similar to the previously reported value. The uncertainty in the biases was approximated by dividing the biases in half, and then treating it as a bounding uncertainty and dividing by √3. The uncertainty in the instrumentation is included in the total benchmark model uncertainty. The instrumentation is not included in the benchmark model but the bias in used to correct the experimental $k_{eff}$. Because the actual dimensions and material properties are approximated, this uncertainty is treated as completely systematic with no random components.

[a] N. Fujimoto, N. Nojiri, and K. Yamashita, "HTTR's Benchmark Calculation of Start-Up Core Physics Tests," Report of the 3rd Research Coordiation Meeting on the CRP, IAEA, Oarai, Japan, March 12-16 (2001).

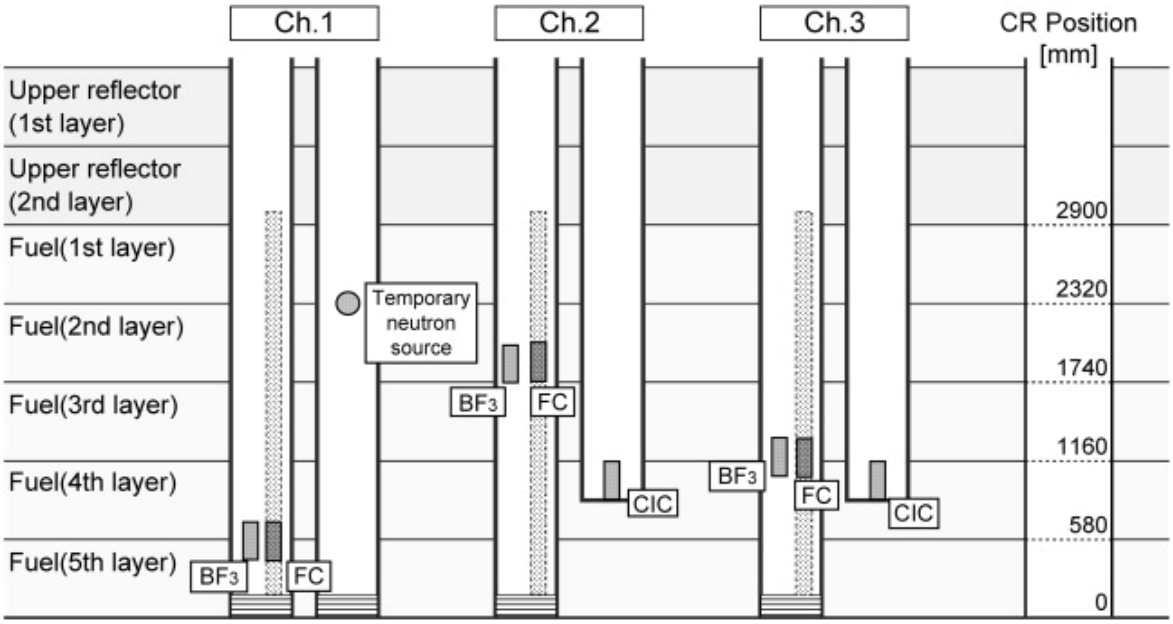


Figure 2.1. Vertical Position of the Temporary Neutron Detectors (Ref 1, p. 314).

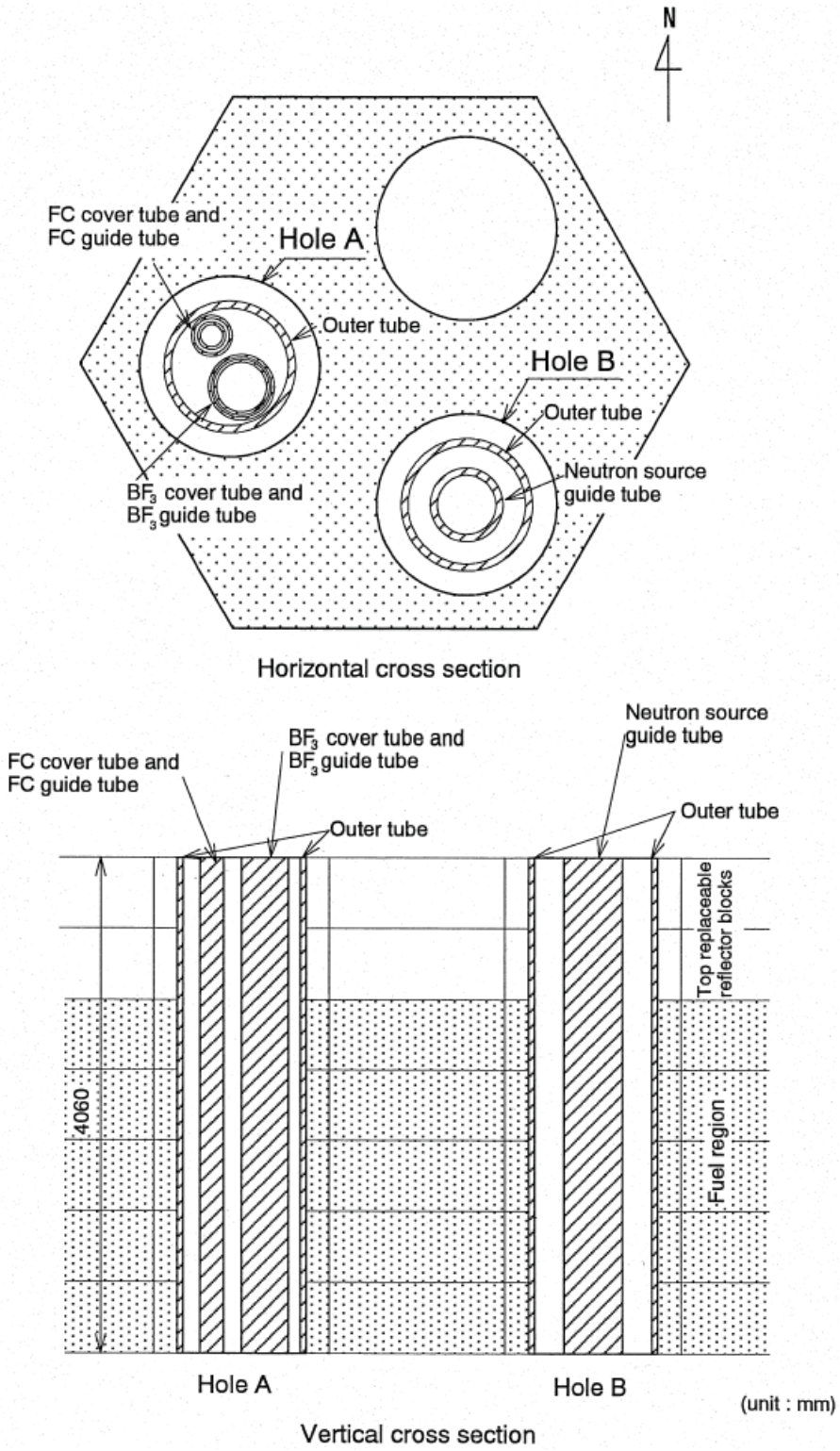


Figure 2.2. Approximation of Instrumentation Channel 1 (Column E05).[a]

[a] N. Fujimoto, N. Nojiri, and K. Yamashita, "HTTR's Benchmark Calculation of Start-Up Core Physics Tests," Report of the 3rd Research Coordination Meeting on the CRP, IAEA, Oarai, Japan, March 12-16 (2001).

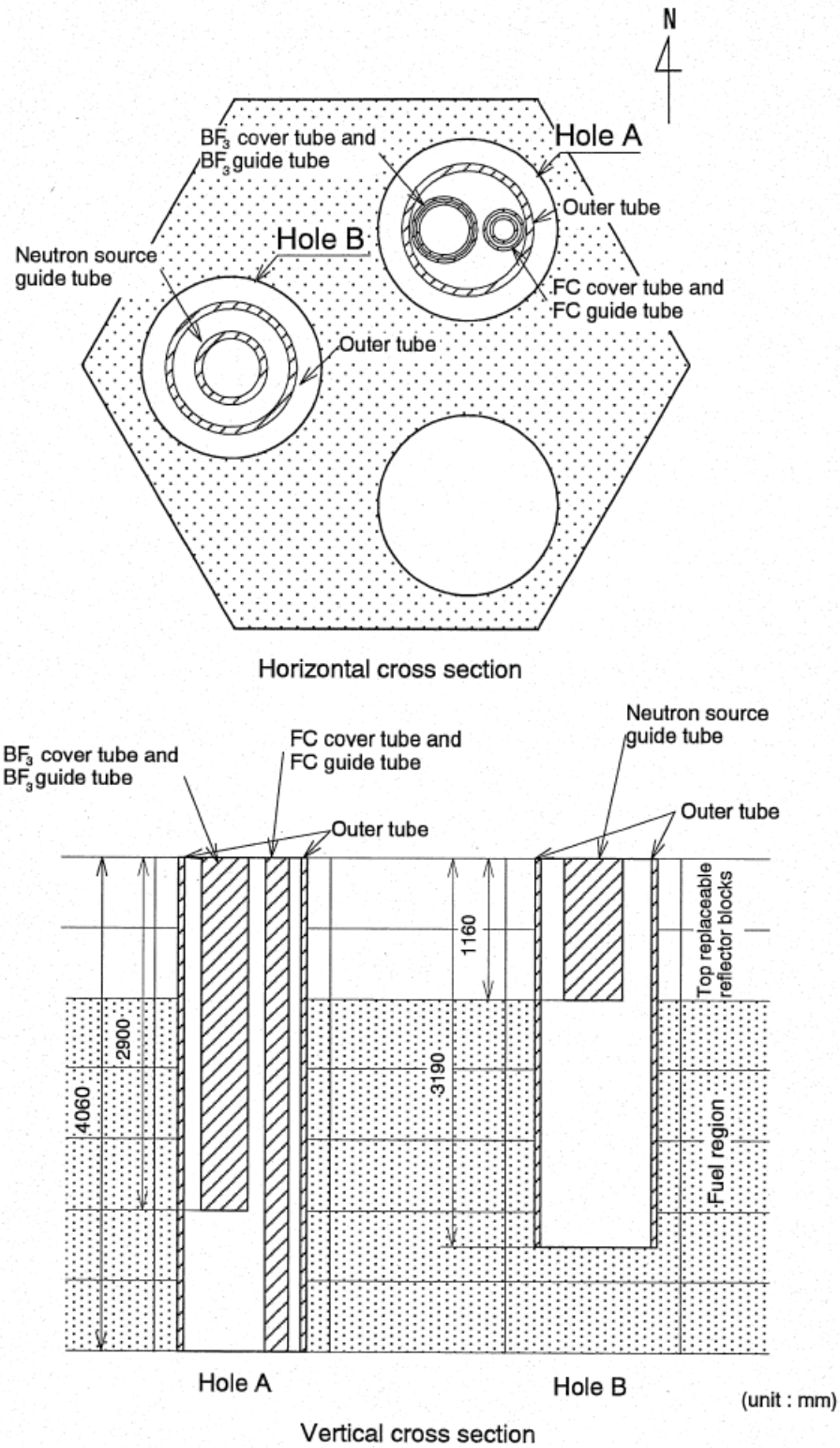


Figure 2.3. Approximation of Instrumentation Channel 2 (Column E13).[a]

[a] N. Fujimoto, N. Nojiri, and K. Yamashita, "HTTR's Benchmark Calculation of Start-Up Core Physics Tests," Report of the 3rd Research Coordination Meeting on the CRP, IAEA, Oarai, Japan, March 12-16 (2001).

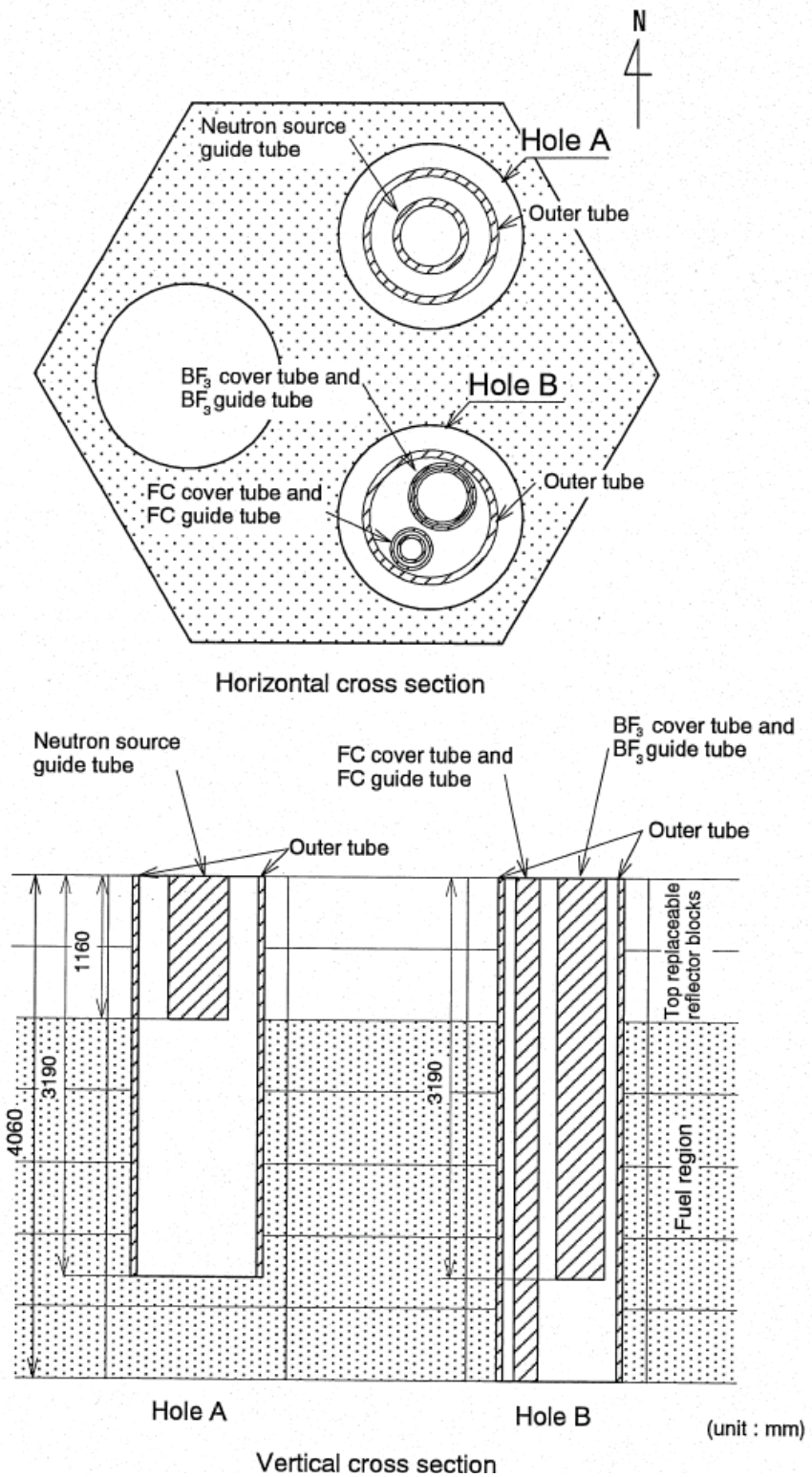


Figure 2.4. Approximation of Instrumentation Channel 3 (Column E21).[a]

[a] N. Fujimoto, N. Nojiri, and K. Yamashita, "HTTR's Benchmark Calculation of Start-Up Core Physics Tests," Report of the 3rd Research Coordination Meeting on the CRP, IAEA, Oarai, Japan, March 12-16 (2001).

*2.1.2.7 Graphite Blocks*

**Block Dimensions**

An uncertainty in the block dimensions was unreported. The uncertainty in the flat-to-flat distance and the height were each varied ±1 mm from their nominal values of 360 and 580 cm (Tables 1.13 and 1.16), respectively, and their effects on the uncertainty of $k_{eff}$ were determined. The average gap between columns was reported as approximately 2 mm (Ref. 2, p. 13), allowing room for the flat-to-flat uncertainty. Results are shown in Table 2.14.

Because of the tight manufacturing tolerances of the fuel compacts and graphite sleeves (Sections 2.1.2.2 and 2.1.2.3, respectively) it is believed that similar tolerances apply to other graphite and boron carbide components of the HTTR. Therefore, the graphite block dimensions are treated with a tolerance (with uniform probability) of ±0.1 mm. The appropriate corrections to the scaling factors have been incorporated into the uncertainty analysis of these parameters.

The total number of graphite blocks used in the core is 549. For determining the random component of the uncertainty, the results in Table 2.14 would be divided by √549.

Table 2.14. Effect of Uncertainty in Graphite Block Dimensions.

| Deviation | $\Delta k$ | ± | $\sigma_{\Delta k}$ | Scaling Factor | $\Delta k_{eff}$ (1σ) | ± | $\sigma_{\Delta keff}$ |
|---|---|---|---|---|---|---|---|
| -1 mm (10 × limit) Flat-to-Flat Distance | -0.00277 | ± | 0.00019 | 10√3 | -0.00016 | ± | 0.00001 |
| +1 mm (10 × limit) Flat-to-Flat Distance | 0.00252 | ± | 0.00020 | 10√3 | 0.00015 | ± | 0.00001 |
| -1 mm (10 × limit) Block H | 0.00097 | ± | 0.00020 | 10√3 | 0.00006 | ± | 0.00001 |
| +1 mm (10 × limit) Block H | -0.00183 | ± | 0.00020 | 10√3 | -0.00011 | ± | 0.00001 |

**Dowel/Socket Dimensions**

Insufficient information is available to completely model and evaluate the uncertainties and biases related to the incorporation of dowels and sockets in the HTTR. Uncertainty in the volume fraction will be included as part of the assessment of the uncertainty in the total density of the graphite blocks.

**Coolant Channel Diameter**

An assumed variation of ±1 mm in the diameter of the coolant channels of the fuel blocks (nominally 41 mm, Table 1.13) and reflector blocks (nominally 23 mm) in the fuel columns was performed to determine the effective uncertainty in $k_{eff}$. Results are shown in Table 2.15.

Insufficient information was available to determine the dimensions of the coolant channels of the lowest reflector blocks. They were modeled similar to the other reflector blocks utilized in the fuel columns. No bias or biased uncertainty was assessed.

Because of the tight manufacturing tolerances of the fuel compacts and graphite sleeves (Sections 2.1.2.2 and 2.1.2.3, respectively) it is believed that similar tolerances apply to other graphite and boron carbide components of the HTTR. Therefore, the coolant channel diameters are treated with a tolerance (with uniform probability) of ±0.1 mm. The appropriate corrections to the scaling factors have been incorporated into the uncertainty analysis of these parameters.

The total number of fuel and reflector coolant channels used in the core is 4,770 and 3,816, respectively. For determining the random component of the uncertainty, the results in Table 2.15 would be divided by √4,770 and √3,816, respectively.

Table 2.15. Effect of Uncertainty in Coolant Channel Diameter.

| Deviation | $\Delta k$ | ± | $\sigma_{\Delta k}$ | Scaling Factor | $\Delta k_{eff}$ (1σ) | ± | $\sigma_{\Delta keff}$ |
|---|---|---|---|---|---|---|---|
| -1 mm (10 × limit) Fueled Channel D | 0.00488 | ± | 0.00019 | 10√3 | 0.00028 | ± | 0.00001 |
| +1 mm (10 × limit) Fueled Channel D | -0.00499 | ± | 0.00019 | 10√3 | -0.00029 | ± | 0.00001 |
| -1 mm (10 × limit) Reflector Channel D | 0.00000 | ± | 0.00020 | 10√3 | 0.00000 | ± | 0.00001 |
| +1 mm (10 × limit) Reflector Channel D | -0.00002 | ± | 0.00020 | 10√3 | 0.00000 | ± | 0.00001 |

## Fuel and Coolant Channel Pitch

An uncertainty in the fuel and coolant channel pitches in the fuel columns was not reported. For the evaluation of this uncertainty, the channels were modeled closer together then further apart by adjusting the pitch between them. A variation of ±1.0 mm from the nominal pitch of 51.5 mm (Figures 1.52 and 1.53) was assumed and the effects on the uncertainty of $k_{eff}$ were determined. Results are shown in Table 2.16.

Because of the tight manufacturing tolerances of the fuel compacts and graphite sleeves (Sections 2.1.2.2 and 2.1.2.3, respectively) it is believed that similar tolerances apply to other graphite and boron carbide components of the HTTR. Therefore, the coolant channel pitch is treated with a tolerance (with uniform probability) of ±0.1 mm. The appropriate corrections to the scaling factors have been incorporated into the uncertainty analysis of these parameters.

The total number of pitch positions used in the core is 8,586. For determining the random component of the uncertainty, the results in Table 2.16 would be divided by √8,586.

Table 2.16. Effect of Uncertainty in Fuel and Coolant Channel Pitch.

| Deviation | $\Delta k$ | ± | $\sigma_{\Delta k}$ | Scaling Factor | $\Delta k_{eff}$ (1σ) | ± | $\sigma_{\Delta keff}$ |
|---|---|---|---|---|---|---|---|
| -1 mm (10 × limit) | -0.00154 | ± | 0.00020 | 10√3 | -0.00009 | ± | 0.00001 |
| +1 mm (10 × limit) | 0.00153 | ± | 0.00020 | 10√3 | 0.00009 | ± | 0.00001 |

## Handling Socket Dimensions

The handling sockets were not included in the model as there was insufficient information to model them completely. The calculated volume of the socket (estimated using dimensions in Figure 1.52) is roughly 0.5 vol. % of the complete block envelope. This volume reduction is included as a reduction in total block density in the benchmark model. A bias has not been assessed. Uncertainty in the volume fraction will be included as part of the assessment of the uncertainty in the total density of the graphite blocks.

## Column Pitch

An uncertainty in column pitch was assumed based upon the average distance between blocks of approximately 2 mm. For the evaluation of this uncertainty, the columns were modeled closer together then further apart by adjusting the pitch between them. A variation of ±2 mm (2 × bounding limit) from the nominal value of 362 mm was analyzed and the effects on the uncertainty of $k_{eff}$ were determined. Results are shown in Table 2.17.

The total number of columns used in the core is 61. For determining the random component of the uncertainty, the results in Table 2.17 would be divided by $\sqrt{61}$.

Table 2.17. Effect of Uncertainty in Column Pitch.

| Deviation | $\Delta k$ | ± | $\sigma_{\Delta k}$ | Scaling Factor | $\Delta k_{eff}$ (1σ) | ± | $\sigma_{\Delta keff}$ |
|---|---|---|---|---|---|---|---|
| -2 mm | 0.00225 | ± | 0.00020 | $2\sqrt{3}$ | 0.00065 | ± | 0.00006 |
| +2 mm | -0.00265 | ± | 0.00020 | $2\sqrt{3}$ | -0.00076 | ± | 0.00006 |

## Control-Rod Channel Diameter

An assumed variation of ±1 mm in the diameter of the control-rod coolant channels (nominal value of 123 mm, Figure 1.64) in the control block columns was performed to determine the effective uncertainty in $k_{eff}$. Results are shown in Table 2.18.

Because of the tight manufacturing tolerances of the fuel compacts and graphite sleeves (Sections 2.1.2.2 and 2.1.2.3, respectively) it is believed that similar tolerances apply to other graphite and boron carbide components of the HTTR. Therefore, the control-rod channel diameter is treated with a tolerance (with uniform probability) of ±0.1 mm. The appropriate corrections to the scaling factors have been incorporated into the uncertainty analysis of these parameters.

The total number of control-rod channels (including empty instrumentation channels) used in the core is approximately 437. For determining the random component of the uncertainty, the results in Table 2.18 would be divided by $\sqrt{437}$.

Table 2.18. Effect of Uncertainty in CR Channel Diameter.

| Deviation | $\Delta k$ | ± | $\sigma_{\Delta k}$ | Scaling Factor | $\Delta k_{eff}$ (1σ) | ± | $\sigma_{\Delta keff}$ |
|---|---|---|---|---|---|---|---|
| -1 mm (10 × limit) | 0.00052 | ± | 0.00020 | $10\sqrt{3}$ | 0.00003 | ± | 0.00001 |
| +1 mm (10 × limit) | -0.00056 | ± | 0.00020 | $10\sqrt{3}$ | -0.00003 | ± | 0.00001 |

## Control-Rod Channel Pitch

An uncertainty in control-rod coolant channel pitch in the fuel and reflector blocks was not reported. For the evaluation of this uncertainty, the channels were modeled closer together then further apart by adjusting the pitch between them. A variation of ±1 mm from the nominal distance of 108 mm from the block axis (Figure 1.64) was assumed and the effects on the uncertainty of $k_{eff}$ were determined. Results are shown in Table 2.19.

Because of the tight manufacturing tolerances of the fuel compacts and graphite sleeves (Sections 2.1.2.2 and 2.1.2.3, respectively) it is believed that similar tolerances apply to other graphite and boron carbide components of the HTTR. Therefore, the control-rod channel pitch is treated with a tolerance (with uniform probability) of ±0.1 mm. The appropriate corrections to the scaling factors have been incorporated into the uncertainty analysis of these parameters.

The total number of control-rod channels (including empty instrumentation channels) used in the core is approximately 437. For determining the random component of the uncertainty, the results in Table 2.19 would be divided by $\sqrt{437}$.

Table 2.19. Effect of Uncertainty in Control-Rod Channel Pitch.

| Deviation | $\Delta k$ | ± | $\sigma_{\Delta k}$ | Scaling Factor | $\Delta k_{eff}$ (1σ) | ± | $\sigma_{\Delta keff}$ |
|---|---|---|---|---|---|---|---|
| -1 mm (10 × limit) | 0.00023 | ± | 0.00020 | $10\sqrt{3}$ | 0.00001 | ± | 0.00001 |
| +1 mm (10 × limit) | -0.00009 | ± | 0.00020 | $10\sqrt{3}$ | -0.00001 | ± | 0.00001 |

### *2.1.2.8 Permanent Reflectors*

Insufficient information is available to model in detail the permanent reflector of the HTTR. A bias was not assessed for any simplification of the permanent reflector. The actual reflector is in the shape of a dodecagon block with an overall diameter and length of 4250 mm and 5250 mm, respectively. It is unclear as to whether the diameter is inscribed within or circumscribed around the polygon.

A radial representation of the permanent reflector had the outer diameter varied ±5 cm to determine the effective change in $\Delta k$. The difference between the reported diameter and an equivalent diameter circle representative of an inscribed or circumscribed dodecagon would by -10 cm and +5 cm, respectively. This uncertainty is treated as a bounding uncertainty. Any uncertainty in the unreported manufacturing tolerances would be negligible. Results are shown in Table 2.20.

The permanent reflector is comprised of 12 circumferential segments in eight axial layers for a total of 96 blocks. However, the uncertainty in the diameter of the model's permanent reflector is not adjusted for random uncertainty and treated as 100% systematic because of the uncertainty in the overall detail of the permanent reflector.

Table 2.20. Effect of Uncertainty in Permanent Reflector Diameter.

| Deviation | $\Delta k$ | ± | $\sigma_{\Delta k}$ | Scaling Factor | $\Delta k_{eff}$ (1σ) | ± | $\sigma_{\Delta keff}$ |
|---|---|---|---|---|---|---|---|
| -5 cm | -0.00028 | ± | 0.00020 | $(\sqrt{3})/2$ | -0.00032 | ± | 0.00023 |
| +5 cm | 0.00061 | ± | 0.00020 | $\sqrt{3}$ | 0.00035 | ± | 0.00011 |

### *2.1.2.9 Dummy Blocks*

Insufficient information is available to model and evaluate the uncertainties and biases related to the utility of dummy blocks in the HTTR. The 30-fuel-column core, however, does not contain dummy blocks. Additional information would be necessary to evaluate the annular HTTR core criticals.

### 2.1.3 Compositional Variations

#### *2.1.3.1 Coated Fuel Particles*

**Uranium Enrichment**

The concentration of $^{234}$U expected in the TRISO fuel had to be determined, as it was not provided. First the weight fractions of isotopes in natural uranium dioxide were determined. Then the enriched weight percent of $^{235}$U was multiplied by the natural weight percent of $^{234}$U (0.0055 at.%) and divided by the natural weight percent of $^{235}$U (0.72 at.%). Thus an approximate concentration of "enriched" $^{234}$U content could be determined for this evaluation, which may slightly underestimate the actual $^{234}$U content.

$$\gamma_{^{234}U}^{Enriched} = \frac{\gamma_{^{234}U}^{Natural}}{\gamma_{^{235}U}^{Natural}} \gamma_{^{235}U}^{Enriched} .$$

Information was not provided regarding the uncertainty in the uranium enrichment of the TRISO kernels. It is reported elsewhere that the manufacturing tolerance limit for the enrichment is 4.5% of the reported weight percent.[a] For example, the enrichment of 3.4 wt.% is bound within a tolerance of ±0.153 wt.%. Each of the twelve enrichments were varied an assumed ±0.1 wt.% in $^{235}$U (1σ), with the $^{234}$U content adjusted to match the effective increase or decrease in enrichment of $^{235}$U, to determine the effective uncertainty in $k_{eff}$. The nominal enrichment values are shown in Figure 1.46 and Table 1.11. Results are shown in Table 2.21. The actual uncertainty in the uranium enrichment is much smaller than the manufacturing limits; however this information is not publicly available. Therefore, the bounding limits are treated with a normal distribution instead of one with uniform probability.

The uncertainty in the uranium enrichment is considered all systematic with no random component.

[a] S. Maruyama, K. Yamashita, N. Fujimoto, I. Murata, R. Shindo, and Y. Sudo, "Determination of Hot Spot Factors for Calculation of the Maximum Fuel Temperatures in the Core Thermal and Hydraulic Design of HTTR," JAERI-M 88-250, JAEA (November 18, 1988). [in Japanese].

Table 2.21. Effect of Uncertainty in Uranium Enrichment.

| Deviation | $\Delta k$ | ± | $\sigma_{\Delta k}$ | Scaling Factor | $\Delta k_{eff}$ (1$\sigma$) | ± | $\sigma_{\Delta keff}$ |
|---|---|---|---|---|---|---|---|
| -0.153 wt.% of 3.4 wt.% | -0.00245 | ± | 0.00016 | 3 | -0.00082 | ± | 0.00005 |
| +0.153 wt.% of 3.4 wt.% | 0.00259 | ± | 0.00016 | 3 | 0.00086 | ± | 0.00005 |
| -0.1755 wt.% of 3.9 wt.% | -0.00234 | ± | 0.00016 | 3 | -0.00078 | ± | 0.00005 |
| +0.1755 wt.% of 3.9 wt.% | 0.00225 | ± | 0.00016 | 3 | 0.00075 | ± | 0.00005 |
| -0.1935 wt.% of 4.3 wt.% | -0.00434 | ± | 0.00016 | 3 | -0.00145 | ± | 0.00005 |
| +0.1935 wt.% of 4.3 wt.% | 0.00399 | ± | 0.00016 | 3 | 0.00133 | ± | 0.00005 |
| -0.216 wt.% of 4.8 wt.% | -0.00128 | ± | 0.00016 | 3 | -0.00043 | ± | 0.00005 |
| +0.216 wt.% of 4.8 wt.% | 0.00117 | ± | 0.00016 | 3 | 0.00039 | ± | 0.00005 |
| -0.234 wt.% of 5.2 wt.% | -0.00083 | ± | 0.00016 | 3 | -0.00028 | ± | 0.00005 |
| +0.234 wt.% of 5.2 wt.% | 0.00106 | ± | 0.00016 | 3 | 0.00035 | ± | 0.00005 |
| -0.2655 wt.% of 5.9 wt.% | -0.00115 | ± | 0.00016 | 3 | -0.00038 | ± | 0.00005 |
| +0.2655 wt.% of 5.9 wt.% | 0.00124 | ± | 0.00016 | 3 | 0.00041 | ± | 0.00005 |
| -0.2835 wt.% of 6.3 wt.% | -0.00063 | ± | 0.00016 | 3 | -0.00021 | ± | 0.00005 |
| +0.2835 wt.% of 6.3 wt.% | 0.00043 | ± | 0.00016 | 3 | 0.00014 | ± | 0.00005 |
| -0.3015 wt.% of 6.7 wt.% | -0.00009 | ± | 0.00016 | 3 | -0.00003 | ± | 0.00005 |
| +0.3015 wt.% of 6.7 wt.% | 0.00020 | ± | 0.00016 | 3 | 0.00007 | ± | 0.00005 |
| -0.324 wt.% of 7.2 wt.% | -0.00034 | ± | 0.00016 | 3 | -0.00011 | ± | 0.00005 |
| +0.324 wt.% of 7.2 wt.% | 0.00014 | ± | 0.00016 | 3 | 0.00005 | ± | 0.00005 |
| -0.3555 wt.% of 7.9 wt.% | -0.00004 | ± | 0.00016 | 3 | -0.00001 | ± | 0.00005 |
| +0.3555 wt.% of 7.9 wt.% | 0.00039 | ± | 0.00016 | 3 | 0.00013 | ± | 0.00005 |
| -0.423 wt.% of 9.4 wt.% | -0.00004 | ± | 0.00016 | 3 | -0.00001 | ± | 0.00005 |
| +0.423 wt.% of 9.4 wt.% | -0.00012 | ± | 0.00016 | 3 | -0.00004 | ± | 0.00005 |
| -0.4455 wt.% of 9.9 wt.% | -0.00004 | ± | 0.00016 | 3 | -0.00001 | ± | 0.00005 |
| +0.4455 wt.% of 9.9 wt.% | 0.00003 | ± | 0.00016 | 3 | 0.00001 | ± | 0.00005 |

## Oxygen to Uranium Ratio

The oxygen to uranium ratio was varied by a best judgement value of ±0.02 (bounding limit) from the nominal value of 2.00 to determine the effective uncertainty in $k_{eff}$. Results are shown in Table 2.22.

The uncertainty in the oxygen to uranium ratio is considered all systematic with no random component.

Table 2.22. Effect of Uncertainty in Oxygen to Uranium Ratio.

| Deviation | $\Delta k$ | ± | $\sigma_{\Delta k}$ | Scaling Factor | $\Delta k_{eff}$ (1$\sigma$) | ± | $\sigma_{\Delta keff}$ |
|---|---|---|---|---|---|---|---|
| -0.02 | -0.00040 | ± | 0.00019 | √3 | -0.00023 | ± | 0.00011 |
| +0.02 | 0.00009 | ± | 0.00020 | √3 | 0.00005 | ± | 0.00011 |

## $UO_2$ Density

The kernel density was varied ±0.26 g/cm$^3$ from a selected value of 10.39 g/cm$^3$ (based on the average uranium mass per fuel rod) to determine the effective uncertainty in $k_{eff}$. It is a bounding limit. The listed $UO_2$ density is 10.41 or 10.63 g/cm$^3$ (Tables 1.13 or 1.14, respectively). However, to achieve the expected fuel content of 188.58 g per fuel rod, the selected density would need to be chosen, with the nominal kernel diameter of 600 μm. The selected density for this evaluation is within the statistical uncertainty provided in Table 1.14. Results are shown in Table 2.23.

The total number of TRISO particles used in the core is approximately 861,140,000. For determining the random component of the uncertainty, the results in Table 2.23 would be divided by √861,140,000.

Because of the overspecification of the TRISO particles in Table 1.14 and the correlation of uranium kernel diameter, density, TRISO packing fraction, and mass, the effect of the uncertainty in the kernel density is not included in the total uncertainty (See Section 2.1.6).

Table 2.23. Effect of Uncertainty in $UO_2$ Density.

| Deviation | Δk | ± | $\sigma_{\Delta k}$ | Scaling Factor | $\Delta k_{eff}$ (1σ) | ± | $\sigma_{\Delta keff}$ |
|---|---|---|---|---|---|---|---|
| -0.26 g/cm$^3$ | -0.00374 | ± | 0.00019 | √3 | -0.00216 | ± | 0.00011 |
| +0.26 g/cm$^3$ | 0.00369 | ± | 0.00020 | √3 | 0.00213 | ± | 0.00011 |

## $UO_2$ Impurity

The kernel impurity was varied from 0-3 ppm by weight of equivalent natural-boron content to determine the bounding uncertainty in $k_{eff}$. The maximum limit was multiplied 10-fold so as to quantify the effective upper uncertainty in the $UO_2$ impurity. The average value is 1.5 ppm by weight (Tables 1.13 and 1.14). Results are shown in Table 2.24.

The uncertainty in the $UO_2$ impurity is considered all systematic with no random component.

Table 2.24. Effect of Uncertainty in $UO_2$ Impurity.

| Deviation | Δk | ± | $\sigma_{\Delta k}$ | Scaling Factor | $\Delta k_{eff}$ (1σ) | ± | $\sigma_{\Delta keff}$ |
|---|---|---|---|---|---|---|---|
| 0 ppm | 0.00030 | ± | 0.00019 | √3 | 0.00017 | ± | 0.00011 |
| 30 ppm | -0.01317 | ± | 0.00020 | 10√3 | -0.00076 | ± | 0.00001 |

## Buffer Density

The buffer density was varied ±0.30 g/cm$^3$ from the nominal value of 1.10 g/cm$^3$ (Table 1.14) to determine the effective uncertainty in $k_{eff}$. This value is three times the bounding limit. The perturbation card, PERT, in MCNP was also employed in an independent analysis to determine the effective uncertainty. The larger uncertainty in $\Delta k_{eff}$ will be applied towards the total uncertainty analysis in Section 2.1.7. Results are shown in Table 2.25.

The total number of TRISO particles used in the core is approximately 861,140,000. For determining the random component of the uncertainty, the results in Table 2.25 would be divided by √861,140,000.

Table 2.25. Effect of Uncertainty in Buffer Density.

| Deviation | $\Delta k$ | ± | $\sigma_{\Delta k}$ | Scaling Factor | $\Delta k_{eff}$ (1σ) | ± | $\sigma_{\Delta keff}$ |
|---|---|---|---|---|---|---|---|
| -0.30 g/cm$^3$ | 0.00003 | ± | 0.00020 | 3√3 | -0.00001 | ± | 0.00004 |
| +0.30 g/cm$^3$ | -0.00008 | ± | 0.00020 | 3√3 | 0.00002 | ± | 0.00004 |
| -0.10 g/cm$^3$ (PERT) | -0.00003 | ± | 0.00002 | √3 | -0.00002 | ± | 0.00001 |
| +0.10 g/cm$^3$ (PERT) | 0.00003 | ± | 0.00002 | √3 | 0.00002 | ± | 0.00001 |

## Buffer Impurity

The buffer impurity was varied from 0-3 ppm by weight of equivalent natural-boron content to determine the bounding uncertainty in $k_{eff}$. The average value is 1.5 ppm by weight (Table 1.13). Results are shown in Table 2.26.

The uncertainty in the buffer impurity is considered all systematic with no random component.

Table 2.26. Effect of Uncertainty in Buffer Impurity.

| Deviation | $\Delta k$ | ± | $\sigma_{\Delta k}$ | Scaling Factor | $\Delta k_{eff}$ (1σ) | ± | $\sigma_{\Delta keff}$ |
|---|---|---|---|---|---|---|---|
| 0 ppm | 0.00019 | ± | 0.00019 | √3 | 0.00011 | ± | 0.00011 |
| 3 ppm | 0.00019 | ± | 0.00019 | √3 | 0.00011 | ± | 0.00011 |

## IPyC Density

The IPyC density was varied +0.30 and -0.15 g/cm$^3$ from the nominal value of 1.85 g/cm$^3$ (Table 1.14) to determine the effective uncertainty in $k_{eff}$. These values are three times the bounding limit. The perturbation card, PERT, in MCNP was also employed in an independent analysis to determine the effective uncertainty. The larger uncertainty in $\Delta k_{eff}$ will be applied towards the total uncertainty analysis in Section 2.1.7. Results are shown in Table 2.27.

The total number of TRISO particles used in the core is approximately 861,140,000. For determining the random component of the uncertainty, the results in Table 2.27 would be divided by √861,140,000.

Table 2.27. Effect of Uncertainty in IPyC Density.

| Deviation | $\Delta k$ | ± | $\sigma_{\Delta k}$ | Scaling Factor | $\Delta k_{eff}$ (1σ) | ± | $\sigma_{\Delta keff}$ |
|---|---|---|---|---|---|---|---|
| -0.15 g/cm$^3$ | -0.00013 | ± | 0.00019 | 3√3 | -0.00003 | ± | 0.00004 |
| +0.30 g/cm$^3$ | 0.00001 | ± | 0.00019 | 3√3 | 0.00000 | ± | 0.00004 |
| -0.05 g/cm$^3$ (PERT) | 0.00002 | ± | 0.00001 | √3 | 0.00001 | ± | 0.00001 |
| +0.10 g/cm$^3$ (PERT) | -0.00001 | ± | 0.00001 | √3 | -0.00001 | ± | 0.00001 |

## IPyC Impurity

The IPyC impurity was varied from 0-3 ppm by weight of equivalent natural-boron content to determine the bounding uncertainty in $k_{eff}$. The average value is 1.5 ppm by weight (Table 1.13). Results are shown in Table 2.28.

The uncertainty in the IPyC impurity is considered all systematic with no random component.

Table 2.28. Effect of Uncertainty in IPyC Impurity.

| Deviation | $\Delta k$ | ± | $\sigma_{\Delta k}$ | Scaling Factor | $\Delta k_{eff}$ (1σ) | ± | $\sigma_{\Delta keff}$ |
|---|---|---|---|---|---|---|---|
| 0 ppm | 0.00011 | ± | 0.00020 | √3 | 0.00006 | ± | 0.00011 |
| 3 ppm | -0.00004 | ± | 0.00020 | √3 | -0.00002 | ± | 0.00011 |

## SiC Density

The SiC density was increased by 0.06 g/cm$^3$, which is typical for SiC material, from the nominal value of 3.20 g/cm$^3$ (Table 1.14) to determine the effective uncertainty in $k_{eff}$. This value is three times the bounding limit. The density was not decreased because of the minimum requirement for SiC density. The perturbation card, PERT, in MCNP was also employed in an independent analysis to determine the effective uncertainty. The larger uncertainty in $\Delta k_{eff}$ will be applied towards the total uncertainty analysis in Section 2.1.7. Results are shown in Table 2.29.

The total number of TRISO particles used in the core is approximately 861,140,000. For determining the random component of the uncertainty, the results in Table 2.29 would be divided by √861,140,000.

Table 2.29. Effect of Uncertainty in SiC Density.

| Deviation | $\Delta k$ | ± | $\sigma_{\Delta k}$ | Scaling Factor | $\Delta k_{eff}$ (1σ) | ± | $\sigma_{\Delta keff}$ |
|---|---|---|---|---|---|---|---|
| +0.06 g/cm$^3$ | -0.00001 | ± | 0.00019 | 3√3 | -0.00000 | ± | 0.00004 |
| +0.02 g/cm$^3$ (PERT) | -0.00001 | ± | 0.00000 | √3 | -0.00001 | ± | 0.00000 |

## SiC Impurity

The SiC impurity was varied from 0-3 ppm by weight of equivalent natural-boron content to determine the bounding uncertainty in $k_{eff}$. The average value is 1.5 ppm by weight (Table 1.13). Results are shown in Table 2.30.

The uncertainty in the SiC impurity is considered all systematic with no random component.

Table 2.30. Effect of Uncertainty in SiC Impurity.

| Deviation | $\Delta k$ | ± | $\sigma_{\Delta k}$ | Scaling Factor | $\Delta k_{eff}$ (1σ) | ± | $\sigma_{\Delta keff}$ |
|---|---|---|---|---|---|---|---|
| 0 ppm | 0.00013 | ± | 0.00020 | √3 | 0.00008 | ± | 0.00011 |
| 3 ppm | -0.00005 | ± | 0.00019 | √3 | -0.00003 | ± | 0.00011 |

## OPyC Density

The OPyC density was varied +0.30 and -0.15 g/cm$^3$ (3σ) from the nominal value of 1.85 g/cm$^3$ (Table 1.14) to determine the effective uncertainty in $k_{eff}$. These values are three times the bounding limit. The perturbation card, PERT, in MCNP was also employed in an independent analysis to determine the effective uncertainty. The larger uncertainty in $\Delta k_{eff}$ will be applied towards the total uncertainty analysis in Section 2.1.7. Results are shown in Table 2.31.

The total number of TRISO particles used in the core is approximately 861,140,000. For determining the random component of the uncertainty, the results in Table 2.31 would be divided by √861,140,000.

Table 2.31. Effect of Uncertainty in OPyC Density.

| Deviation | Δk | ± | $\sigma_{\Delta k}$ | Scaling Factor | $\Delta k_{eff}$ (1σ) | ± | $\sigma_{\Delta keff}$ |
|---|---|---|---|---|---|---|---|
| -0.15 g/cm$^3$ | -0.00028 | ± | 0.00019 | 3√3 | -0.00005 | ± | 0.00004 |
| +0.30 g/cm$^3$ | 0.00021 | ± | 0.00020 | 3√3 | 0.00004 | ± | 0.00004 |
| -0.05 g/cm$^3$ (PERT) | 0.00004 | ± | 0.00002 | √3 | 0.00002 | ± | 0.00001 |
| +0.10 g/cm$^3$ (PERT) | -0.00002 | ± | 0.00001 | √3 | -0.00001 | ± | 0.00001 |

## OPyC Impurity

The OPyC impurity was varied from 0-3 ppm by weight of equivalent natural-boron content to determine the bounding uncertainty in $k_{eff}$. The average value is 1.5 ppm by weight (Table 1.13). Results are shown in Table 2.32.

The uncertainty in the OPyC impurity is considered all systematic with no random component.

Table 2.32. Effect of Uncertainty in OPyC Impurity.

| Deviation | Δk | ± | $\sigma_{\Delta k}$ | Scaling Factor | $\Delta k_{eff}$ (1σ) | ± | $\sigma_{\Delta keff}$ |
|---|---|---|---|---|---|---|---|
| 0 ppm | 0.00000 | ± | 0.00020 | √3 | 0.00000 | ± | 0.00011 |
| 3 ppm | 0.00028 | ± | 0.00020 | √3 | 0.00016 | ± | 0.00011 |

## Overcoat Density

Because insufficient data is available for the final composition and density of the graphite overcoat, this layer is being treated with equal properties to that of the surrounding compact graphite matrix. The overcoat density was varied ±0.15 g/cm$^3$ to determine the effective uncertainty in $k_{eff}$. This value is three times the bounding limit. The perturbation card, PERT, in MCNP was also employed in an independent analysis to determine the effective uncertainty. The larger uncertainty in $\Delta k_{eff}$ will be applied towards the total uncertainty analysis in Section 2.1.7. Results are shown in Table 2.33.

The total number of TRISO particles used in the core is approximately 861,140,000. For determining the random component of the uncertainty, the results in Table 2.33 would be divided by √861,140,000.

Table 2.33. Effect of Uncertainty in Overcoat Density.

| Deviation | $\Delta k$ | ± | $\sigma_{\Delta k}$ | Scaling Factor | $\Delta k_{eff}$ (1σ) | ± | $\sigma_{\Delta keff}$ |
|---|---|---|---|---|---|---|---|
| -0.15 g/cm$^3$ | -0.00053 | ± | 0.00019 | 3√3 | -0.00010 | ± | 0.00004 |
| +0.15 g/cm$^3$ | 0.00051 | ± | 0.00019 | 3√3 | -0.00010 | ± | 0.00004 |
| -0.05 g/cm$^3$ (PERT) | 0.00013 | ± | 0.00002 | √3 | 0.00008 | ± | 0.00001 |
| +0.05 g/cm$^3$ (PERT) | -0.00013 | ± | 0.00002 | √3 | -0.00008 | ± | 0.00001 |

## Overcoat Composition

Because insufficient data is available for the final composition and density of the graphite overcoat, this layer is being treated with equal properties to that of the surrounding compact graphite matrix. In essence, the uncertainty has already been accounted for, as the surrounding graphite matrix has been characterized for uncertainties, and the overcoat has been demonstrated elsewhere to have negligible impact on the calculation of $k_{eff}$ when it is not explicitly modeled, but included in the surrounding matrix.[a]

## Overcoat Impurity

The overcoat impurity was varied from 0-5 ppm by weight of equivalent natural-boron content to determine the bounding uncertainty in $k_{eff}$. The average value of the coated fuel particles is 1.5 ppm by weight (Table 1.13); it is assumed that the overcoat would have a comparable impurity amount. The alternative is to use the impurity of the compact (matrix) material, which is 0.82 ppm by weight (Table 1.27). The larger amount is selected, i.e. 1.5 ppm. Results are shown in Table 2.34.

The uncertainty in the overcoat impurity is considered all systematic with no random component.

Table 2.34. Effect of Uncertainty in Overcoat Impurity.

| Deviation | $\Delta k$ | ± | $\sigma_{\Delta k}$ | Scaling Factor | $\Delta k_{eff}$ (1σ) | ± | $\sigma_{\Delta keff}$ |
|---|---|---|---|---|---|---|---|
| 0 ppm | 0.00066 | ± | 0.00020 | √3 | 0.00038 | ± | 0.00011 |
| 5 ppm | -0.00153 | ± | 0.00020 | √3 | -0.00088 | ± | 0.00011 |

### *2.1.3.2 Prismatic Fuel Compact*

## Density

The compact matrix density was varied ±0.15 g/cm$^3$ from the nominal value of 1.70 g/cm$^3$ (Table 1.14) to determine the effective uncertainty in $k_{eff}$. This value is three times the bounding limit. The perturbation card, PERT, in MCNP was also employed in an independent analysis to determine the effective uncertainty. The larger uncertainty in $\Delta k_{eff}$ will be applied towards the total uncertainty analysis in Section 2.1.7. Results are shown in Table 2.35.

[a] W. Ji, J. L. Conlin, W. R. Martin, J. C. Lee, and F. B. Brown, "Explicit Modeling of Particle Fuel for the Very-High Temperature Gas-Cooled Reactor," *Trans. Am. Nucl. Soc.*, **92** (June 2005).

The total number of fuel compacts used in the core is 66,780. For determining the random component of the uncertainty, the results in Table 2.35 would be divided by √66,780.

Table 2.35. Effect of Uncertainty in Compact Matrix Density.

| Deviation | $\Delta k$ | ± | $\sigma_{\Delta k}$ | Scaling Factor | $\Delta k_{eff}$ (1σ) | ± | $\sigma_{\Delta keff}$ |
|---|---|---|---|---|---|---|---|
| -0.15 g/cm$^3$ | -0.00023 | ± | 0.00020 | 3√3 | -0.00004 | ± | 0.00004 |
| +0.15 g/cm$^3$ | 0.00028 | ± | 0.00020 | 3√3 | 0.00005 | ± | 0.00004 |
| -0.05 g/cm$^3$ (PERT) | 0.00005 | ± | 0.00001 | √3 | 0.00003 | ± | 0.00001 |
| +0.05 g/cm$^3$ (PERT) | -0.00005 | ± | 0.00001 | √3 | -0.00003 | ± | 0.00001 |

## Impurity

The compact matrix impurity was varied from 0-5 ppm by weight of equivalent natural-boron content (Table 1.14) to determine the bounding uncertainty in $k_{eff}$. The nominal impurity is 0.82 ppm of natural boron by weight (Table 1.27). Results are shown in Table 2.36.

The uncertainty in the fuel compact impurity is considered all systematic with no random component.

Table 2.36. Effect of Uncertainty in Compact Matrix Impurity.

| Deviation | $\Delta k$ | ± | $\sigma_{\Delta k}$ | Scaling Factor | $\Delta k_{eff}$ (1σ) | ± | $\sigma_{\Delta keff}$ |
|---|---|---|---|---|---|---|---|
| 0 ppm | 0.00012 | ± | 0.00019 | √3 | 0.00007 | ± | 0.00011 |
| 5 ppm | -0.00070 | ± | 0.00019 | √3 | -0.00040 | ± | 0.00011 |

## Free Uranium Content

The free uranium fraction in the fuel compacts was varied between bounding limits of 0 and 0.00015 with a median of 0.000075 (see Table 1.14) to determine the effective uncertainty in $k_{eff}$. The bounding limit was tripled to 0.00045 in order to assess the uncertainty, but the effects were still negligible. The free uranium was assumed to be 100 % $^{235}$U so as to assess the maximum uncertainty. The free uranium content in the graphite compact was not included in the benchmark model and a bias was not applied because the effect was negligible. Results are shown in Table 2.37.

The uncertainty in the free uranium content is considered all systematic with no random component.

Table 2.37. Effect of Uncertainty in Compact Free Uranium Content.

| Deviation | $\Delta k$ | ± | $\sigma_{\Delta k}$ | Scaling Factor | $\Delta k_{eff}$ (1σ) | ± | $\sigma_{\Delta keff}$ |
|---|---|---|---|---|---|---|---|
| 75 ppm (median composition) | -0.00015 | ± | 0.00020 | 1 | NA | ± | NA |
| 150 ppm | 0.00002 | ± | 0.00020 | 2√3 | 0.00001 | ± | 0.00006 |
| 450 ppm | -0.00014 | ± | 0.00020 | 6√3 | -0.00001 | ± | 0.00002 |

### *2.1.3.3 Graphite Sleeves*

#### Density

The graphite sleeve density was varied an assumed ±0.03 g/cm$^3$ from the nominal value of 1.770 g/cm$^3$ (Table 1.27) to determine the effective uncertainty in $k_{eff}$. This value is the bounding limit. The graphite sleeves are composed of IG-110 graphite, and the assumed uncertainty of 0.03 g/cm$^3$ encompasses the range of reported densities for IG-110 graphite throughout Section 1. Results are shown in Table 2.38.

The total number of graphite sleeves used in the core is 4,770. For determining the random component of the uncertainty, the results in Table 2.38 would be divided by √4,770.

Table 2.38. Effect of Uncertainty in Graphite Sleeve Density.

| Deviation | Δk | ± | $\sigma_{\Delta k}$ | Scaling Factor | $\Delta k_{eff}$ (1σ) | ± | $\sigma_{\Delta keff}$ |
|---|---|---|---|---|---|---|---|
| -0.03 g/cm$^3$ | -0.00043 | ± | 0.00019 | √3 | -0.00025 | ± | 0.00011 |
| +0.03 g/cm$^3$ | 0.00037 | ± | 0.00020 | √3 | 0.00021 | ± | 0.00011 |

#### Impurity

The graphite sleeve impurity was varied from 0-1 ppm by weight of equivalent natural-boron content (Table 1.13) to determine the bounding uncertainty in $k_{eff}$. The nominal impurity is 0.37 ppm of natural boron by weight (Table 1.27). Results are shown in Table 2.39.

The uncertainty in the graphite sleeve impurity is considered all systematic with no random component.

Table 2.39. Effect of Uncertainty in Graphite Sleeve Impurity.

| Deviation | Δk | ± | $\sigma_{\Delta k}$ | Scaling Factor | $\Delta k_{eff}$ (1σ) | ± | $\sigma_{\Delta keff}$ |
|---|---|---|---|---|---|---|---|
| 0 ppm | 0.00058 | ± | 0.00019 | √3 | 0.00033 | ± | 0.00011 |
| 1 ppm | -0.00036 | ± | 0.00020 | √3 | -0.00021 | ± | 0.00011 |

### *2.1.3.4 Burnable Poisons*

#### Absorber Density

The absorber density was varied ±0.03 g/cm$^3$ from the average value of 1.8 g/cm$^3$ to determine the effective uncertainty in $k_{eff}$. This value is the bounding limit. The density uncertainty is based upon uncertainty typically found in sintered $B_4C$/C pellets (Table 1.29). Results are shown in Table 2.40.

The total number of burnable poison pellets used in the core is 5,520. For determining the random component of the uncertainty, the results in Table 2.40 would be divided by √5,520.

Table 2.40. Effect of Uncertainty in BP Absorber Density.

| Deviation | $\Delta k$ | ± | $\sigma_{\Delta k}$ | Scaling Factor | $\Delta k_{eff}$ (1σ) | ± | $\sigma_{\Delta keff}$ |
|---|---|---|---|---|---|---|---|
| -0.03 g/cm$^3$ | 0.00087 | ± | 0.00020 | √3 | 0.00050 | ± | 0.00011 |
| +0.03 g/cm$^3$ | -0.00096 | ± | 0.00020 | √3 | -0.00055 | ± | 0.00011 |

## Absorber Content

The uncertainty in the absorber content was not provided and the variation provided in Table 1.29 appears too excessive for the quantities utilized in the BP pellets. A variation of approximately ±0.25 % by weight was assumed for each of the two absorber pellet types, and the effective uncertainty in $k_{eff}$ was determined. This value is treated as a bounding limit. The uncertainty of ±0.25 % is based upon the assumption that burnable poison pellets with boron contents between 1.75 and 2.25 wt.% would have an average content of 2.00 wt.% and boron contents between 2.25 and 2.75 wt.% would have an average content of 2.50 wt.% bin. Further information would be necessary to reduce the range of the uncertainty. Results are shown in Table 2.41.

The total number of burnable poison pellets with weight percents of 2.00 and 2.50 used in the core are 3,600 and 1,920, respectively. For determining the random component of the uncertainty, the results in Table 2.41 would be divided by √3,600 and √1,920, respectively.

Table 2.41. Effect of Uncertainty in BP Absorber Content.

| Deviation | $\Delta k$ | ± | $\sigma_{\Delta k}$ | Scaling Factor | $\Delta k_{eff}$ (1σ) | ± | $\sigma_{\Delta keff}$ |
|---|---|---|---|---|---|---|---|
| -0.25 wt.% (2.00 wt.%) | 0.00605 | ± | 0.00020 | √3 | 0.00349 | ± | 0.00011 |
| +0.25 wt.% (2.00 wt.%) | -0.00499 | ± | 0.00020 | √3 | -0.00288 | ± | 0.00011 |
| -0.25 wt.% (2.50 wt.%) | 0.00183 | ± | 0.00020 | √3 | 0.00106 | ± | 0.00011 |
| +0.25 wt.% (2.50 wt.%) | -0.00152 | ± | 0.00019 | √3 | -0.00088 | ± | 0.00011 |

## Absorber Impurity

No information was available regarding any impurities present in the sintered $B_4C$/C material for the BP pellets. However, the impurity limits provided in Table 1.29 can be applied to approximate a rough estimate of the impact of additional impurities. Sodium and manganese were added with a concentrations of 100 and 10 ppm (by weight), respectively. Concentrations of 1000 ppm (by weight) of aluminum, silicon, calcium, and titanium were also included. The effective uncertainty in $k_{eff}$ was determined and is shown in Table 2.42. This value is treated as a bounding limit.

The uncertainty in the absorber impurity is considered all systematic with no random component.

Table 2.42. Effect of Uncertainty in Absorber Impurity.

| Deviation | $\Delta k$ | ± | $\sigma_{\Delta k}$ | Scaling Factor | $\Delta k_{eff}$ (1σ) | ± | $\sigma_{\Delta keff}$ |
|---|---|---|---|---|---|---|---|
| Added Impurities | -0.00052 | ± | 0.00020 | 2√3 | -0.00015 | ± | 0.00006 |

## Absorber Isotopic Abundance

According to the 16th edition of the Chart of the Nuclides, the natural isotopic abundance of $^{10}B$ has been measured between 19.1 and 20.3 at.% with a nominal value of 19.9 at.%.[a] The abundance of $^{10}B$ in the BPs was therefore evaluated at the minimum and maximum bounding values to determine the effective uncertainty in $k_{eff}$. Table 1.28 states that the abundance of $^{10}B$ is 18.7 wt.%, which correlates to approximately 20.2 at.%. Results are shown in Table 2.43. The benchmark model was evaluated at 19.9 at.%.

The uncertainty in the absorber isotopic abundance is considered all systematic with no random component.

Table 2.43. Effect of Uncertainty in BP Isotopic Abundance of $^{10}B$.

| Deviation | $\Delta k$ | ± | $\sigma_{\Delta k}$ | Scaling Factor | $\Delta k_{eff}$ (1σ) | ± | $\sigma_{\Delta keff}$ |
|---|---|---|---|---|---|---|---|
| 19.1% | 0.00267 | ± | 0.00019 | √3 | 0.00154 | ± | 0.00011 |
| 20.3% | -0.00093 | ± | 0.00020 | √3 | -0.00054 | ± | 0.00011 |

## Graphite Disk Density

An uncertainty in the density of the graphite disks was not reported. A variation of ±0.09 g/cm$^3$ was assumed and the effects on the uncertainty of $k_{eff}$ were determined. This value is three times the bounding limit. The graphite disks are composed of IG-110 graphite, and the assumed uncertainty of 0.03 g/cm$^3$ encompasses the range of reported densities for IG-110 graphite throughout Section 1. The perturbation card, PERT, in MCNP was also employed in an independent analysis to determine the effective uncertainty. The larger uncertainty in $\Delta k_{eff}$ will be applied towards the total uncertainty analysis in Section 2.1.7. Results are shown in Table 2.44.

The total number of graphite disks used in the core is 300. For determining the random component of the uncertainty, the results in Table 2.44 would be divided by √300.

Table 2.44. Effect of Uncertainty in Graphite Disk Density.

| Deviation | $\Delta k$ | ± | $\sigma_{\Delta k}$ | Scaling Factor | $\Delta k_{eff}$ (1σ) | ± | $\sigma_{\Delta keff}$ |
|---|---|---|---|---|---|---|---|
| -0.09 g/cm$^3$ | -0.00004 | ± | 0.00019 | 3√3 | -0.00001 | ± | 0.00004 |
| +0.09 g/cm$^3$ | -0.00004 | ± | 0.00020 | 3√3 | -0.00001 | ± | 0.00004 |
| -0.03 g/cm$^3$ (PERT) | 0.00000 | ± | 0.00000 | √3 | 0.00000 | ± | 0.00000 |
| +0.03 g/cm$^3$ (PERT) | 0.00000 | ± | 0.00000 | √3 | 0.00000 | ± | 0.00000 |

## Graphite Disk Impurity

The assumed graphite disk impurity was varied from 0-5 ppm by weight of equivalent natural-boron content to determine the bounding uncertainty in $k_{eff}$. The nominal impurity is 0.37 ppm of natural boron by weight (Table 1.28). Results are shown in Table 2.45.

[a] Nuclides and Isotopes: Chart of the Nuclides, 16th edition, (2002).

The uncertainty in the graphite disk impurity is considered all systematic with no random component.

Table 2.45. Effect of Uncertainty in Graphite Disk Impurity.

| Deviation | $\Delta k$ | ± | $\sigma_{\Delta k}$ | Scaling Factor | $\Delta k_{eff}$ (1σ) | ± | $\sigma_{\Delta keff}$ |
|---|---|---|---|---|---|---|---|
| 0 ppm | 0.00014 | ± | 0.00019 | √3 | 0.00008 | ± | 0.00011 |
| 5 ppm | -0.00009 | ± | 0.00020 | √3 | 0.00005 | ± | 0.00011 |

### *2.1.3.5 Control Rods*

**Absorber Density**

The absorber density was varied ±0.09 g/cm$^3$ from the nominal value of 1.9 g/cm$^3$ (Table 1.15) to determine the effective uncertainty in $k_{eff}$. This value is three times the bounding limit. The uncertainty is taken from Table 1.29. The perturbation card, PERT, in MCNP was also employed in an independent analysis to determine the effective uncertainty. The larger uncertainty in $\Delta k_{eff}$ will be applied towards the total uncertainty analysis in Section 2.1.7. Results are shown in Table 2.46.

The total number of control rod absorber pellets used in the core is approximately 975. The assumption is based on that only 13 control positions are approximately 30% inserted into the core. For determining the random component of the uncertainty, the results in Table 2.46 would be divided by √975.

Table 2.46. Effect of Uncertainty in CR Absorber Density.

| Deviation | $\Delta k$ | ± | $\sigma_{\Delta k}$ | Scaling Factor | $\Delta k_{eff}$ (1σ) | ± | $\sigma_{\Delta keff}$ |
|---|---|---|---|---|---|---|---|
| -0.09 g/cm$^3$ | 0.00028 | ± | 0.00020 | 3√3 | 0.00005 | ± | 0.00004 |
| +0.09 g/cm$^3$ | -0.00005 | ± | 0.00020 | 3√3 | 0.00001 | ± | 0.00004 |
| -0.03 g/cm$^3$ (PERT) | 0.00007 | ± | 0.00000 | √3 | 0.00004 | ± | 0.00000 |
| +0.03 g/cm$^3$ (PERT) | -0.00007 | ± | 0.00000 | √3 | -0.00004 | ± | 0.00000 |

**Absorber Content**

The boron content was varied ±9 wt.% from the nominal value of 30 wt.% (Table 1.15) and the effect on the uncertainty in $k_{eff}$ was determined. This value is three times the bounding limit. The uncertainty is taken from Table 1.29. Results are shown in Table 2.47.

The total number of control rod absorber pellets used in the core is approximately 975. The assumption is based on that only 13 control positions are approximately 30% inserted into the core. For determining the random component of the uncertainty, the results in Table 2.47 would be divided by √975.

Table 2.47. Effect of Uncertainty in CR Absorber Content.

| Deviation | $\Delta k$ | ± | $\sigma_{\Delta k}$ | Scaling Factor | $\Delta k_{eff}$ (1σ) | ± | $\sigma_{\Delta keff}$ |
|---|---|---|---|---|---|---|---|
| -9 wt.% | 0.00058 | ± | 0.00020 | 3√3 | 0.00011 | ± | 0.00004 |
| +9 wt.% | -0.00063 | ± | 0.00020 | 3√3 | -0.00012 | ± | 0.00004 |

## Absorber Impurity

No information was available regarding any impurities present in the sintered $B_4C/C$ material for the control rod absorbers. However, the impurity limits provided in Table 1.29 can be applied to approximate a rough estimate of the impact of additional impurities. Sodium and manganese were added with a concentrations of 100 and 10 ppm (by weight), respectively. Concentrations of 1000 ppm (by weight) of aluminum, silicon, calcium, and titanium were also included. The effective uncertainty in $k_{eff}$ was determined and is shown in Table 2.48. This value is treated as a bounding limit.

The uncertainty in the absorber impurity is considered all systematic with no random component.

Table 2.48. Effect of Uncertainty in Absorber Impurity.

| Deviation | $\Delta k$ | $\pm$ | $\sigma_{\Delta k}$ | Scaling Factor | $\Delta k_{eff}$ (1$\sigma$) | $\pm$ | $\sigma_{\Delta keff}$ |
|---|---|---|---|---|---|---|---|
| Added Impurities | -0.00052 | ± | 0.00019 | 2√3 | -0.00015 | ± | 0.00006 |

## Absorber Isotopic Abundance

According to the 16th edition of the Chart of the Nuclides, the natural isotopic abundance of $^{10}B$ has been measured between 19.1 and 20.3% with a nominal value of 19.9%.[a] The abundance of $^{10}B$ in the control rods was therefore evaluated at the minimum and maximum bounding values to determine the effective uncertainty in $k_{eff}$. Table 1.28 states that the abundance of $^{10}B$ is 18.7 wt.%, which correlates to approximately 20.2 at.%. The model was not evaluated for a $^{10}B$ abundance of 18.7 wt.%. Results are shown in Table 2.49. The benchmark model was evaluated at 19.9 at.%.

The uncertainty in the absorber isotopic abundance is considered all systematic with no random component.

Table 2.49. Effect of Uncertainty in CR Isotopic Abundance of $^{10}B$.

| Deviation | $\Delta k$ | $\pm$ | $\sigma_{\Delta k}$ | Scaling Factor | $\Delta k_{eff}$ (1$\sigma$) | $\pm$ | $\sigma_{\Delta keff}$ |
|---|---|---|---|---|---|---|---|
| 19.1% | 0.00018 | ± | 0.00019 | √3 | 0.00010 | ± | 0.00011 |
| 20.3% | -0.00017 | ± | 0.00020 | √3 | -0.00010 | ± | 0.00011 |

## Clad Density

Two references were compared to confirm the composition and density of the Alloy 800H material.[b,c] The density of Alloy 800H is taken to be 8.03 g/cm$^3$ with an estimated uncertainty of ±0.03 g/cm$^3$, which is the difference between the reported density values in the two references. This value is the bounding limit. The effective change in $k_{eff}$ was determined. Results are shown in Table 2.50.

[a] Nuclides and Isotopes: Chart of the Nuclides, 16th edition, (2002).

[b] Specification Sheet: Alloy 800, 800H, and 800AT, Sandmeyer Steel Company (April 2004).

[c] Material Characteristics: Alloy 800H, PhilipCornes, http://www.cornes.com.sg/a800h.htm (Accessed August 5, 2008).

The total number of control rod sections used in the core is approximately 97.5. The assumption is based on that only 13 control positions are approximately 30% inserted into the core. For determining the random component of the uncertainty, the results in Table 2.50 would be divided by √97.5.

Table 2.50. Effect of Uncertainty in Clad Density.

| Deviation | $\Delta k$ | ± | $\sigma_{\Delta k}$ | Scaling Factor | $\Delta k_{eff}$ (1σ) | ± | $\sigma_{\Delta keff}$ |
|---|---|---|---|---|---|---|---|
| -0.03 g/cm$^3$ (1σ) | 0.00026 | ± | 0.00020 | √3 | 0.00015 | ± | 0.00011 |
| +0.03 g/cm$^3$ (1σ) | 0.00020 | ± | 0.00019 | √3 | 0.00012 | ± | 0.00011 |

## Clad Composition

The clad composition used in the benchmark model is derived from the aforementioned references for Alloy 800H, where the second reference provides a composition range and the first reference provides a nominal composition. A summary of the composition of Alloy 800H is provided in Table 2.51. The nominal distribution is used in the benchmark model. The composition of the clad material was varied from the nominal value. In the first case, the minimum compositions of all elements were used with iron as the remaining balance. The second case uses the maximum weights of all the elements with a reduction in the iron content until the minimum value is achieved; then nickel is reduced to achieve a total of 100 wt.%. The effective change in $k_{eff}$ for these two cases was determined. Results are shown in Table 2.52.

The uncertainty in the clad composition is considered all systematic with no random component.

Table 2.51. Composition of Alloy 800H.

| Element | Minimum wt.% | Maximum wt.% | Nominal wt.% |
|---|---|---|---|
| C | 0.06 | 0.1 | 0.08 |
| Al | 0.15 | 0.6 | 0.375 |
| Si | -- | 1.0 | 0.35 |
| P | -- | -- | 0.02 |
| S | -- | 0.015 | 0.01 |
| Ti | 0.15 | 0.6 | 0.375 |
| Cr | 19 | 23 | 21 |
| Mn | -- | 1.5 | 1 |
| Fe | 39.5 | -- | 43.99 |
| Ni | 30 | 35 | 32.5 |
| Cu | -- | 0.75 | 0.3 |
| Total | -- | -- | 100.000 |

Table 2.52. Effect of Uncertainty in Clad Composition.

| Deviation | $\Delta k$ | ± | $\sigma_{\Delta k}$ | Scaling Factor | $\Delta k_{eff}$ (1σ) | ± | $\sigma_{\Delta keff}$ |
|---|---|---|---|---|---|---|---|
| Minimum Fe | 0.00012 | ± | 0.00020 | √3 | 0.00007 | ± | 0.00011 |
| Maximum Fe | 0.00001 | ± | 0.00020 | √3 | 0.00001 | ± | 0.00011 |

## Clad Impurity

No information was available regarding any impurities present in the Alloy 800H metal. Concentrations of minor and trace elements found commonly in nickel alloy[a] were added to the clad material in the benchmark model (where neutron cross-section libraries were available) to determine the effective uncertainty in $k_{eff}$. Because these impurities are not necessarily those that would have been in the alloy, and the total amount is ~10 wt.%, the atom density of the primary alloy composition was not reduced. Thus the total atom density of the material was increased by including the additional materials. A list of the additional impurities is shown in Table 2.53, and results are shown in Table 2.54. This value is treated as a bounding limit.

The uncertainty in the clad impurity is considered all systematic with no random component.

[a] J. H. Zaidi, S. Waheed, and S. Ahmed, "Determination of Trace Impurities in Nickel-Based Alloy using Neutron Activation Analysis," *J. Radioanal. Nucl. Ch.*, **242**: 259-263 (1999).

Table 2.53. Concentration (by weight) of Minor and Trace Elements in Nickel Alloy.

| Element | Concentration | Library Available? | Element | Concentration | Library Available? |
|---|---|---|---|---|---|
| As | 63.7 µg/g | Yes | Mo | 9.8 µg/g | Yes |
| Ba | 215 µg/g | Yes | Na | 0.45 % | Yes |
| Br | 8.9 µg/g | Yes | Nd | 16.2 µg/g | Yes |
| Ca | 5.9 % | Yes | Rb | 24 ng/g | Yes |
| Ce | 0.33 % | No | Sb | 2.2 µg/g | Yes |
| Co | 9.96 µg/g | Yes | Sc | 0.13 µg/g | Yes |
| Cs | 4.34 µg/g | Yes | Se | 0.16 µg/g | No |
| Dy | 6.12 µg/g | No | Sm | 0.23 µg/g | Yes |
| Er | 2.8 µg/g | No | Sn | 0.25 µg/g | Yes |
| Eu | 1.17 µg/g | Yes | Sr | 371 µg/g | No |
| Ga | 107.5 µg/g | Yes | Ta | 1.21 µg/g | Yes |
| Gd | 1.7 µg/g | Yes | Tb | 1.24 µg/g | No |
| Hf | 19.5 µg/g | Yes | Th | 18.3 µg/g | Yes |
| Hg | 6 ng/g | Yes | U | 4.3 µg/g | Yes |
| In | 245 ng/g | Yes | Yb | 2.48 µg/g | No |
| La | 2.34 µg/g | No | V | 0.75 % | Yes |
| Lu | 1.16 µg/g | Yes | Zn | 93.4 µg/g | Yes |
| Mg | 2.14 % | Yes | | | |

Table 2.54. Effect of Uncertainty in Clad Impurity.

| Deviation | $\Delta k$ | ± | $\sigma_{\Delta k}$ | Scaling Factor | $\Delta k_{eff}$ (1σ) | ± | $\sigma_{\Delta keff}$ |
|---|---|---|---|---|---|---|---|
| Added Impurities | -0.00014 | ± | 0.00020 | 2√3 | -0.00004 | ± | 0.00006 |

### *2.1.3.6 Instrumentation*

Insufficient information is available to model and comprehensively evaluate the uncertainties and biases related to the utility of instrumentation in the HTTR. A basic analysis of the general description of the instrumentation was performed, as discussed in Section 2.1.2.6.

### *2.1.3.7 Graphite Blocks*

**Density**

The IG-110 graphite density was varied ±0.04 g/cm$^3$ from a nominal value selected as 1.76 g/cm$^3$ (ranging from 1.75 to 1.78 g/cm$^3$, Tables 1.13, 1.19, and 1.27) to determine the effective uncertainty in $k_{eff}$. A variation of 0.03 g/cm$^3$ accounts for the difference in density between the various samples of IG-110 blocks, and a variation of 0.01 g/cm$^3$ is assumed to encompass the variability in the volume fraction caused by eliminating various features such as the dowels, sockets, fuel handling position, and ridged

features on the fuel rods. The assumed uncertainty of 0.03 g/cm$^3$ for the IG-110 graphite encompasses the range of reported densities found throughout Section 1. Results are shown in Table 2.55. This value is treated as a bounding limit.

Previous results[a] state that a graphite weight difference of less than 1% should result in a bias of -0.3 % Δk/k. Scaling the results provided in Table 2.55 provides an uncertainty of approximately 0.245 % Δk/k, comparable to the previously published information.

The total number of graphite blocks used in the core is 549. For determining the random component of the uncertainty, the results in Table 2.55 would be divided by √549.

Table 2.55. Effect of Uncertainty in IG-110 Density in Graphite Blocks.

| Deviation | Δk | ± | $\sigma_{\Delta k}$ | Scaling Factor | $\Delta k_{eff}$ (1σ) | ± | $\sigma_{\Delta keff}$ |
|---|---|---|---|---|---|---|---|
| -0.04 g/cm$^3$ | -0.00562 | ± | 0.00020 | √3 | -0.00324 | ± | 0.00011 |
| +0.04 g/cm$^3$ | 0.00550 | ± | 0.00019 | √3 | 0.00318 | ± | 0.00011 |

## Impurity

The graphite block impurity was varied from 0-3 ppm by weight of equivalent natural-boron content (Table 1.13), where the 3 ppm value is 3 times the bounding limit, to determine the bounding uncertainty in $k_{eff}$. The nominal impurity is 0.40 ppm or 0.37 ppm of natural boron by weight for the fuel/control blocks and reflector blocks, respectively (Table 1.27). However, characterization of the graphite first loaded into the reactor determined the equivalent boron content for IG-110 graphite to be 0.59 ppm.[b] This latter value is used in the benchmark model. Results are shown in Table 2.56.

It has been reported that the estimated air content in the graphite blocks would provide -0.4 % Δk/k to the computational model.[a] Reference 1 states that an uncertainty factor of ~0.52 % Δk/k should be used. The inclusion of air in the benchmark model did not produce a noticeable change in reactivity; this was done by modeling air, at atmospheric pressure, distributed throughout the block in the quantity equivalent to the volume fraction to the void space generated for the dowels, sockets, fuel handling position, and other miscellaneous block features. However, it is unclear exactly how much air could be entrapped within the graphite blocks. Air can be entrapped during the graphitization process or absorbed onto the graphite surface. Typically, significant contribution to the equivalent boron content in a graphite block is caused by impurities in the graphite. Methods to measure the impurity content in graphite have improved over the past several years, and the impurity content of the HTTR graphite may need to be reassessed.[c]

Graphite is also somewhat hydroscopic and can absorb water into its pores after fabrication. At low temperatures, the water would still be present in the graphite. Information regarding possible water content in the graphite blocks is unavailable, however.

The uncertainty in the graphite block impurity is considered all systematic with no random component.

---

[a] Fujimoto, N., Nakano, M., Takeuchi, M., Fujisaki, S., and Yamashita, K., "Start-Up Core Physics Tests of High Temperature Engineering Test Reactor (HTTR), (II): First Criticality by an Annular Form Fuel Loading and Its Criticality Prediction Method," *J. Atomic Energy Society Japan*, **42**(5), 458-464 (2000).

[b] Sumita, J., Shibata, T., Hanawa, S., Ishihara, M., Iyoku, T., and Sawa, K., "Characteristics of First Loaded IG-110 Graphite in HTTR Core," *JAEA Technol 2006-048*, October (2006).

[c] Private communication with Rob Bratton at Idaho National Laboratory (November 20, 2008).

Table 2.56. Effect of Uncertainty in IG-110 Impurity in Graphite Blocks.

| Deviation | $\Delta k$ | ± | $\sigma_{\Delta k}$ | Scaling Factor | $\Delta k_{eff}$ (1σ) | ± | $\sigma_{\Delta keff}$ |
|---|---|---|---|---|---|---|---|
| 0 ppm | 0.00848 | ± | 0.00016 | √3 | 0.00490 | ± | 0.00009 |
| 3 ppm | -0.03036 | ± | 0.00016 | 3√3 | -0.00584 | ± | 0.00003 |

### *2.1.3.8 Permanent Reflectors*

**Density**

The PGX graphite density was varied ±0.04 g/cm$^3$ from a nominal value selected as 1.73 g/cm$^3$ (ranging from 1.73 to 1.74 g/cm$^3$, Tables 1.19, 1.20, and 1.27) to determine the effective uncertainty in $k_{eff}$. A variation of 0.03 g/cm$^3$ accounts for the PGX, and a variation of 0.01 g/cm$^3$ is assumed to encompass the variability in the volume fraction, which is not provided. The assumed uncertainty of 0.03 g/cm$^3$ for the PGX graphite encompasses the range of reported densities found throughout Section 1. Results are shown in Table 2.57. This value is treated as a bounding limit.

The total number of permanent reflector blocks used in the core is 96. For determining the random component of the uncertainty, the results in Table 2.57 would be divided by √96.

Table 2.57. Effect of Uncertainty in PGX Density in Permanent Reflector.

| Deviation | $\Delta k$ | ± | $\sigma_{\Delta k}$ | Scaling Factor | $\Delta k_{eff}$ (1σ) | ± | $\sigma_{\Delta keff}$ |
|---|---|---|---|---|---|---|---|
| -0.04 g/cm$^3$ | -0.00031 | ± | 0.00020 | √3 | -0.00018 | ± | 0.00011 |
| +0.04 g/cm$^3$ | 0.00057 | ± | 0.00020 | √3 | 0.00033 | ± | 0.00011 |

**Impurity**

The permanent reflector impurity was varied from 0-5 ppm by weight of equivalent natural-boron content (Table 1.16) to determine the bounding uncertainty in $k_{eff}$. The nominal impurity is 1.91 ppm of natural boron by weight (Table 1.27). Results are shown in Table 2.58.

The uncertainty in the permanent reflector impurity is considered all systematic with no random component.

Table 2.58. Effect of Uncertainty in PGX Impurity in Permanent Reflector.

| Deviation | $\Delta k$ | ± | $\sigma_{\Delta k}$ | Scaling Factor | $\Delta k_{eff}$ (1σ) | ± | $\sigma_{\Delta keff}$ |
|---|---|---|---|---|---|---|---|
| 0 ppm | 0.00411 | ± | 0.00019 | √3 | 0.00237 | ± | 0.00011 |
| 5 ppm | -0.00518 | ± | 0.00020 | √3 | -0.00299 | ± | 0.00011 |

### *2.1.3.9 Dummy Blocks*

The 30-fuel-column core does not contain dummy blocks.

*2.1.3.10 Helium Coolant*

## Density

The density of helium gas was evaluated using the ideal gas law, PV=nRT, at a pressure of 1 atm and temperature of 25 ºC. The helium coolant was modeled with a atom density of $2.4616 \times 10^{-4}$ atoms/b-cm (mass density of $1.6361 \times 10^{-4}$ g/cm$^3$).

The helium density was varied approximately ±3.5% (1σ) to determine the effective uncertainty in $k_{eff}$. Results are shown in Table 2.59. The perturbation card, PERT, in MCNP was also employed in an independent analysis to determine the effective uncertainty. The larger uncertainty in $\Delta k_{eff}$ will be applied towards the total uncertainty analysis in Section 2.1.7.

The effect of neglecting the helium content and replacing it with an empty void was also performed. The effective change in change in $k_{eff}$ was determined. Results are shown in Table 2.59.

The uncertainty in the helium density is considered all systematic with no random component.

Table 2.59. Effect of Uncertainty in Helium Coolant Density.

| Deviation | Δk | ± | $\sigma_{\Delta k}$ | Scaling Factor | $\Delta k_{eff}$ (1σ) | ± | $\sigma_{\Delta keff}$ |
|---|---|---|---|---|---|---|---|
| void | -0.00035 | ± | 0.00020 | 1 | NA | ± | NA |
| -3.5% (1σ) | -0.00030 | ± | 0.00020 | 1 | -0.00030 | ± | 0.00020 |
| +3.5% (1σ) | 0.00007 | ± | 0.00020 | 1 | 0.00007 | ± | 0.00020 |
| void (PERT) | -0.00002 | ± | 0.00001 | 1 | NA | ± | NA |
| -3.5% (1σ, PERT) | 0.00000 | ± | 0.00000 | 1 | 0.00000 | ± | 0.00000 |
| +3.5% (1σ, PERT) | 0.00000 | ± | 0.00000 | 1 | 0.00000 | ± | 0.00000 |

## Impurity

The upper impurity limit in the helium coolant was included in the model to determine its effect upon the uncertainty in $k_{eff}$. Upper concentration limits from Table 1.10 were included although the impurity content in helium at room temperature would be considerably less; therefore it will be treated as a bounding limit. The bounding limit was tripled for each component in order to assess the uncertainty, but the effects were still negligible. Results are shown in Table 2.60.

The uncertainty in the helium impurity is considered all systematic with no random component.

Table 2.60. Effect of Uncertainty in Helium Coolant Impurity.

| Deviation | Δk | ± | $\sigma_{\Delta k}$ | Scaling Factor | $\Delta k_{eff}$ (1σ) | ± | $\sigma_{\Delta keff}$ |
|---|---|---|---|---|---|---|---|
| max impurities | -0.00008 | ± | 0.00019 | $2\sqrt{3}$ | -0.00002 | ± | 0.00006 |
| 3 × maximum | -0.00004 | ± | 0.00019 | $6\sqrt{3}$ | 0.00000 | ± | 0.00002 |

### 2.1.4 Additional Analyses

#### *2.1.4.1 Room Return*

Insufficient information is available to model and evaluate the uncertainties and biases related to any room return effects in the HTTR. Shielding plugs, plates, and blocks are incorporated within the HTTR vessel and would considerably reduce room return effects from the surrounding reactor vessel, reactor internals, and HTTR infrastructure and facility due to the content of sintered $B_4C/C$ neutron absorber.

A conservative analysis of the HTTR benchmark model surrounded by shielding material, steel, and concrete provided an insignificant effect because the slight increase in the effective multiplication factor was below the statistical uncertainty of the analysis. Actual room return effects would be assumed quite negligible.

#### *2.1.4.2 TRISO Particle Placement*

Currently MCNP has a limited capability for modeling stochastic geometries. The HTTR core is unique in the fact that it has 12 different enrichments throughout the core. MCNP could effectively model randomness for only two types of TRISO particles at once because the URAN card used to create stochastic models has a maximum limit of two universes per model. Therefore a complete analysis of the random particle placement of the fuel particles in a complete core model can only be evaluated by creating six models, each model having random particle placement of particles of two enrichment types per input deck. The summation of the six $\Delta k_{eff}$ values yields a total uncertainty of 0.00095±0.00039, or 0.10±0.04 $\%\Delta k_{eff}$.

In a separate, bounding, approximation of the uncertainty in the effects of random TRISO placement, the fuel compacts were modeled with a uniform cell lattice of TRISO particles (including partial particles). Figures 2.5 and 2.6 show a cross section of the fuel compacts with ordered and uniformly-filled TRISO distributions, respectively. The effective difference in the multiplication factor is shown in Table 2.61. The 30 vol. % packing fraction and uranium mass per fuel rod is conserved in this comparison. In order to conserve the uranium mass, the volume was estimated for the uranium kernels along the edges of the fuel compacts (using linear approximation of the cylindrical surface and spherical dome formulas)[a] to determine the approximate fuel content in each compact. Then the uniform cell lattice was adjusted such that the modeled fuel content matched the reported HTTR value. The reduction in resonance shielding effects in partial particles (i.e. fuel kernels not completely surrounded by graphite coatings) along the edges is not considered in this analysis. There is a slight mass uncertainty that is unaccounted for in this approximation. Because this is a bounding application, the result in Table 2.61 needs to be divided by the square-root of three.

An analysis performed at the University of Michigan to look at the effects of explicitly modeling particle fuel in a very-high temperature gas-cooled reactor found that in a full core model, the effect of modeling with a uniform lattice and clipped TRISO particles would have a reduced $k_{eff}$ of approximately 0.1 %.[b] The results shown in Table 2.61 and for the approach presented at the beginning of this section are approximately 0.1 %. The value calculated in Table 2.61 is used to represent the uncertainty in random TRISO particle placement in the HTTR. This uncertainty is treated as 100% systematic to capture the complete uncertainty in random particle placement.

A driver for this phenomenom might be explained by the Dancoff-Ginsberg factor, where in a lattice, the closer the lumps of fissionable material are to each other, the greater the shadowing effect and the smaller

[a] "Spherical and Ellipsoid Dome Formulas," Monolithic Dome Institute, Italy, Texas (2001).

[b] W. Ji, J. L. Conlin, W. R. Martin, J. C. Lee, and F. B. Brown, "Explicit Modeling of Particle Fuel for the Very-High Temperature Gas-Cooled Reactor," *Trans. Am. Nucl. Soc.*, **92** (June 2005).

the resonance integral for the interacting lattice, which results in an increase in the non-leakage probability and net increase in $k_{eff}$.[a]

A competing argument is that self-shielding and shadowing effects are quite negligible (2nd-order effect) and that small variations in fuel conservation actually lead to the difference in the calculated value of $k_{eff}$.[b,c] Further discussion of the relevance of fuel particle parameters upon the reactivity of the system can be read elsewhere.[d] It remains up to the user's discretion to assess whether and how an uncertainty might apply to the modeling of this reactor system.

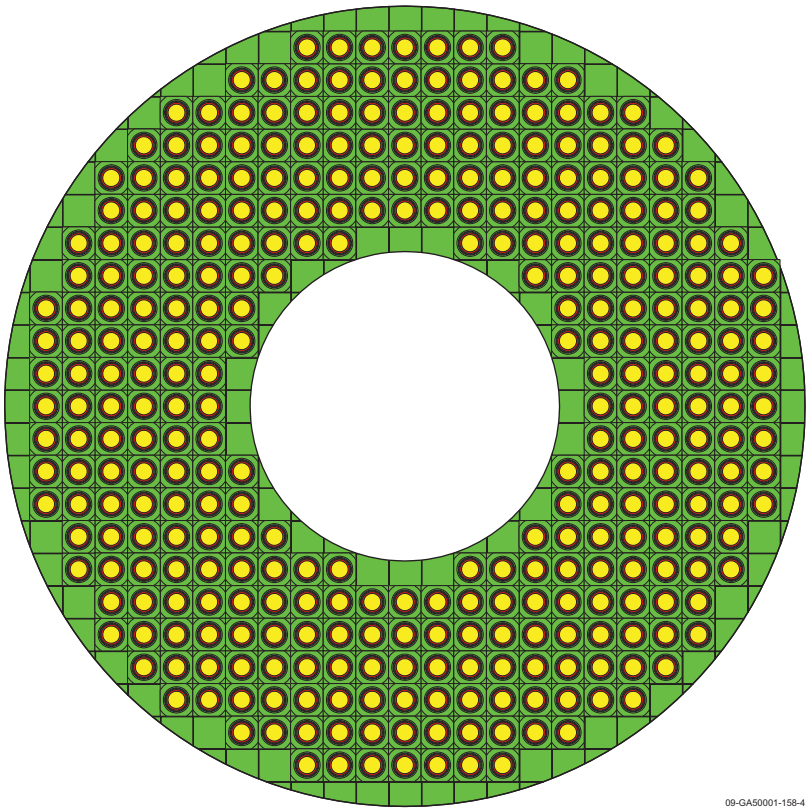


Figure 2.5. MCNP Ordered TRISO Lattice within the Fuel Compacts.

[a] J. R. Lamarsh, *Introduction to Nuclear Reactor Theory*, Addison-Wesley Publishing Company, Reading, Massachusetts, pp. 399-400 (1966).

[b] Personal communication between Luka Snoj and Forrest Brown from Los Alamos National Laboratory (November 20, 2008).

[c] F. B. Brown, "Monte Carlo Advances & Challenges," *Proc. Frederic Joliot and Otto Hahn Summer School 2005*, Karlsruhe, Germany, August 24 – September 2 (2005).

[d] L. Snoj and M. Ravnik, "Effect of Fuel Particles' Size and Position Variations on Multiplication Factor in Pebble-Bed Nuclear Reactors," *Kerntechnik*, **72** (2007).

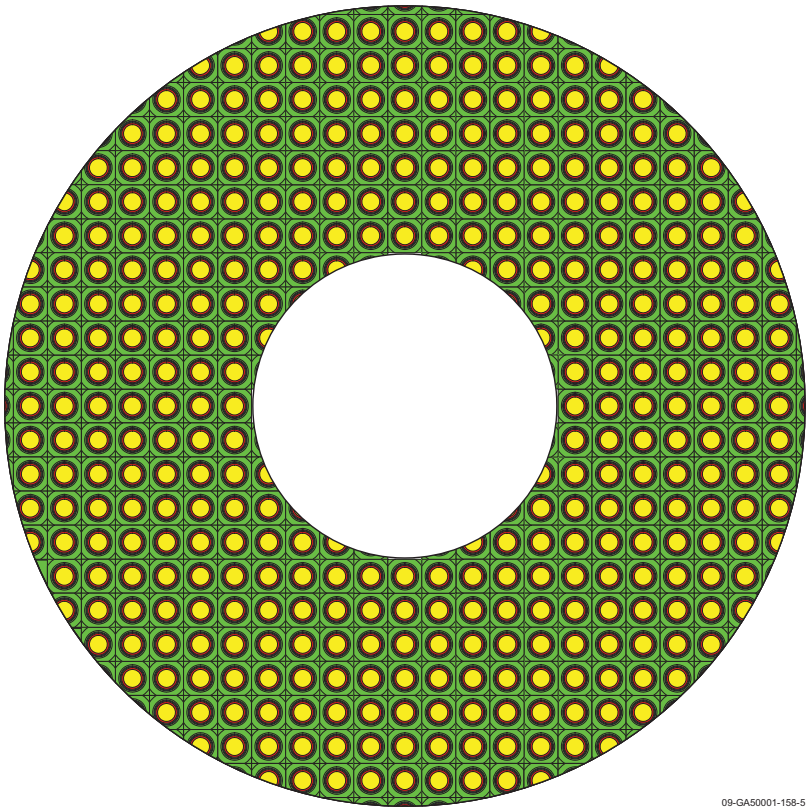


Figure 2.6. MCNP Uniformly-Filled TRISO Lattice within the Fuel Compacts.

Table 2.61. Comparison of Uniform and Organized TRISO Fill in Fuel Compacts.

| Organized Distribution (Figure 2.5) | | | Uniform Fill (Figure 2.6) | | | Bounding Difference | | | 1σ Uncertainty | | |
|---|---|---|---|---|---|---|---|---|---|---|---|
| $k_{eff}$ | ± | $\sigma_k$ | $k_{eff}$ | ± | $\sigma_k$ | $\Delta k$ | ± | $\sigma_{\Delta k}$ | $\Delta k$ | ± | $\sigma_{\Delta k}$ |
| 1.02532 | ± | 0.00014 | 1.02367 | ± | 0.00014 | 0.00165 | ± | 0.00020 | 0.00095 | ± | 0.00011 |

### *2.1.4.3 Block Stack Alignment*

As discussed in the previous section, MCNP has a limited capability for modeling stochastic geometries for systems with multiple unique components. Whereas the HTTR core model is comprised of 61 columns each containing 9 bricks, a comprehensive analysis of the stochastic nature of block stacking could not be evaluated.

### *2.1.4.4 MCNP Random Number Generation*

The random number seed was changed for the benchmark model and compared with the original to determine the uncertainty in utilizing Monte Carlo analysis methods. Results are shown in Table 2.62. The uncertainty in the average is the standard deviation of the six averaged eigenvalues.

Table 2.62. Analysis of the Effect of Random Number Generation in MCNP.

| Seed | $k_{eff}$ | ± | $\sigma_{keff}$ |
|---|---|---|---|
| 123456787 | 1.02544 | ± | 0.00014 |
| 9876543279 | 1.02504 | ± | 0.00014 |
| 198765432799 | 1.02545 | ± | 0.00013 |
| 17623486105893 | 1.02559 | ± | 0.00014 |
| 19073486328125[(a)] | 1.02532 | ± | 0.00014 |
| 32160231045432797 | 1.02545 | ± | 0.00014 |
| Average | 1.02538 | ± | 0.00019 |

(a) Primary seed value for evaluation.

#### *2.1.4.5 Simplification Biases and Uncertainties*

Whereas insufficient information is publicly available, a comprehensive analysis of simplification biases and their respective uncertainties could not be appropriately assessed. Currently only an approximate bias for the instrumentation components in the reactor has been assessed (Section 2.1.2.6). As additional information becomes available, highly detailed and simplified benchmark models can be generated and their biases can be adequately determined.

### 2.1.5 Systematic Biases and Uncertainties

There was no information regarding systematic biases or uncertainties publicly available for these experiments. Previous efforts of the Japanese in analyzing the 19-fuel-column core (Case 1) obtained an analytical excess reactivity of 2.7 % Δk/k, with an estimated Monte Carlo calculation overestimate of 1.2 % Δk/k.[a] Additional information would be necessary to completely verify published results to generate an analytical bias for MCNP.

As discussed at the beginning of Section 2, all uncertainties are treated as 25% systematic, with no reduction in uncertainty due to the multiplicity of core components, and as 75% random.

### 2.1.6 Analysis of HTTR Uranium Content

The parameters (dimensions, density, etc.) of the TRISO particles fabricated during the manufacturing process are very normally distributed, except for any defective particles. The fuel content, or mass, is the most well-known specification and measured with the highest accuracy.[b]

Because of the overspecification of the TRISO particles in Table 1.14 and the correlation of uranium kernel diameter, density, packing fraction, and mass, the effect of the uncertainties in the kernel diameter, density, and packing fraction are not included in the total uncertainty. The uranium content of the fuel rods of 188.58 ± 5.66 g (Table 1.14) is the parameter most likely known with the greatest accuracy. Therefore, the diameter of the kernels will be fixed at 600 μm, and the density will be varied ± 0.32 g/cm$^3$ (bounding limit) from a nominal value of 10.39 g/cm$^3$ to determine the effective uncertainty in $k_{eff}$

[a] Fujimoto, N., Nakano, M., Takeuchi, M., Fujisaki, S., and Yamashita, K., "Start-Up Core Physics Tests of High Temperature Engineering Test Reactor (HTTR), (II): First Criticality by an Annular Form Fuel Loading and Its Criticality Prediction Method," *J. Atomic Energy Society Japan*, **42**(5), 458-464 (2000).

[b] Personal communication with David Petti from the Idaho National Laboratory (September 28, 2009).

due to the uranium mass uncertainty. Results derived from those shown in Table 2.23 are shown in Table 2.63.

The total number of fuel rods used in the core is approximately 4,770. For determining the random component of the uncertainty, the results in Table 2.63 would be divided by √4,770.

Table 2.63. Effect of Uncertainty in Uranium Mass.

| Deviation | $\Delta k$ | ± | $\sigma_{\Delta k}$ | Scaling Factor | $\Delta k_{eff}$ (1σ) | ± | $\sigma_{\Delta keff}$ |
|---|---|---|---|---|---|---|---|
| -0.26 g/cm$^3$ | -0.00374 | ± | 0.00019 | × (0.32/0.26)/√3 | -0.00266 | ± | 0.00014 |
| +0.26 g/cm$^3$ | 0.00369 | ± | 0.00020 | × (0.32/0.26)/√3 | 0.00262 | ± | 0.00014 |

### 2.1.7 Total Experimental Uncertainty (Fully-Loaded Core Critical)

A compilation of the total evaluated uncertainty in the HTTR model is shown in Table 2.64 for the 30-fuel-column core design. As discussed earlier, each of the evaluated uncertainties is divided into a systematic component (25 %) and random component (75 %), where appropriate. The random component is then divided by the square-root of the number of random objects. The root-mean square of each subcomponent is taken to determine the uncertainty in either the random or systematic components of the total evaluated uncertainty. The total evaluated uncertainty is then the root-mean square of the random and systematic uncertainties.

Uncertainties less than 0.00001 are reported as negligible (neg). When calculated uncertainties in $\Delta k_{eff}$ are less than their statistical uncertainties, the statistical uncertainties are used in the calculation of the total uncertainty. Table listings where calculations were not performed or otherwise not available are labeled with 'NA'. For uncertainties where a random component is not applicable, the uncertainty is denoted with '--'.

The most significant contributions to the overall uncertainty from the systematic uncertainties include the impurities in the IG-110 graphite blocks and impurities in the PGX graphite blocks. All uncertainties providing at least 0.1 % $\Delta k_{eff}$ are highlighted in gray in Table 2.64. All of the random uncertainties are less than 0.1 % $\Delta k_{eff}$. The overall uncertainty is less than 1% $\Delta k_{eff}$; it is expected that the total uncertainty will be reduced as additional parameters that characterize the HTTR are obtained.

Table 2.64. Total Experimental Uncertainty of the Fully-Loaded 30-Fuel-Column Core.

| Varied Parameter | Systematic Uncertainty | | Random Uncertainty | |
|---|---|---|---|---|
| | $-\Delta k_{eff}$ (1σ) | $+\Delta k_{eff}$ (1σ) | $-\Delta k_{eff}$ (1σ) | $+\Delta k_{eff}$ (1σ) |
| Temperature | 0.00013 | -0.00013 | -- | -- |
| Control Rod Positions | -0.00013 | 0.00016 | -0.00010 | 0.00012 |
| Measured Value of $k_{eff}$ | neg | neg | neg | neg |
| Kernel Diameter | Correlated Parameter (see Section 2.1.6) | | | |
| Buffer Diameter | 0.00003 | neg | neg | neg |
| IPyC Diameter | neg | neg | neg | neg |
| SiC Diameter | 0.00013 | -0.00009 | neg | neg |
| OPyC Diameter | neg | neg | neg | neg |
| Overcoat Diameter | NA | NA | NA | NA |
| Compact Inner Diameter | 0.00004 | 0.00004 | neg | neg |
| Compact Outer Diameter | -0.00003 | 0.00008 | neg | neg |
| Compact Height | neg | neg | neg | neg |
| Compact Packing Fraction | Correlated Parameter (see Section 2.1.6) | | | |
| Sleeve Inner Diameter | 0.00004 | -0.00005 | neg | neg |
| Sleeve Outer Diameter | -0.00006 | 0.00006 | neg | neg |
| Sleeve Height | 0.00001 | neg | neg | neg |
| BP Diameter | 0.00020 | -0.00018 | neg | neg |
| BP Stack Height | 0.00011 | -0.00009 | 0.00001 | -0.00001 |
| BP Hole Diameter | 0.00002 | -0.00001 | neg | neg |
| Graphite Disk Diameter | neg | neg | neg | neg |
| Disk Stack Height | neg | 0.00003 | neg | neg |
| CR Absorber Inner Diameter | neg | neg | neg | neg |
| CR Absorber Outer Diameter | neg | neg | neg | neg |
| CR Absorber Height | 0.00001 | -0.00001 | neg | neg |
| CR Clad Inner Diameter | neg | neg | neg | neg |
| CR Clad Outer Diameter | -0.00002 | 0.00001 | neg | neg |
| CR Clad Height | 0.00001 | -0.00001 | neg | neg |
| CR Spine Diameter | neg | neg | neg | neg |
| Instrumentation Dimensions | -0.00073 | 0.00073 | -- | -- |
| Block Flat-to-Flat Distance | -0.00004 | 0.00004 | neg | neg |
| Graphite Block Height | 0.00001 | -0.00003 | neg | neg |
| Dowel/Socket Dimensions | NA | NA | NA | NA |
| Fuel Channel Diameter | 0.00007 | -0.00007 | neg | neg |
| Reflector Channel Diameter | neg | neg | neg | neg |
| Channel Pitch | -0.00002 | 0.00002 | neg | neg |

Table 2.64 (cont'd.). Total Experimental Uncertainty of the Fully-Loaded 30-Fuel-Column Core.

| Varied Parameter | Systematic Uncertainty | | Random Uncertainty | |
|---|---|---|---|---|
| | $-\Delta k_{eff}$ (1σ) | $+\Delta k_{eff}$ (1σ) | $-\Delta k_{eff}$ (1σ) | $+\Delta k_{eff}$ (1σ) |
| Handling Socket Dimensions | NA | NA | NA | NA |
| Column Pitch | 0.00016 | -0.00019 | 0.00006 | -0.00007 |
| CR Channel Diameter | neg | neg | neg | neg |
| CR Channel Pitch | neg | neg | neg | neg |
| Permanent Reflector Diameter | -0.00032 | 0.00035 | -- | -- |
| Dummy Block Dimensions | NA | NA | NA | NA |
| 3.4 wt.% Enrichment | -0.00082 | 0.00086 | -- | -- |
| 3.9 wt.% Enrichment | -0.00078 | 0.00075 | -- | -- |
| 4.3 wt.% Enrichment | -0.00145 | 0.00133 | -- | -- |
| 4.8 wt.% Enrichment | -0.00043 | 0.00039 | -- | -- |
| 5.2 wt.% Enrichment | -0.00028 | 0.00035 | -- | -- |
| 5.9 wt.% Enrichment | -0.00038 | 0.00041 | -- | -- |
| 6.3 wt.% Enrichment | -0.00021 | 0.00014 | -- | -- |
| 6.7 wt.% Enrichment | 0.00005 | 0.00007 | -- | -- |
| 7.2 wt.% Enrichment | -0.00011 | 0.00005 | -- | -- |
| 7.9 wt.% Enrichment | 0.00005 | 0.00013 | -- | -- |
| 9.4 wt.% Enrichment | 0.00005 | 0.00005 | -- | -- |
| 9.9 wt.% Enrichment | 0.00005 | 0.00005 | -- | -- |
| Oxygen to Uranium Ratio | -0.00023 | 0.00011 | -- | -- |
| $UO_2$ Density | Correlated Parameter (see Section 2.1.6) | | | |
| $UO_2$ Impurity | 0.00017 | -0.00076 | -- | -- |
| Buffer Density | neg | neg | neg | neg |
| Buffer Impurity | 0.00011 | 0.00011 | -- | -- |
| IPyC Density | neg | neg | neg | neg |
| IPyC Impurity | 0.00011 | 0.00011 | -- | -- |
| SiC Density | NA | neg | NA | neg |
| SiC Impurity | 0.00011 | 0.00011 | -- | -- |
| OPyC Density | -0.00001 | 0.00001 | neg | neg |
| OPyC Impurity | neg | 0.00016 | -- | -- |
| Overcoat Density | -0.00003 | 0.00002 | neg | neg |
| Overcoat Composition | NA | NA | NA | NA |
| Overcoat Impurity | 0.00038 | -0.00088 | -- | -- |
| Compact Density | -0.00001 | 0.00001 | neg | neg |
| Compact Impurity | 0.00011 | -0.00040 | -- | -- |
| Compact Free U Content | NA | 0.00002 | -- | -- |

Table 2.64 (cont'd.). Total Experimental Uncertainty of the Fully-Loaded 30-Fuel-Column Core.

| Varied Parameter | Systematic Uncertainty | | Random Uncertainty | |
|---|---|---|---|---|
| | $-\Delta k_{eff}$ (1σ) | $+\Delta k_{eff}$ (1σ) | $-\Delta k_{eff}$ (1σ) | $+\Delta k_{eff}$ (1σ) |
| Sleeve Density | -0.00006 | 0.00005 | neg | neg |
| Sleeve Impurity | 0.00033 | -0.00021 | -- | -- |
| BP Absorber Density | 0.00013 | -0.00014 | neg | neg |
| BP Absorber Content, 2.0 wt.% | 0.00087 | -0.00072 | 0.00004 | -0.00004 |
| BP Absorber Content, 2.5 wt.% | 0.00026 | -0.00022 | 0.00002 | -0.00002 |
| BP Absorber Impurity | NA | -0.00015 | -- | -- |
| BP Isotopic Abundance of $^{10}B$ | 0.00154 | -0.00054 | -- | -- |
| Graphite Disk Density | neg | neg | neg | neg |
| Graphite Disk Impurity | 0.00011 | 0.00011 | -- | -- |
| CR Absorber Density | 0.00001 | neg | neg | neg |
| CR Absorber Content | 0.00003 | -0.00003 | neg | neg |
| CR Absorber Impurity | NA | -0.00015 | -- | -- |
| CR Isotopic Abundance of $^{10}B$ | 0.00011 | 0.00011 | -- | -- |
| CR Clad Density | 0.00004 | 0.00003 | 0.00001 | neg |
| CR Clad Composition | 0.00011 | neg | -- | -- |
| CR Clad Impurity | NA | 0.00006 | -- | -- |
| Instrumentation Composition | See Section 2.1.2.6 | | | |
| IG-110 Density in Blocks | -0.00081 | 0.00079 | -0.00010 | 0.00010 |
| IG-110 Impurity in Blocks | 0.00442 | -0.00565 | -- | -- |
| PGX Density | -0.00004 | 0.00008 | -0.00001 | 0.00003 |
| PGX Impurity | 0.00237 | -0.00299 | -- | -- |
| Dummy Block Composition | NA | NA | NA | NA |
| Helium Coolant Density | -0.00030 | 0.00020 | -- | -- |
| Helium Coolant Impurity | NA | neg | -- | -- |
| Room Return | NA | NA | NA | NA |
| TRISO Particle Placement | 0.00095 | 0.00095 | neg | neg |
| Block Stack Alignment | NA | NA | NA | NA |
| MCNP Random Number Seed | -- | -- | 0.00019 | 0.00019 |
| Uranium Fuel Mass (Sec. 2.1.6) | -0.00066 | 0.00066 | -0.00003 | 0.00003 |
| Total Uncertainty of Components | 0.00596 | 0.00706 | 0.00025 | 0.00026 |
| **Total Evaluation Uncertainty** | **0.00597** | **0.00707** | | |

### 2.1.8 Total Experimental Uncertainty (Fully-Loaded Core Subcritical)

The benchmark model for the critical configuration analyzed in Section 2.1 and described in Section 3.1 was utilized in the analysis of the subcritical configuration.

An uncertainty analysis similar to that performed for the fully-loaded core critical was applied to the subcritical configuration. However, only the constituents providing the greatest uncertainty in the Table 2.64 were assessed for the subcritical configuration.

The only difference between the critical and subcritical configurations is the control rod positions. All rods in the subcritical configuration are at a height of -55 mm below the bottom surface of the lowest fuel block. An instrumentation bias and uncertainty were also assessed for the subcritical configuration.

It is interesting to note that many of the uncertainties of significance in the critical configuration are less significant in the subcritical configuration. Furthermore, the calculated uncertainties are all relatively insignificant compared to the subcritical measurement uncertainty of 1.0%. Results are shown in Table 2.65.

The subcritical configurations developed during initial core loading were not evaluated.

Table 2.65. Total Experimental Uncertainty of the Fully-Loaded Subcritical Core.

| Varied Parameter | Systematic Uncertainty | | Random Uncertainty | |
|---|---|---|---|---|
| | $-\Delta k_{eff}$ (1σ) | $+\Delta k_{eff}$ (1σ) | $-\Delta k_{eff}$ (1σ) | $+\Delta k_{eff}$ (1σ) |
| Sleeve Outer Diameter | -0.00010 | 0.00011 | neg | neg |
| BP Diameter | 0.00009 | -0.00009 | neg | neg |
| Instrumentation Dimensions | -0.00075 | 0.00075 | -- | -- |
| 3.4 wt.% Enrichment | -0.00006 | 0.00005 | -- | -- |
| 3.9 wt.% Enrichment | -0.00011 | 0.00005 | -- | -- |
| 4.3 wt.% Enrichment | -0.00020 | 0.00016 | -- | -- |
| 4.8 wt.% Enrichment | -0.00018 | 0.00005 | -- | -- |
| 5.2 wt.% Enrichment | -0.00048 | 0.00040 | -- | -- |
| 5.9 wt.% Enrichment | -0.00027 | 0.00015 | -- | -- |
| 6.3 wt.% Enrichment | -0.00042 | 0.00036 | -- | -- |
| 6.7 wt.% Enrichment | -0.00034 | 0.00033 | -- | -- |
| 7.2 wt.% Enrichment | -0.00055 | 0.00038 | -- | -- |
| 7.9 wt.% Enrichment | -0.00067 | 0.00054 | -- | -- |
| 9.4 wt.% Enrichment | -0.00054 | 0.00043 | -- | -- |
| 9.9 wt.% Enrichment | -0.00034 | 0.00022 | -- | -- |
| BP Isotopic Abundance of $^{10}B$ | 0.00023 | -0.00007 | -- | -- |
| IG-110 Density in Blocks | -0.00144 | 0.00141 | -0.00018 | 0.00018 |
| IG-110 Impurity in Blocks | 0.00163 | -0.00101 | -- | -- |
| PGX Density | -0.00003 | 0.00002 | -0.00001 | 0.00001 |
| PGX Impurity | 0.00083 | -0.00072 | -- | -- |
| Uranium Fuel Mass (Sec. 2.1.6) | -0.00065 | 0.00065 | -0.00003 | neg |
| Experimental Measurement | 0.010 | 0.010 | -- | -- |
| Total Uncertainty of Components | 0.01041 | 0.01028 | 0.00020 | 0.00019 |
| **Total Evaluation Uncertainty** | **0.01041** | **0.01028** | | |

### 2.1.9 Total Experimental Uncertainty (Fully-Loaded Core Warm Critical)

The warm critical of the fully-loaded core has not been evaluated. It was determined that the information provided in Reference 2 does not reflect actual experimental data. Warm-critical configurations developed during the analysis of core configurations elsewhere,[a] with accompanying control rod position and worth data, indicate that the control rod positions for a core operating at 480 K would need to be withdrawn to approximately 1970 mm instead of the reported 1825 mm. The control rods are withdrawn to a heights of 1873 and 1903 mm for respective temperatures of approximately 400 and 420 K. Therefore, this configuration is considered not representative of a valid benchmark.

[a] N. Fujimoto, N. Nojiri, E. Takada, K. Saito, S. Kobayashi, H. Sawahata, and S. Kokusen, "Control Rod Position and Temperature Coefficient in HTTR Power-rise Tests," JAERI-Tech 2000-091 (2001).

## 2.2 Evaluation of Buckling and Extrapolation Length Data

Buckling and extrapolation length measurements were not made.

## 2.3 Evaluation of Spectral Characteristics Data

Spectral characteristics measurements were not made.

## 2.4 Evaluation of Reactivity Effects Data

The benchmark model for the critical configuration analyzed in Section 2.1 and described in Section 3.1 was utilized in the analysis of the reactor physics experiments in Section 1.4.

Monte Carlo n-Particle (MCNP) version 5.1.40 was utilized to predict the biases and uncertainties associated with the experimental results for HTTR critical configurations in this evaluation. MCNP is a general-purpose, continuous-energy, generalized-geometry, time-dependent, coupled n-particle, Monte Carlo transport code. The Evaluated Neutron Data File library, ENDF/B-VI.8, was utilized in analysis of the benchmark model biases and uncertainties.

### 2.4.1 Excess Reactivity

The revised excess reactivity data from Section 1.4.2.1, Table 1.30, and the paragraph before it were evaluated as benchmark experiment data. The experimental results are summarized in Table 2.66.

Table 2.66. Benchmark Experiment Excess Reactivity Measurements in the HTTR.

| Data Point | Fuel Columns | Excess Reactivity $\Delta\rho_{exm}$ (% Δk/k) | | | Excess Reactivity $\rho_{exm}$ (% Δk/k) | | |
|---|---|---|---|---|---|---|---|
| 1 | 19 | | -- | | 2.4[(a)] | ± | 0.24[(b)] |
| 2 | 21 | | -- | | 4.0 | ± | 1.1 |
| 3 | 24 | 3.7 | ± | 1.0 | 7.7 | ± | 2.1 |
| 4 | 27 | 3.0 | ± | 0.9 | 10.7 | ± | 3.0 |
| 5 | 30 | 1.3 | ± | 0.3 | 12.0 | ± | 3.3 |

(a) This value represents the cumulative worth of fuel addition from the -0.9 % Δk/k subcritical 18-fuel-column core and the +1.5 % Δk/k 19-fuel-column core.
(b) An uncertainty of 10 % is assumed, based upon measurement uncertainty in Table 1.30.

Excess reactivity measurements were evaluated by taking the annular core configurations described in Section 3.1 of HTTR-GCR-RESR-002 for the 19-, 21-, 24-, and 27-fuel-column core configurations along with the 30-fuel-column core configuration described in Section 3.1 of this benchmark. The control rod positions were adjusted to assess the reactivity worth of the addition of fuel block columns into the HTTR core. All control rods in the 19-fuel-column configuration were fully withdrawn and the new eigenvalue is compared to that from the critical configuration. Then for the remaining four configurations, the rods positions were removed only to their respective positions in the prior core configuration; i.e. the 21-fuel-column configuration had the control rod positions raised to those for the critical configuration of the 19-fuel-column configuration. All the control rods were also completely

withdrawn from the fully-loaded 30-fuel-column core configuration to provide an additional assessment of the total core excess reactivity. The cumulative excess reactivity values were determined by summation of the individual excess reactivity values. Reactor core configurations and control rod positions are depicted in detail in Sections 3.1.2.11 and 3.1.2.12, respectively, of HTTR-GCR-RESR-002.

No additional parameters were assessed for the total uncertainty in the excess reactivity measurements due to their large experimental uncertainty. Therefore, the uncertainty values reported in Table 2.66 represent the total benchmark uncertainty for the excess reactivity measurements.

### 2.4.2 Shutdown Margin

Evaluation of the data provided in Section 1.4.2.2 (Table 1.33) yields that there exist only three shutdown margin benchmark measurements:

1. Full insertion of the radial reflector control rods, R2 and R3, from the critical core configuration (Section 3.1),
2. Full insertion of the fuel region control rods, C and R1, from the previous configuration, and
3. Full insertion of all control rods from the critical core configuration (Section 3.1).

The IK method was used to determine the subcriticality of the core with all rods inserted. As reported in Section 1.1.2.5, the subcritical effective multiplication factor of 0.685 ± 0.010 when the control rods were completely inserted. This reported value equates to approximately 45.99 ± 2.13 % Δk/k. Therefore, the uncertainty in the reactivity effects data is assumed to have measurement uncertainties on the order of ±2.13 % Δk/k for a fully subcritical configuration.

The HTR-PROTEUS reports an uncertainty in the IK method of less than 5 %.[a] For a shutdown margin of 46.5 % Δk/k, the uncertainty would be approximately ±2.3 % Δk/k. An uncertainty of ±5 % is assumed for all reactivity effects measurements unless it is otherwise observed in the published literature.

Rod drop uncertainty is reported as approximately 5-6 % for a TRIGA reactor,[b] <10 % for a LMFBR,[c] and approximately 5-6 % for the MASURCA reactor.[d] An uncertainty of 6 % is assumed for rod drop measurements in the HTTR.

Reproduction of the shutdown margins measured for the HTTR with estimated uncertainties are provided in Table 2.67. The uncertainty for all control rods dropped is the two-step approach using the IK method is the square root of the sum of the squares of the uncertainties for each step in this approach.

---

[a] "Critical Experiments and Reactor Physics Calculations for Low-Enriched High Temperature Gas Cooled Reactors," IAEA-TECDOC-1249, International Atomic Energy Agency, Vienna, 2001.

[b] C. Jammes, B. Geslot, R. Rosa, G. Imel, and P. Fougeras, "Comparison of Reactivity Estimations Obtained from Rod-Drop and Pulsed Neutron Source Experiments," *Ann. Nucl. Energy*, **32**, 1131 (2005).

[c] E. F. Bennett, "Methods and Erros in Subcriticality Measurements by Rod Drop Flux Profile Analysis," ANL-7966, Argonne National Laboratory (May 1976).

[d] G. Perret, C. Jammes, G. Inel, C. Destouches, P. Chaussonnet, J. M. Laurens, R. Soule, G. M. Thomas, W. Assal, P. Fougeras, P. Blaise, J-P. Hudelot, H. Philibert, and G. Bignan, "Determination of Reactivity by a Revised Rod-Drop Technique in the MUSE-4 Programme – Comparison with Dynamic Measurements," *Proc. 7th Information Exchange Meeting on Actinide and Fission Product Partitioning and Transmutation*, Juju, Korea, October 14-16 (2002).

Table 2.67. Shutdown Margins with Estimated Measurement Uncertainties.

| Configuration | Experiment (% Δk/k) | |
|---|---|---|
| | IK Method | Rod Drop Method |
| One-Step Scram | | |
| 3. All Control Rods | -46.7 ± 2.3 | -43.7 ± 2.6 |
| Two-Step Scram | | |
| 1. 1st: Control Rods in Reflector Region | -12.1 ± 0.6 | -- |
| 2. 2nd: Control Rods in Fuel Region | -34.2 ± 1.7 | -- |
| 3. All Control Rods (Total) | -46.3 ± 1.8 | -49 ± 2.9 |

A variance-weighted average is computed for the all-control-rods shutdown margin because there are four separate measurements. The variance-weighted average and 1σ uncertainty is -46.3 ± 1.2 % Δk/k.

No additional parameters were assessed for the total uncertainty in the shutdown margin measurements due to their large experimental uncertainty. Therefore, the uncertainty values reported in Table 2.68 represent the total benchmark uncertainty for the excess reactivity measurements.

### 2.4.3 Control Rod Worth

The differential control rod worth in Figure 1.87 for the fully-loaded 30-fuel-column core at zero power operation was digitized to allow for further comparative analysis with computational results. Table 2.68 and Figure 2.7 represent the digitized data.

Uncertainties in the experimental measurements were not reported and uncertainties are not currently assessed for the differential control rod worth measurements. Measurement uncertainties of approximately 5 % are assumed.

Analysis of the differential control rod worth measurements for the center control rod is provided in Appendix D. This data has been judged unacceptable as benchmark quality due to the lack of necessary information such as control rod positions and worths throughout the HTTR core.

Table 2.68. Digitized Differential Center Control Rod Worth for the Fully-Loaded Core.

| Height (mm) | Rod Worth ($\times 10^{-3}$ % $\Delta$k/k-mm) |
|---|---|
| 3412.7 | 0.0180 |
| 2531.2 | 0.1048 |
| 2196 | 0.2575 |
| 2044.5 | 0.3952 |
| 1938.9 | 0.5180 |
| 1870.1 | 0.5778 |
| 1833.4 | 0.6467 |
| 1778.3 | 0.7784 |
| 1714 | 0.8713 |
| 1658.9 | 0.9970 |
| 1599.2 | 1.0299 |
| 1553.3 | 1.1407 |
| 1507.4 | 1.2275 |
| 1461.5 | 1.2515 |
| 1420.2 | 1.2754 |
| 1383.4 | 1.2545 |
| 1332.9 | 1.3084 |
| 1300.8 | 1.3024 |
| 1254.9 | 1.3593 |
| 1218.2 | 1.2934 |
| 1172.2 | 1.3623 |
| 1140.1 | 1.3204 |
| 1103.4 | 1.3084 |
| 1057.5 | 1.2754 |
| 1020.7 | 1.2335 |
| 970.2 | 1.2695 |
| 938.1 | 1.2096 |
| 887.6 | 1.1826 |
| 841.7 | 1.1527 |
| 791.2 | 1.0778 |
| 740.7 | 0.9910 |
| 676.4 | 0.9012 |
| 607.5 | 0.8234 |
| 529.5 | 0.7365 |
| 446.9 | 0.6228 |
| 341.3 | 0.5150 |
| 198.9 | 0.3683 |
| 47.4 | 0.2515 |

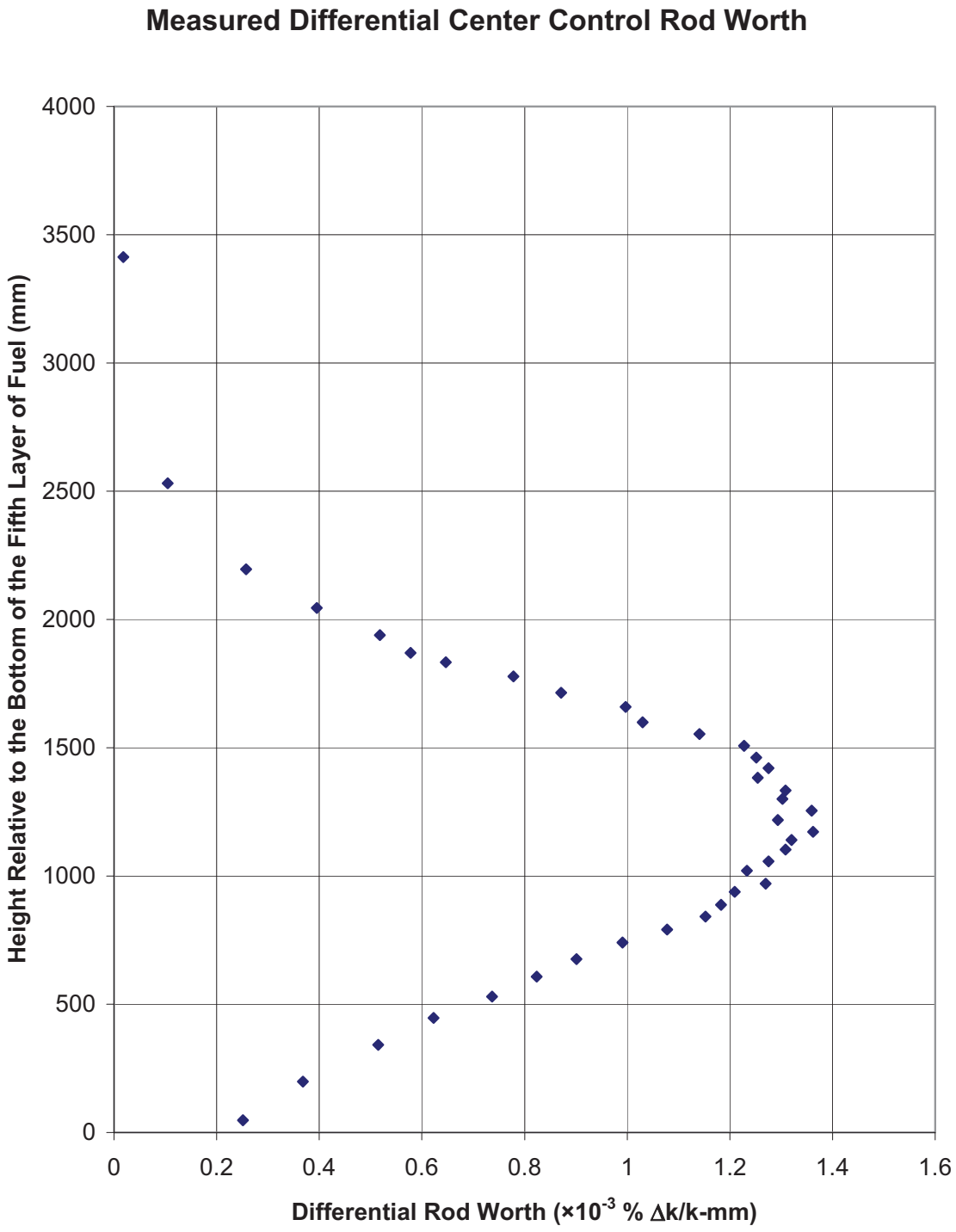


Figure 2.7. Digitized Differential Center Control Rod Worth Chart for the Fully-Loaded Core.

## 2.5 Evaluation of Reactivity Coefficient Data

Reactivity coefficient measurements have not been evaluated.

## 2.6 Evaluation of Kinetics Measurements Data

Kinetics measurements have not been evaluated.

## 2.7 Evaluation of Reaction-Rate Distributions

The benchmark model for the critical configuration analyzed in Section 2.1 and described in Section 3.1 was utilized in the analysis of the reactor physics experiments in Section 1.7.

Monte Carlo n-Particle (MCNP) version 5.1.40 was utilized to predict the biases and uncertainties associated with the experimental results for HTTR critical configurations in this evaluation. MCNP is a general-purpose, continuous-energy, generalized-geometry, time-dependent, coupled n-particle, Monte Carlo transport code. The Evaluated Neutron Data File library, ENDF/B-VI.8, was utilized in analysis of the benchmark model biases and uncertainties.

It should be noted that the neutron flux could not be measured directly in the core, but the fission chambers (FCs), containing $^{235}U$, were used to indirectly measure the flux as fission reaction rates. A fixed FC in one of the instrumentation columns was used to normalize the reaction-rate measurements from the FC that was moved to various positions in another column. This was to account for variation in the flux due to movement effects of the detector and its respective components.

### 2.7.1 Axial Reaction Rate Distribution

The axial fission neutron reaction-rate distribution in Figures 1.89 and 1.90 for the fully-loaded 30-fuel-column core were digitized to allow for further comparative analysis with computational results. Table 2.69 and Figure 2.8 represent the digitized data. As seen in the figure and table, eight of the data points approximately match between the two figures. The third and fourth data points do not have an equivalent match between data sets. The data sets were averaged and then renormalized to establish the benchmark reference values of the axial neutron reaction-rate in the instrumentation columns of the HTTR.

The reported experimental uncertainty was approximately 0.2 %.

The digitization of the charts was performed by Chris White at the Idaho National Laboratory using Marisoft Digitizer.[a] The chart is imported into the program and bound within a grid system; each individual data point is then marked and exported as numerical data. The most practical means to determine the accuracy of the digitization process is to compare a known data point to that determined using the digitization process. The fourth and fifth data points on Figure 1.89 were digitized to values slightly greater than their normalized reaction-rate value of unity. This difference was taken to represent the uncertainty incurred via the digitization process. The effective uncertainty in digitizing the data from Figures 1.89 and 1.90 is judged to be less than 0.03 %.

An uncertainty pertaining to the repeatability, or reproducibility, of a given reaction-rate at a given position is estimated by taking the half the difference in the reaction-rate from data points at the same relative position. Because there are only single values for the third and fourth data points, the difference between these two reaction-rate values was used as the uncertainty in both data points, as the

[a] M. Mitchell, Marisoft Digitizer Application Version 3.3, http://digitizer.sourceforge.net/, © 1997.

repeatability uncertainty of measurements at the peak should be minimal.. The uncertainties applied for repetition of reaction-rate measurements are tabulated in Table 2.70.

Table 2.69. Digitized Axial Neutron Fission Reaction-Rate Distribution Data for the Fully-Loaded Core.

| Data Point | Figure 1.89[a] | | Figure 1.90 | | Average | | Renormalized | |
|---|---|---|---|---|---|---|---|---|
| | Normalized Reaction Rate | Height (cm)[b] | Normalized Reaction Rate | Height (cm)[b] | Reaction Rate | Height (cm)[b] | Normalized Reaction Rate | Height (cm)[b] |
| 1 | 0.8464 | 19.57 | 0.8339 | 19.79 | 0.8402 | 19.68 | 0.8381 | 19.68 |
| 2 | 0.8844 | 27.89 | 0.8717 | 29.05 | 0.8781 | 28.47 | 0.8759 | 28.47 |
| 3 | -- | -- | 1.0016 | 71.81 | 1.0016 | 71.81 | 0.9991 | 71.81 |
| 4 | 1.0025 | 82.53 | -- | -- | 1.0025 | 82.53 | 1.0000 | 82.53 |
| 5 | 1.0026 | 86.24 | 0.9591 | 86.80 | 0.9809 | 86.52 | 0.9784 | 86.52 |
| 6 | 1.0005 | 93.35 | 0.9449 | 93.86 | 0.9727 | 93.61 | 0.9703 | 93.61 |
| 7 | 0.7944 | 143.87 | 0.7441 | 144.56 | 0.7693 | 144.22 | 0.7673 | 144.22 |
| 8 | 0.3842 | 202.24 | 0.3567 | 202.31 | 0.3705 | 202.28 | 0.3695 | 202.28 |
| 9 | 0.1382 | 261.43 | 0.1228 | 260..95 | 0.1305 | 261.19 | 0.1302 | 261.19 |
| 10 | 0.048 | 318.67 | 0.0402 | 319.59 | 0.0441 | 319.13 | 0.0440 | 319.13 |

(a) The 30-fuel-column core reaction rate data are from the bottommost chart in Figure 1.89.
(b) The height is in reference to the position relative to the bottom of the fifth layer of fuel.

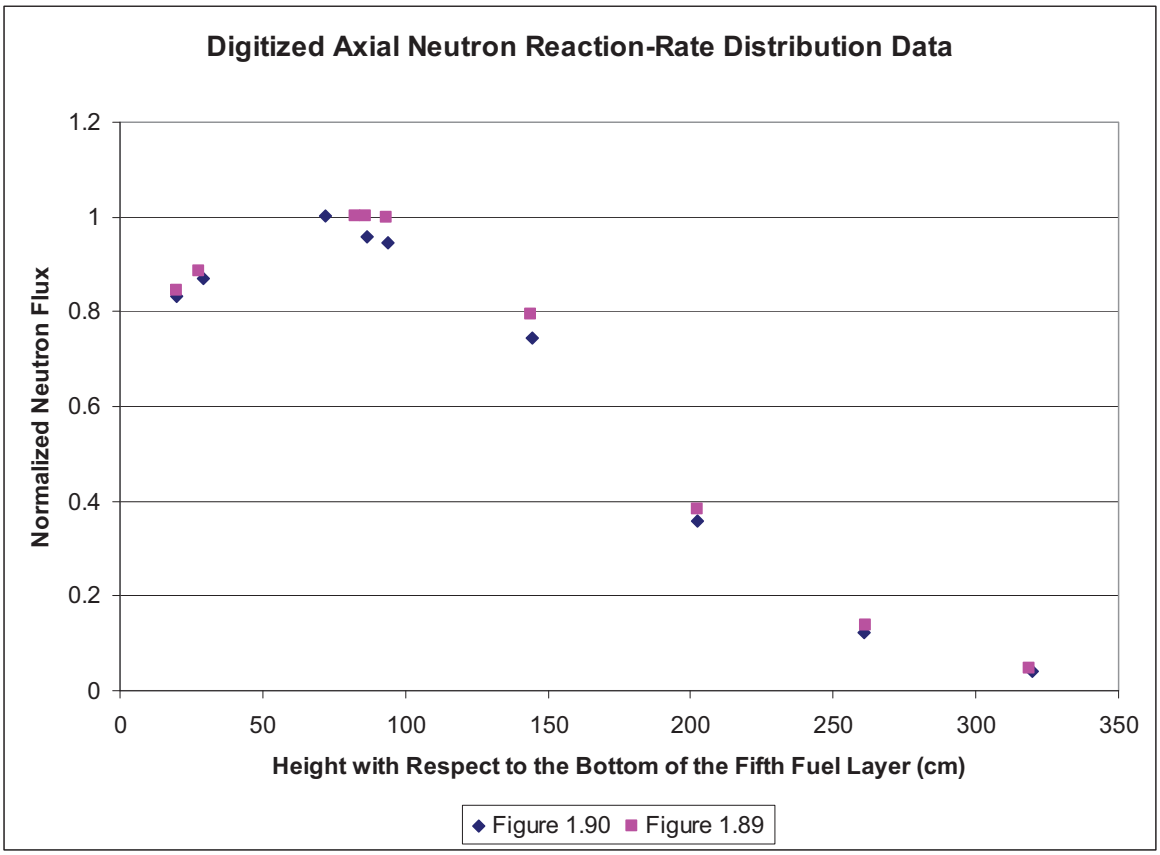


Figure 2.8. Digitized Axial Neutron Reaction-Rate Distribution Chart for the Fully-Loaded Core.

Table 2.70. Effective Uncertainty in the Repeatability of Neutron Reaction-Rate Measurements.

| Data Point | Uncertainty (%) |
|---|---|
| 1 | 0.63 |
| 2 | 0.63 |
| 3 | 0.09[(a)] |
| 4 | 0.09[(a)] |
| 5 | 2.18 |
| 6 | 2.78 |
| 7 | 2.52 |
| 8 | 1.38 |
| 9 | 0.77 |
| 10 | 0.39 |

(a) These data points were not repeated, and the difference between the reaction-rates at these two points was used to represent their uncertainty.

The axial neutron fission reaction-rate in the instrumentation columns were calculated by taking the benchmark model of the fully-loaded 30-fuel-column core in Section 3.1 and superimposing a flux tally over each of the instrumentation column positions: E05, E13, and E21. The flux was computed for 6.15-cm radius discs with a thickness of 1 cm located at the center of one instrumentation channel in each instrumentation column (see Figure 2.9). A total of 522 cm, representing the total height of the core fuel and reflector blocks, was modeled. The (x, y) coordinates used for columns E05, E13, and E21, are (114.6005, 72.4), (5.4, -135.447), and (-120, 63.04693), respectively, where the origin is located at the radial center of the core.

The F4 flux tally is used in MCNP, which determines the flux across a cell volume by tabulating the average track length of the neutrons.[a] The tally is then modified by a tally multiplier card, Fm, that accounts for the total fission cross section of $^{235}$U, the fissile material in the fission chambers, to obtain the neutron reaction-rate in each instrumentation column.

The calculated neutron fission reaction rates are obtained by taking the variance-weighted average of results obtained using six variations of the input deck (Appendix A.1) with different random number seeds and tallies of the neutron reaction rate (Appendix A.3). This approach was used to reduce the statistical uncertainty in the neutron flux tallies because the relative error values obtained can underpredict the true uncertainty in the calculated neutron flux.[b] Therefore, the final calculated values are obtained from a total of 18 reaction-rate tallies (6 input decks with 3 instrumentation columns each).

[a] X-5 Monte Carlo Team, "MCNP – A General Monte Carlo N-Particle Transport Code, Version 5, Volume II: User's Guide," LA-CP-03-0245 (April 24, 2003; revised October 2, 2005).

[b] F. B. Brown, "A Review of Best Practices for Monte Carlo Criticality Calculations," *Proc. NCSD 2009*, Richland, WA, September 13-17 (2009).

The average of the neutron reaction-rate in each position is taken and normalized to represent the calculated axial neutron reaction-rate profile. The variability in calculated reaction-rate in the three instrumentation columns is shown in Figure 2.10.

$$\phi(z)_{normalized} = \frac{\phi(z)}{\phi_{maximum}},$$

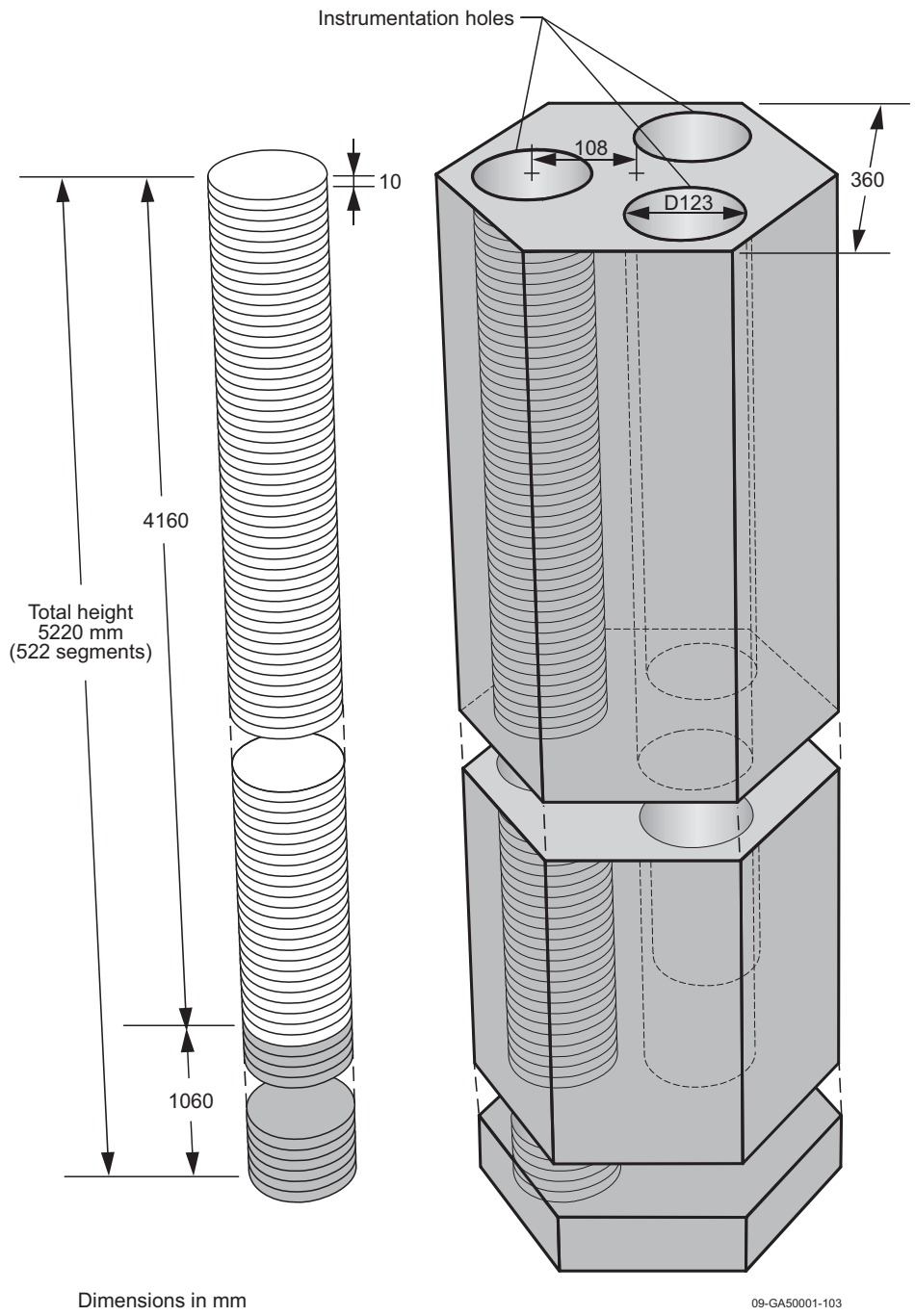


Figure 2.9. Placement of Axial Flux Tally in the Instrumentation Column.

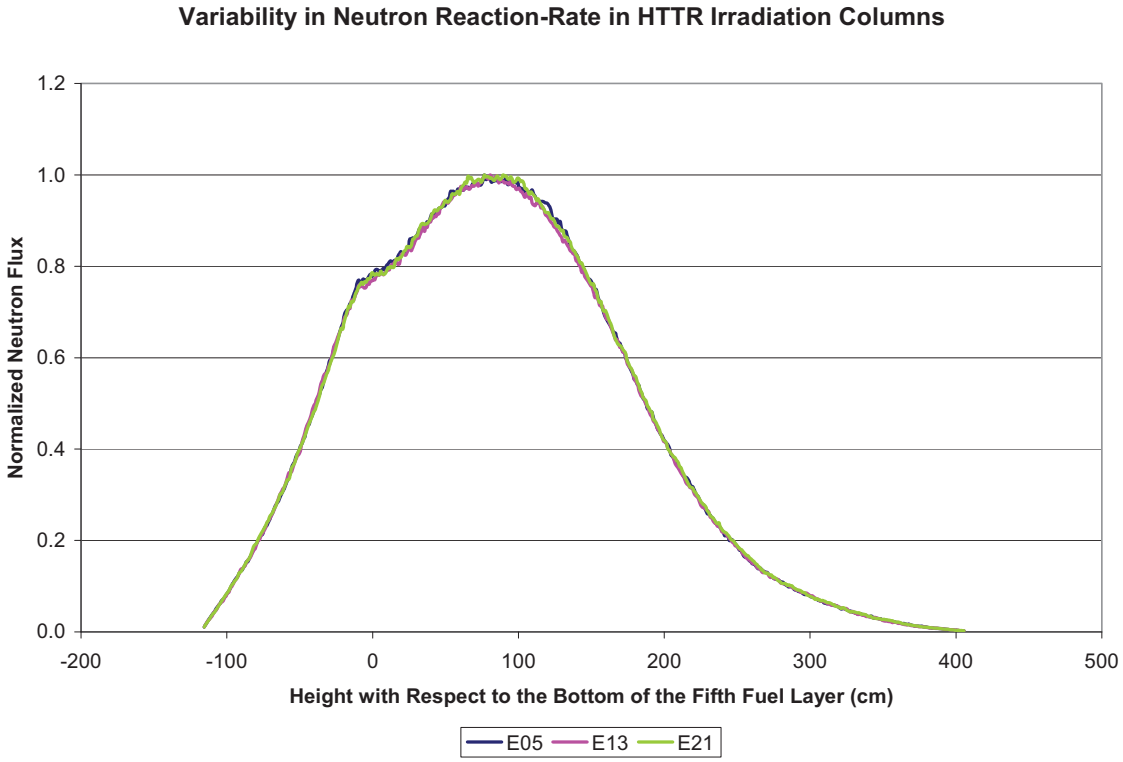


Figure 2.10. Variability in the Axial Reaction-Rate Profile for the Three Irradiation Columns.

Model variations were performed to demonstrate the influence of the uncertainties of greatest interest in the critical configuration upon the calculated neutron reaction rates. The density and boron content of the IG-110 and PGX graphite blocks were adjusted to their upper and lower bounding limits as described in Sections 2.1.3.7 and 2.1.3.8. The upper and lower bounding limits were determined from the maximum and minimum normalized reaction-rate values calculated for all three instrumentation columns and all eight perturbations of graphite materials. Results are shown in Figure 2.11 and Table 2.71 for the reported data points. The values in Table 2.71 represent the 1σ standard deviation of the 27 perturbation values used to analyze a single data-point position.

A similar assessment was performed to account for variations in control rod positions, graphite block dimensions, and core column pitch (see Sections 2.1.1.2, 2.1.2.7, and 2.1.2.7, respectively, for 1σ uncertainty values. These uncertainties are also included in Table 2.71.

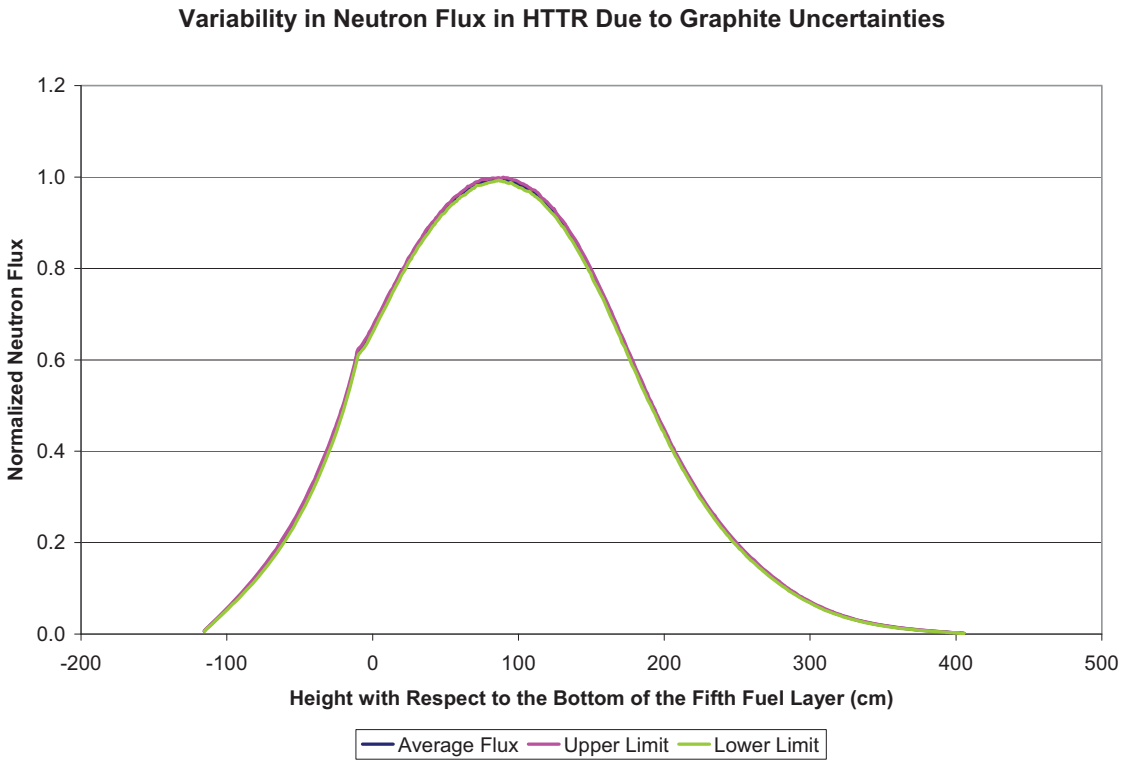


Figure 2.11. Variability in Neutron Reaction-Rate in HTTR Due to Graphite Uncertainties.

Table 2.71. Variability in Neutron Reaction Rate Due to Perturbation Analysis.

| Data Point | Uncertainty Due to Graphite Composition (%) | Uncertainty Due to Graphite Dimensions and Control Rod Positions | Total Uncertainty in Reaction Rate (%) |
|---|---|---|---|
| 1 | 0.52 | 0.59 | 0.79 |
| 2 | 0.57 | 0.48 | 0.74 |
| 3 | 0.45 | 0.78 | 0.90 |
| 4 | 0.40 | 0.61 | 0.73 |
| 5 | 0.27 | 0.55 | 0.61 |
| 6 | 0.54 | 0.78 | 0.95 |
| 7 | 0.69 | 0.60 | 0.91 |
| 8 | 0.52 | 0.36 | 0.63 |
| 9 | 0.32 | 0.21 | 0.38 |
| 10 | 0.12 | 0.16 | 0.21 |

The total uncertainty in each averaged data point was determined as the square-root of the sum of the squares. Then the total uncertainty in the benchmark normalized flux values were determined by incorporating the uncertainty from the fourth data point as follows:

$$\sigma_{\phi_{i,norm}} = \sqrt{\left(\frac{\sigma_{\phi_{i,ave}}}{\phi_{\max}}\right)^2 + \left(\frac{\phi_{i,ave}\sigma_{\phi_{\max}}}{\phi_{\max}^2}\right)^2}$$

The total benchmark uncertainty in the axial neutron reaction-rate for the instrumentation columns is reported in Table 2.72, and is between approximately 1 and 13 % Δk.

Table 2.72. Total Uncertainty (%, 1σ) in Axial Neutron Reaction-Rate in the Instrumentation Columns.

| Data Point | Experimental Uncertainty | Digization Uncertainty | Repeatability Uncertainty | Perturbation Uncertainty | Total Benchmark Uncertainty | Percent of Normalized Reaction Rate |
|---|---|---|---|---|---|---|
| 1 | 0.002 | 0.003 | 0.0063 | 0.0079 | 0.0127 | 1.51 |
| 2 | 0.002 | 0.003 | 0.0063 | 0.0074 | 0.0126 | 1.44 |
| 3 | 0.002 | 0.003 | 0.0009 | 0.0090 | 0.0128 | 1.28 |
| 4 | 0.002 | 0.003 | 0.0009 | 0.0073 | 0.0116 | 1.16 |
| 5 | 0.002 | 0.003 | 0.0218 | 0.0061 | 0.0242 | 2.48 |
| 6 | 0.002 | 0.003 | 0.0278 | 0.0095 | 0.0306 | 3.16 |
| 7 | 0.002 | 0.003 | 0.0252 | 0.0091 | 0.0277 | 3.61 |
| 8 | 0.002 | 0.003 | 0.0138 | 0.0063 | 0.0158 | 4.29 |
| 9 | 0.002 | 0.003 | 0.0077 | 0.0038 | 0.0094 | 7.21 |
| 10 | 0.002 | 0.003 | 0.0039 | 0.0021 | 0.0057 | 12.97 |

## 2.8 Evaluation of Power Distribution Data

Power distribution measurements were not made.

## 2.9 Evaluation of Isotopic Measurements

Isotopic measurements were not made.

## 2.10 Evaluation of Other Miscellaneous Types of Measurements

Other miscellaneous types of measurements were not made.

# 3.0 BENCHMARK SPECIFICATIONS

## 3.1 Benchmark-Model Specifications for Critical and / or Subcritical Measurements

Whereas insufficient information is publicly available, a finely-detailed benchmark model could not be established. A benchmark of the HTTR was prepared and analyzed with as much detail as feasible. The simplification bias for this model could also not be fully determined. However, the uncertainties in the benchmark model are believed to be of sufficient magnitude to encompass any biases incurred due to the simplification process of the benchmark model and a bias for the removal of the core instrumentation has been estimated. It is currently difficult to obtain the necessary information to improve the confidence in the benchmark model; the necessary data is proprietary and its released is being restricted, because the benchmark configuration of the HTTR core is the same that is currently in operation. Once this information is made available, the HTTR benchmark can be adjusted as appropriate.

Only the fully-loaded 30-fuel-column core critical with its associated subcritical configuration is modeled in this benchmark. The annular core configurations of the HTTR can be found in HTTR-GCR-RESR-002. The warm critical configuration of the fully-loaded core is not currently evaluated.

### 3.1.1 Description of the Benchmark Model Simplifications

Significant simplifications were incurred to develop a benchmark model of the HTTR because of a lack of information publicly available to determine dimensions and compositions. Simplifications will be discussed where applicable in the descriptions of the dimension and material properties of the model.

As stated previously, biases of the model were not assessed but will be addressed as additional HTTR information becomes available. Biases that have been partially investigated are listed in Section 3.1.1.1.

The fuel handling positions, dowels, and sockets were not included in the model due to insufficient data specifications, but were accounted for with a void fraction of 0.5 % reduction in graphite density (based upon volume calculations using dimensions provided in Figure 1.52). The burnable poison insertion holes were placed on the same pitch as the fuel channels to simplify the model.

It is apparent from a comparison of Figures 1.65 and 1.67 that the depth to which the control rod, reserve shutdown system, and instrumentation holes are drilled varies. A depth of 1060 mm above the bottom of the core was selected for all positions to simplify the model. No bias was assessed.

Insufficient information was available to model the bottom-most reflector block according to actual design; therefore it was modeled with the same design as the two top reflector blocks and the other bottom reflector block. The top and bottom of each coolant channel is expected to taper from the 21-mm diameter to the 41-mm diameter of the fuel assemblies, but information was unavailable to describe taper in the model. Therefore channels in the reflector blocks were modeled with 21-mm diameters.

Individual sections of the dodecagon-block-shaped permanent reflector were not modeled due to insufficient information. It was modeled as a cylindrical region surrounding the core columns. A bias could not be assessed.

Insufficient information was available to model the shielding blocks surrounding the core and shielding plugs in the core. Therefore, they were not included in the benchmark model. It is assumed that all neutrons reaching the core boundaries are lost and not scattered back by the shielding material. A conservative estimate of room-return effects demonstrated a negligible change in $k_{eff}$.

In the materials section, impurity contents in the materials are based upon natural boron equivalency. In the model, however, only the $^{10}B$ component is included, as the effect of the $^{11}B$ content would be insignificant.

The density is the same (1.80 g/cm$^3$) for both types of burnable poison pellets. The boron content in the pellets is based on the reported weight percents instead of the atomic percents.

Too much information was available to specify parameters for the TRISO particle fuel. Because the fuel mass of an individual rod would most probably be the most accurate measured parameter, it was preserved in the benchmark model with some variation to other parameters as necessary. The TRISO kernel diameter is maintained at the nominal value of 600 μm and the density of the fuel is 10.39 g/cm$^3$, which is within approximately 95% of the theoretical density of $UO_2$. The number of TRISO particles in a given compact was reduced from 13,000 to 12,987, with a packing fraction of 30 %, in order to conserve a nominal fuel mass per rod of 188.58 g.

#### *3.1.1.1 Assessed Biases*

Although some biases have been partially investigated, there is incomplete information regarding the HTTR to properly address simplification biases in order to adjust the benchmark $k_{eff}$. As stated previously, a conservative estimate of potential room-return effects provided negligible results. As shown in Section 2.1.3.2 in Table 2.37, the effect of neglecting the free uranium content of the fuel compacts was negligible. Finally, the effect of modeling the helium coolant as void material was also negligible (as shown in Section 2.1.3.10, Table 2.59). The reported literature bias for air content in the graphite could not be verified (Section 2.1.3.7).

Previous efforts of the Japanese in analyzing the 19-fuel-column core (Case 1) obtained an analytical excess reactivity of 2.7 % Δk/k, with an estimated Monte Carlo calculation overestimate of 1.2 % Δk/k.[a] Additional information would be necessary to completely verify published results.

An approximate bias for the removal of reactor instrumentation from the three instrumentation columns in the core was calculated, as discussed in Section 2.1.2.6. The bias for the fully-loaded core model was determined to be 0.254 ± 0.073 % Δk.

The instrumentation bias determined for the subcritical model was determined to be 0.261 ± 0.075 % Δk., using the same method as described in Section 2.1.2.6, but applied to the subcritical configuration.

An instrumentation bias for the warm critical configuration has not been evaluated.

### 3.1.2 Dimensions

#### *3.1.2.1 Prismatic Pin-in-Block Fuel*

**TRISO Particles**

The basic ingredient for HTTR fuel is the TRISO particle. A $UO_2$ kernel is surrounded by four coatings: a low density porous pyrolytic carbon (PyC) buffer layer, a high density inner isotropic PyC layer, a SiC layer, and a final outer PyC layer. A resinated graphite overcoat is then deposited around each TRISO particle. Figure 3.1 depicts the TRISO layers and their respective dimensions.

[a] Fujimoto, N., Nakano, M., Takeuchi, M., Fujisaki, S., and Yamashita, K., "Start-Up Core Physics Tests of High Temperature Engineering Test Reactor (HTTR), (II): First Criticality by an Annular Form Fuel Loading and Its Criticality Prediction Method," *J. Atomic Energy Society Japan*, **42**(5), 458-464 (2000).

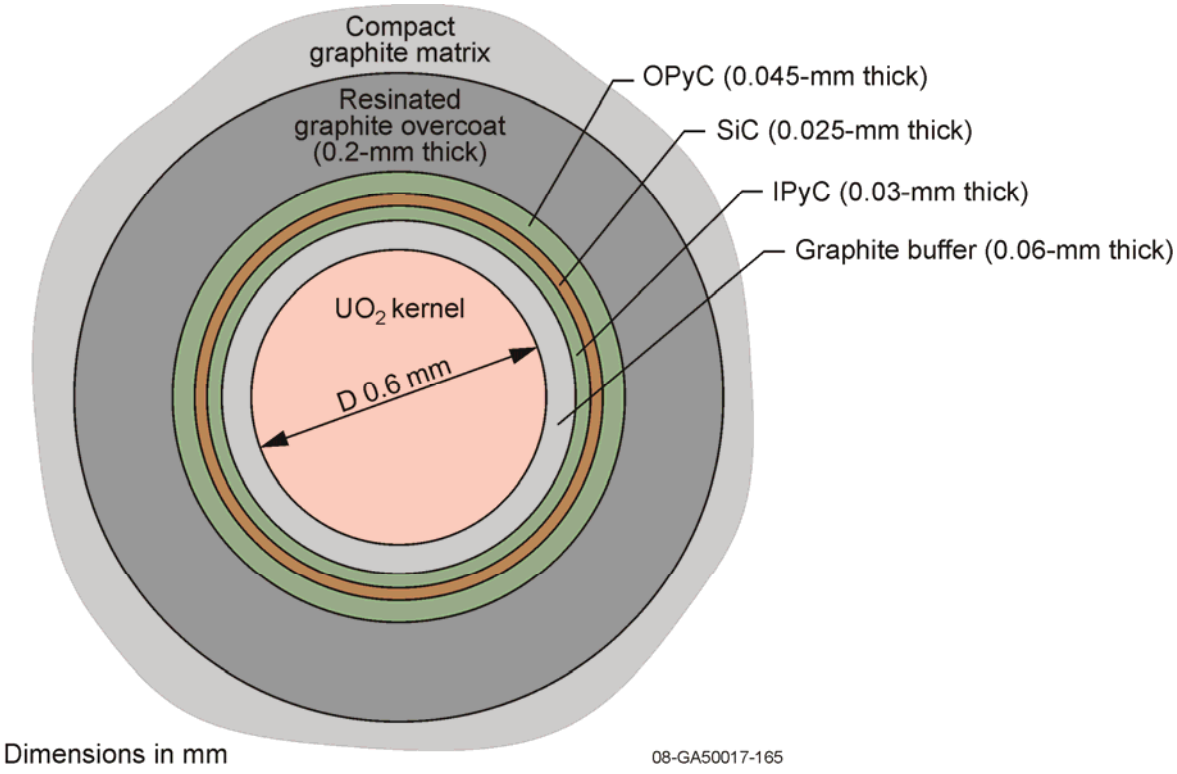


Figure 3.1. TRISO-Coated Fuel Particle.

## Compacts

All fourteen fuel compacts in a single fuel pin are modeled as a single unit filled with the TRISO lattice. The stacked compacts have an inner diameter of 1 cm, an outer diameter of 2.6 cm, and an overall height of 54.6 cm.

A horizontal cross section of the compacts is shown in Figure 3.2. In the benchmark model, 12,987 TRISO particles are randomly distributed throughout the compact matrix in a single compact. For a stack of 14 compacts, as modeled in this benchmark, the total number of TRISO particles is 181,818

A key parameter is that the total fuel mass of a single fuel rod (14 stacked compacts) is approximately 188.58 g.

While the benchmark model retains randomness in distribution, many computer codes cannot properly model such configurations. It is up to the user to determine which method is most appropriate while accounting for its impact on the reactivity of the model. Example means for analyzing this model are provided in Section 4.1. The difference in methods for accurately modeling random TRISO particles in a full-core reactor is on the order of ~0.1 % of $k_{eff}$.[a]

[a] W. Ji, J. L. Conlin, W. R. Martin, J. C. Lee, and F. B. Brown, "Explicit Modeling of Particle Fuel for the Very-High Temperature Gas-Cooled Reactor," *Trans. Am. Nucl. Soc.*, **92** (June 2005).

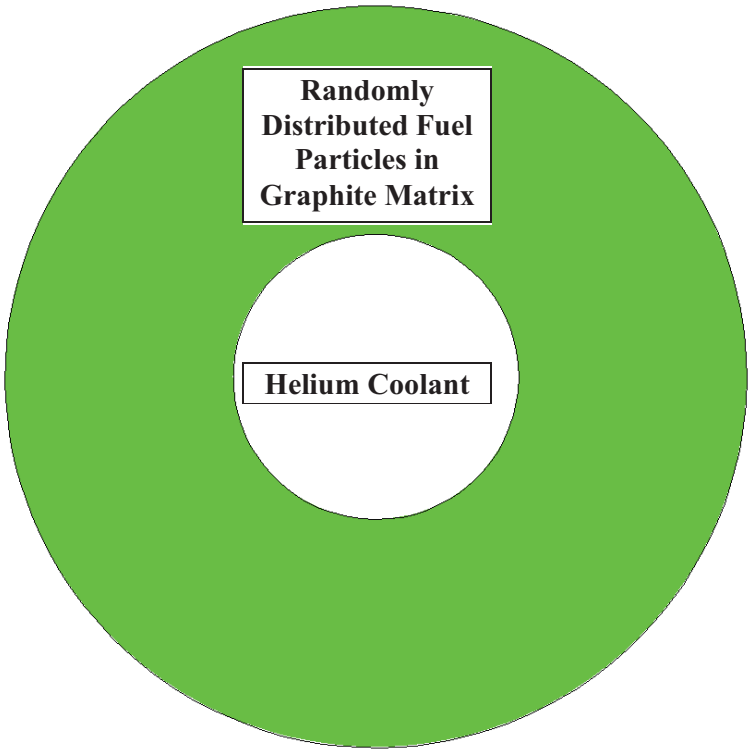


Figure 3.2. Fuel Compact Filled with Randomly Distributed TRISO Particles (Particles Not Shown).

## Fuel Element

A description of the HTTR fuel element is modeled (Figure 3.3).

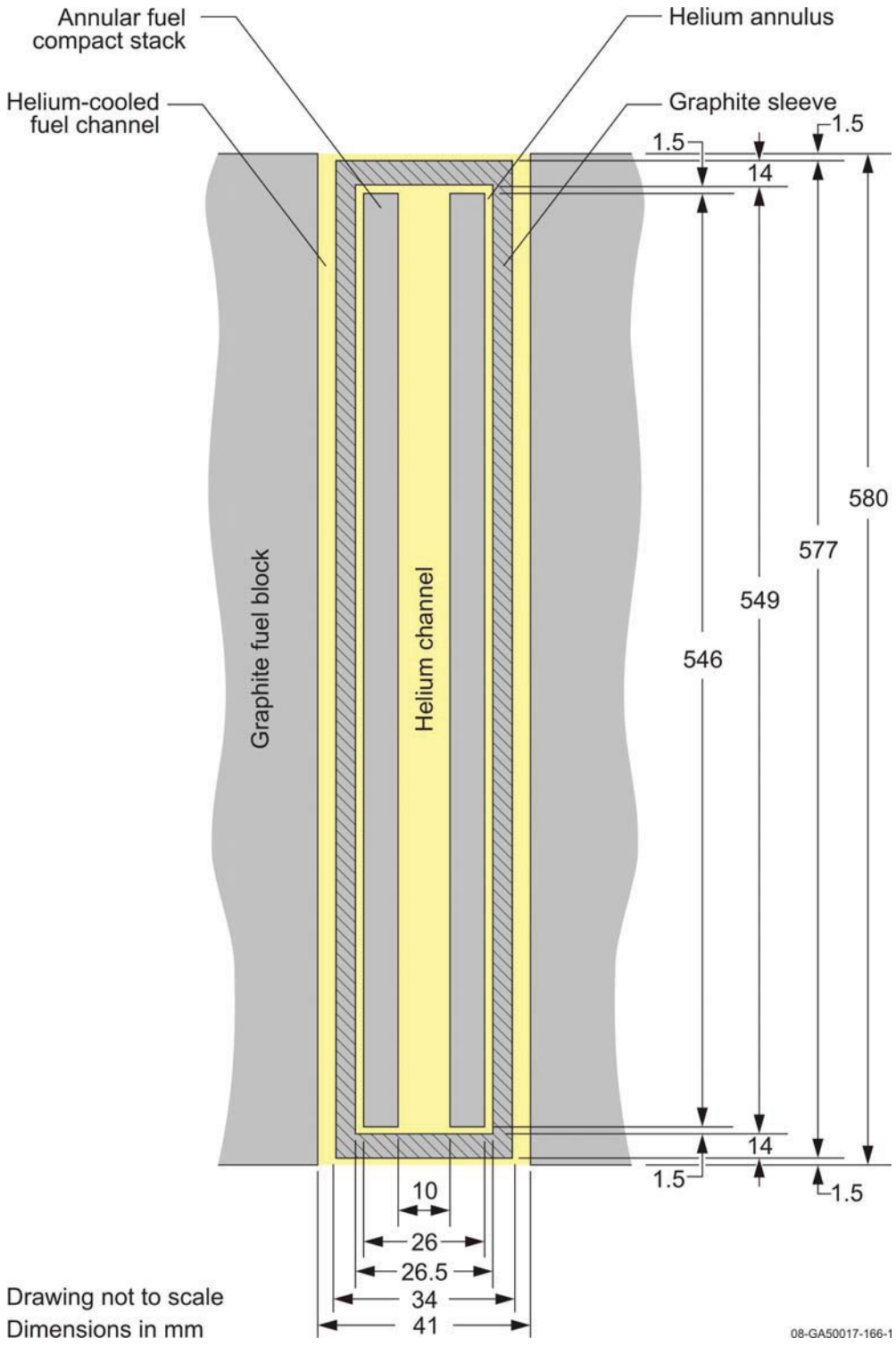


Figure 3.3. Benchmark HTTR Fuel Element.

### *3.1.2.2 Burnable Poisons*

The burnable poison pellets and graphite disks were modeled as individual stacks contained within a pin position in the fuel blocks (Figure 3.4). Each fuel block contained two BP pins and one empty pin position.

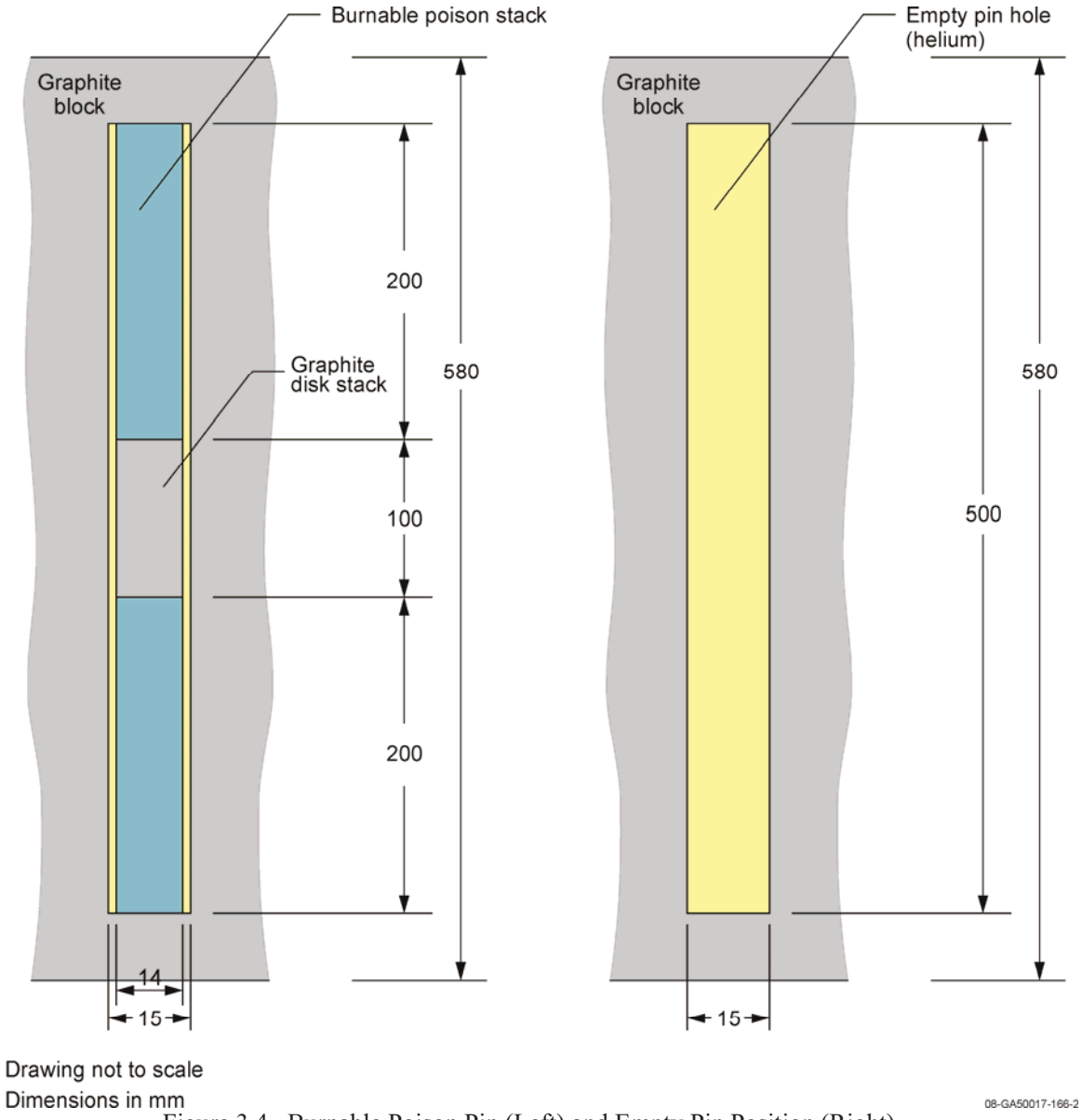


Figure 3.4. Burnable Poison Pin (Left) and Empty Pin Position (Right).

### *3.1.2.3 Fuel Blocks*

The HTTR contains two types of regular hexagonal fuel blocks: 33-pin (Zones 1 and 2) and 31-pin (Zones 3 and 4). Diagrams of each fuel block design implemented in the benchmark model are shown in Figures 3.5 and 3.6, respectively. The pitch for all positions is 51.5 mm.

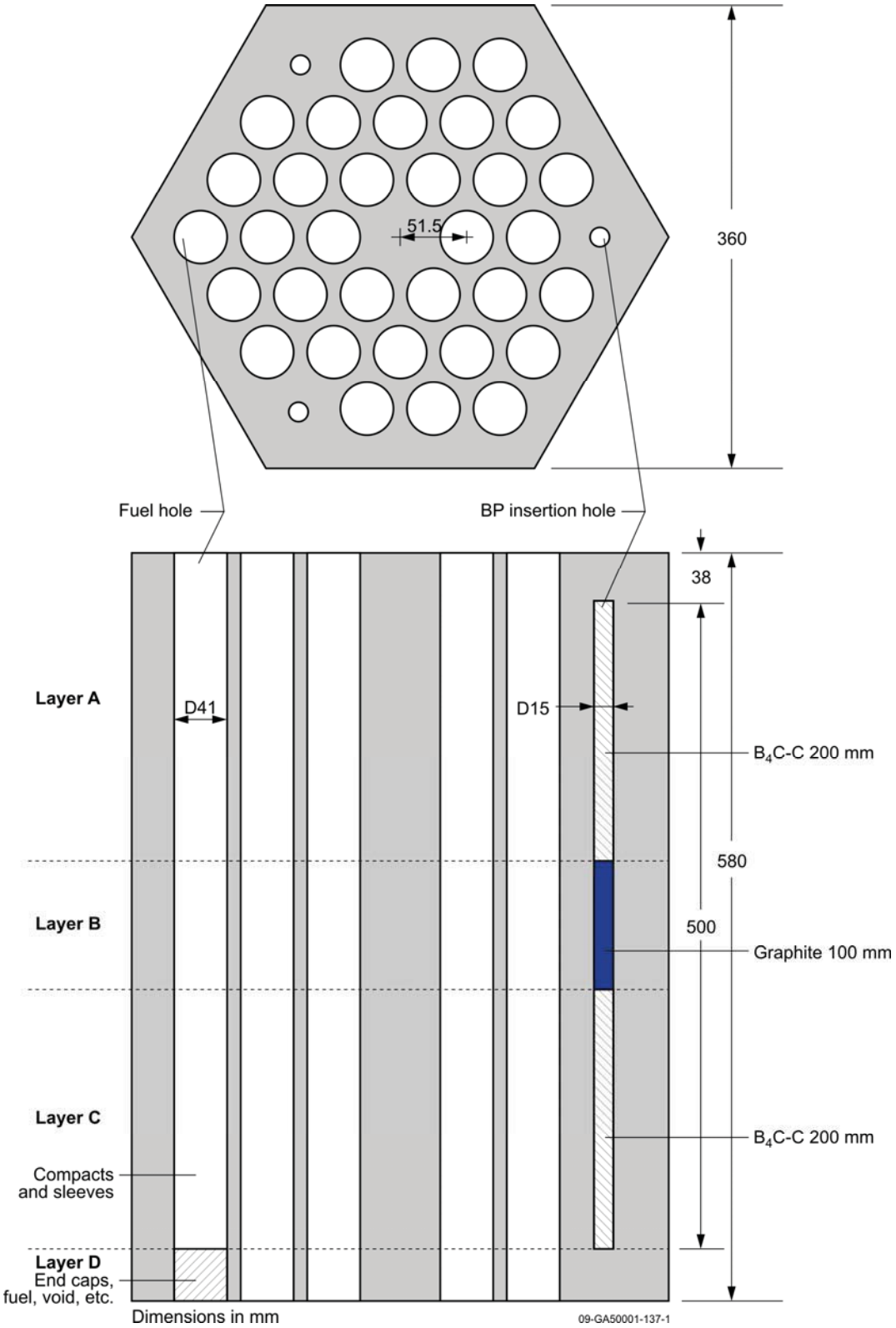


Figure 3.5. Fuel Block for 33-Pin Fuel Assembly. Dxx represents the diameter in xx (mm).

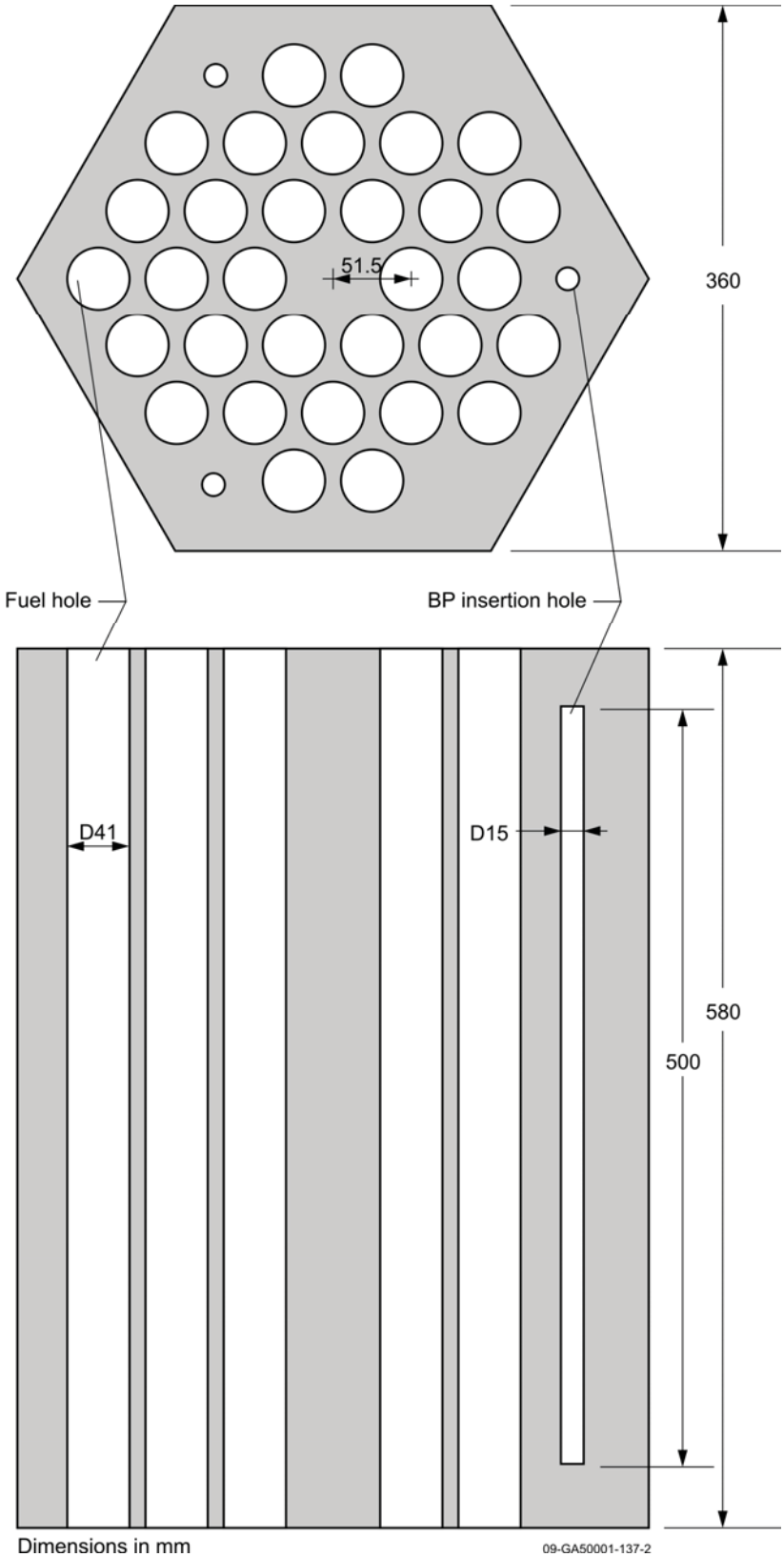


Figure 3.6. Fuel Block for 31-Pin Fuel Assembly. Dxx represents the diameter in xx (mm).

### *3.1.2.4 Dummy Blocks*

The 30-fuel-column core does not contain dummy blocks.

### *3.1.2.5 Control Rod System*

**Control Rods**

A diagram of a control rod section is shown in Figure 3.7. The absorber compacts are modeled as a single unit. Detailed dimensions regarding the cladding infrastructure for each section was unavailable, and the clad is therefore modeled without detail. A single control rod is comprised of ten sections (Figure 3.8) with a total height of 3.1 m.

The control rods are divided up into four sets: center position (C), ring 1 (R1), ring 2 (R2), and ring 3 (R3). The center position contains two control rods. The other rings are comprised of six, six, and three positions, containing a total of twelve, twelve, and six control rods, respectively. Control rods in each set are synchronously moved.

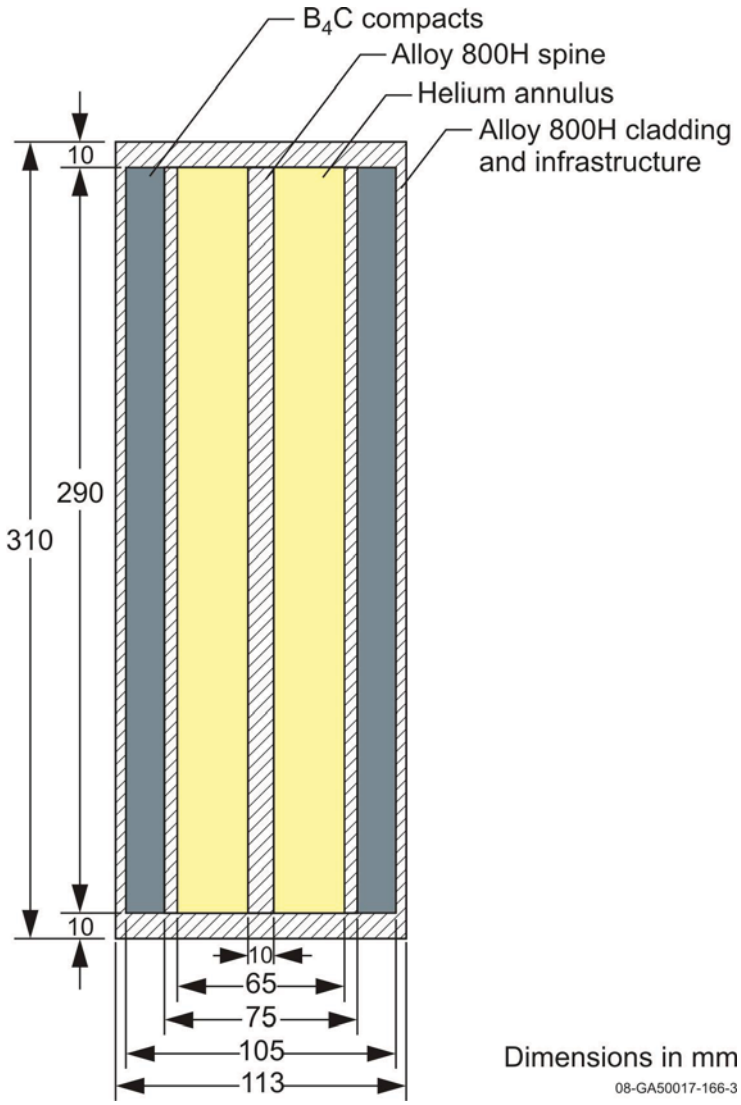


Figure 3.7. Control Rod Section.

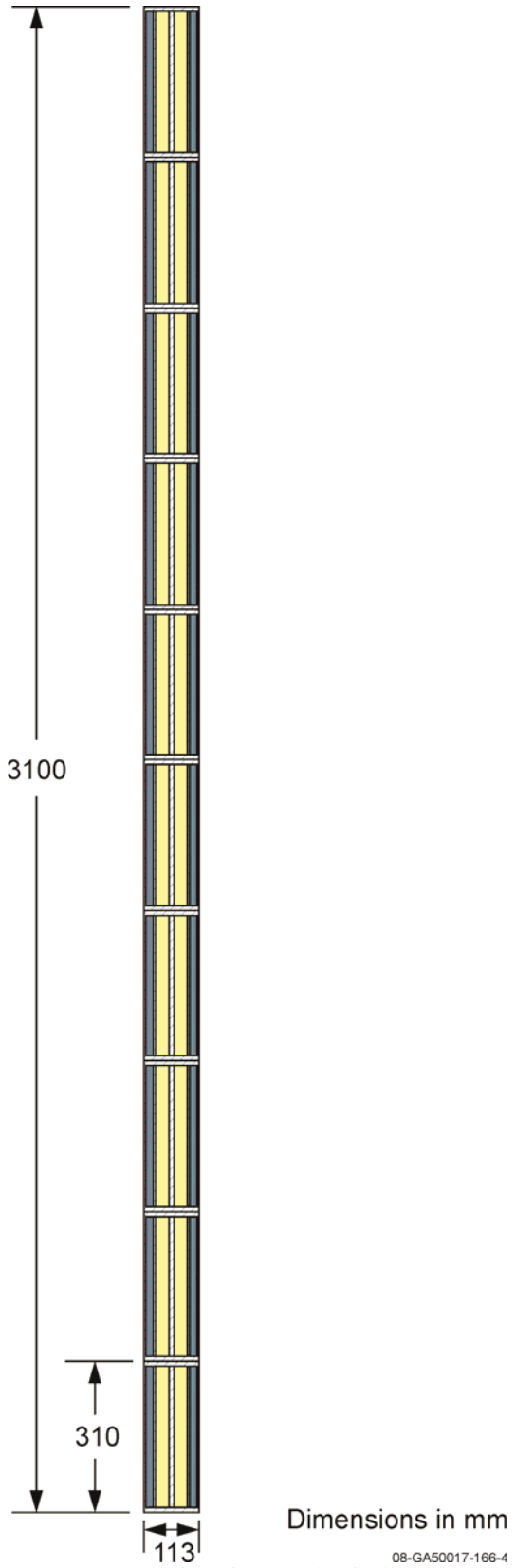


Figure 3.8. Control Rod Comprised of Ten Sections.

## Control Rod Columns

Individual control rod blocks were not modeled. A single control rod column was modeled with three holes to accommodate two control rods and an empty position (for the reserved shutdown system). A diagram of a generic control column (without control rods) is shown in Figure 3.9. The holes in the control rod and instrumentation columns are equidistant from each other, with an angle of 120º.

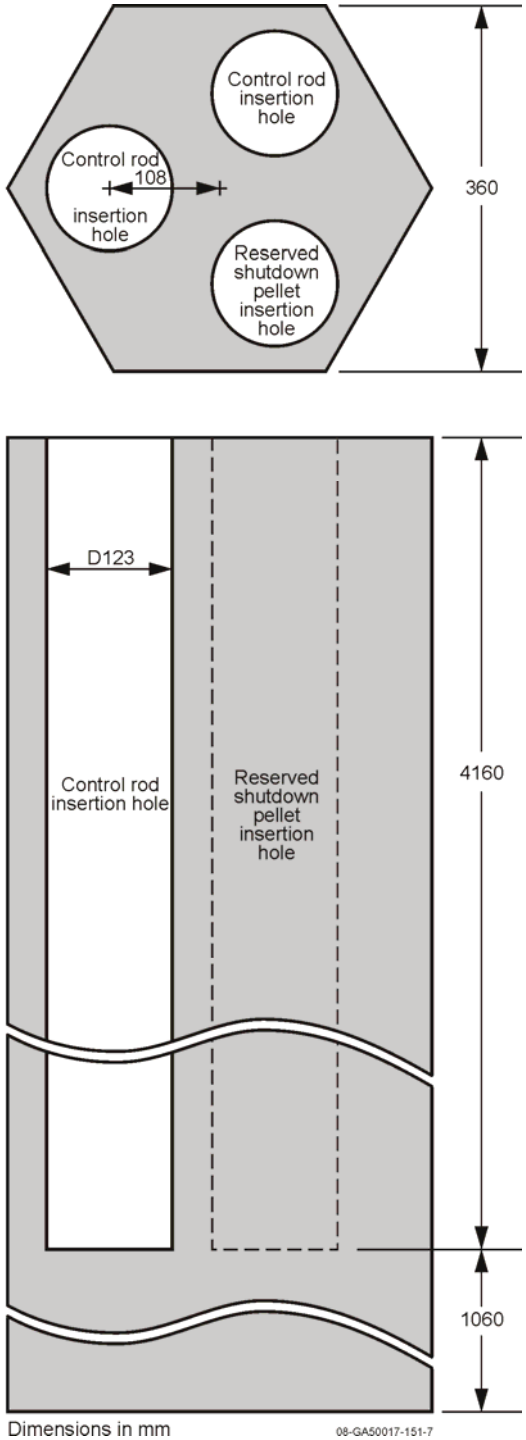


Figure 3.9. Control Rod Column. Dxx represents the diameter in xx (mm).

*3.1.2.6 Instrumentation*

**Instrumentation Components**

Instrumentation was not included in the benchmark model of the HTTR. An approximate bias with uncertainty was determined applied to the benchmark model (see Sections 2.1.2.6 and 3.1.1.1).

**Instrumentation Columns**

Instrumentation columns are modeled as a single unit without blocks, similar to the control rod columns. However, all three positions are empty (Figure 3.10).

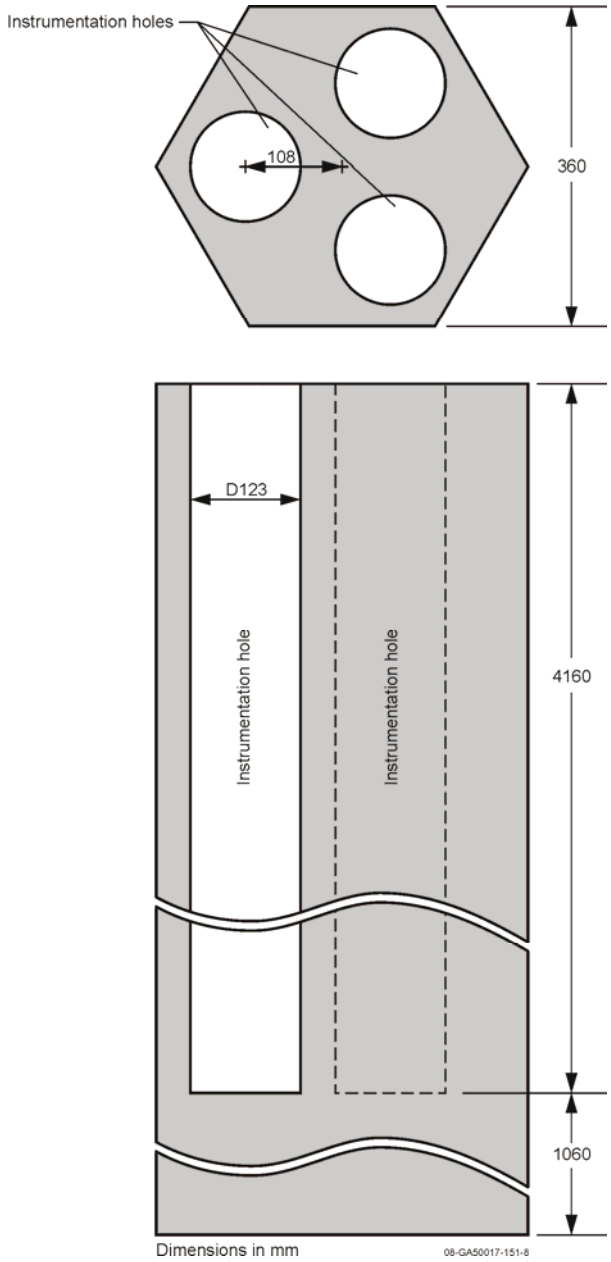


Figure 3.10. Instrumentation Column. Dxx represents the diameter in xx (mm).

### *3.1.2.7 Replaceable Reflector Columns*

The replaceable reflector columns are modeled as a solid unit and not as individual blocks, similar to the control rod and instrumentation columns but without any channels (Figure 3.11).

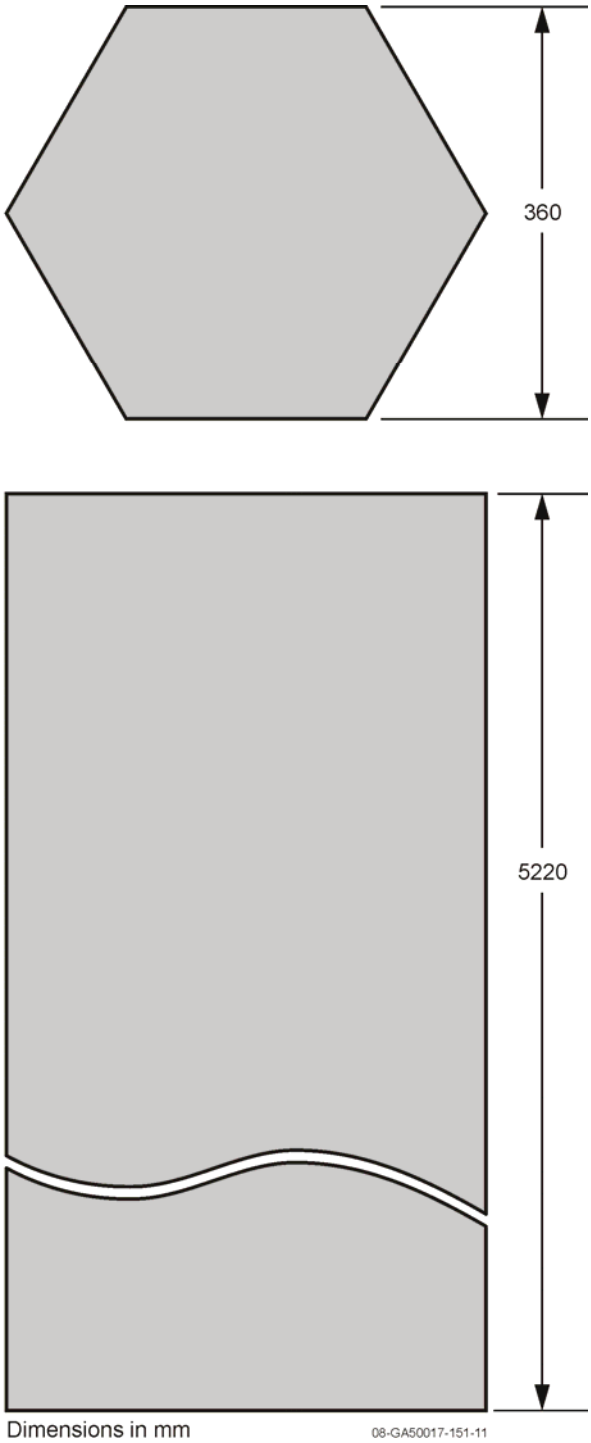


Figure 3.11. Replaceable Reflector Column.

### *3.1.2.8 Replaceable Reflectors Blocks in Fuel Columns*

The replaceable reflector blocks, located at the top and the bottom fuel columns, are shown in Figures 3.12 and 3.13, for the 33-pin and 31-pin fuel assemblies, respectively. The replaceable reflector blocks have the same regular hexagonal shape and pitch as described for the fuel blocks.

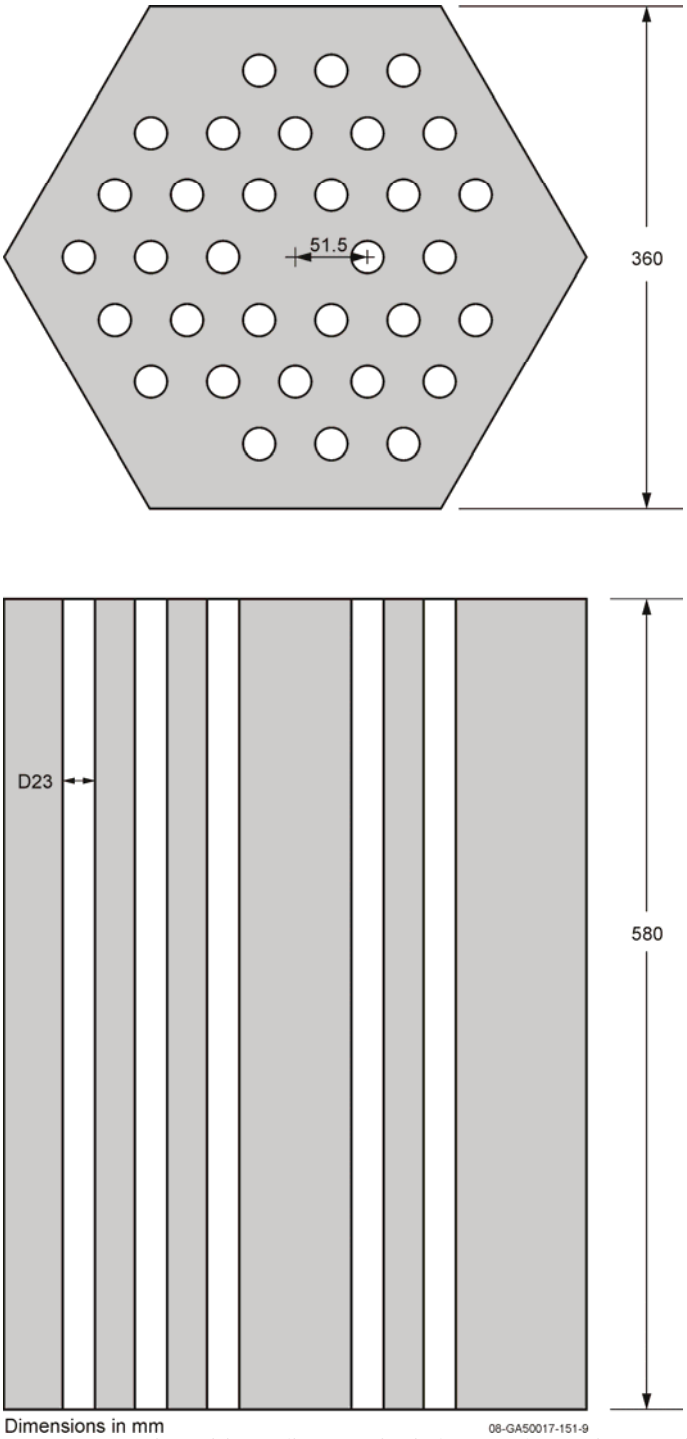


Figure 3.12. Replaceable Reflector Block for 33-Pin Fuel Assembly.
Dxx represents the diameter in xx (mm).

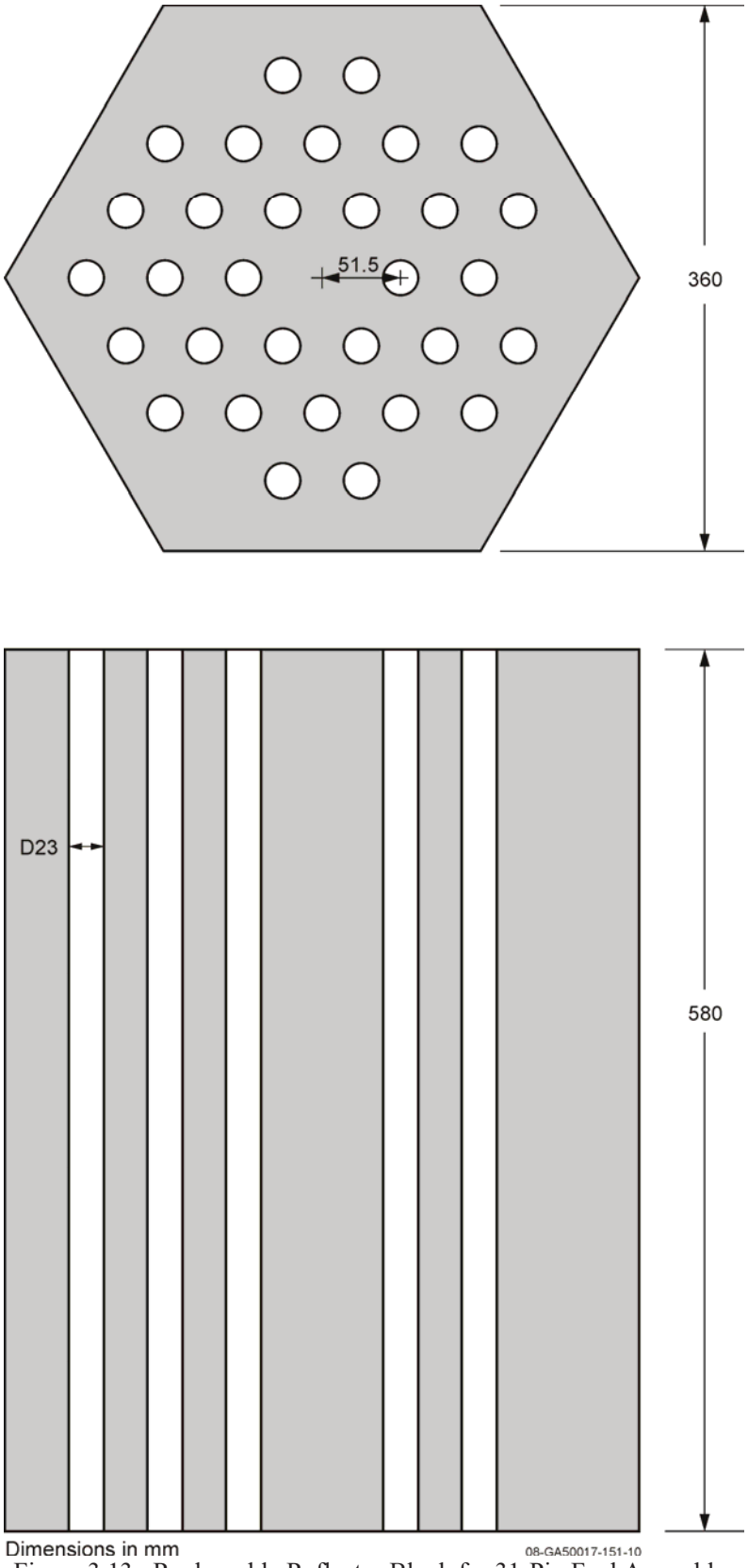


Figure 3.13. Replaceable Reflector Block for 31-Pin Fuel Assembly. Dxx represents the diameter in xx (mm).

*3.1.2.9 Fuel Columns*

The fuel columns are separated into four zones (as shown in Figure 1.46). Each zone has a specified pattern of uranium enrichment. Each column contains two top replaceable reflector blocks (Figure 3.12 for Zones 1 and 2 or Figure 3.13 for Zones 3 and 4), five fuel blocks (Figure 3.5 for Zones 1 and 2 and Figure 3.6 for Zones 3 and 4), and two bottom replaceable reflector blocks (Figure 3.11 for Zones 1 and 2 or Figure 3.13 for Zones 3 and 4). The second and third fuel blocks from the top contain burnable poison pellets that are more enriched than the pellets in the other three positions. Figure 3.14 shows the enrichment of the uranium (wt.%) in the TRISO fuel (upper left) and the natural boron content (wt.%) in the burnable pellets (lower right).

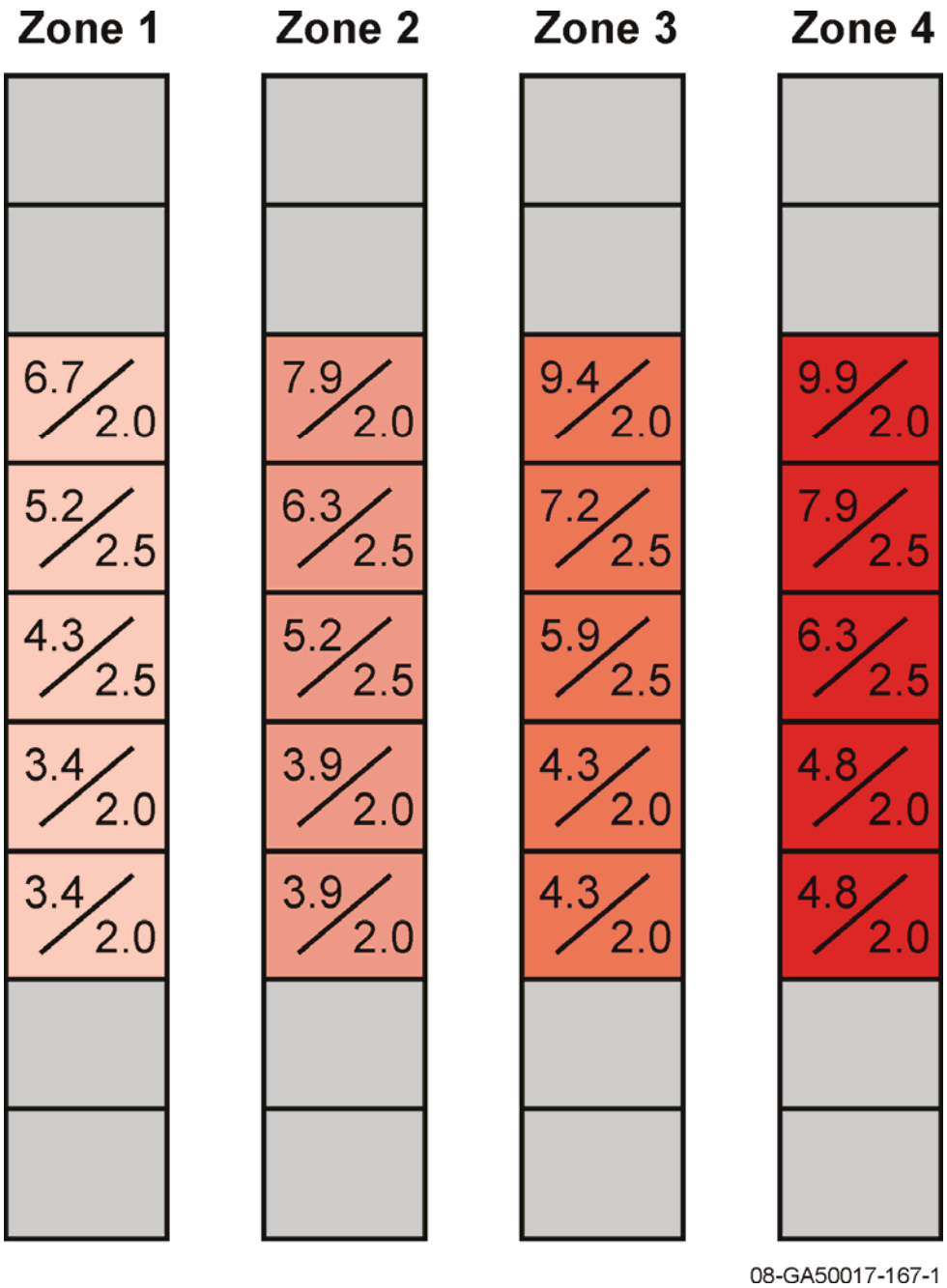


Figure 3.14. HTTR Fuel Zones.

### *3.1.2.10 Reactor Core Configuration*

The HTTR core configuration is shown in Figures 3.15, 3.16, 3.17. The first figure identifies the positions in the core for a given column type. The second figure provides the orientation of each column within its respective position in the core. The third figure shows the column identification number for each position in the core. Figure 3.18 shows a basic cross section of the HTTR core generated in MCNP.

The permanent reflector surrounding the core has been circularized with a radius of 2125 mm and height of 5220 mm.

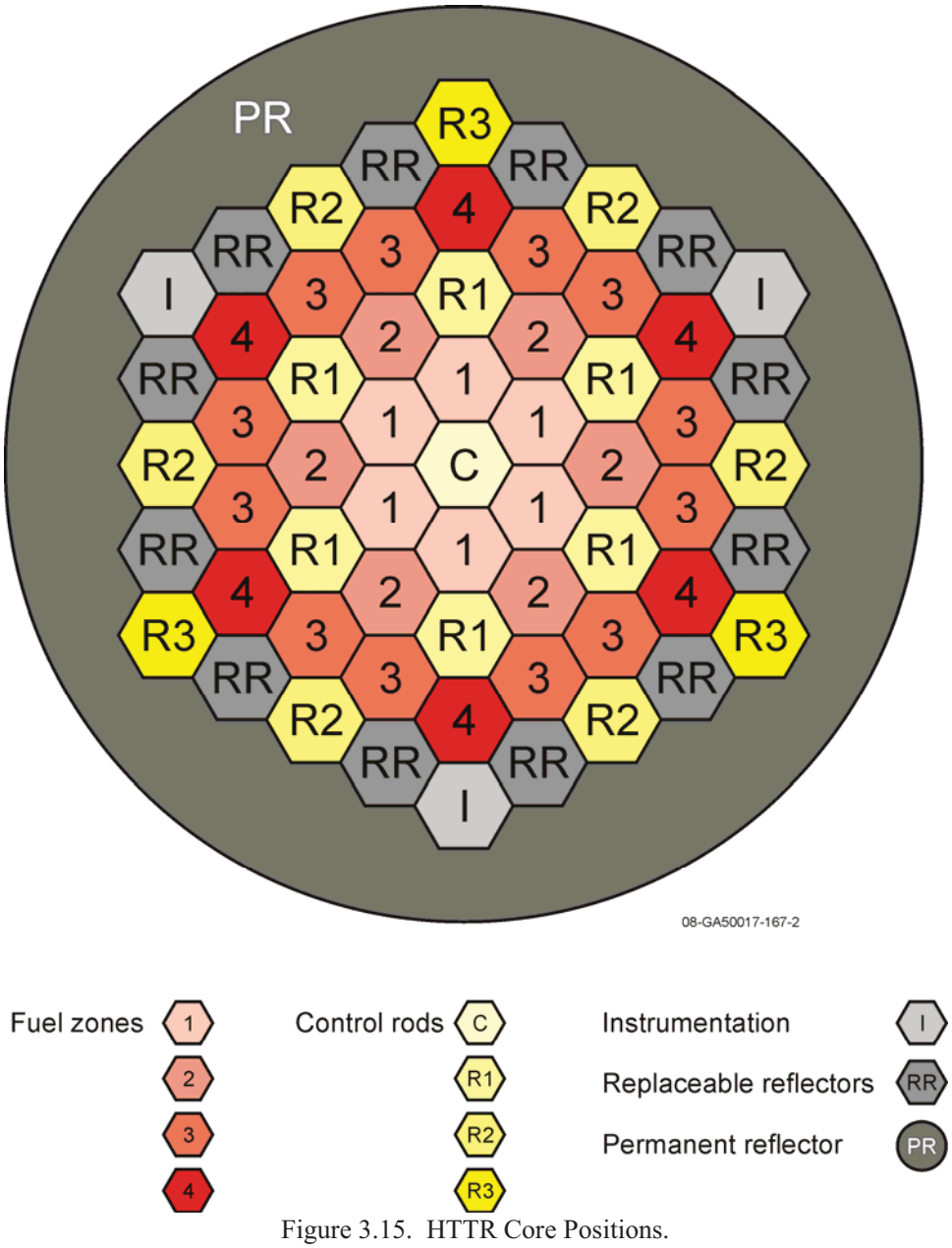


Figure 3.15. HTTR Core Positions.

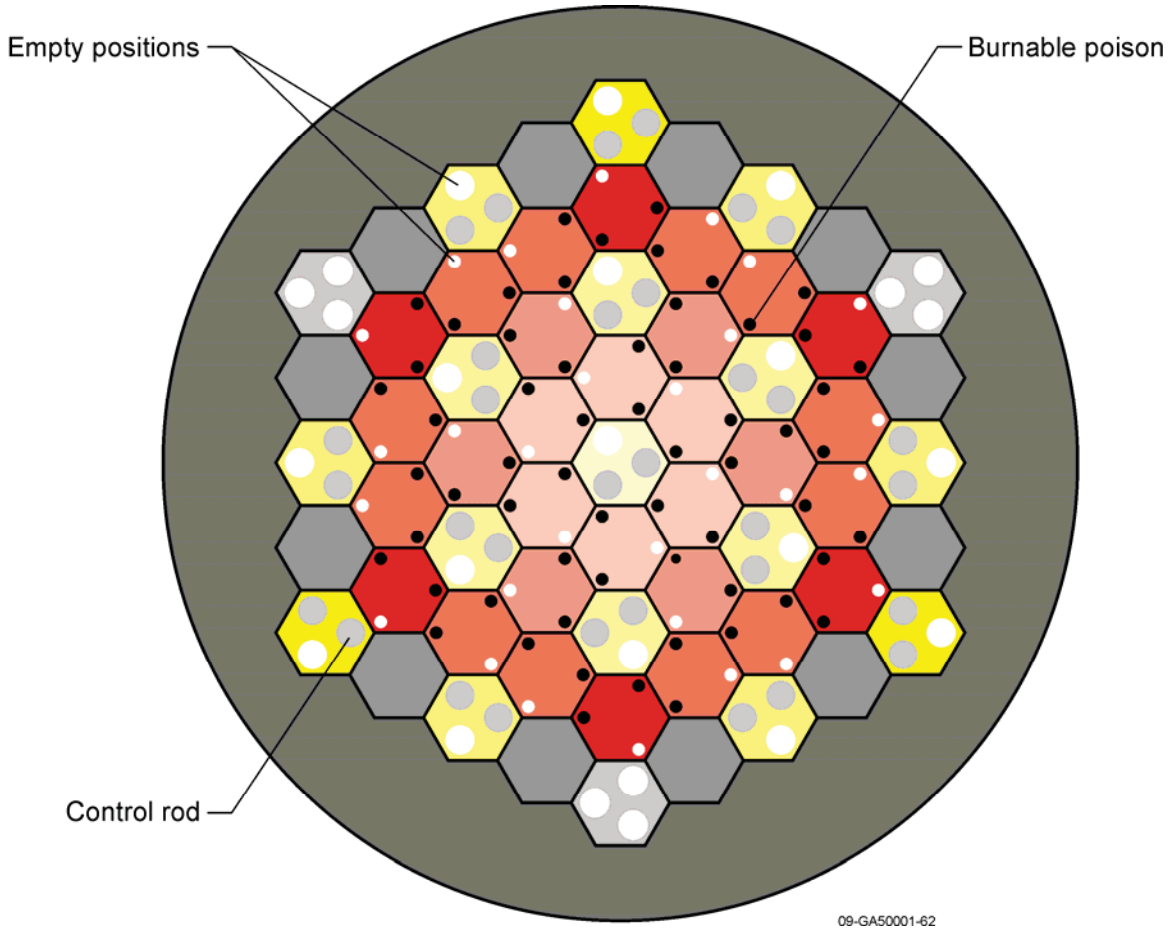


Figure 3.16. Fuel and Control Rod Column Orientations.

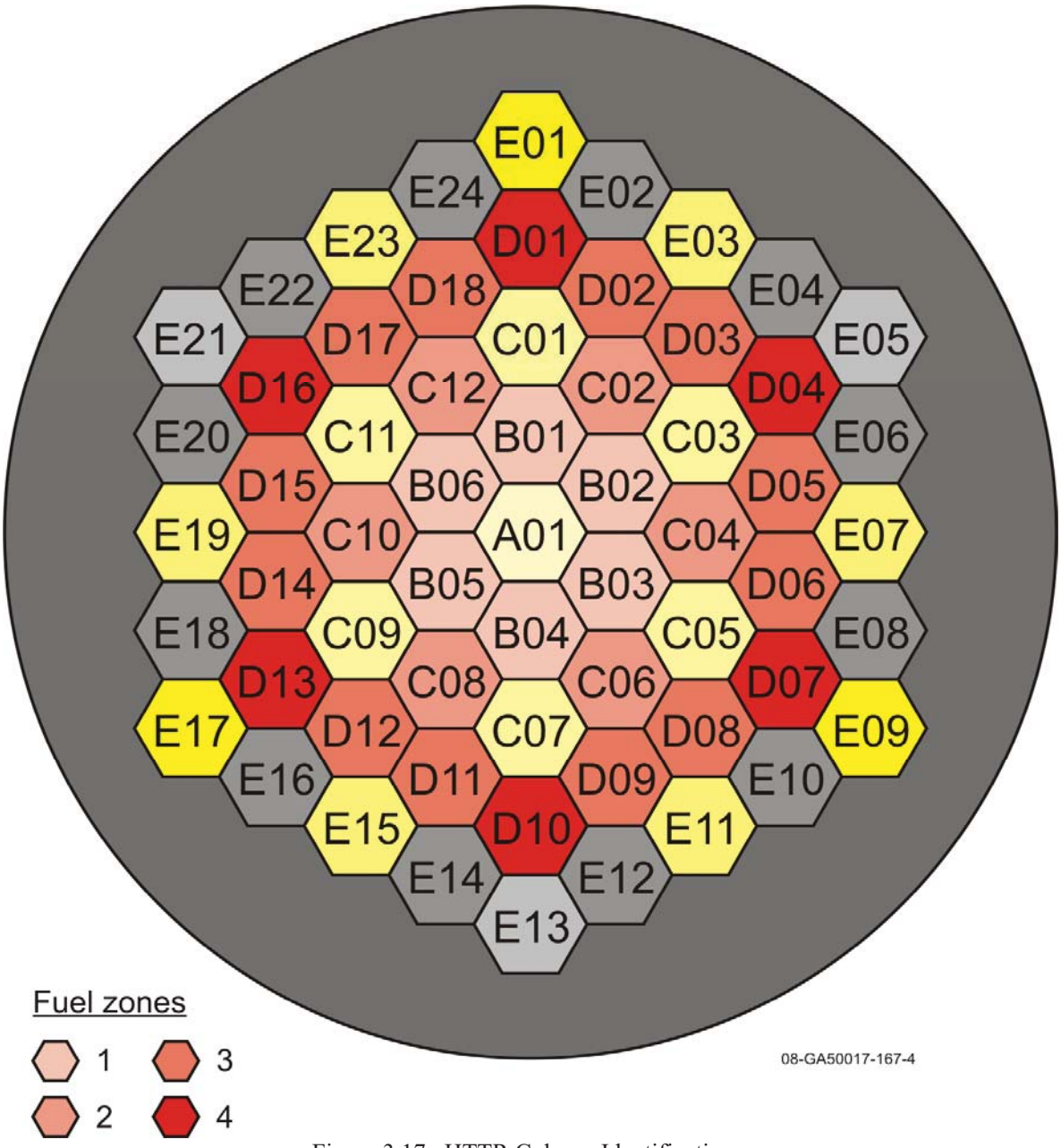


Figure 3.17. HTTR Column Identification.

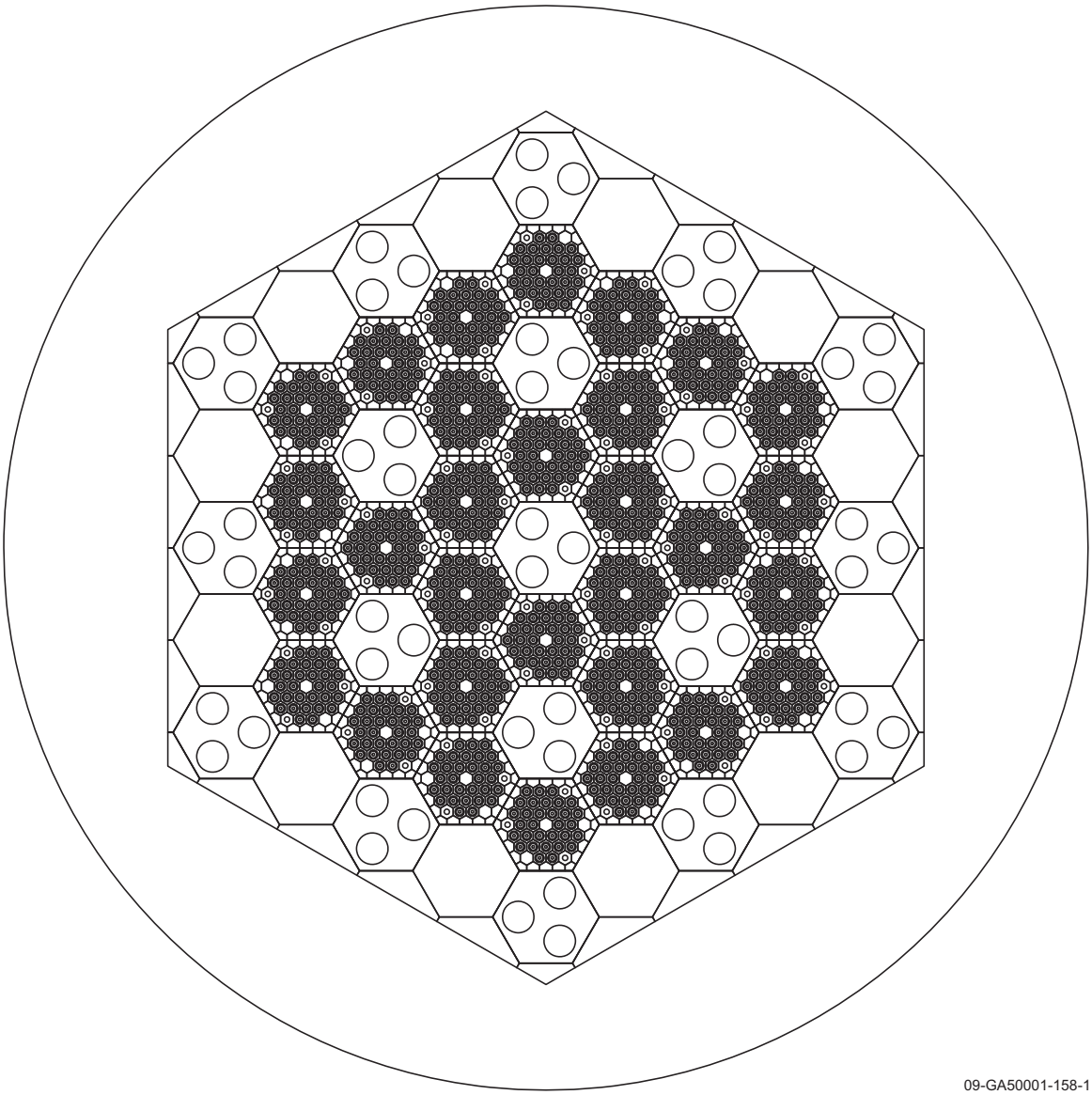

09-GA50001-158-1

Figure 3.18. Cross Section of the HTTR Core.

### *3.1.2.11 Critical Rod Positions*

Control rod positions are described with the zero position defined as level with the bottom place of the lowest fuel block (i.e. 1160 mm from the bottom of the core graphite).

The critical rod positions for the 30-fuel-column core are 1775 mm for the C, R1, and R2 positions, and 4049 mm for the R3 positions. All control rod positions are distances above the bottom of the lowest fuel block. Figure 3.19 provides reference between the various column types in the core and the control rod positions.

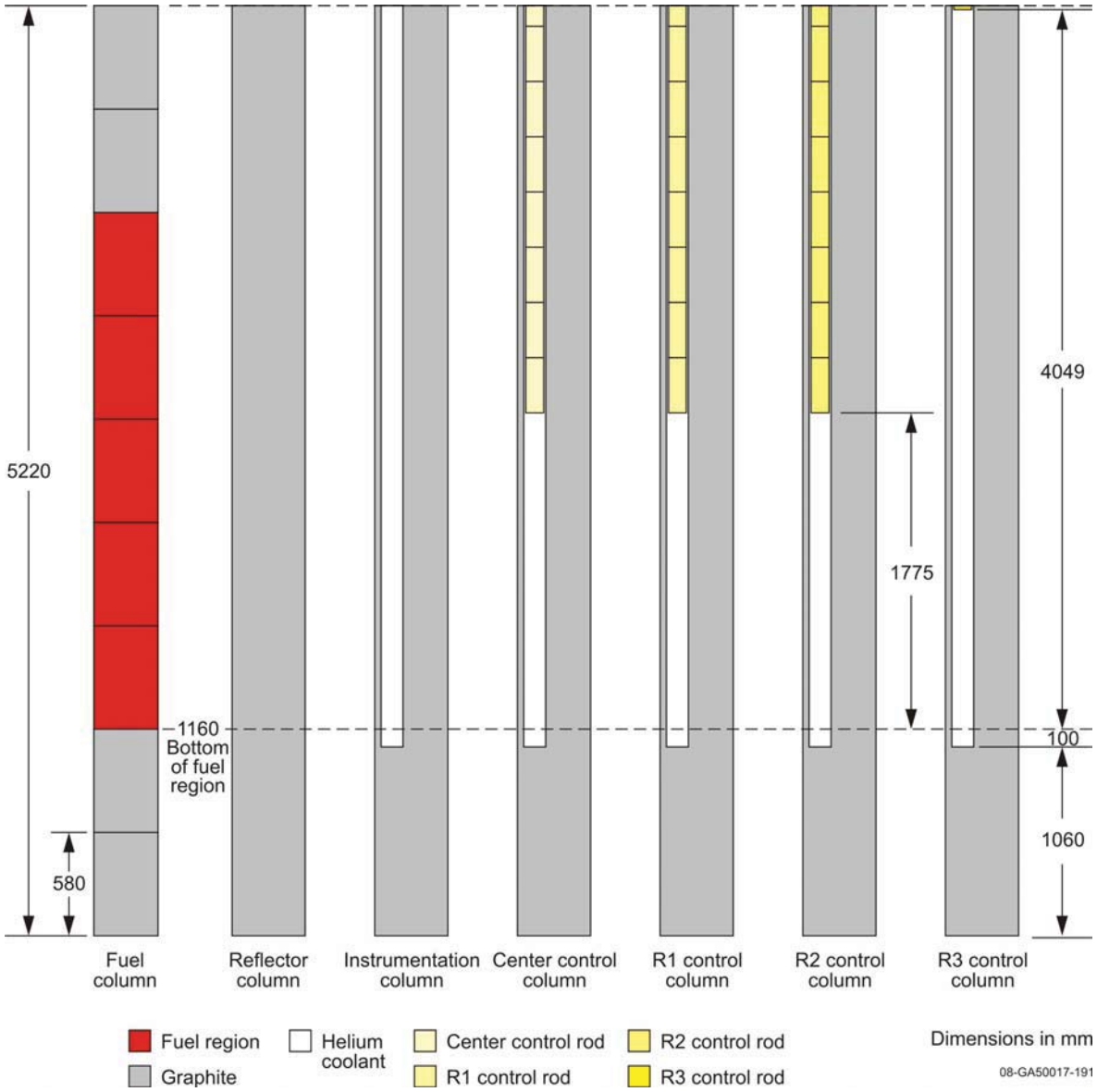


Figure 3.19. Axial Profile of Columns and Control Rod Positions.

### *3.1.2.12 Fully-Loaded Core Subcritical*

The benchmark model for the subcritical configuration is identical to the critical configuration except that all control rod pairs are inserted to a depth 55 mm below the bottom of the fuel region, as shown in Figure 3.20.

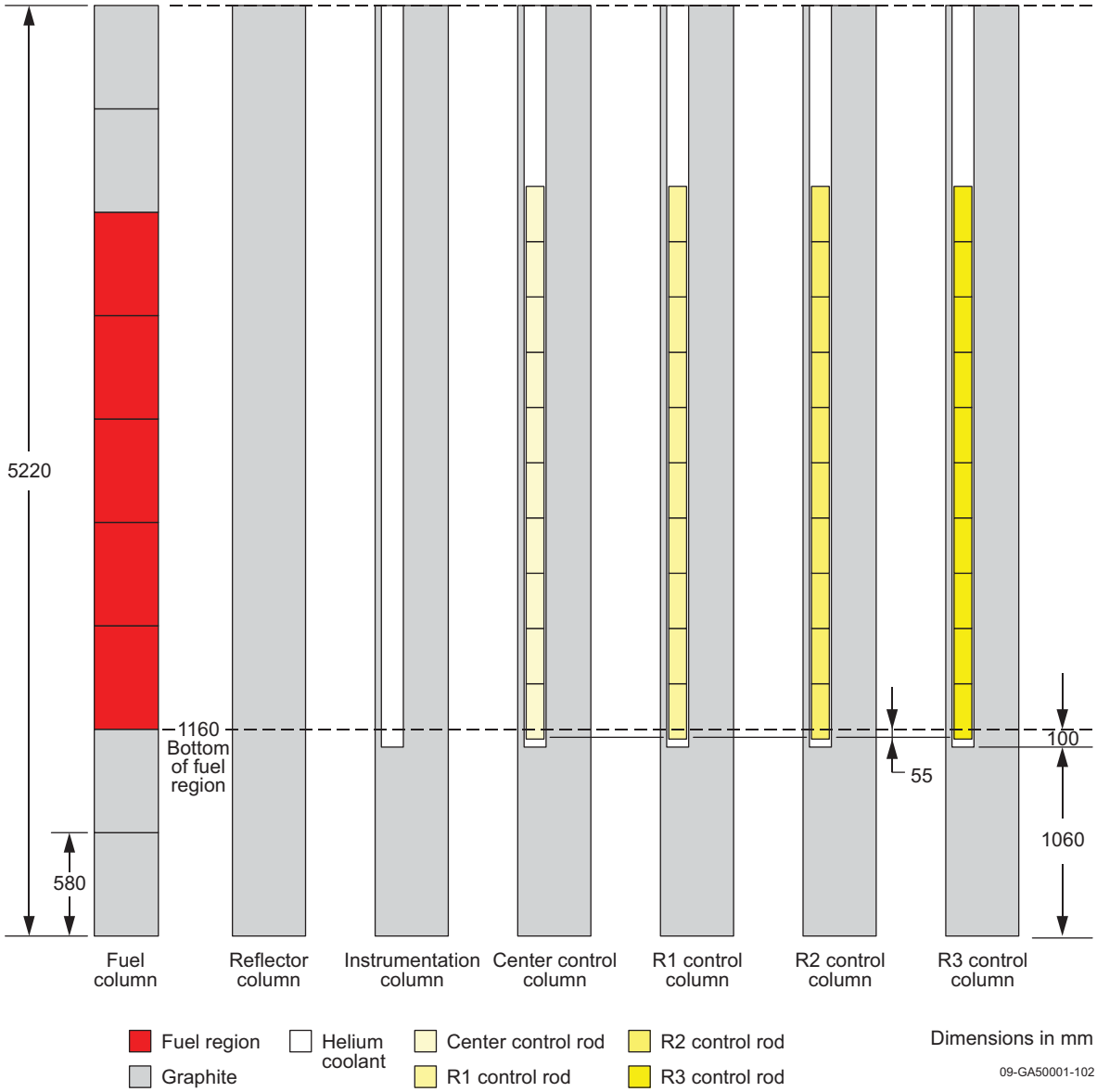


Figure 3.20. Axial Profile of Columns and Control Rod Positions for Subcritical Configuration.

### *3.1.2.13 Fully-Loaded Core Warm Critical*

The warm critical of the fully-loaded core has not been evaluated. Unfortunately, this data does not represent a valid benchmark experiment (see Section 2.1.9).

### 3.1.3 Material Data

*3.1.3.1 Pin-in-Block Fuel*

**TRISO Particles**

The mass density of the TRISO-coated $UO_2$ fuel kernels is 10.40363 g/cm$^3$ (such that the total uranium mass per fuel rod is 188.58 g) with an O/U ratio of ~2.00 and an equivalent natural-boron impurity content of 0.00015 wt.%. A summary of the atomic densities and compositions for the twelve enrichments found throughout the core are provided in Table 3.1.

Table 3.1. Atomic Densities (atoms/b-cm) of the $UO_2$ Kernels for Varying Enrichments.

| Isotope | 3.40 wt.% | 3.90 wt.% | 4.30 wt.% | 4.80 wt.% | 5.20 wt.% | 5.90 wt.% |
|---|---|---|---|---|---|---|
| $^{10}$B | 1.7299E-07 | 1.7299E-07 | 1.7299E-07 | 1.7299E-07 | 1.7299E-07 | 1.7299E-07 |
| O | 4.6404E-02 | 4.6404E-02 | 4.6404E-02 | 4.6404E-02 | 4.6404E-02 | 4.6404E-02 |
| $^{234}$U | 6.1026E-06 | 7.0000E-06 | 7.7180E-06 | 8.6154E-06 | 9.3334E-06 | 1.0590E-05 |
| $^{235}$U | 7.9888E-04 | 9.1637E-04 | 1.0104E-03 | 1.1278E-03 | 1.2218E-03 | 1.3863E-03 |
| $^{238}$U | 2.2405E-02 | 2.2288E-02 | 2.2195E-02 | 2.2078E-02 | 2.1984E-02 | 2.1821E-02 |
| Total | 6.9614E-02 | 6.9616E-02 | 6.9617E-02 | 6.9618E-02 | 6.9619E-02 | 6.9622E-02 |

Table 3.1 (cont'd.) Atomic Densities (atoms/b-cm) of the $UO_2$ Kernels for Varying Enrichments.

| Isotope | 6.30 wt.% | 6.70 wt.% | 7.20 wt.% | 7.90 wt.% | 9.40 wt.% | 9.90 wt.% |
|---|---|---|---|---|---|---|
| $^{10}$B | 1.7299E-07 | 1.7299E-07 | 1.7299E-07 | 1.7299E-07 | 1.7299E-07 | 1.7299E-07 |
| O | 4.6404E-02 | 4.6404E-02 | 4.6404E-02 | 4.6404E-02 | 4.6404E-02 | 4.6404E-02 |
| $^{234}$U | 1.1308E-05 | 1.2026E-05 | 1.2923E-05 | 1.4180E-05 | 1.6872E-05 | 1.7769E-05 |
| $^{235}$U | 1.4803E-03 | 1.5743E-03 | 1.6918E-03 | 1.8562E-03 | 2.2087E-03 | 2.3262E-03 |
| $^{238}$U | 2.1727E-02 | 2.1634E-02 | 2.1517E-02 | 2.1353E-02 | 2.1002E-02 | 2.0886E-02 |
| Total | 6.9623E-02 | 6.9624E-02 | 6.9625E-02 | 6.9628E-02 | 6.9632E-02 | 6.9634E-02 |

The material properties of the TRISO layers and graphite overcoat are provided in Table 3.2.

Table 3.2. Material Properties of the TRISO Coatings and Graphite Overcoat.

| Property | Buffer | IPyC | SiC | OPyC | Overcoat |
|---|---|---|---|---|---|
| Mass Density (g/cm$^3$) | 1.1 | 1.85 | 3.2 | 1.85 | 1.7 |
| B-nat Impurity (wppm) | 1.5 | 1.5 | 1.5 | 1.5 | 1.5 |
| Atomic Density (atoms/b-cm) | 5.5153E-02 | 9.2758E-02 | 9.6122E-02 | 9.2758E-02 | 8.5237E-02 |
| $^{10}$B | 1.8290E-08 | 3.0761E-08 | 5.3208E-08 | 3.0761E-08 | 2.8267E-08 |
| C-nat | 5.5153E-02 | 9.2758E-02 | 4.8061E-02 | 9.2758E-02 | 8.5237E-02 |
| Si | -- | -- | 4.8061E-02 | -- | -- |

## Compacts

The mass density of the fuel compact graphite matrix is 1.7 g/cm$^3$ with an equivalent natural-boron impurity content of 0.000082 wt.%. The atomic density and composition of the compact matrix is shown in Table 3.3.

Table 3.3. Atomic Densities of the Fuel Compact Graphite Matrix.

| Isotope | Atoms/b-cm |
|---|---|
| $^{10}$B | 1.5452E-08 |
| C-nat | 8.5237E-02 |
| Total | 8.5237E-02 |

## Fuel Element

The IG-110 graphite sleeve and end caps for the fuel pins have a mass density of 1.77 g/cm$^3$ and an equivalent natural-boron content of 0.000037 wt.%. The atomic density and composition of the graphite used in the fuel element is shown in Table 3.4.

Table 3.4. Atomic Densities of the Graphite Fuel Sleeve.

| Isotope | Atoms/b-cm |
|---|---|
| $^{10}$B | 7.2596E-09 |
| C-nat | 8.8747E-02 |
| Total | 8.8747E-02 |

### *3.1.3.2 Burnable Poisons*

The burnable poison pellets have a mass density of 1.80 g/cm$^3$; a summary of the atomic densities and compositions for the two natural-boron concentrations employed in the core are provided in Table 3.5. The mass density of the graphite disks used to separate the burnable poison pellets is 1.77 g/cm$^3$ with an equivalent natural-boron content of 0.000037 wt.%. The atomic density and composition of the graphite disks is also found in Table 3.5

Table 3.5. Atomic Densities (atoms/b-cm) of the Burnable Poison Pellets and Graphite Disks.

| Isotope | 2.00 wt.% | 2.50 wt.% | Disks |
|---|---|---|---|
| $^{10}$B | 3.9906E-04 | 4.9882E-04 | 7.2596E-09 |
| $^{11}$B | 1.6063E-03 | 2.0078E-03 | -- |
| C-nat | 8.8446E-02 | 8.7995E-02 | 8.8747E-02 |
| Total | 9.0451E-02 | 9.0501E-02 | 8.8747E-02 |

### *3.1.3.3 Fuel Blocks*

The IG-110 graphite fuel blocks have a mass density of 1.7512 g/cm$^3$ (1.76 g/cm$^3$ base density decreased by a 0.5 % void fraction) and an equivalent natural-boron content of 0.000059 wt.%. The atomic density and composition of the graphite fuel blocks is shown in Table 3.6.

Table 3.6. Atomic Densities of the Graphite Fuel Blocks.

| Isotope | Atoms/b-cm |
|---|---|
| $^{10}$B | 1.1453E-08 |
| C-nat | 8.7804E-02 |
| Total | 8.7804E-02 |

### *3.1.3.4 Dummy Blocks*

The 30-fuel-column core does not contain dummy blocks.

### *3.1.3.5 Control Rod System*

**Control Rods**

The absorber compacts have a mass density of 1.9 g/cm$^3$ and have a composition and atomic density as described in Table 3.7.

Table 3.7. Atomic Densities of the Absorber Compacts.

| Isotope | Atoms/b-cm |
|---|---|
| $^{10}$B | 6.3184E-03 |
| $^{11}$B | 2.5432E-02 |
| C-nat | 6.6685E-02 |
| Total | 9.8436E-02 |

The Alloy 800H cladding of the control rods has a mass density of 8.03 g/cm$^3$ with a composition and atomic density as shown in Table 3.8.

Table 3.8. Atomic Densities of the Alloy 800H Clad.

| Isotope | Atoms/b-cm |
|---|---|
| C-nat | 3.2210E-04 |
| Al | 6.7209E-04 |
| Si | 6.0263E-04 |
| P | 3.1225E-05 |
| S | 1.5081E-05 |
| Ti | 3.7884E-04 |
| Cr | 1.9530E-02 |
| Mn | 8.8022E-04 |
| Fe | 3.8092E-02 |
| Ni | 2.6777E-02 |
| Cu | 2.2830E-04 |
| Total | 8.7530E-02 |

**Control Rod Columns**

The IG-110 graphite fuel columns are modeled with the same physical properties as the fuel blocks in Section 3.1.3.3 and Table 3.6.

### *3.1.3.6 Instrumentation*

**Instrumentation Components**

Insufficient information was available to adequately model instrumentation in the HTTR. An approximate bias with uncertainty was determined applied to the benchmark model (see Sections 2.1.2.6 and 3.1.1.1).

**Instrumentation Columns**

The IG-110 graphite instrumentation columns are modeled with the same physical properties as the fuel blocks in Section 3.1.3.3 and Table 3.6.

### *3.1.3.7 Replaceable Reflector Columns*

The IG-110 replaceable reflector columns are modeled with the same physical properties as the fuel blocks in Section 3.1.3.3 and Table 3.6.

### *3.1.3.8 Replaceable Reflectors Blocks in Fuel Columns*

The IG-110 replaceable reflector blocks are modeled with the same physical properties as the fuel blocks in Section 3.1.3.3 and Table 3.6.

### *3.1.3.9 Permanent Reflector*

The PGX graphite permanent reflector has a mass density of 1.71789 g/cm$^3$ (1.76 g/cm$^3$ base density decreased by a 0.7 % void fraction) and an equivalent natural-boron content of 0.000191 wt.%. The atomic density and composition of the permanent reflector is shown in Table 3.9.

Table 3.9. Atomic Densities of the Permanent Reflector.

| Isotope | Atoms/b-cm |
|---|---|
| $^{10}$B | 3.6372E-08 |
| C-nat | 8.6134E-02 |
| Total | 8.6134E-02 |

### *3.1.3.10 Helium Coolant*

The helium coolant has an atomic density of 2.4616E-05 atoms/b-cm (mass density of 1.6361 × 10$^{-4}$ g/cm$^3$). No impurities are modeled in the coolant.

$$\frac{n}{V}=\frac{P\cdot N_A}{R\cdot T}=\frac{(1atm)\cdot\left(0.60221\frac{atoms\cdot cm^2}{mol\cdot b}\right)}{\left(0.082054\frac{L\cdot atm}{mol\cdot K}\right)\cdot(298.15K)}\cdot\left(\frac{1L}{1000cm^3}\right)=2.4616\times10^{-5}\frac{atoms}{b\cdot cm}.$$

$$\rho=\frac{n}{V}\cdot\frac{M}{N_A}=2.4616\times10^{-5}\frac{atoms}{b\cdot cm}\cdot\frac{4.002602\frac{g}{mol}}{\left(0.60221\frac{atoms\cdot cm^2}{mol\cdot b}\right)}=1.6361\times10^{-4}\frac{g}{cm^3}.$$

#### *3.1.3.11 Fully-Loaded Core Subcritical*

The materials in the benchmark model for the subcritical configuration are identical to those in the critical configuration.

#### *3.1.3.12 Fully-Loaded Core Warm Critical*

The warm critical of the fully-loaded core has not been evaluated. Unfortunately, this data does not represent a valid benchmark experiment (see Section 2.1.9).

### 3.1.4 Temperature Data

#### *3.1.4.1 Fully-Loaded Core Critical*

The benchmark model temperature is 300 K.

#### *3.1.4.2 Fully-Loaded Core Subcritical*

The benchmark model temperature is 300 K.

#### *3.1.4.3 Fully-Loaded Core Warm Critical*

The warm critical of the fully-loaded core has not been evaluated. Unfortunately, this data does not represent a valid benchmark experiment (see Section 2.1.9).

### 3.1.5 Experimental and Benchmark-Model $k_{eff}$ and / or Subcritical Parameters

#### *3.1.5.1 Fully-Loaded Core Critical*

The experimental $k_{eff}$ was approximately at unity, made to delayed critical. A comprehensive bias assessment could not be performed; therefore, the experimental $k_{eff}$ was adjusted only for the bias incurred by removing the instrumentation in the core (Section 3.1.1.1). Furthermore, the uncertainty in the benchmark model is the same as the uncertainty evaluated for the experimental model, as the bias uncertainty for instrumentation has already been included.

The biased benchmark model $k_{eff}$ is 1.0025 with an evaluated uncertainty between -0.0060 and +0.0071.

#### *3.1.5.2 Fully-Loaded Core Subcritical*

The experimental $k_{eff}$ was 0.685. A comprehensive bias assessment could not be performed; therefore, the experimental $k_{eff}$ was adjusted only for the bias incurred by removing the instrumentation in the core (Section 3.1.1.1). Furthermore, the uncertainty in the benchmark model is the same as the uncertainty evaluated for the experimental model, as the bias uncertainty for instrumentation has already been included.

The biases benchmark model $k_{eff}$ is 0.6876 with an evaluated uncertainty of ±0.0104.

The subcritical configurations developed during initial core loading were not evaluated.

#### *3.1.5.3 Fully-Loaded Core Warm Critical*

The warm critical of the fully-loaded core has not been evaluated. Unfortunately, this data does not represent a valid benchmark experiment (see Section 2.1.9).

## 3.2 Benchmark-Model Specifications for Buckling and Extrapolation-Length Measurements

Buckling and extrapolation length measurements were not made.

## 3.3 Benchmark-Model Specifications for Spectral Characteristics Measurements

Spectral characteristics measurements were not made.

## 3.4 Benchmark-Model Specifications for Reactivity Effects Measurements

### 3.4.1 Description of the Benchmark Model Simplifications

The simplifications of the benchmark model for determination of the reactivity effects measurements in the HTTR (described in Section 1.4) are identical to those of the critical fully-loaded core configuration described in Section 3.1.1.

The benchmark models for excess reactivity measurements also utilize the models for the 19-, 21-, 24-, and 27-fuel-column core configurations described in Section 3.1 of HTTR-GCR-RESR-002.

### 3.4.2 Dimensions

#### *3.4.2.1 Excess Reactivity*

The dimensions of the benchmark model for determination of the excess reactivity measurements in the HTTR are identical to those of the critical core configurations described in Section 3.1.2 of this benchmark report and in HTTR-GCR-RESR-002.

The control rod positions are adjusted to assess the reactivity worth of the addition of fuel block columns into the HTTR core. All control rods in the 19-fuel-column configuration are fully withdrawn and the new eigenvalue is compared to that from the critical configuration. Then for the remaining four configurations, the rods positions are removed only to their respective positions in the prior core configuration; i.e. the 21-fuel-column configuration has the control rod positions raised to those for the critical configuration of the 19-fuel-column configuration. All the control rods are also completely withdrawn from the fully-loaded 30-fuel-column core configuration to provide an additional assessment of the total core excess reactivity. The cumulative excess reactivity values are determined by summation of the individual excess reactivity values.

#### *3.4.2.2 Shutdown Margin*

The benchmark models for determination of the shutdown margins is identical to the critical configuration except for the control rod pair positioning. There are three shutdown margin configurations:

1. Full insertion of the radial reflector control rods, R2 and R3, from the critical core configuration (Section 3.1),
2. Full insertion of the fuel region control rods, C and R1, from the previous configuration, and
3. Full insertion of all control rods from the critical core configuration (Section 3.1).

The control rod positions for the full core configuration are shown in Figure 3.19. The configuration of the control rods for the subcritical configuration in which all control rods are fully inserted is shown in Figure 3.20. The intermediary configuration with only the radial reflector control rods fully inserted is shown in Figure 3.21.

The shutdown margin is determined by computing the reactivity difference for the three configurations outlined above.

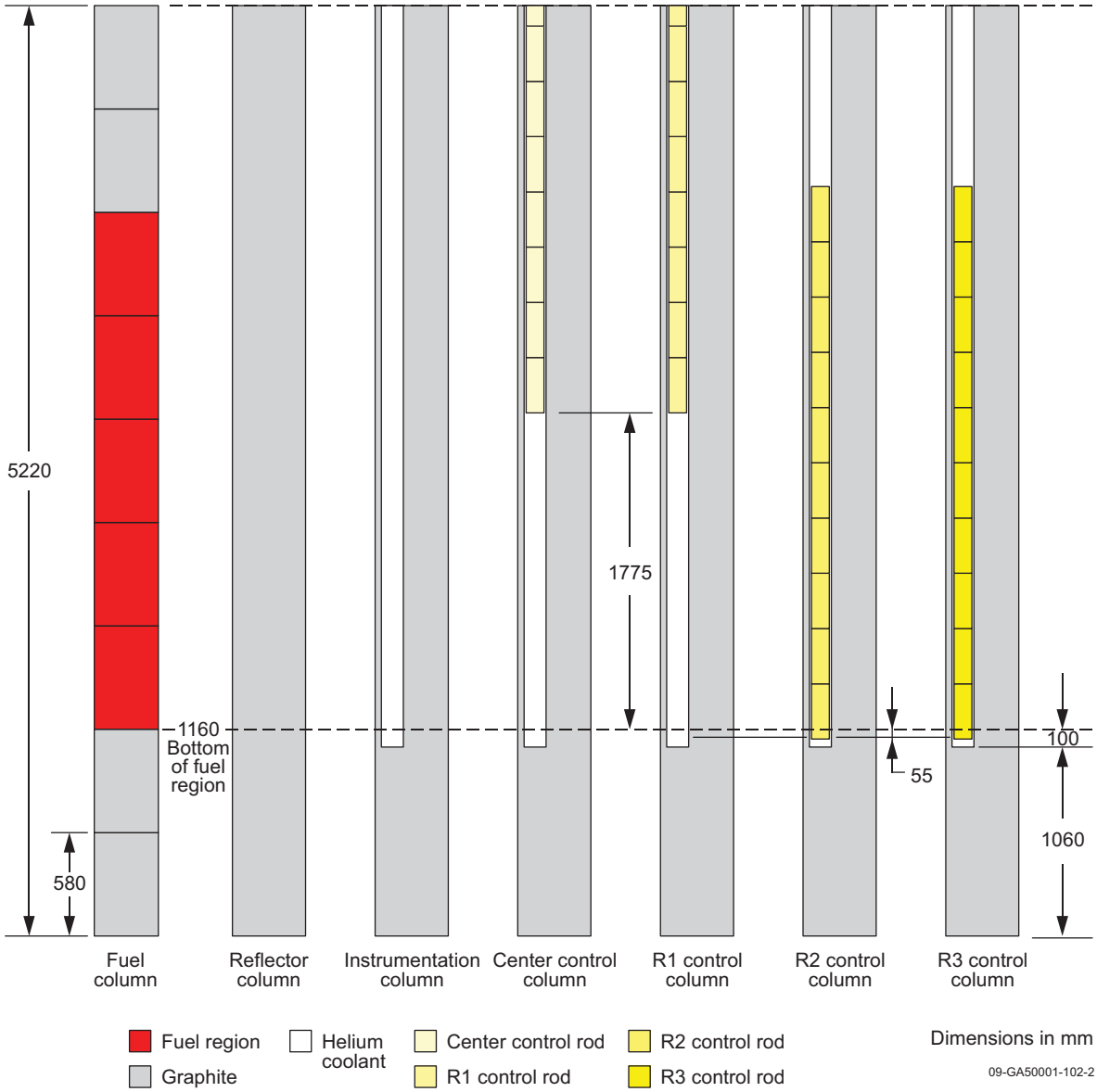


Figure 3.21. Axial Profile of Columns and Control Rod Positions for Full Insertation of Radial Reflector Control Rod.

### *3.4.2.3 Control Rod Worth*

Benchmark values for the control rod worths have not been completely evaluated. Further analysis is necessary to assess the current discrepancies between the computational and experimental data.

## 3.4.3 Material Data

The materials in the benchmark model for determination of the reactivity effects measurements in the HTTR are identical to those of the critical fully-loaded core configuration described in Section 3.1.3.

The benchmark models for excess reactivity measurements also utilize the dummy block material for the 19-, 21-, 24-, and 27-fuel-column core configurations described in Section 3.1.3 of HTTR-GCR-RESR-002.

### 3.4.4 Temperature Data

The benchmark model temperature is 300 K.

### 3.4.5 Benchmark-Model Specification for Reactivity Effects Parameters

#### *3.4.5.1 Excess Reactivity*

The expected benchmark values for the excess reactivity measurements in the HTTR, with their respective uncertainties (from Section 2.4.1), are shown in Table 3.10.

Table 3.10. Excess Reactivity Measurements in the HTTR.

| Data Point | Fuel Columns | Excess Reactivity $\Delta\rho_{exm}$ (% $\Delta$k/k) | Excess Reactivity $\rho_{exm}$ (% $\Delta$k/k) |
|---|---|---|---|
| 1 | 19 | -- | 2.4 ± 0.24 |
| 2 | 21 | -- | 4.0 ± 1.1 |
| 3 | 24 | 3.7 ± 1.0 | 7.7 ± 2.1 |
| 4 | 27 | 3.0 ± 0.9 | 10.7 ± 3.0 |
| 5 | 30 | 1.3 ± 0.3 | 12.0 ± 3.3 |

#### *3.4.5.2 Shutdown Margin*

The expected benchmark values for the shutdown margin measurements in the HTTR, with their respective uncertainties (from Section 2.4.2), are shown in Table 3.11.

Table 3.11. Shutdown Margin Measurements for the HTTR.

| Configuration | | Benchmark (% $\Delta$k/k) |
|---|---|---|
| 1 | Insertion of Control Rods in Reflector Region | -12.1 ± 0.6 |
| 2 | Insertion of Control Rods in Fuel Region | -34.2 ± 1.7 |
| 3 | Insertion of All Control Rods | -46.3 ± 1.2 |

#### *3.4.5.3 Control Rod Worth*

Benchmark values for the control rod worths have not been completely evaluated. Further analysis is necessary to assess the current discrepancies between the computational and experimental data.

## 3.5 Benchmark-Model Specifications for Reactivity Coefficient Measurements

Reactivity coefficient measurements have not been evaluated.

## 3.6 Benchmark-Model Specifications for Kinetics Measurements

Kinetics measurements have not been evaluated.

## 3.7 Benchmark-Model Specifications for Reaction-Rate Distribution Measurements

### 3.7.1 Description of the Benchmark Model Simplifications

The simplifications of the benchmark model for determination of the axial neutron fission reaction-rate in the instrumentation columns of the HTTR (described in Section 1.7) are identical to those of the critical fully-loaded core configuration described in Section 3.1.1.

### 3.7.2 Dimensions

The dimensions of the benchmark model for determination of the axial neutron reaction-rate in the instrumentation columns of the HTTR are identical to those of the critical fully-loaded core configuration described in Section 3.1.2.

The axial neutron fission reaction-rate in the instrumentation columns is calculated by taking the benchmark model of the fully-loaded 30-fuel-column core and superimposing a flux tally over one of the instrumentation column positions: E05, E13, or E21. The flux is computed for 6.15-cm radius discs with a thickness of 1 cm located at the center of one instrumentation channel in each instrumentation column (see Figure 3.22). A total of 522 cm, representing the total height of the core fuel and reflector blocks, was modeled. The (x, y) coordinates used for columns E05, E13, and E21, are (114.6005, 72.4), (5.4, -135.447), and (-120, 63.04693), respectively, where the origin is located at the radial center of the core.

The F4 flux tally is used in MCNP, which determines the flux across a cell volume by tabulating the average track length of the neutrons.[a] The tally is then modified by a tally multiplier card, Fm, that accounts for the total fission cross section of $^{235}$U, the fissile material in the fission chambers, to obtain the neutron reaction-rate in each instrumentation column.

The calculated neutron fission reaction rates are obtained by taking the variance-weighted average of results obtained using six variations of the input deck (Appendix A.1) with different random number seeds and tallies of the neutron reaction rate (Appendix A.3). This approach was used to reduce the statistical uncertainty in the neutron flux tallies because the relative error values obtained can underpredict the true uncertainty in the calculated neutron flux.[b] Therefore, the final calculated values are obtained from a total of 18 reaction-rate tallies (6 input decks with 3 instrumentation columns each).

The average of the neutron reaction-rate in each position is taken and normalized to represent the calculated axial neutron reaction-rate profile:

$$\phi(z)_{normalized} = \frac{\phi(z)}{\phi_{maximum}},$$

[a] X-5 Monte Carlo Team, "MCNP – A General Monte Carlo N-Particle Transport Code, Version 5, Volume II: User's Guide," LA-CP-03-0245 (April 24, 2003; revised October 2, 2005).

[b] F. B. Brown, "A Review of Best Practices for Monte Carlo Criticality Calculations," *Proc. NCSD 2009*, Richland, WA, September 13-17 (2009).

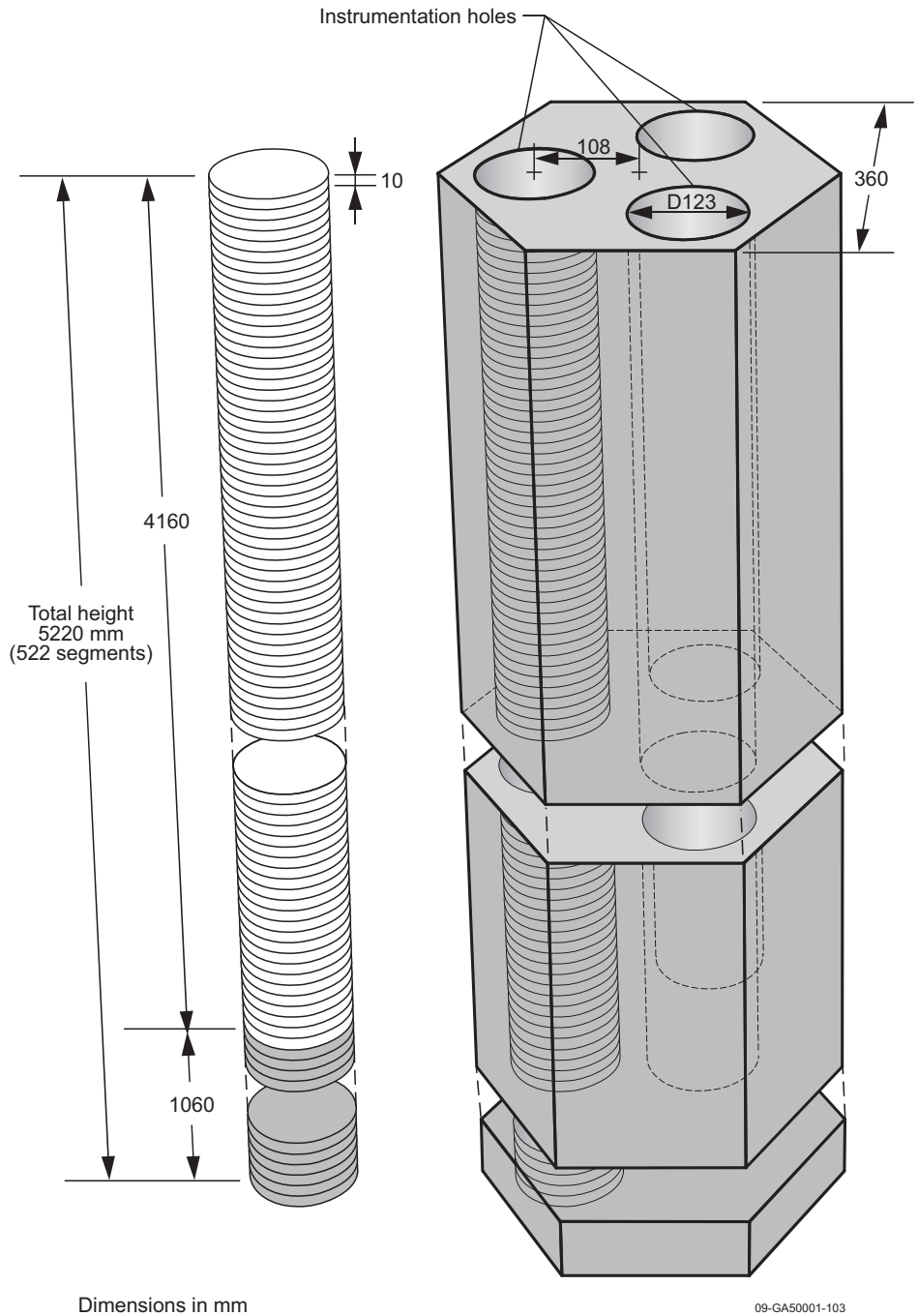


Figure 3.22. Placement of Axial Flux Tally in the Instrumentation Column.

### 3.7.3 Material Data

The materials in the benchmark model for determination of the axial neutron reaction-rate in the instrumentation columns of the HTTR are identical to those in the critical fully-loaded core configuration described in Section 3.1.3.

### 3.7.4 Temperature Data

The benchmark model temperature is 300 K.

### 3.7.5 Benchmark-Model Specification for Reaction-Rate Distribution Parameters

The expected benchmark values for the normalized axial neutron reaction-rate in the instrumentation columns of the HTTR, with their respective uncertainties (from Section 2.7.1), are shown in Table 3.12. The normalization is to the highest reaction-rate value, which is data point 4 at a height of 82.53 cm.

Table 3.12. Axial Neutron Fission Reaction Rate in the Instrumentation Columns of the HTTR.

| Data Point | Height (cm)[(a)] | Normalized Benchmark Reaction Rate | ± | 1σ | 1σ (%) |
|---|---|---|---|---|---|
| 1 | 19.68 | 0.8381 | ± | 0.0127 | 1.51 |
| 2 | 28.47 | 0.8759 | ± | 0.0126 | 1.44 |
| 3 | 71.81 | 0.9991 | ± | 0.0128 | 1.28 |
| 4 | 82.53 | 1.0000 | ± | 0.0116 | 1.16 |
| 5 | 86.52 | 0.9784 | ± | 0.0242 | 2.48 |
| 6 | 93.61 | 0.9703 | ± | 0.0306 | 3.16 |
| 7 | 144.22 | 0.7673 | ± | 0.0277 | 3.61 |
| 8 | 202.28 | 0.3695 | ± | 0.0158 | 4.29 |
| 9 | 261.19 | 0.1302 | ± | 0.0094 | 7.21 |
| 10 | 319.13 | 0.0440 | ± | 0.0057 | 12.97 |

(a) The height is in reference to the position relative to the bottom of the fifth layer of fuel.

## 3.8 Benchmark-Model Specifications for Power Distribution Measurements

Power distribution measurements were not made.

## 3.9 Benchmark-Model Specifications for Isotopic Measurements

Isotopic measurements were not made.

## 3.10 Benchmark-Model Specifications for Other Miscellaneous Types of Measurements

Other miscellaneous types of measurements were not made.

## 4.0 RESULTS OF SAMPLE CALCULATIONS

### 4.1 Results of Calculations of the Critical or Subcritical Configurations

Random particles cannot be easily modeled in MCNP. Therefore an ordered-lattice approach for modeling the benchmark was implemented, and results are provided.

The computed $k_{eff}$ values for the benchmark model of the fully-loaded 30-fuel-column core evaluated with MCNP using the ENDF/B-V.2, -VI.8, and -VII.0, JEFF-3.1, and JENDL-3.3 cross section libraries. All benchmark model calculations are compared against the expected benchmark value reported in Section 3.1.5. The total uncertainty in the expected value of $k_{eff}$ is taken from Section 2.1.6. The JENDL-3.3 analysis was performed with the inclusion of ENDF/B-VII.0 thermal neutron scattering data because it was not included in the JENDL-3.3 library. Thermal neutron scattering, or $S(\alpha,\beta)$, adjusts the neutron cross sections for neutron upscatter at thermal energies and provides scattering data for elements bound within specific materials. The $k_{eff}$ values were also calculated using ENDF/B-VII.0 and MCNPX. The MCNP5 calculations were performed with 1,050 generations (skipping the first 50) and 50,000 neutrons per generation.

It is currently difficult to obtain the necessary information to further improve the confidence in the benchmark model and effectively reduce the overall uncertainty; the necessary data is proprietary and its released is being restricted, because the benchmark configuration of the HTTR core is the same that is currently in operation. Once this information is made available, the HTTR benchmark can be adjusted as appropriate.

#### 4.1.1 Ordered TRISO Lattice within the Fuel Compacts

The TRISO particles are modeled in rectangular lattices with the dimensions of 0.106 cm (length) × 0.106 cm (width) × 0.1 cm (height) to generate a volumetric packing fraction of 30 % (not including the graphite overcoat) when only complete particles are placed within the compact. A cross-sectional view of the TRISO lattice block is shown in Figure 4.1. The graphite overcoat isn't completely represented in the lattice.

A horizontal cross section of the compacts is shown in Figure 4.2. As can be seen, selective placement of TRISO particles was necessary to conserve the fuel rod mass of 188.58 g. For the current configuration, 12,987 TRISO particles are present within a standard fuel compact; this value is slightly less than the reported value of approximately 13,000.

The effective multiplication factor is shown in Table 4.1. Calculated values of $k_{eff}$ differ from the benchmark model values by between 1.5 to 2.1 %. Reevaluation of the HTTR model as additional information becomes available might improve the quality of this benchmark. The benchmark model is most sensitive to graphite impurities, and graphite cross section data may also contributed to the bias.

The results for the fully-loaded subcritical configuration of the HTTR are shown in Table 4.2. The subcritical configurations developed during initial core loading were not evaluated.

The warm critical configuration has not been evaluated. Unfortunately, this data does not represent a valid benchmark experiment (see Section 2.1.9).

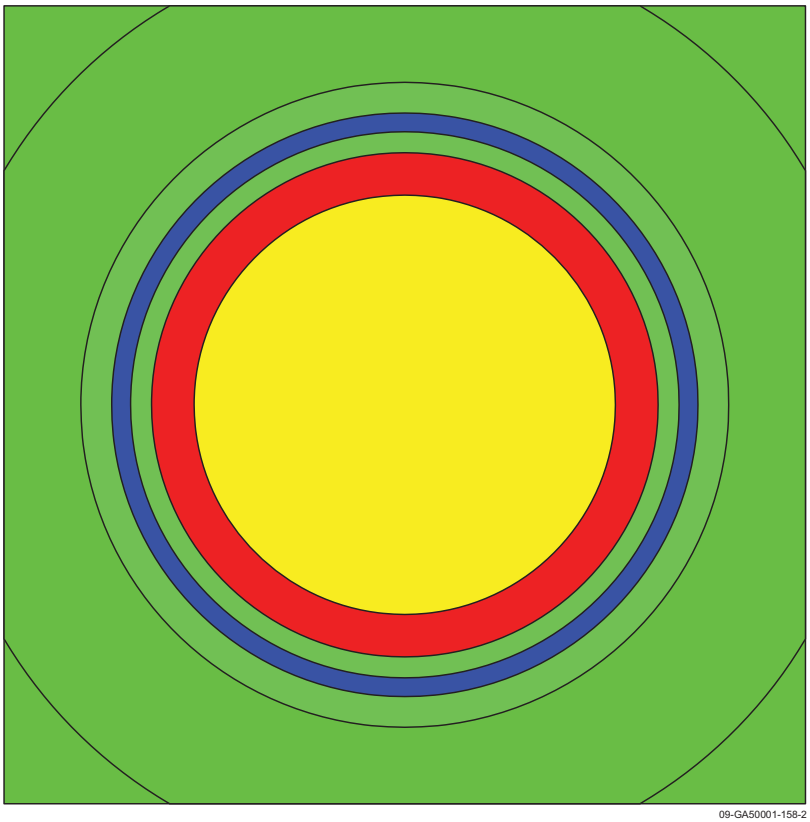


Figure 4.1. MCNP TRISO Lattice Unit Cell.

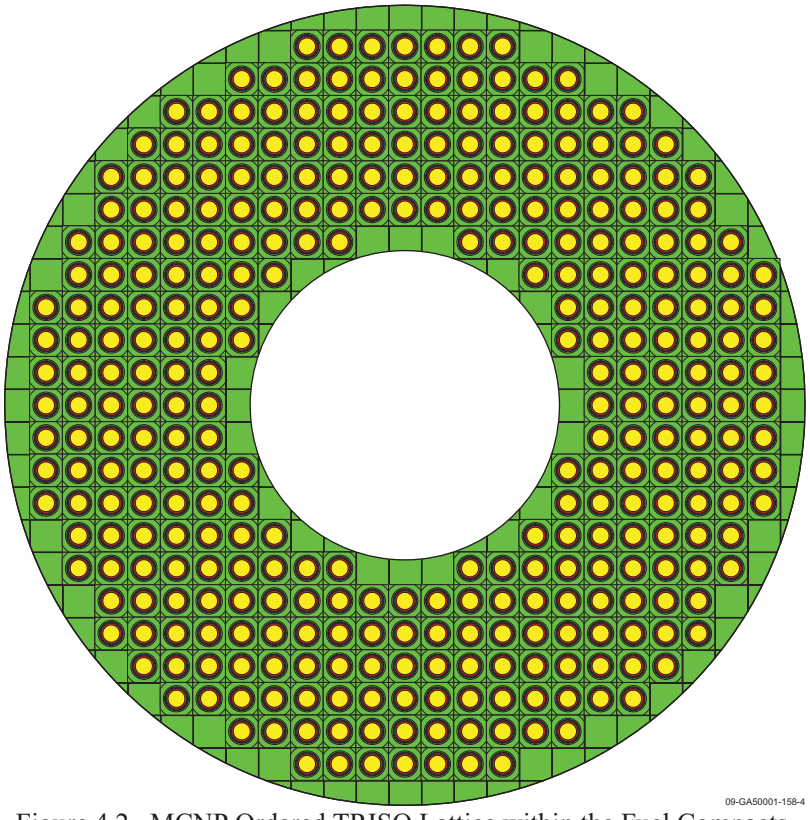


Figure 4.2. MCNP Ordered TRISO Lattice within the Fuel Compacts.

Table 4.1. Final Results for the HTTR Benchmark Model Evaluation of the Fully-Loaded Core Critical.

| Neutron Cross-Section Library | Calculated $k_{eff}$ ± σ | Benchmark $k_{eff}$ | Uncertainty -σ (%) | Uncertainty +σ (%) | (C-E)/E (%) |
|---|---|---|---|---|---|
| ENDF/B-V.2 | 1.0198 ± 0.0001 | 1.0025[(a)] | 0.0060 | 0.0071 | 1.72 |
| ENDF/B-VI.8 | 1.0222 ± 0.0001 | 1.0025[(a)] | 0.0060 | 0.0071 | 1.96 |
| END/B-VII.0 | 1.0229 ± 0.0001 | 1.0025[(a)] | 0.0060 | 0.0071 | 2.03 |
| JEFF-3.1 | 1.0236 ± 0.0001 | 1.0025[(a)] | 0.0060 | 0.0071 | 2.10 |
| JENDL-3.3 with ENDF/B-VI.8 S(α,β) | 1.0178 ± 0.0001 | 1.0025[(a)] | 0.0060 | 0.0071 | 1.53 |
| ENDF/B-VII.0 (MCNPX) | 1.0231 ± 0.0001 | 1.0025[(a)] | 0.0060 | 0.0071 | 2.05 |

(a) No biases have been currently evaluated for correcting the expected experimental $k_{eff}$, besides the bias for removing the reactor instrumentation in the instrumentation columns.

Table 4.2. Final Results for the HTTR Benchmark Model Evaluation of the Subcritical Core.

| Neutron Cross-Section Library | Calculated $k_{eff}$ ± σ | Benchmark $k_{eff}$ | Uncertainty ±σ (%) | (C-E)/E (%) |
|---|---|---|---|---|
| ENDF/B-V.2 | 0.7016 ± 0.0001 | 0.6876[(a)] | 0.0104 | 2.04 |
| ENDF/B-VI.8 | 0.7025 ± 0.0001 | 0.6876[(a)] | 0.0104 | 2.17 |
| END/B-VII.0 | 0.6999 ± 0.0001 | 0.6876[(a)] | 0.0104 | 1.78 |
| JEFF-3.1 | 0.7036 ± 0.0001 | 0.6876[(a)] | 0.0104 | 2.33 |
| JENDL-3.3 with ENDF/B-VI.8 S(α,β) | 0.6979 ± 0.0001 | 0.6876[(a)] | 0.0104 | 1.50 |
| ENDF/B-VII.0 (MCNPX) | 0.7001 ± 0.0001 | 0.6876[(a)] | 0.0104 | 1.82 |

(a) No biases have been currently evaluated for correcting the expected experimental $k_{eff}$, besides the bias for removing the reactor instrumentation in the instrumentation columns.

## 4.2 Results of Buckling and Extrapolation Length Calculations

Buckling and extrapolation length measurements were not made.

## 4.3 Results of Spectral-Characteristics Calculations

Spectral characteristics measurements were not made.

## 4.4 Results of Reactivity-Effects Calculations

The benchmark model for the critical configuration described in Section 3.1 was utilized in the analysis of the reactor physics experiments in Section 1.4. The modeling approach described in Section 4.1

applies to the analysis in this section except that all calculations were performed only using the ENDF/B-VI.8 neutron cross-section library.

### 4.4.1 Excess Reactivity

The calculated individual and cumulative excess reactivity values in the HTTR are shown in Tables 4.3 and 4.4, respectively. The calculated excess reactivity values generally appear to be approximately 7-8 % greater than the experimental measurements.

Table 4.3. Calculated Incremental Excess Reactivity Values in the HTTR.

| Data Points | Fuel Columns | Benchmark (% Δk/k) | Calculated (% Δk/k) | (C-E)/E (%) |
|---|---|---|---|---|
| 1 | 19 | -- | -- | -- |
| 2 | 21 | -- | 2.30 ± 0.01 | -- |
| 3 | 24 | 3.7 ± 1.0 | 4.01 ± 0.02 | 8.27 |
| 4 | 27 | 3.0 ± 0.9 | 3.23 ± 0.02 | 7.76 |
| 5 | 30 | 1.3 ± 0.3 | 1.30 ± 0.01 | 0.08 |

Table 4.4. Calculated Cumulative Excess Reactivity Values in the HTTR.

| Data Points | Fuel Columns | Benchmark (% Δk/k) | Calculated (% Δk/k) | (C-E)/E (%) |
|---|---|---|---|---|
| 1 | 19 | 2.4 ± 0.24 | 1.98[(a)] ± 0.02 | -17.59 |
| 2 | 21 | 4.0 ± 1.1 | 4.28 ± 0.02 | 7.05 |
| 3 | 24 | 7.7 ± 2.1 | 8.29 ± 0.03 | 7.63 |
| 4 | 27 | 10.7 ± 3.0 | 11.52 ± 0.03 | 7.67 |
| 5 | 30 | 12.0 ± 3.3 | 12.82 ± 0.03 | 6.85 |
| | | | 11.38[(b)] ± 0.01 | -11.79 |

(a) This value represents the cumulative worth of fuel addition from the subcritical 18-fuel-column core and the 19-fuel-column core.
(b) This value represents the excess reactivity calculated by completely withdrawing all control rods from the fully-loaded 30-fuel-column core configuration.

### 4.4.2 Shutdown Margin

The calculated shutdown margin values in the HTTR are shown in Table 4.5. The calculated shutdown margin values appear to be in general agreement with the experimental measurements although the shutdown margin for the insertion of only the radial reflector control rods calculates lower than expected.

Table 4.5. Calculated Shutdown Margin Values for the HTTR.

| Configuration | | Benchmark (% Δk/k) | Calculated (% Δk/k) | (C-E)/E (%) |
|---|---|---|---|---|
| 1 | Insertion of Control Rods in Reflector Region | -12.1 ± 0.6 | -9.27 ± 0.02 | -23.4 |
| 2 | Insertion of Control Rods in Fuel Region | -34.2 ± 1.7 | -37.31 ± 0.03 | 9.1 |
| 3 | Insertion of All Control Rods | -46.3 ± 1.2 | -46.59 ± 0.03 | 0.6 |

### 4.4.3 Control Rod Worth

Calculations using the benchmark models for the control rod worths have not been completely evaluated. Further analysis is necessary to assess the current discrepancies between the computational and experimental data.

## 4.5 Results of Reactivity Coefficient Calculations

Reactivity coefficient measurements have not been evaluated.

## 4.6 Results of Kinetics Parameter Calculations

Kinetics measurements have not been evaluated.

## 4.7 Results of Reaction-Rate Distribution Calculations

### 4.7.1 Axial Reaction Rate Distribution

The benchmark model for the critical configuration described in Section 3.1 was utilized in the analysis of the reactor physics experiments in Section 1.7. The modeling approach described in Section 4.1 applies to the analysis in this section except that all calculations were performed only using the ENDF/B-VII.0 neutron cross-section library. Computed axial neutron reaction rates in the instrumentation columns of the HTTR, averaged and normalized from tallies across the three columns from input decks using six different random number seeds, are summarized in Table 4.6 and depicted in Figure 4.3. The calculated reaction rate with uncertainty bars is shown in Figure 4.4.

The calculated reaction rates are renormalized such that at data point 4, both the benchmark and calculated values are 1.0000, using Equations 4.1 and 4.2, where the normalized flux at the $i^{th}$ position, $\varphi_{i,n}$, is obtained by dividing the reaction rate at that position by the maximum flux, $\varphi_{i,max}$. Then the calculated reaction rate, subscript C, is renormalized to the maximum reaction rate of the benchmark experiment, subscript E.

$$\varphi_{i,n} = \frac{\varphi_i}{\varphi_{i,\max}}. \tag{4.1}$$

$$\varphi_{i,n,C} = \frac{\varphi_{i,n,C}}{\varphi_{i,n,\max,E}}. \tag{4.2}$$

The calculated axial neutron fission reaction rate values appear to be in good agreement with the experimental measurements; all values are within 3σ, with the first six data points within 1σ. The values reported in the right-hand column of Table 4.6 represent the difference between the calculated (C) and the expected benchmark (E) values.

Table 4.6. Calculated Axial Neutron Fission Reaction Rate in the Instrumentation Columns of the HTTR.

| Data Point | Height (cm)[(a)] | Benchmark Reaction Rate | ± | 1σ | Calculated Reaction Rate | ± | 1σ | C/E |
|---|---|---|---|---|---|---|---|---|
| 1 | 19.68 | 0.8381 | ± | 0.0127 | 0.8307 | ± | 0.0013 | 0.991 |
| 2 | 28.47 | 0.8759 | ± | 0.0126 | 0.8650 | ± | 0.0014 | 0.988 |
| 3 | 71.81 | 0.9991 | ± | 0.0128 | 0.9918 | ± | 0.0015 | 0.993 |
| 4 | 82.53 | 1.0000 | ± | 0.0116 | 1.0000 | ± | 0.0015 | 1.000 |
| 5 | 86.52 | 0.9784 | ± | 0.0242 | 0.9989 | ± | 0.0015 | 1.021 |
| 6 | 93.61 | 0.9703 | ± | 0.0306 | 0.9920 | ± | 0.0015 | 1.022 |
| 7 | 144.22 | 0.7673 | ± | 0.0277 | 0.7981 | ± | 0.0013 | 1.040 |
| 8 | 202.28 | 0.3695 | ± | 0.0158 | 0.4070 | ± | 0.0009 | 1.101 |
| 9 | 261.19 | 0.1302 | ± | 0.0094 | 0.1505 | ± | 0.0006 | 1.156 |
| 10 | 319.13 | 0.0440 | ± | 0.0057 | 0.0552 | ± | 0.0004 | 1.255 |

(a) The height is in reference to the position relative to the bottom of the fifth layer of fuel.

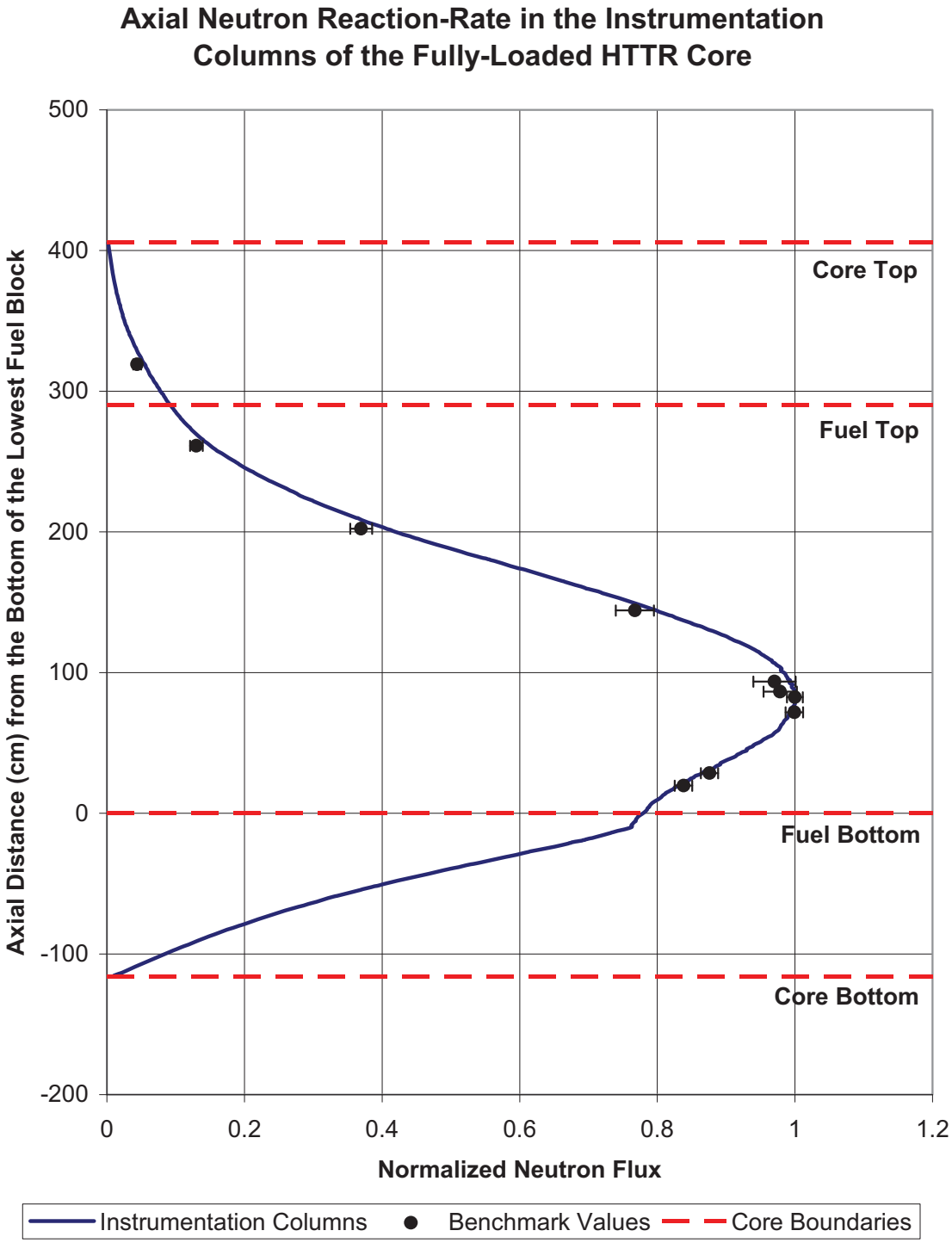


Figure 4.3. Calculated Axial Neutron Reaction Rate in the Instrumentation Columns of the HTTR.

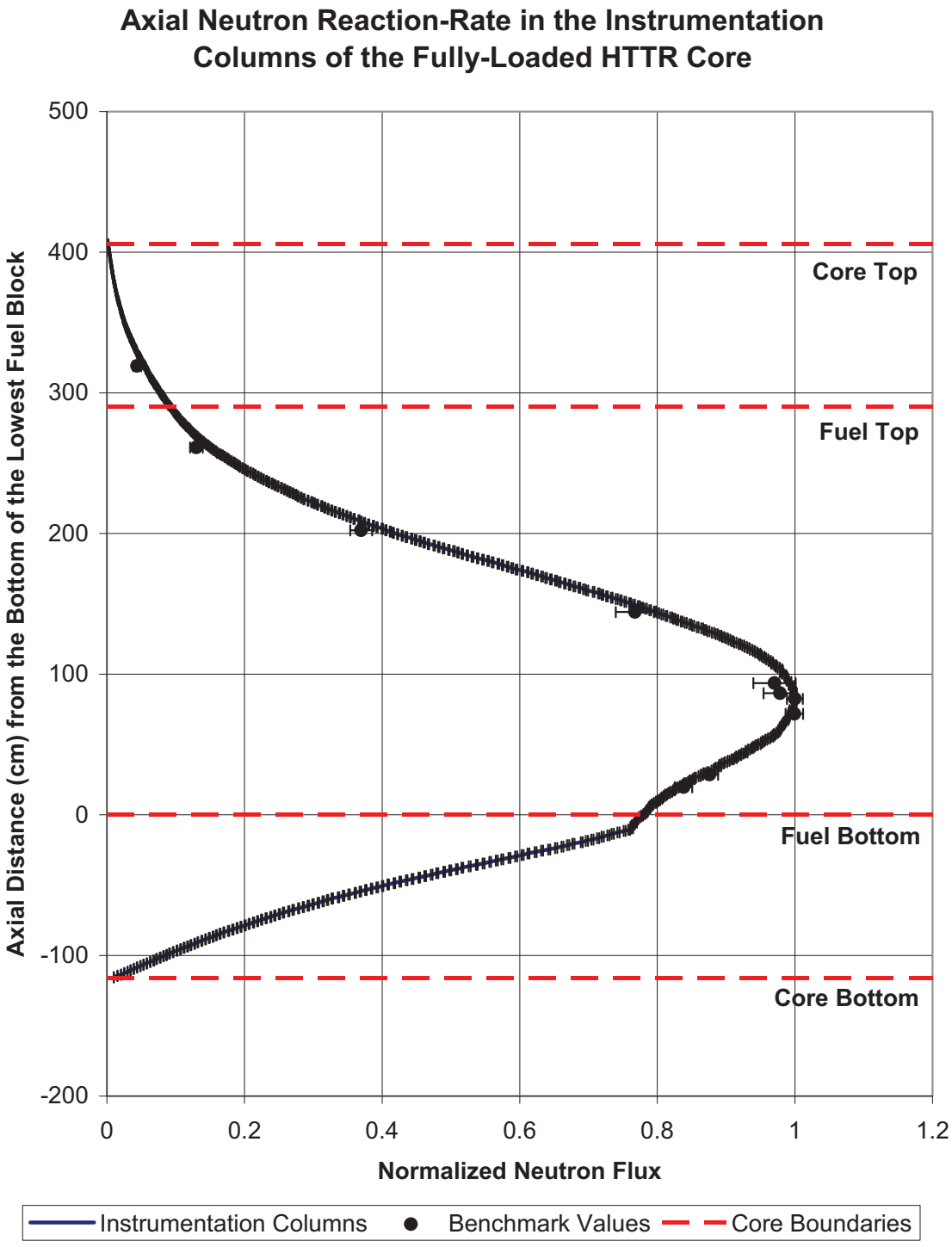


Figure 4.4. Calculated Axial Neutron Flux with Uncertainty (1σ).

## 4.8 Results of Power Distribution Calculations

Power distribution measurements were not made.

## 4.9 Results of Isotopic Calculations

Isotopic measurements were not made.

## 4.10 Results of Calculations for Other Miscellaneous Types of Measurements

Other miscellaneous types of measurements were not made.

## 5.0 REFERENCES

1. N. Fujimoto, K. Yamashita, N. Nojiri, M. Takeuchi, and S. Fujisaki, "Annular Core Experiments in HTTR's Start-Up Core Physics Tests," *Nucl. Sci. Eng.*, **150**, 310-321 (2005).

2. "Evaluation of High Temperature Gas Cooled Reactor Performance: Benchmark Analysis Related to Initial Testing of the HTTR and HTR-10," IAEA-TECDOC-1382, International Atomic Energy Agency, Vienna, November 2003.

3. S. Shiozawa, S. Fujikawa, T. Iyoku, K. Kunitomi, and Y. Tachibana, "Overview of HTTR Design Features," *Nucl. Eng. Des.*, **233**:11-21 (2004).

4. N. Fujimoto, N. Nojiri, H. Ando, and K. Yamashita, "Nuclear Design," *Nucl. Eng. Des.*, **233**: 23-36 (2004).

5. T. Iyoku, S. Ueta, J. Sumita, M. Umeda, and M. Ishihara, "Design of Core Components," *Nucl. Eng. Des.*, **233**: 71-79 (2004).

6. J. Sumita, M. Ishihara, S. Nakagawa, T. Kikuchi, and T. Iyoku, "Reactor Internals Design," *Nucl. Eng. Des.*, **233**: 81-88 (2004).

7. Y. Tachibana, H. Sawahata, T. Iyoku, and T. Nakazawa, "Reactivity Control System of the High Temperature Engineering Test Reactor," *Nucl. Eng. Des.*, **233**: 89-101 (2004).

8. Y. Tachibana, S. Nakagawa, and T. Iyoku, "Reactor Pressure Vessel Design of the High Temperature Engineering Test Reactor," *Nucl. Eng. Des.*, **233**: 103-112 (2004).

9. T. Furusawa, M. Shinozaki, S. Hamamoto, and Y. Oota, "Cooling System Design and Structural Integrity Evaluation," *Nucl. Eng. Des.*, **233**: 113-124 (2004).

10. N. Sakaba, K. Iigaki, M. Kondo, and K. Emori, "Leak-Tightness Characteristics Concerning the Containment Structures of the HTTR," *Nucl. Eng. Des.*, **233**: 135-145 (2004).

11. N. Sakaba, T. Furusawa, T. Kawamoto, Y. Ishii, and Y. Oota, "Short Design Descriptions of Other Systems of the HTTR," *Nucl. Eng. Des.*, **233**: 147-154 (2004).

12. Y. Tachibana and T. Iyoku, "Structural Design of High Temperature Metallic Components," *Nucl. Eng. Des.*, **233**: 261-272 (2004).

13. N. Nojiri, S. Shimakawa, N. Fujimoto, and M. Goto, "Characteristic Test of Initial HTTR Core," *Nucl. Eng. Des.*, **233**: 283-290 (2004).

14. I. Minatsuki, M. Tanihira, Y. Mizokami, Y. Miyoshi, H. Hayakawa, F. Okamoto, I. Maekawa, K. Takeuchi, H. Kodama, M. Fukuie, N. Kan, S. Kato, K. Nishimura, and T. Konishi, "The Role of Japan's Industry in the HTTR Design and Construction," *Nucl. Eng. Des.*, **233**: 377-390 (2004).

15. S. Saito, T. Tanaka, Y. Sudo, O. Baba, M. Shindo, S. Shiozawa, H. Mogi, M. Okubo, N. Ito, R. Shindo, N. Kobayashi, R. Kurihara, K. Hayashi, K. Hada, Y. Kurata, K. Yamashita, K. Kawasaki, T. Iyoku, K. Kunitomi, S. Maruyama, M. Ishihara, K. Sawa, N. Fujimoto, I. Murata, S. Nakagawa, Y. Tachibana, T. Nishimara, S. Oshita, M. Shinozaki, T. Takeda, S. Sakaba, A. Saikusa, Y. Tazawa, Y. Fukaya, H. Nagahori, T. Kikuchi, S. Kawaji, M. Isozaki, S. Matsuzaki, I. Sakama, K. Hara, N. Ueda, and S. Kokusen, "Design of High Temperature Test Reactor (HTTR)," JAERI 1332, Japan Atomic Energy Research Institute, Tokaimura, September 1994.

# APPENDIX A: COMPUTER CODES, CROSS SECTIONS, AND TYPICAL INPUT LISTINGS

## A.1 Critical and Subcritical Configurations

### A.1.1 Name(s) of code system(s) used.

1. Monte Carlo n-Particle, version 5.1.40 (MCNP5)
2. Monte Carlo n-Particle Extensions, version 2.5.0 (MCNPX)

### A.1.2 Bibliographic references for the codes used.

1. X-5 Monte Carlo Team, "MCNP – a General Monte Carlo n-Particle Transport Code, version 5," LA-UR-03-1987, Los Alamos National Laboratory (2003).
2. J.S. Hendricks, et al., "MCNPX Extensions," LA-UR-05-2675, Los Alamos National Laboratory (April 2005).

### A.1.3 Origin of cross-section data.

The Evaluated Neutron Data File library, ENDF/B-VI.8, was utilized in the benchmark model analysis. Other versions, including ENDF/B-V.2[a] and ENDF/B-VII.0,[b] were used with the benchmark model for a baseline comparison. The European Joint Evaluated Fission and Fusion File, JEFF-3.1[c] and the Japanese Evaluated Nuclear Data Library, JENDL-3.3,[d] were also included for a basic evaluative comparison. Such comparisons are typical.[ef] The JENDL-3.3 analysis was performed with the inclusion of ENDF/B-VII.0 thermal neutron scattering data because it was not included in the JENDL-3.3 library. Thermal neutron scattering, or S($\alpha$,$\beta$), adjusts the neutron cross sections for neutron upscatter at thermal energies and provides scattering data for elements bound within specific materials.

### A.1.4 Spectral calculations and data reduction methods used.

Not applicable

### A.1.5 Number of energy groups or if continuous-energy cross sections are used in the different phases of the calculation.

Continuous-energy cross sections

---

[a] R. Kinsey, Ed., ENDF/B Summary Documentation, BNL-NCS-17542 (ENDF-201), 3rd ed., Brookhaven National Laboratory (1979).

[b] M. B. Chadwick, et al., "ENDF/B-VII.0: Next Generation Evaluated Nuclear Data Library for Nuclear Science and Technology," *Nucl. Data Sheets*, **107**: 2931-3060 (2006).

[c] A. Koning, R. Forrest, M. Kellett, R. Mills, H. Henriksson, and Y. Rugama, "The JEFF-3.1 Nuclear Data Library," JEFF Report 21, Organisation for Economic Co-operation and Development, Paris (2006).

[d] K. Shibata, et al., "Japanese Evaluated Nuclear Data Library Version 3 Revision-3: JENDL-3.3," *J. Nucl. Sci. Tech.*, **39**(11): 1125-1136 (November 2002).

[e] A. C. Kahler, "Monte Carlo Eigenvalue Calculations withENDF/B-VI.8, JEFF-3.0, and JENDL-3.3 Cross Sections for a Selection of International Criticality Safety Benchmark Evaluation Project Handbook Benchmarks," *Nucl. Sci. Eng.*, **145**: 213-224 (2003).

[f] M. Goto, N. Nojiri, and S. Shimakawa, "Neutronics Calculations of HTTR with Several Nuclear Data Libraries," *J. Nucl. Sci. Tech.*, **43**(10): 1237-1244 (2006).

### A.1.6 Component calculations.

- Type of cell calculation – Reactor core and reflectors
- Geometry – Cylindrical
- Theory used – Not applicable
- Method used – Monte Carlo
- Calculation characteristics – histories/cycles/cycles skipped = 50,000/1,050/50
  continuous-energy cross sections

### A.1.7 Other assumptions and characteristics.

Not applicable

### A.1.8 Typical input listings.

*MCNP5 and MCNPX Input Deck for the fully-loaded 30-fuel-column core critical of the HTTR:*

```
HTTR Start-Up Core Critical (30 fuel columns) --
c
c John Darrell Bess - Idaho National Laboratory
c Last Updated: November 13, 2009
c
c Cell Cards ******************************************************************
c --- Fuel Column -----------------------------------------------------------
c ------ TRISO Particles ------
1    1  6.9614E-02   -1 imp:n=1 u=13 $ 3.4% kernel
2    13 5.5153E-02 1 -2 imp:n=1 u=13 $ buffer
3    14 9.2758E-02 2 -3 imp:n=1 u=13 $ IPyC
4    15 9.6122E-02 3 -4 imp:n=1 u=13 $ SiC
5    16 9.2758E-02 4 -5 imp:n=1 u=13 $ OPyC
6    17 8.5237E-02 5 -6 imp:n=1 u=13 $ overcoat
7    18 8.5237E-02 6 901 -902 903 -904 905 -906 imp:n=1 u=13 $ compact fill
11   like 1 but mat=2 u=14 rho=6.9616E-02 $ 3.9% kernel ---
12   like 2 but u=14 $ buffer
13   like 3 but u=14 $ IPyC
14   like 4 but u=14 $ SiC
15   like 5 but u=14 $ OPyC
16   like 6 but u=14 $ overcoat
17   like 7 but u=14 $ compact fill
21   like 1 but mat=3 u=15 rho=6.9617E-02 $ 4.3% kernel ---
22   like 2 but u=15 $ buffer
23   like 3 but u=15 $ IPyC
24   like 4 but u=15 $ SiC
25   like 5 but u=15 $ OPyC
26   like 6 but u=15 $ overcoat
27   like 7 but u=15 $ compact fill
31   like 1 but mat=4 u=16 rho=6.9618E-02 $ 4.8% kernel ---
32   like 2 but u=16 $ buffer
33   like 3 but u=16 $ IPyC
34   like 4 but u=16 $ SiC
35   like 5 but u=16 $ OPyC
36   like 6 but u=16 $ overcoat
37   like 7 but u=16 $ compact fill
41   like 1 but mat=5 u=17 rho=6.9619E-02 $ 5.2% kernel ---
42   like 2 but u=17 $ buffer
43   like 3 but u=17 $ IPyC
44   like 4 but u=17 $ SiC
45   like 5 but u=17 $ OPyC
46   like 6 but u=17 $ overcoat
47   like 7 but u=17 $ compact fill
51   like 1 but mat=6 u=18 rho=6.9622E-02 $ 5.9% kernel ---
52   like 2 but u=18 $ buffer
53   like 3 but u=18 $ IPyC
54   like 4 but u=18 $ SiC
55   like 5 but u=18 $ OPyC
56   like 6 but u=18 $ overcoat
57   like 7 but u=18 $ compact fill
61   like 1 but mat=7 u=19 rho=6.9623E-02 $ 6.3% kernel ---
62   like 2 but u=19 $ buffer
```

```
63   like 3 but u=19 $ IPyC
64   like 4 but u=19 $ SiC
65   like 5 but u=19 $ OPyC
66   like 6 but u=19 $ overcoat
67   like 7 but u=19 $ compact fill
71   like 1 but mat=8 u=20 rho=6.9624E-02 $ 6.7% kernel ---
72   like 2 but u=20 $ buffer
73   like 3 but u=20 $ IPyC
74   like 4 but u=20 $ SiC
75   like 5 but u=20 $ OPyC
76   like 6 but u=20 $ overcoat
77   like 7 but u=20 $ compact fill
81   like 1 but mat=9 u=21 rho=6.9625E-02 $ 7.2% kernel ---
82   like 2 but u=21 $ buffer
83   like 3 but u=21 $ IPyC
84   like 4 but u=21 $ SiC
85   like 5 but u=21 $ OPyC
86   like 6 but u=21 $ overcoat
87   like 7 but u=21 $ compact fill
91   like 1 but mat=10 u=22 rho=6.9628E-02 $ 7.9% kernel ---
92   like 2 but u=22 $ buffer
93   like 3 but u=22 $ IPyC
94   like 4 but u=22 $ SiC
95   like 5 but u=22 $ OPyC
96   like 6 but u=22 $ overcoat
97   like 7 but u=22 $ compact fill
101  like 1 but mat=11 u=23 rho=6.9632E-02 $ 9.4% kernel ---
102  like 2 but u=23 $ buffer
103  like 3 but u=23 $ IPyC
104  like 4 but u=23 $ SiC
105  like 5 but u=23 $ OPyC
106  like 6 but u=23 $ overcoat
107  like 7 but u=23 $ compact fill
111  like 1 but mat=12 u=24 rho=6.9634E-02 $ 9.9% kernel ---
112  like 2 but u=24 $ buffer
113  like 3 but u=24 $ IPyC
114  like 4 but u=24 $ SiC
115  like 5 but u=24 $ OPyC
116  like 6 but u=24 $ overcoat
117  like 7 but u=24 $ compact fill
c
c ------ Compacts ------
120  18 8.5237E-02 901 -902 903 -904 905 -906 imp:n=1 u=300 $ compact fill
163  0 911 -912 913 -914 915 -916 imp:n=1 u=25 lat=1 fill=-13:13 -13:13 0:0
     300 26r 300 26r 300 9r 13 6r 300 9r 300 7r 13 10r 300 7r
     300 5r 13 14r 300 5r 300 4r 13 16r 300 4r 300 3r 13 18r 300 3r
     300 3r 13 18r 300 3r 300 2r 13 8r 300 2r 13 8r 300 2r
     300 1r 13 7r 300 6r 13 6r 300 2r 300 1r 13 6r 300 8r 13 6r 300 1r
     300 1r 13 6r 300 8r 13 6r 300 1r 300 1r 13 5r 300 10r 13 5r 300 1r
     300 1r 13 5r 300 10r 13 5r 300 1r 300 1r 13 5r 300 10r 13 5r 300 1r
     300 1r 13 6r 300 8r 13 6r 300 1r 300 1r 13 6r 300 8r 13 6r 300 1r
     300 2r 13 6r 300 6r 13 6r 300 2r 300 2r 13 8r 300 2r 13 8r 300 2r
     300 3r 13 18r 300 3r 300 3r 13 18r 300 3r 300 4r 13 16r 300 4r
     300 5r 13 14r 300 5r 300 7r 13 10r 300 7r 300 9r 13 6r 300 9r
     300 26r 300 26r
164  like 163 but u=26 fill=-13:13 -13:13 0:0
     300 26r 300 26r 300 9r 14 6r 300 9r 300 7r 14 10r 300 7r
     300 5r 14 14r 300 5r 300 4r 14 16r 300 4r 300 3r 14 18r 300 3r
     300 3r 14 18r 300 3r 300 2r 14 8r 300 2r 14 8r 300 2r
     300 1r 14 7r 300 6r 14 6r 300 2r 300 1r 14 6r 300 8r 14 6r 300 1r
     300 1r 14 6r 300 8r 14 6r 300 1r 300 1r 14 5r 300 10r 14 5r 300 1r
     300 1r 14 5r 300 10r 14 5r 300 1r 300 1r 14 5r 300 10r 14 5r 300 1r
     300 1r 14 6r 300 8r 14 6r 300 1r 300 1r 14 6r 300 8r 14 6r 300 1r
     300 2r 14 6r 300 6r 14 6r 300 2r 300 2r 14 8r 300 2r 14 8r 300 2r
     300 3r 14 18r 300 3r 300 3r 14 18r 300 3r 300 4r 14 16r 300 4r
     300 5r 14 14r 300 5r 300 7r 14 10r 300 7r 300 9r 14 6r 300 9r
     300 26r 300 26r
165  like 163 but u=27 fill=-13:13 -13:13 0:0
     300 26r 300 26r 300 9r 15 6r 300 9r 300 7r 15 10r 300 7r
     300 5r 15 14r 300 5r 300 4r 15 16r 300 4r 300 3r 15 18r 300 3r
     300 3r 15 18r 300 3r 300 2r 15 8r 300 2r 15 8r 300 2r
     300 1r 15 7r 300 6r 15 6r 300 2r 300 1r 15 6r 300 8r 15 6r 300 1r
     300 1r 15 6r 300 8r 15 6r 300 1r 300 1r 15 5r 300 10r 15 5r 300 1r
     300 1r 15 5r 300 10r 15 5r 300 1r 300 1r 15 5r 300 10r 15 5r 300 1r
     300 1r 15 6r 300 8r 15 6r 300 1r 300 1r 15 6r 300 8r 15 6r 300 1r
     300 2r 15 6r 300 6r 15 6r 300 2r 300 2r 15 8r 300 2r 15 8r 300 2r
```

```
     300 3r 15 18r 300 3r 300 3r 15 18r 300 3r 300 4r 15 16r 300 4r
     300 5r 15 14r 300 5r 300 7r 15 10r 300 7r 300 9r 15 6r 300 9r
     300 26r 300 26r
166  like 163 but u=28 fill=-13:13 -13:13 0:0
     300 26r 300 26r 300 9r 16 6r 300 9r 300 7r 16 10r 300 7r
     300 5r 16 14r 300 5r 300 4r 16 16r 300 4r 300 3r 16 18r 300 3r
     300 3r 16 18r 300 3r 300 2r 16 8r 300 2r 16 8r 300 2r
     300 1r 16 7r 300 6r 16 6r 300 2r 300 1r 16 6r 300 8r 16 6r 300 1r
     300 1r 16 6r 300 8r 16 6r 300 1r 300 1r 16 5r 300 10r 16 5r 300 1r
     300 1r 16 5r 300 10r 16 5r 300 1r 300 1r 16 5r 300 10r 16 5r 300 1r
     300 1r 16 6r 300 8r 16 6r 300 1r 300 1r 16 6r 300 8r 16 6r 300 1r
     300 2r 16 6r 300 6r 16 6r 300 2r 300 2r 16 8r 300 2r 16 8r 300 2r
     300 3r 16 18r 300 3r 300 3r 16 18r 300 3r 300 4r 16 16r 300 4r
     300 5r 16 14r 300 5r 300 7r 16 10r 300 7r 300 9r 16 6r 300 9r
     300 26r 300 26r
167  like 163 but u=29 fill=-13:13 -13:13 0:0
     300 26r 300 26r 300 9r 17 6r 300 9r 300 7r 17 10r 300 7r
     300 5r 17 14r 300 5r 300 4r 17 16r 300 4r 300 3r 17 18r 300 3r
     300 3r 17 18r 300 3r 300 2r 17 8r 300 2r 17 8r 300 2r
     300 1r 17 7r 300 6r 17 6r 300 2r 300 1r 17 6r 300 8r 17 6r 300 1r
     300 1r 17 6r 300 8r 17 6r 300 1r 300 1r 17 5r 300 10r 17 5r 300 1r
     300 1r 17 5r 300 10r 17 5r 300 1r 300 1r 17 5r 300 10r 17 5r 300 1r
     300 1r 17 6r 300 8r 17 6r 300 1r 300 1r 17 6r 300 8r 17 6r 300 1r
     300 2r 17 6r 300 6r 17 6r 300 2r 300 2r 17 8r 300 2r 17 8r 300 2r
     300 3r 17 18r 300 3r 300 3r 17 18r 300 3r 300 4r 17 16r 300 4r
     300 5r 17 14r 300 5r 300 7r 17 10r 300 7r 300 9r 17 6r 300 9r
     300 26r 300 26r
168  like 163 but u=30 fill=-13:13 -13:13 0:0
     300 26r 300 26r 300 9r 18 6r 300 9r 300 7r 18 10r 300 7r
     300 5r 18 14r 300 5r 300 4r 18 16r 300 4r 300 3r 18 18r 300 3r
     300 3r 18 18r 300 3r 300 2r 18 8r 300 2r 18 8r 300 2r
     300 1r 18 7r 300 6r 18 6r 300 2r 300 1r 18 6r 300 8r 18 6r 300 1r
     300 1r 18 6r 300 8r 18 6r 300 1r 300 1r 18 5r 300 10r 18 5r 300 1r
     300 1r 18 5r 300 10r 18 5r 300 1r 300 1r 18 5r 300 10r 18 5r 300 1r
     300 1r 18 6r 300 8r 18 6r 300 1r 300 1r 18 6r 300 8r 18 6r 300 1r
     300 2r 18 6r 300 6r 18 6r 300 2r 300 2r 18 8r 300 2r 18 8r 300 2r
     300 3r 18 18r 300 3r 300 3r 18 18r 300 3r 300 4r 18 16r 300 4r
     300 5r 18 14r 300 5r 300 7r 18 10r 300 7r 300 9r 18 6r 300 9r
     300 26r 300 26r
169  like 163 but u=31 fill=-13:13 -13:13 0:0
     300 26r 300 26r 300 9r 19 6r 300 9r 300 7r 19 10r 300 7r
     300 5r 19 14r 300 5r 300 4r 19 16r 300 4r 300 3r 19 18r 300 3r
     300 3r 19 18r 300 3r 300 2r 19 8r 300 2r 19 8r 300 2r
     300 1r 19 7r 300 6r 19 6r 300 2r 300 1r 19 6r 300 8r 19 6r 300 1r
     300 1r 19 6r 300 8r 19 6r 300 1r 300 1r 19 5r 300 10r 19 5r 300 1r
     300 1r 19 5r 300 10r 19 5r 300 1r 300 1r 19 5r 300 10r 19 5r 300 1r
     300 1r 19 6r 300 8r 19 6r 300 1r 300 1r 19 6r 300 8r 19 6r 300 1r
     300 2r 19 6r 300 6r 19 6r 300 2r 300 2r 19 8r 300 2r 19 8r 300 2r
     300 3r 19 18r 300 3r 300 3r 19 18r 300 3r 300 4r 19 16r 300 4r
     300 5r 19 14r 300 5r 300 7r 19 10r 300 7r 300 9r 19 6r 300 9r
     300 26r 300 26r
180  like 163 but u=32 fill=-13:13 -13:13 0:0
     300 26r 300 26r 300 9r 20 6r 300 9r 300 7r 20 10r 300 7r
     300 5r 20 14r 300 5r 300 4r 20 16r 300 4r 300 3r 20 18r 300 3r
     300 3r 20 18r 300 3r 300 2r 20 8r 300 2r 20 8r 300 2r
     300 1r 20 7r 300 6r 20 6r 300 2r 300 1r 20 6r 300 8r 20 6r 300 1r
     300 1r 20 6r 300 8r 20 6r 300 1r 300 1r 20 5r 300 10r 20 5r 300 1r
     300 1r 20 5r 300 10r 20 5r 300 1r 300 1r 20 5r 300 10r 20 5r 300 1r
     300 1r 20 6r 300 8r 20 6r 300 1r 300 1r 20 6r 300 8r 20 6r 300 1r
     300 2r 20 6r 300 6r 20 6r 300 2r 300 2r 20 8r 300 2r 20 8r 300 2r
     300 3r 20 18r 300 3r 300 3r 20 18r 300 3r 300 4r 20 16r 300 4r
     300 5r 20 14r 300 5r 300 7r 20 10r 300 7r 300 9r 20 6r 300 9r
     300 26r 300 26r
181  like 163 but u=33 fill=-13:13 -13:13 0:0
     300 26r 300 26r 300 9r 21 6r 300 9r 300 7r 21 10r 300 7r
     300 5r 21 14r 300 5r 300 4r 21 16r 300 4r 300 3r 21 18r 300 3r
     300 3r 21 18r 300 3r 300 2r 21 8r 300 2r 21 8r 300 2r
     300 1r 21 7r 300 6r 21 6r 300 2r 300 1r 21 6r 300 8r 21 6r 300 1r
     300 1r 21 6r 300 8r 21 6r 300 1r 300 1r 21 5r 300 10r 21 5r 300 1r
     300 1r 21 5r 300 10r 21 5r 300 1r 300 1r 21 5r 300 10r 21 5r 300 1r
     300 1r 21 6r 300 8r 21 6r 300 1r 300 1r 21 6r 300 8r 21 6r 300 1r
     300 2r 21 6r 300 6r 21 6r 300 2r 300 2r 21 8r 300 2r 21 8r 300 2r
     300 3r 21 18r 300 3r 300 3r 21 18r 300 3r 300 4r 21 16r 300 4r
     300 5r 21 14r 300 5r 300 7r 21 10r 300 7r 300 9r 21 6r 300 9r
     300 26r 300 26r
182  like 163 but u=34 fill=-13:13 -13:13 0:0
```

```
     300 26r 300 26r 300 9r 22 6r 300 9r 300 7r 22 10r 300 7r
     300 5r 22 14r 300 5r 300 4r 22 16r 300 4r 300 3r 22 18r 300 3r
     300 3r 22 18r 300 3r 300 2r 22 8r 300 2r 22 8r 300 2r
     300 1r 22 7r 300 6r 22 6r 300 2r 300 1r 22 6r 300 8r 22 6r 300 1r
     300 1r 22 6r 300 8r 22 6r 300 1r 300 1r 22 5r 300 10r 22 5r 300 1r
     300 1r 22 5r 300 10r 22 5r 300 1r 300 1r 22 5r 300 10r 22 5r 300 1r
     300 1r 22 6r 300 8r 22 6r 300 1r 300 1r 22 6r 300 8r 22 6r 300 1r
     300 2r 22 6r 300 6r 22 6r 300 2r 300 2r 22 8r 300 2r 22 8r 300 2r
     300 3r 22 18r 300 3r 300 3r 22 18r 300 3r 300 4r 22 16r 300 4r
     300 5r 22 14r 300 5r 300 7r 22 10r 300 7r 300 9r 22 6r 300 9r
     300 26r 300 26r
183  like 163 but u=35 fill=-13:13 -13:13 0:0
     300 26r 300 26r 300 9r 23 6r 300 9r 300 7r 23 10r 300 7r
     300 5r 23 14r 300 5r 300 4r 23 16r 300 4r 300 3r 23 18r 300 3r
     300 3r 23 18r 300 3r 300 2r 23 8r 300 2r 23 8r 300 2r
     300 1r 23 7r 300 6r 23 6r 300 2r 300 1r 23 6r 300 8r 23 6r 300 1r
     300 1r 23 6r 300 8r 23 6r 300 1r 300 1r 23 5r 300 10r 23 5r 300 1r
     300 1r 23 5r 300 10r 23 5r 300 1r 300 1r 23 5r 300 10r 23 5r 300 1r
     300 1r 23 6r 300 8r 23 6r 300 1r 300 1r 23 6r 300 8r 23 6r 300 1r
     300 2r 23 6r 300 6r 23 6r 300 2r 300 2r 23 8r 300 2r 23 8r 300 2r
     300 3r 23 18r 300 3r 300 3r 23 18r 300 3r 300 4r 23 16r 300 4r
     300 5r 23 14r 300 5r 300 7r 23 10r 300 7r 300 9r 23 6r 300 9r
     300 26r 300 26r
184  like 163 but u=36 fill=-13:13 -13:13 0:0
     300 26r 300 26r 300 9r 24 6r 300 9r 300 7r 24 10r 300 7r
     300 5r 24 14r 300 5r 300 4r 24 16r 300 4r 300 3r 24 18r 300 3r
     300 3r 24 18r 300 3r 300 2r 24 8r 300 2r 24 8r 300 2r
     300 1r 24 7r 300 6r 24 6r 300 2r 300 1r 24 6r 300 8r 24 6r 300 1r
     300 1r 24 6r 300 8r 24 6r 300 1r 300 1r 24 5r 300 10r 24 5r 300 1r
     300 1r 24 5r 300 10r 24 5r 300 1r 300 1r 24 5r 300 10r 24 5r 300 1r
     300 1r 24 6r 300 8r 24 6r 300 1r 300 1r 24 6r 300 8r 24 6r 300 1r
     300 2r 24 6r 300 6r 24 6r 300 2r 300 2r 24 8r 300 2r 24 8r 300 2r
     300 3r 24 18r 300 3r 300 3r 24 18r 300 3r 300 4r 24 16r 300 4r
     300 5r 24 14r 300 5r 300 7r 24 10r 300 7r 300 9r 24 6r 300 9r
     300 26r 300 26r
9163 0 921 -922 923 -924 925 -926 imp:n=1 u=925 lat=1 fill=25
9164 like 9163 but u=926 fill=26
9165 like 9163 but u=927 fill=27
9166 like 9163 but u=928 fill=28
9167 like 9163 but u=929 fill=29
9168 like 9163 but u=930 fill=30
9169 like 9163 but u=931 fill=31
9180 like 9163 but u=932 fill=32
9181 like 9163 but u=933 fill=33
9182 like 9163 but u=934 fill=34
9183 like 9163 but u=935 fill=35
9184 like 9163 but u=936 fill=36
185  0 12 -13 imp:n=1 u=37 fill=925
186  like 185 but u=38 fill=926
187  like 185 but u=39 fill=927
188  like 185 but u=40 fill=928
189  like 185 but u=41 fill=929
190  like 185 but u=42 fill=930
191  like 185 but u=43 fill=931
192  like 185 but u=44 fill=932
193  like 185 but u=45 fill=933
194  like 185 but u=46 fill=934
195  like 185 but u=47 fill=935
196  like 185 but u=48 fill=936
c
c ------ Fuel Pins ------
251  27 2.4616E-05 -12 imp:n=1 u=37 $ central hole
252  like 251 but u=38
253  like 251 but u=39
254  like 251 but u=40
255  like 251 but u=41
256  like 251 but u=42
257  like 251 but u=43
258  like 251 but u=44
259  like 251 but u=45
260  like 251 but u=46
261  like 251 but u=47
262  like 251 but u=48
263  27 2.4616E-05 13 -21 imp:n=1 u=37 $ annulus between compact and sleeve
264  like 263 but u=38
265  like 263 but u=39
```

```
266  like 263 but u=40
267  like 263 but u=41
268  like 263 but u=42
269  like 263 but u=43
270  like 263 but u=44
271  like 263 but u=45
272  like 263 but u=46
273  like 263 but u=47
274  like 263 but u=48
275  19 8.8747E-02 21 -22 imp:n=1 u=37 $ graphite sleeve
1275 like 275 but u=38
276  like 275 but u=39
277  like 275 but u=40
278  like 275 but u=41
279  like 275 but u=42
280  like 275 but u=43
281  like 275 but u=44
282  like 275 but u=45
283  like 275 but u=46
284  like 275 but u=47
285  like 275 but u=48
c
c ------ Coolant Channels ------
286  27 2.4616E-05 22 -31 imp:n=1 u=37 $ annulus between sleeve and block
287  like 286 but u=38
288  like 286 but u=39
289  like 286 but u=40
290  like 286 but u=41
291  like 286 but u=42
292  like 286 but u=43
293  like 286 but u=44
294  like 286 but u=45
295  like 286 but u=46
296  like 286 but u=47
297  like 286 but u=48
298  25 8.7804E-02 31 imp:n=1 u=37 $ graphite block
299  like 298 but u=38
300  like 298 but u=39
301  like 298 but u=40
302  like 298 but u=41
303  like 298 but u=42
304  like 298 but u=43
305  like 298 but u=44
306  like 298 but u=45
307  like 298 but u=46
308  like 298 but u=47
309  like 298 but u=48
c
c ------ BP Pins ------
351  20 9.0451E-02 -41 imp:n=1 u=50 $ 2.0%
352  like 351 but mat=21 rho=9.0501E-02 u=51 $ 2.5%
353  22 8.8747E-02 -42 imp:n=1 u=50 $ graphite disks
354  like 353 but u=51
355  20 9.0451E-02 -43 imp:n=1 u=50 $ 2.0%
356  like 355 but mat=21 rho=9.0501E-02 u=51 $ 2.5%
357  27 2.4616E-05 41 42 43 -44 imp:n=1 u=50 $ pin gap
358  like 357 but u=51
359  27 2.4616E-05 -44 imp:n=1 u=52 $ empty pin position
360  25 8.7804E-02 44 imp:n=1 u=50 $ graphite block
361  like 360 but u=51
362  like 360 but u=52
c
c ------ Blocks ------
401  25 8.7804E-02 -501 imp:n=1 u=61 lat=2 fill= -5:5 -5:5 0:0 $ Zone 1 Lvl 4/5
     61 10r
     61 10r
     61  4r       50  37  37  37       61 1r
     61  3r     37  37  37  37  37     61 1r
     61  2r   37  37  37  37  37  37   61 1r
     61  1r 37  37  37  61  37  37  52 61 1r
     61  1r   37  37  37  37  37  37   61 2r
     61  1r     37  37  37  37  37     61 3r
     61  1r       50  37  37  37       61 4r
     61 10r
     61 10r
402  25 8.7804E-02 -501 imp:n=1 u=62 lat=2 fill= -5:5 -5:5 0:0 $ Zone 1 Lvl 3
```

```
     62 10r
     62 10r
     62  4r       51  39  39  39       62 1r
     62  3r     39  39  39  39  39     62 1r
     62  2r   39  39  39  39  39  39   62 1r
     62  1r 39  39  39  62  39  39  52 62 1r
     62  1r   39  39  39  39  39  39   62 2r
     62  1r     39  39  39  39  39     62 3r
     62  1r       51  39  39  39       62 4r
     62 10r
     62 10r
403  25 8.7804E-02 -501 imp:n=1 u=63 lat=2 fill= -5:5 -5:5 0:0 $ Zone 1 Lvl 2
     63 10r
     63 10r
     63  4r       51  41  41  41       63 1r
     63  3r     41  41  41  41  41     63 1r
     63  2r   41  41  41  41  41  41   63 1r
     63  1r 41  41  41  63  41  41  52 63 1r
     63  1r   41  41  41  41  41  41   63 2r
     63  1r     41  41  41  41  41     63 3r
     63  1r       51  41  41  41       63 4r
     63 10r
     63 10r
404  25 8.7804E-02 -501 imp:n=1 u=64 lat=2 fill= -5:5 -5:5 0:0 $ Zone 1 Lvl 1
     64 10r
     64 10r
     64  4r       50  44  44  44       64 1r
     64  3r     44  44  44  44  44     64 1r
     64  2r   44  44  44  44  44  44   64 1r
     64  1r 44  44  44  64  44  44  52 64 1r
     64  1r   44  44  44  44  44  44   64 2r
     64  1r     44  44  44  44  44     64 3r
     64  1r       50  44  44  44       64 4r
     64 10r
     64 10r
405  25 8.7804E-02 -501 imp:n=1 u=65 lat=2 fill= -5:5 -5:5 0:0 $ Zone 2 Lvl 4/5
     65 10r
     65 10r
     65  4r       50  38  38  38       65 1r
     65  3r     38  38  38  38  38     65 1r
     65  2r   38  38  38  38  38  38   65 1r
     65  1r 38  38  38  65  38  38  52 65 1r
     65  1r   38  38  38  38  38  38   65 2r
     65  1r     38  38  38  38  38     65 3r
     65  1r       50  38  38  38       65 4r
     65 10r
     65 10r
406  25 8.7804E-02 -501 imp:n=1 u=66 lat=2 fill= -5:5 -5:5 0:0 $ Zone 2 Lvl 3
     66 10r
     66 10r
     66  4r       51  41  41  41       66 1r
     66  3r     41  41  41  41  41     66 1r
     66  2r   41  41  41  41  41  41   66 1r
     66  1r 41  41  41  66  41  41  52 66 1r
     66  1r   41  41  41  41  41  41   66 2r
     66  1r     41  41  41  41  41     66 3r
     66  1r       51  41  41  41       66 4r
     66 10r
     66 10r
407  25 8.7804E-02 -501 imp:n=1 u=67 lat=2 fill= -5:5 -5:5 0:0 $ Zone 2 Lvl 2
     67 10r
     67 10r
     67  4r       51  43  43  43       67 1r
     67  3r     43  43  43  43  43     67 1r
     67  2r   43  43  43  43  43  43   67 1r
     67  1r 43  43  43  67  43  43  52 67 1r
     67  1r   43  43  43  43  43  43   67 2r
     67  1r     43  43  43  43  43     67 3r
     67  1r       51  43  43  43       67 4r
     67 10r
     67 10r
408  25 8.7804E-02 -501 imp:n=1 u=68 lat=2 fill= -5:5 -5:5 0:0 $ Zone 2 Lvl 1
     68 10r
     68 10r
     68  4r       50  46  46  46       68 1r
     68  3r     46  46  46  46  46     68 1r
```

```
     68  2r   46  46  46  46  46  46   68 1r
     68  1r 46  46  46  68  46  46  52 68 1r
     68  1r   46  46  46  46  46  46   68 2r
     68  1r     46  46  46  46  46     68 3r
     68  1r       50  46  46  46       68 4r
     68 10r
     68 10r
409  25 8.7804E-02 -501 imp:n=1 u=69 lat=2 fill= -5:5 -5:5 0:0 $ Zone 3 Lvl 4/5
     69 10r
     69 10r
     69  4r       50  39  39  69       69 1r
     69  3r     39  39  39  39  39     69 1r
     69  2r   39  39  39  39  39  39   69 1r
     69  1r 39  39  39  69  39  39  52 69 1r
     69  1r   39  39  39  39  39  39   69 2r
     69  1r     39  39  39  39  39     69 3r
     69  1r       50  39  39  69       69 4r
     69 10r
     69 10r
410  25 8.7804E-02 -501 imp:n=1 u=70 lat=2 fill= -5:5 -5:5 0:0 $ Zone 3 Lvl 3
     70 10r
     70 10r
     70  4r       51  42  42  70       70 1r
     70  3r     42  42  42  42  42     70 1r
     70  2r   42  42  42  42  42  42   70 1r
     70  1r 42  42  42  70  42  42  52 70 1r
     70  1r   42  42  42  42  42  42   70 2r
     70  1r     42  42  42  42  42     70 3r
     70  1r       51  42  42  70       70 4r
     70 10r
     70 10r
411  25 8.7804E-02 -501 imp:n=1 u=71 lat=2 fill= -5:5 -5:5 0:0 $ Zone 3 Lvl 2
     71 10r
     71 10r
     71  4r       51  45  45  71       71 1r
     71  3r     45  45  45  45  45     71 1r
     71  2r   45  45  45  45  45  45   71 1r
     71  1r 45  45  45  71  45  45  52 71 1r
     71  1r   45  45  45  45  45  45   71 2r
     71  1r     45  45  45  45  45     71 3r
     71  1r       51  45  45  71       71 4r
     71 10r
     71 10r
412  25 8.7804E-02 -501 imp:n=1 u=72 lat=2 fill= -5:5 -5:5 0:0 $ Zone 3 Lvl 1
     72 10r
     72 10r
     72  4r       50  47  47  72       72 1r
     72  3r     47  47  47  47  47     72 1r
     72  2r   47  47  47  47  47  47   72 1r
     72  1r 47  47  47  72  47  47  52 72 1r
     72  1r   47  47  47  47  47  47   72 2r
     72  1r     47  47  47  47  47     72 3r
     72  1r       50  47  47  72       72 4r
     72 10r
     72 10r
413  25 8.7804E-02 -501 imp:n=1 u=73 lat=2 fill= -5:5 -5:5 0:0 $ Zone 4 Lvl 4/5
     73 10r
     73 10r
     73  4r       50  40  40  73       73 1r
     73  3r     40  40  40  40  40     73 1r
     73  2r   40  40  40  40  40  40   73 1r
     73  1r 40  40  40  73  40  40  52 73 1r
     73  1r   40  40  40  40  40  40   73 2r
     73  1r     40  40  40  40  40     73 3r
     73  1r       50  40  40  73       73 4r
     73 10r
     73 10r
414  25 8.7804E-02 -501 imp:n=1 u=74 lat=2 fill= -5:5 -5:5 0:0 $ Zone 4 Lvl 3
     74 10r
     74 10r
     74  4r       51  43  43  74       74 1r
     74  3r     43  43  43  43  43     74 1r
     74  2r   43  43  43  43  43  43   74 1r
     74  1r 43  43  43  74  43  43  52 74 1r
     74  1r   43  43  43  43  43  43   74 2r
     74  1r     43  43  43  43  43     74 3r
```

```
     74  1r       51  43  43  74       74 4r
     74 10r
     74 10r
415  25 8.7804E-02 -501 imp:n=1 u=75 lat=2 fill= -5:5 -5:5 0:0 $ Zone 4 Lvl 2
     75 10r
     75 10r
     75  4r       51  46  46  75       75 1r
     75  3r     46  46  46  46  46     75 1r
     75  2r   46  46  46  46  46  46   75 1r
     75  1r 46  46  46  75  46  46  52 75 1r
     75  1r   46  46  46  46  46  46   75 2r
     75  1r     46  46  46  46  46     75 3r
     75  1r       51  46  46  75       75 4r
     75 10r
     75 10r
416  25 8.7804E-02 -501 imp:n=1 u=76 lat=2 fill= -5:5 -5:5 0:0 $ Zone 4 Lvl 1
     76 10r
     76 10r
     76  4r       50  48  48  76       76 1r
     76  3r     48  48  48  48  48     76 1r
     76  2r   48  48  48  48  48  48   76 1r
     76  1r 48  48  48  76  48  48  52 76 1r
     76  1r   48  48  48  48  48  48   76 2r
     76  1r     48  48  48  48  48     76 3r
     76  1r       50  48  48  76       76 4r
     76 10r
     76 10r
451  0 -502 imp:n=1 u=81 fill=61
452  like 451 but u=82 fill=62
453  like 451 but u=83 fill=63
454  like 451 but u=84 fill=64
455  like 451 but u=85 fill=65
456  like 451 but u=86 fill=66
457  like 451 but u=87 fill=67
458  like 451 but u=88 fill=68
459  like 451 but u=89 fill=69
460  like 451 but u=90 fill=70
461  like 451 but u=91 fill=71
462  like 451 but u=92 fill=72
463  like 451 but u=93 fill=73
464  like 451 but u=94 fill=74
465  like 451 but u=95 fill=75
466  like 451 but u=96 fill=76
467  27 2.4616E-05 502 imp:n=1 u=81
468  like 467 but u=82
469  like 467 but u=83
470  like 467 but u=84
471  like 467 but u=85
472  like 467 but u=86
473  like 467 but u=87
474  like 467 but u=88
475  like 467 but u=89
476  like 467 but u=90
477  like 467 but u=91
478  like 467 but u=92
479  like 467 but u=93
480  like 467 but u=94
481  like 467 but u=95
482  like 467 but u=96
c
c ------ Reflectors ------
483  27 2.4616E-05 -201 imp:n=1 u=97 $ coolant channels
484  25 8.7804E-02  201 imp:n=1 u=97 $ graphite block
485  25 8.7804E-02 -501 imp:n=1 u=98 lat=2 fill= -5:5 -5:5 0:0 $ 33-hole
     98 10r
     98 10r
     98  4r       98  97  97  97       98 1r
     98  3r     97  97  97  97  97     98 1r
     98  2r   97  97  97  97  97  97   98 1r
     98  1r 97  97  97  98  97  97  98 98 1r
     98  1r   97  97  97  97  97  97   98 2r
     98  1r     97  97  97  97  97     98 3r
     98  1r       98  97  97  97       98 4r
     98 10r
     98 10r
486  25 8.7804E-02 -501 imp:n=1 u=99 lat=2 fill= -5:5 -5:5 0:0 $ 31-hole
```

```
     99 10r
     99 10r
     99  4r       99  97  97  99       99 1r
     99  3r     97  97  97  97  97     99 1r
     99  2r   97  97  97  97  97  97   99 1r
     99  1r 97  97  97  99  97  97  99 99 1r
     99  1r   97  97  97  97  97  97   99 2r
     99  1r     97  97  97  97  97     99 3r
     99  1r       99  97  97  99       99 4r
     99 10r
     99 10r
489  0 -502 imp:n=1 u=100 fill=98
490  0 -502 imp:n=1 u=101 fill=99
491  like 467 but u=100
492  like 467 but u=101
c
c ------ Columns ------
501  27 2.4616E-05 -503 imp:n=1 u=121 lat=2 fill= -1:1 -1:1 -5:5 $ Zone 1
     121 121 121 121 121 121 121 121 121
     121 121 121 121 100 121 121 121 121
     121 121 121 121 100 121 121 121 121
     121 121 121 121  81 121 121 121 121
     121 121 121 121  81 121 121 121 121
     121 121 121 121  82 121 121 121 121
     121 121 121 121  83 121 121 121 121
     121 121 121 121  84 121 121 121 121
     121 121 121 121 100 121 121 121 121
     121 121 121 121 100 121 121 121 121
     121 121 121 121 121 121 121 121 121
502  27 2.4616E-05 -503 imp:n=1 u=122 lat=2 fill= -1:1 -1:1 -5:5 $ Zone 2
     122 122 122 122 122 122 122 122 122
     122 122 122 122 100 122 122 122 122
     122 122 122 122 100 122 122 122 122
     122 122 122 122  85 122 122 122 122
     122 122 122 122  85 122 122 122 122
     122 122 122 122  86 122 122 122 122
     122 122 122 122  87 122 122 122 122
     122 122 122 122  88 122 122 122 122
     122 122 122 122 100 122 122 122 122
     122 122 122 122 100 122 122 122 122
     122 122 122 122 122 122 122 122 122
503  27 2.4616E-05 -503 imp:n=1 u=123 lat=2 fill= -1:1 -1:1 -5:5 $ Zone 3
     123 123 123 123 123 123 123 123 123
     123 123 123 123 100 123 123 123 123
     123 123 123 123 100 123 123 123 123
     123 123 123 123  89 123 123 123 123
     123 123 123 123  89 123 123 123 123
     123 123 123 123  90 123 123 123 123
     123 123 123 123  91 123 123 123 123
     123 123 123 123  92 123 123 123 123
     123 123 123 123 101 123 123 123 123
     123 123 123 123 101 123 123 123 123
     123 123 123 123 123 123 123 123 123
504  27 2.4616E-05 -503 imp:n=1 u=124 lat=2 fill= -1:1 -1:1 -5:5 $ Zone 4
     124 124 124 124 124 124 124 124 124
     124 124 124 124 100 124 124 124 124
     124 124 124 124 100 124 124 124 124
     124 124 124 124  93 124 124 124 124
     124 124 124 124  93 124 124 124 124
     124 124 124 124  94 124 124 124 124
     124 124 124 124  95 124 124 124 124
     124 124 124 124  96 124 124 124 124
     124 124 124 124 101 124 124 124 124
     124 124 124 124 101 124 124 124 124
     124 124 124 124 124 124 124 124 124
525  0 -950 imp:n=1 u=125 fill=121 $ B04
526  like 525 but u=126 fill=121 *trcl=(0 0 0 180 90 90 270 180 90 90 90 0) $ B01
527  like 525 but u=127 fill=121 *trcl=(0 0 0 120 30 90 210 120 90 90 90 0) $ B02
528  like 525 but u=128 fill=121 *trcl=(0 0 0 60 330 90 150 60 90 90 90 0) $ B03
529  like 525 but u=129 fill=121 *trcl=(0 0 0 300 210 90 30 300 90 90 90 0) $ B05
530  like 525 but u=130 fill=121 *trcl=(0 0 0 240 150 90 330 240 90 90 90 0) $ B06
531  0 -950 imp:n=1 u=131 fill=122 $ C02
532  like 531 but u=132 fill=122 *trcl=(0 0 0 300 210 90 30 300 90 90 90 0) $ C04
533  like 531 but u=133 fill=122 *trcl=(0 0 0 240 150 90 330 240 90 90 90 0) $ C06
534  like 531 but u=134 fill=122 *trcl=(0 0 0 180 90 90 270 180 90 90 90 0) $ C08
535  like 531 but u=135 fill=122 *trcl=(0 0 0 120 30 90 210 120 90 90 90 0) $ C10
```

```
536  like 531 but u=136 fill=122 *trcl=(0 0 0 60 330 90 150 60 90 90 90 0) $ C12
537  0 -950 imp:n=1 u=137 fill=123 $ D05/09
538  like 537 but u=138 fill=123 *trcl=(0 0 0 60 330 90 150 60 90 90 90 0) $ D02/06
539  like 537 but u=139 fill=123 *trcl=(0 0 0 120 30 90 210 120 90 90 90 0) $ D03/17
540  like 537 but u=140 fill=123 *trcl=(0 0 0 300 210 90 30 300 90 90 90 0) $ D08/12
541  like 537 but u=141 fill=123 *trcl=(0 0 0 240 150 90 330 240 90 90 90 0) $ D11/15
542  like 537 but u=142 fill=123 *trcl=(0 0 0 180 90 90 270 180 90 90 90 0) $ D14/18
543  0 -950 imp:n=1 u=143 fill=124 $ D07
544  like 543 but u=144 fill=124 *trcl=(0 0 0 120 30 90 210 120 90 90 90 0) $ D01
545  like 543 but u=145 fill=124 *trcl=(0 0 0 60 330 90 150 60 90 90 90 0) $ D04
546  like 543 but u=146 fill=124 *trcl=(0 0 0 300 210 90 30 300 90 90 90 0) $ D10
547  like 543 but u=147 fill=124 *trcl=(0 0 0 240 150 90 330 240 90 90 90 0) $ D13
548  like 543 but u=148 fill=124 *trcl=(0 0 0 180 90 90 270 180 90 90 90 0) $ D16
c
c --- Control Column ------------------------------------------------------------
c ------ Control Rod Segments ------
601  24 8.7530E-02 -103 imp:n=1 u=150 $ spine
602  27 2.4616E-05 103 -104 imp:n=1 u=150 $ helium gap
603  24 8.7530E-02 104 -101 imp:n=1 u=150 $ inner clad
604  23 9.8436E-02 101 -102 imp:n=1 u=150 $ absorber
605  24 8.7530E-02 102 -105 imp:n=1 u=150 $ outer clad
606  27 2.4616E-05 105 imp:n=1 u=150 $ helium
607  0 -151 imp:n=1 u=151 lat=2 fill=150 $ rod segment
608  0 -152 imp:n=1 u=152 fill=151 $ control rod
609  27 2.4616E-05 152 imp:n=1 u=152 $ helium
c
c ------ Positions ------
610  0 -999 imp:n=1 u=153 fill=152 (0 0 177.5) $ C
611  0 -154 imp:n=1 u=154 fill=153 (10.8 0 0)
612  0 -155 imp:n=1 u=154 fill=153 (-5.4 -9.35307 0)
613  27 2.4616E-05 -156 imp:n=1 u=154 $ RSS
614  like 610 but u=155 fill=152 (0 0 177.5) $ R1
615  like 611 but u=156 fill=155 (10.8 0 0)
616  like 612 but u=156 fill=155 (-5.4 -9.35307 0)
617  like 613 but u=156
618  like 610 but u=157 fill=152 (0 0 177.5) $ R2
619  like 611 but u=158 fill=157 (10.8 0 0)
620  like 612 but u=158 fill=157 (-5.4 -9.35307 0)
621  like 613 but u=158
622  like 610 but u=159 fill=152 (0 0 404.9) $ R3
623  like 611 but u=160 fill=159 (10.8 0 0)
624  like 612 but u=160 fill=159 (-5.4 -9.35307 0)
625  like 613 but u=160
c
c ------ C Column ------
626  25 8.7804E-02 154 155 156 -550 imp:n=1 u=154 $ graphite blocks
627  27 2.4616E-05 550 imp:n=1 u=154
628  0 -950 imp:n=1 u=161 fill=154 $ A01
c
c ------ R1 Columns ------
629  25 8.7804E-02 154 155 156 -550 imp:n=1 u=156 $ graphite blocks
630  like 627 but u=156
631  like 628 but u=162 fill=156 $ C01
632  like 631 but u=163 *trcl=(0 0 0 300 210 90 30 300 90 90 90 0) $ C03
633  like 631 but u=164 *trcl=(0 0 0 240 150 90 330 240 90 90 90 0) $ C05
634  like 631 but u=165 *trcl=(0 0 0 180 90 90 270 180 90 90 90 0) $ C07
635  like 631 but u=166 *trcl=(0 0 0 120 30 90 210 120 90 90 90 0) $ C09
636  like 631 but u=167 *trcl=(0 0 0 60 330 90 150 60 90 90 90 0) $ C11
c
c ------ R2 Columns ------
637  25 8.7804E-02 154 155 156 -550 imp:n=1 u=158 $ graphite blocks
638  like 627 but u=158
639  like 628 but u=168 fill=158 $ E23
640  like 639 but u=169 *trcl=(0 0 0 300 210 90 30 300 90 90 90 0) $ E03
641  like 639 but u=170 *trcl=(0 0 0 240 150 90 330 240 90 90 90 0) $ E07
642  like 639 but u=171 *trcl=(0 0 0 180 90 90 270 180 90 90 90 0) $ E11
643  like 639 but u=172 *trcl=(0 0 0 120 30 90 210 120 90 90 90 0) $ E15
644  like 639 but u=173 *trcl=(0 0 0 60 330 90 150 60 90 90 90 0) $ E19
c
c ------ R3 Columns ------
645  25 8.7804E-02 154 155 156 -550 imp:n=1 u=160 $ graphite blocks
646  like 627 but u=160
647  like 628 but u=174 fill=160 $ E01
648  like 647 but u=175 *trcl=(0 0 0 240 150 90 330 240 90 90 90 0) $ E09
649  like 647 but u=176 *trcl=(0 0 0 120 30 90 210 120 90 90 90 0) $ E17
c
```

```
c --- Instrumentation Column ---------------------------------------------------
c ------ Positions ------
661  27 2.4616E-05 -155 imp:n=1 u=181
662  27 2.4616E-05 -154 imp:n=1 u=181
663  27 2.4616E-05 -156 imp:n=1 u=181
c
c ------ Columns ------
664  25 8.7804E-02 154 155 156 -550 imp:n=1 u=181 $ graphite blocks
665  like 627 but u=181
666  0 -950 imp:n=1 u=182 fill=181
c
c --- Reflector Column ---------------------------------------------------------
c ------ Columns ------
671  25 8.7804E-02 -550 imp:n=1 u=183 $ graphite blocks
672  like 627 but u=183
673  0 -950 imp:n=1 u=184 fill=183
c
c --- HTTR Core ----------------------------------------------------------------
c ------ Core Map ------
701  26 8.6134E-02 -551 imp:n=1 lat=2 u=200 fill=-6:6 -6:6 0:0
     200 12r
     200 12r
     200 5r          175 184 170 184 182          200 1r
     200 4r        184 143 138 137 145 184        200 1r
     200 3r      171 140 164 132 163 139 169      200 1r
     200 2r    184 137 133 128 127 131 138 184    200 1r
     200 1r  182 146 165 125 161 126 162 144 174  200 1r
     200 1r    184 141 134 129 130 136 142 184    200 2r
     200 1r      172 140 166 135 167 139 168      200 3r
     200 1r       184 147 142 141 148 184         200 4r
     200 1r         176 184 173 184 182           200 5r
     200 12r
     200 12r
c
c ------ Core Map Legend ---
c    u 12r
c    u 12r
c    u 5r      Z G Y G I      u 1r
c    u 4r     G 4 3 3 4 G     u 1r
c    u 3r    Y 3 X 2 X 3 Y    u 1r           |
c    u 2r   G 3 2 1 1 2 3 G   u 1r           |     \
c    u 1r  I 4 X 1 C 1 X 4 Z  u 1r   --------+------> N
c    u 1r   G 3 2 1 1 2 3 G   u 2r           |     /
c    u 1r    Y 3 X 2 X 3 Y    u 3r           |
c    u 1r     G 4 3 3 4 G     u 4r
c    u 1r      Z G Y G I      u 5r
c    u 12r
c    u 12r
c
c    1 = Fuel Columns #1
c    2 = Fuel Columns #2
c    3 = Fuel Columns #3
c    4 = Fuel Columns #4
c    C = Central Control Column
c    X = R1 Control Columns
c    Y = R2 Control Columns
c    Z = R3 Control Columns
c    I = Instrumentation Columns
c    G = Removable Reflector Columns
c
702  0  -602 imp:n=1 fill=200
c
c --- Permanent Reflector ------------------------------------------------------
711  26 8.6134E-02 602 -651 imp:n=1
c
c --- The Great Void -----------------------------------------------------------
999  0 651 imp:n=0
c

c Surface Cards ****************************************************************
c --- Fuel Blocks --------------------------------------------------------------
c ------ TRISO Particles ------
1    so 0.03   $ UO2 kernal
2    so 0.036  $ buffer
3    so 0.039  $ IPyC
4    so 0.0415 $ SiC
```

```
5    so 0.046  $ OPyC
6    so 0.066  $ overcoat
901 px -0.125
902 px  0.125
903 py -0.125
904 py  0.125
905 pz -0.125
906 pz  0.125
c
c ------ Compacts ------
911 px -0.053
912 px  0.053
913 py -0.053
914 py  0.053
915 pz -0.05
916 pz 0.05
921 px -1.31
922 px 1.31
923 py -1.31
924 py 1.31
925 pz -0.05
926 pz 0.05
12   rcc 0 0 -27.3 0 0 54.6 0.5 $ inside
13   rcc 0 0 -27.3 0 0 54.6 1.3 $ outside
c
c ------ Fuel Pins ------
21   rcc 0 0 -27.45 0 0 54.9 1.325 $ inside
22   rcc 0 0 -28.85 0 0 57.7 1.7   $ outside
c
c ------ Coolant Channels ------
31   rcc 0 0 -31 0 0 62 2.05
c
c ------ BP Pins ------
41   rcc 0 0 -25 0 0 20 0.7  $ BP
42   rcc 0 0  -5 0 0 10 0.7  $ graphite
43   rcc 0 0   5 0 0 20 0.7  $ BP
44   rcc 0 0 -25 0 0 50 0.75 $ pin
c
c --- Control Blocks -----------------------------------------------------------
c ------ Control Rod Segments ------
101  rcc 0 0 11 0 0 29 3.75 $ inside
102  rcc 0 0 11 0 0 29 5.25 $ outside
103  rcc 0 0 11 0 0 29 0.5 $ spine
104  rcc 0 0 11 0 0 29 3.25 $ inside clad
105  rcc 0 0 10 0 0 31 5.65 $ outside clad
c
c ------ Positions ------
151  hex 0 0 10 0 0 31 10 $ "box"
152  rcc 0 0 -145 0 0 310 6.30 $ control rod
154  rcc 10.8 0 -155 0 0 416 6.15 $ control rod hole
155  rcc -5.4 -9.35307 -155 0 0 416 6.15 $ control rod hole
156  rcc -5.4 9.35307 -155 0 0 416 6.15 $ control rod hole
c
c --- Reflector Blocks ---------------------------------------------------------
c ------ Coolant Channels ------
201  rcc 0 0 -31 0 0 62 1.15
c
c --- Blocks -------------------------------------------------------------------
501  hex 0 0 -30 0 0 60 2.575 0 0 $ pitch
502  hex 0 0 -29.5 0 0 59 0 18 0 $ graphite
503  hex 0 0 -29 0 0 58 0 18.2 0 $ helium
c
c --- Columns ------------------------------------------------------------------
550  hex 0 0 -261.5 0 0 523 0 18 0
551  hex 0 0 -261 0 0 522 0 18.1 0
c
c --- HTTR Core ----------------------------------------------------------------
602  hex 0 0 -261 0 0 522 -148 0 0
c
c --- Permanent Reflector ------------------------------------------------------
651  rcc 0 0 -261 0 0 522 212.5
c
c --- Auxiliary Organization ---------------------------------------------------
950  rcc 0 0 -1000 0 0 2000 25 $ small cylinder
999  rcc 0 0 -2500 0 0 5000 2500 $ big cylinder
c
```

```
c Data Cards ******************************************************************
c --- Material Cards ------------------------------------------------------------
c ------ Kernel (3.4%) ------
m1    5010.00c 1.7299E-07
      8016.00c 4.6386E-02
      8017.00c 1.7633E-05
     92234.00c 6.1026E-06
     92235.00c 7.9888E-04
     92238.00c 2.2405E-02
c    Total     6.9614E-02
mt1   OUO2.00t
      UUO2.00t
c
c ------ Kernel (3.9%) ------
m2    5010.00c 1.7299E-07
      8016.00c 4.6386E-02
      8017.00c 1.7633E-05
     92234.00c 7.0000E-06
     92235.00c 9.1637E-04
     92238.00c 2.2288E-02
c    Total     6.9616E-02
mt2   OUO2.00t
      UUO2.00t
c
c ------ Kernel (4.3%) ------
m3    5010.00c 1.7299E-07
      8016.00c 4.6386E-02
      8017.00c 1.7633E-05
     92234.00c 7.7180E-06
     92235.00c 1.0104E-03
     92238.00c 2.2195E-02
c    Total     6.9617E-02
mt3   OUO2.00t
      UUO2.00t
c
c ------ Kernel (4.8%) ------
m4    5010.00c 1.7299E-07
      8016.00c 4.6386E-02
      8017.00c 1.7633E-05
     92234.00c 8.6154E-06
     92235.00c 1.1278E-03
     92238.00c 2.2078E-02
c    Total     6.9618E-02
mt4   OUO2.00t
      UUO2.00t
c
c ------ Kernel (5.2%) ------
m5    5010.00c 1.7299E-07
      8016.00c 4.6386E-02
      8017.00c 1.7633E-05
     92234.00c 9.3334E-06
     92235.00c 1.2218E-03
     92238.00c 2.1984E-02
c    Total     6.9619E-02
mt5   OUO2.00t
      UUO2.00t
c
c ------ Kernel (5.9%) ------
m6    5010.00c 1.7299E-07
      8016.00c 4.6386E-02
      8017.00c 1.7633E-05
     92234.00c 1.0590E-05
     92235.00c 1.3863E-03
     92238.00c 2.1821E-02
c    Total     6.9622E-02
mt6   OUO2.00t
      UUO2.00t
c
c ------ Kernel (6.3%) ------
m7    5010.00c 1.7299E-07
      8016.00c 4.6386E-02
      8017.00c 1.7633E-05
     92234.00c 1.1308E-05
     92235.00c 1.4803E-03
     92238.00c 2.1727E-02
```

```
c    Total     6.9623E-02
mt7   OUO2.00t
      UUO2.00t
c
c ------ Kernel (6.7%) ------
m8    5010.00c 1.7299E-07
      8016.00c 4.6386E-02
      8017.00c 1.7633E-05
     92234.00c 1.2026E-05
     92235.00c 1.5743E-03
     92238.00c 2.1634E-02
c    Total     6.9624E-02
mt8   OUO2.00t
      UUO2.00t
c
c ------ Kernel (7.2%) ------
m9    5010.00c 1.7299E-07
      8016.00c 4.6386E-02
      8017.00c 1.7633E-05
     92234.00c 1.2923E-05
     92235.00c 1.6918E-03
     92238.00c 2.1517E-02
c    Total     6.9625E-02
mt9   OUO2.00t
      UUO2.00t
c
c ------ Kernel (7.9%) ------
m10   5010.00c 1.7299E-07
      8016.00c 4.6386E-02
      8017.00c 1.7633E-05
     92234.00c 1.4180E-05
     92235.00c 1.8562E-03
     92238.00c 2.1353E-02
c    Total     6.9628E-02
mt10  OUO2.00t
      UUO2.00t
c
c ------ Kernel (9.4%) ------
m11   5010.00c 1.7299E-07
      8016.00c 4.6386E-02
      8017.00c 1.7633E-05
     92234.00c 1.6872E-05
     92235.00c 2.2087E-03
     92238.00c 2.1002E-02
c    Total     6.9632E-02
mt11  OUO2.00t
      UUO2.00t
c
c ------ Kernel (9.9%) ------
m12   5010.00c 1.7299E-07
      8016.00c 4.6386E-02
      8017.00c 1.7633E-05
     92234.00c 1.7769E-05
     92235.00c 2.3262E-03
     92238.00c 2.0886E-02
c    Total     6.9634E-02
mt12  OUO2.00t
      UUO2.00t
c
c ------ Buffer Layer ------
m13   5010.00c 1.8290E-08
      6000.00c 5.5153E-02
c    Total     5.5153E-02
mt13 Graph.00t
c
c ------ IPyC Layer ------
m14   5010.00c 3.0761E-08
      6000.00c 9.2758E-02
c    Total     9.2758E-02
mt14 Graph.00t
c
c ------ SiC Layer ------
m15   5010.00c 5.3208E-08
      6000.00c 4.8061E-02
     14028.00c 4.4327E-02
     14029.00c 2.2508E-03
```

```
     14030.00c 1.4837E-03
c    Total     9.6122E-02
mt15 Graph.00t
c
c ------ OPyC Layer ------
m16   5010.00c 3.0761E-08
      6000.00c 9.2758E-02
c    Total     9.2758E-02
mt16 Graph.00t
c
c ------ Graphite Overcoat ------
m17   5010.00c 2.8267E-08
      6000.00c 8.5237E-02
c    Total     8.5237E-02
mt17 Graph.00t
c
c ------ Graphite Compact ------
m18   5010.00c 1.5452E-08
      6000.00c 8.5237E-02
c    Total     8.5237E-02
mt18 Graph.00t
c
c ------ Graphite Sleeve ------
m19   5010.00c 7.2596E-09
      6000.00c 8.8747E-02
c    Total     8.8747E-02
mt19 Graph.00t
c
c ------ Burnable Poison (2.0%) ------
m20   5010.00c 3.9906E-04
      5011.00c 1.6063E-03
      6000.00c 8.8446E-02
c    Total     9.0451E-02
mt20 Graph.00t
c
c ------ Burnable Poison (2.5%) ------
m21   5010.00c 4.9882E-04
      5011.00c 2.0078E-03
      6000.00c 8.7995E-02
c    Total     9.0501E-02
mt21 Graph.00t
c
c ------ Graphite Disks ------
m22   5010.00c 7.2596E-09
      6000.00c 8.8747E-02
c    Total     8.8747E-02
mt22 Graph.00t
c
c ------ Neutron Absorber ------
m23   5010.00c 6.3184E-03
      5011.00c 2.5432E-02
      6000.00c 6.6685E-02
c    Total     9.8436E-02
mt23 Graph.00t
c
c ------ Alloy 800H ------
m24   6000.00c 3.2210E-04
     13027.00c 6.7209E-04
     14028.00c 5.5580E-04
     14029.00c 2.8222E-05
     14030.00c 1.8604E-05
     15031.00c 3.1225E-05
     16032.00c 1.4316E-05
     16033.00c 1.1462E-07
     16034.00c 6.4698E-07
     16036.00c 3.0162E-09
     22046.00c 3.1254E-05
     22047.00c 2.8186E-05
     22048.00c 2.7928E-04
     22049.00c 2.0495E-05
     22050.00c 1.9624E-05
     24050.00c 8.4860E-04
     24052.00c 1.6364E-02
     24053.00c 1.8556E-03
     24054.00c 4.6189E-04
     25055.00c 8.8022E-04
```

```
     26054.00c 2.2265E-03
     26056.00c 3.4951E-02
     26057.00c 8.0717E-04
     26058.00c 1.0742E-04
     28058.00c 1.8229E-02
     28060.00c 7.0217E-03
     28061.00c 3.0523E-04
     28062.00c 9.7320E-04
     28064.00c 2.4785E-04
     29063.00c 1.5791E-04
     29065.00c 7.0383E-05
c    Total     8.7530E-02
mt24    Fe.00t
        Al.00t
c
c ------ IG-110 Graphite ------
m25   5010.00c 1.1453E-08
      6000.00c 8.7804E-02
c    Total     8.7804E-02
mt25 Graph.00t
c
c ------ PGX Graphite ------
m26   5010.00c 3.6372E-08
      6000.00c 8.6134E-02
c    Total     8.6134E-02
mt26 Graph.00t
c
c ------ Helium Coolant ------
m27   2003.00c 3.3724E-11
      2004.00c 2.4616E-05
c    Total     2.4616E-05
c
c --- Control Cards -----------------------------------------------------------
mode  n
kcode 50000 1 50 1050
ksrc  93.545       0 -20  93.545       0 20
     -93.545       0 -20 -93.545       0 20
      55.050  76.350 -20  55.050  76.350 20
     -55.050  76.350 -20 -55.050  76.350 20
      55.050 -76.350 -20  55.050 -76.350 20
     -55.050 -76.350 -20 -55.050 -76.350 20
c print
```

*MCNP5 and MCNPX Input Deck for the fully-loaded 30-fuel-column core subcritical of the HTTR:*

This subcritical input deck would be identical to that of the critical configuration except the following cell cards replace the same numbered cards in the critical input deck:

```
610  0 -999 imp:n=1 u=153 fill=152 (0 0 -5.5) $ C
614  like 610 but u=155 fill=152 (0 0 -5.5) $ R1
618  like 610 but u=157 fill=152 (0 0 -5.5) $ R2
622  like 610 but u=159 fill=152 (0 0 -5.5) $ R3
```

*MCNP5 and MCNPX Input Deck for the fully-loaded warm core critical of the HTTR:*

The warm critical configuration has not been evaluated. Unfortunately, this data does not represent a valid benchmark experiment (see Section 2.1.9).

## A.2 Buckling and Extrapolation Length Configurations

Buckling and extrapolation length measurements were not made.

## A.3 Spectral-Characteristics Configurations

Spectral characteristics measurements were not made.

## A.4 Reactivity-Effects Configurations

*MCNP5 Input Deck for the excess reactivity measurements of the HTTR:*
The input decks from the 30-fuel-column core configuration in this benchmark report and the 19-, 21-, 24-, and 27-fuel-column core configurations in HTTR-GCR-RESR-002 are used to determine the excess reactivity of the HTTR core loading. Control rod positions are either fully withdrawn or adjusted to positions already reported in this report and HTTR-GCR-RESR-002.

*MCNP5 Input Deck for the shutdown margin measurements of the HTTR:*

The input decks used for the shutdown margin calculations include the critical and subcritical configurations along with an intermediate configuration with the following input deck substitution to the critical configuration input deck:

```
618  like 610 but u=157 fill=152 (0 0 -5.5) $ R2
622  like 610 but u=159 fill=152 (0 0 -5.5) $ R3
```

*MCNP5 Input Deck for the center control rod worth of the HTTR:*

The input deck for analysis of the center control rod worth is that of the critical configuration with the center control rod positioned at varying heights so as to ascertain the differential rod worth.

## A.5 Reactivity Coefficient Configurations

Reactivity coefficient measurements have not been evaluated.

## A.6 Kinetics Parameter Configurations

Kinetics measurements have not been evaluated.

## A.7 Reaction-Rate Configurations

*MCNP5 Input Deck for the axial neutron fission reaction rate in the instrumentation columns of the HTTR:*

The input deck used to determine the axial reaction rate in the instrumentation columns is that of the critical configuration with the following appended coding to the end of the input deck:

```
c --- Tally Cards ------------------------------------------------------------
c ------ Plutonium Foil in Fission Chamber ------
m101 92235.00c 1.
c
fmesh4:n geom cyl origin 114.6005 72.4 -261
         imesh 6.15 jmesh 522 jints 522 kmesh 1
fm4  (1 101 -6)
fmesh14:n geom cyl origin 5.4 -135.447 -261
          imesh 6.15 jmesh 522 jints 522 kmesh 1
```

```
fm14 (1 101 -6)
fmesh24:n geom cyl origin -120 63.04693 -261
          imesh 6.15 jmesh 522 jints 522 kmesh 1
fm24 (1 101 -6)
c
```

## A.8 Power Distribution Configuration

Power distribution measurements were not made.

## A.9 Isotopic Configurations

Isotopic measurements were not made.

## A.10 Configurations of Other Miscellaneous Types of Measurements

Other miscellaneous types of measurements were not made.

# APPENDIX B: CALCULATED SPECTRAL DATA

## B.1 Spectral Data for the Critical and Subcritical Configurations

Data generated in the MCNP5 output files include information regarding the energy of the average lethargy causing fission (EALF) and the percentages of fission caused by thermal, intermediate, and fast energy neutrons for each case shown in Table 4.1; results are shown in Table B.1 for the critical configuration. There was no significant difference between libraries in the spectra. It should be noted, that cases without cross section data to account for the upscatter of thermal neutrons have EALF values approximately 20% smaller. The MCNP5 calculations were performed with 1,050 generations (skipping the first 50) and 50,000 neutrons per generation. The JENDL-3.3 analysis was performed with the inclusion of ENDF/B-VII.0 thermal neutron scattering data because it was not included in the JENDL-3.3 library.

The spectral data for the subcritical configuration of the fully-loaded core is in Table B.2. The warm critical configuration has not been evaluated. Unfortunately, this data does not represent a valid benchmark experiment (see Section 2.1.9).

Table B.1. Spectral Data for the HTTR Benchmark Model Evaluation of the Fully-Loaded Core Critical.

| Neutron Cross-Section Library | EALF (eV) | Percentage of Neutrons Causing Fission | | |
|---|---|---|---|---|
| | | <0.625 eV | 0.625 eV – 100 keV | >100 keV |
| ENDF/B-V.2 | 0.0802 | 92.18 | 6.91 | 0.91 |
| ENDF/B-VI.8 | 0.0783 | 92.36 | 6.74 | 0.90 |
| END/B-VII.0 | 0.0784 | 92.36 | 6.73 | 0.91 |
| JEFF-3.1 | 0.0779 | 92.37 | 6.73 | 0.90 |
| JENDL-3.3 with ENDF/B-VI.8 S(α,β) | 0.0787 | 92.34 | 6.75 | 0.91 |

Table B.2. Spectral Data for the HTTR Benchmark Model Evaluation of the Subcritical Core.

| Neutron Cross-Section Library | EALF (eV) | Percentage of Neutrons Causing Fission | | |
|---|---|---|---|---|
| | | <0.625 eV | 0.625 eV – 100 keV | >100 keV |
| ENDF/B-V.2 | 0.1472 | 86.37 | 12.19 | 1.44 |
| ENDF/B-VI.8 | 0.1432 | 86.64 | 11.93 | 1.43 |
| END/B-VII.0 | 0.1444 | 86.58 | 11.98 | 1.44 |
| JEFF-3.1 | 0.1425 | 86.67 | 11.91 | 1.42 |
| JENDL-3.3 with ENDF/B-VI.8 S(α,β) | 0.1448 | 86.56 | 11.99 | 1.45 |

# APPENDIX C: DATA FROM THE 16TH EDITION CHART OF THE NUCLIDES[a]

## C.1 Isotopic Abundances and Atomic Weights

This evaluation incorporated atomic weights and isotopic abundances found in the 16th edition of the Chart of the Nuclides. A list of the values used in the benchmark model or in the generation of the MCNP input deck is compiled in Table C.1.

Table C.1. Summary of Data Employed from the 16th Ed. of the Chart of the Nuclides.

| Isotope or | Atomic | Isotopic |
|---|---|---|
| He | 4.002602 | -- |
| $^{3}$He | -- | 0.000137 |
| $^{4}$He | -- | 99.999863 |
| $^{10}$B | 10.0129370 | 19.9 |
| $^{11}$B | 11.0093055 | 80.1 |
| C | 12.0107 | -- |
| N | 14.0067 | -- |
| $^{14}$N | -- | 99.632 |
| $^{15}$N | -- | 0.368 |
| O | 15.9994 | -- |
| $^{16}$O | -- | 99.757 |
| $^{17}$O | -- | 0.038 |
| $^{18}$O$^{(a)}$ | -- | 0.205 |
| Na | 22.989770 | -- |
| Al | 26.981538 | -- |
| Si | 28.0855 | -- |
| $^{28}$Si | -- | 92.2297 |
| $^{29}$Si | -- | 4.6832 |
| $^{30}$Si | -- | 3.0872 |
| P | 30.973761 | -- |
| S | 32.065 | -- |
| $^{32}$S | -- | 94.93 |
| $^{33}$S | -- | 0.76 |
| $^{34}$S | -- | 4.29 |
| $^{36}$S | -- | 0.02 |
| Ca | 40.078 | -- |

[a] Nuclides and Isotopes: Chart of the Nuclides, 16th edition, (2002).

Table C.1 (cont'd.). Summary of Data Employed from the 16th Ed. of the Chart of the Nuclides.

| Isotope or Element | Atomic Weight | Isotopic Abundance |
|---|---|---|
| $^{40}$Ca | -- | 96.941 |
| $^{42}$Ca | -- | 0.647 |
| $^{43}$Ca | -- | 0.135 |
| $^{44}$Ca | -- | 2.086 |
| $^{46}$Ca | -- | 0.004 |
| $^{48}$Ca | -- | 0.187 |
| Ti | 47.867 | -- |
| $^{46}$Ti | -- | 8.25 |
| $^{47}$Ti | -- | 7.44 |
| $^{48}$Ti | -- | 73.72 |
| $^{49}$Ti | -- | 5.41 |
| $^{50}$Ti | -- | 5.18 |
| Cr | 51.9961 | -- |
| $^{50}$Cr | -- | 4.345 |
| $^{52}$Cr | -- | 83.789 |
| $^{53}$Cr | -- | 9.501 |
| $^{54}$Cr | -- | 2.365 |
| Mn | 54.938049 | -- |
| Fe | 55.845 | -- |
| $^{54}$Fe | -- | 5.845 |
| $^{56}$Fe | -- | 91.754 |
| $^{57}$Fe | -- | 2.119 |
| $^{58}$Fe | -- | 0.282 |
| Ni | 58.6934 | -- |
| $^{58}$Ni | -- | 68.0769 |
| $^{60}$Ni | -- | 26.2231 |
| $^{61}$Ni | -- | 1.1399 |
| $^{62}$Ni | -- | 3.6345 |
| $^{64}$Ni | -- | 0.9256 |
| Cu | 63.546 | -- |
| $^{63}$Cu | -- | 69.17 |
| $^{65}$Cu | -- | 30.83 |

Table C.1 (cont'd.). Summary of Data Employed from the 16th Ed. of the Chart of the Nuclides.

| Isotope or Element | Atomic Weight | Isotopic Abundance |
|---|---|---|
| $^{234}$U | 234.040946 | 0.0055[(b)] |
| $^{235}$U | 235.043923 | 0.7200[(b)] |
| $^{238}$U | 238.050783 | 99.2745[(b)] |

(a) Neutronically, $^{18}$O is treated as $^{16}$O.
(b) Natural isotopic abundance of U.

# APPENDIX D: ANALYSIS OF DIFFERENTIAL CONTROL ROD WORTH MEASUREMENTS

## D.1 Differential Worth Measurements for the Center Control Rod

The fully-loaded critical configuration benchmark model of the HTTR was used to computationally assess the differential worth of the center control rod pair. The vertical position of the control rod was varied while maintaining all other aspects of the input deck constant. Eigenvalues were computed and then compared between adjacent data points to ascertain an approximate differential reactivity as a function of control rod position. Calculated results are shown in Table D.1 and Figure D.1. Unfortunately, the calculated results are approximately 2.5 times greater than the reported experimental measurements (see Figure D.2).

A second analysis was performed moving a single control rod of the center pair. Results are shown in Table D.2 and Figure D.3 with a comparison to the reported experimental values in Figure D.4. Unfortunately, the calculated results are approximately 1.6 times greater than the experimental values.

It is unclear what is causing the discrepancy between calculated and experimental values; further evaluation is necessary before benchmark values can be established. It is most likely that knowledge of the worths and positions of the other control rods during these differential control worth measurements will be needed for a more direct analysis.

Table D.1. Calculated Differential Center Control Rod Worth for the Fully-Loaded Core.

| Height (mm) | Rod Worth ($\times 10^{-3}$ % $\Delta$k/k-mm) | | |
|---|---|---|---|
| 3500 | -0.02 | ± | 0.02 |
| 3000 | 0.05 | ± | 0.02 |
| 2500 | 0.31 | ± | 0.02 |
| 2200 | 0.57 | ± | 0.03 |
| 1900 | 0.97 | ± | 0.08 |
| 1800 | 1.43 | ± | 0.08 |
| 1700 | 1.84 | ± | 0.08 |
| 1600 | 1.99 | ± | 0.08 |
| 1500 | 2.36 | ± | 0.08 |
| 1400 | 2.78 | ± | 0.08 |
| 1300 | 2.95 | ± | 0.09 |
| 1200 | 3.14 | ± | 0.08 |
| 1100 | 3.35 | ± | 0.08 |
| 1000 | 3.51 | ± | 0.08 |
| 900 | 3.56 | ± | 0.08 |
| 800 | 3.43 | ± | 0.09 |
| 700 | 3.29 | ± | 0.08 |
| 600 | 3.21 | ± | 0.09 |
| 500 | 2.99 | ± | 0.08 |
| 400 | 2.62 | ± | 0.08 |
| 300 | 2.33 | ± | 0.08 |
| 200 | 1.74 | ± | 0.08 |
| 100 | 1.27 | ± | 0.08 |
| 20 | 1.06 | ± | 0.11 |

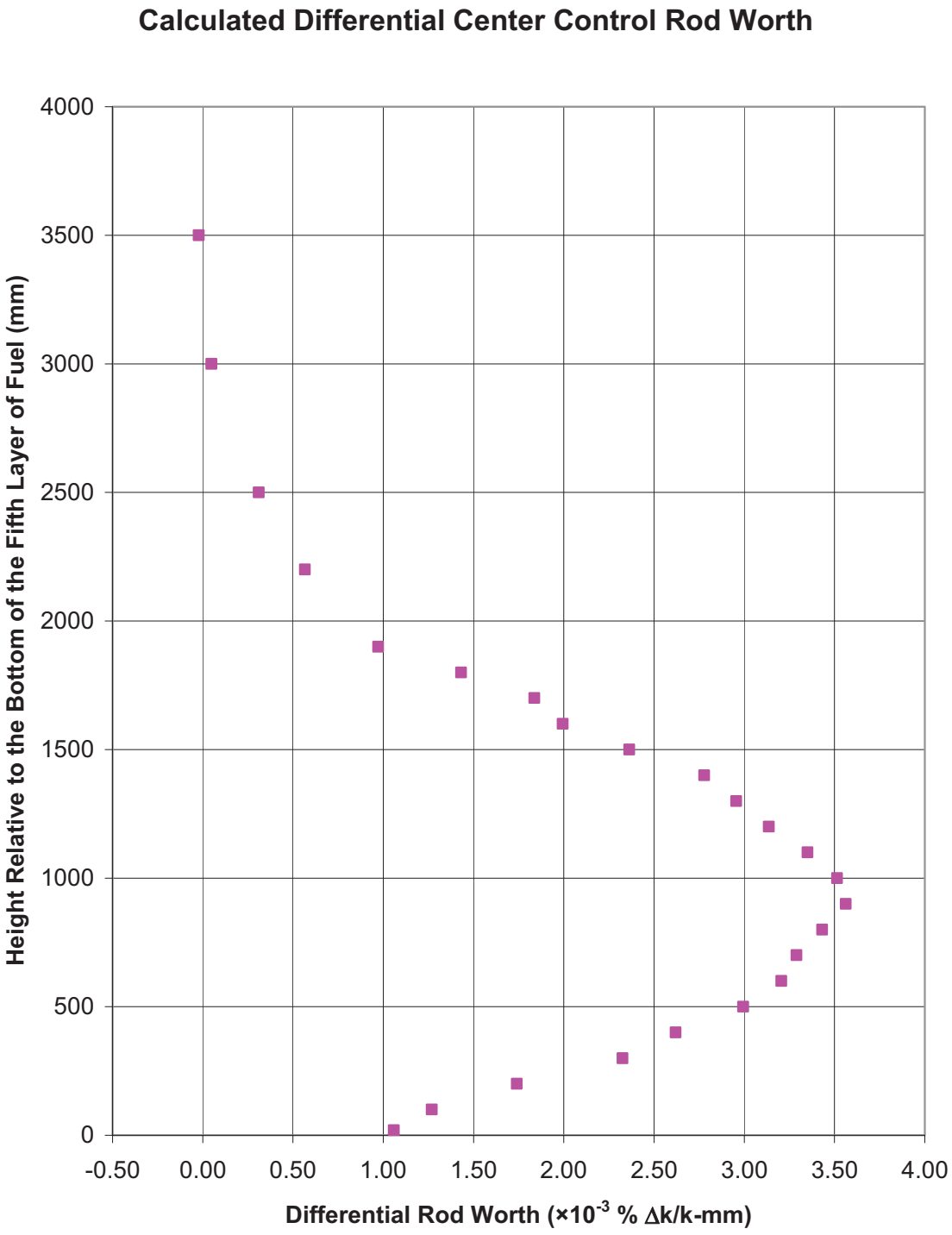


Figure D.1. Calculated Differential Center Control Rod Worth Chart for the Fully-Loaded Core.

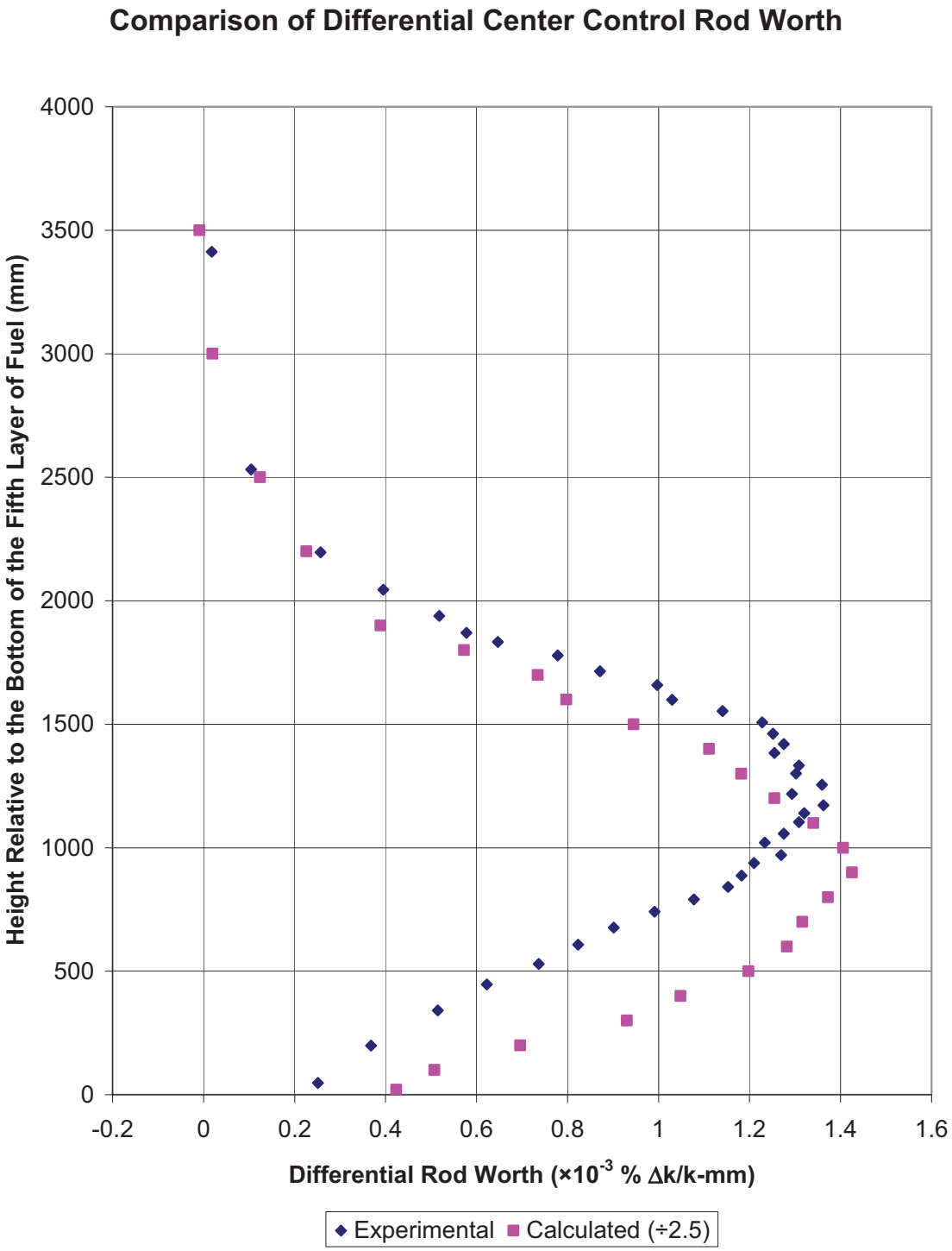


Figure D.2. Comparison of Experimental and Calculated Differential Center Control Rod Worth.

Table D.2. Calculated Differential Center Control Rod Worth for a Single Rod.

| Height (mm) | Rod Worth ($\times 10^{-3}$ % $\Delta$k/k-mm) | | |
|---|---|---|---|
| 3500 | 0.03 | ± | 0.01 |
| 3000 | 0.04 | ± | 0.01 |
| 2500 | 0.16 | ± | 0.01 |
| 2200 | 0.31 | ± | 0.02 |
| 1900 | 0.74 | ± | 0.05 |
| 1800 | 0.92 | ± | 0.05 |
| 1700 | 1.01 | ± | 0.05 |
| 1600 | 1.26 | ± | 0.05 |
| 1500 | 1.50 | ± | 0.05 |
| 1400 | 1.76 | ± | 0.05 |
| 1300 | 1.96 | ± | 0.05 |
| 1200 | 2.05 | ± | 0.05 |
| 1100 | 2.04 | ± | 0.06 |
| 1000 | 2.08 | ± | 0.06 |
| 900 | 2.24 | ± | 0.06 |
| 800 | 2.12 | ± | 0.06 |
| 700 | 2.05 | ± | 0.06 |
| 600 | 2.07 | ± | 0.06 |
| 500 | 1.85 | ± | 0.06 |
| 400 | 1.68 | ± | 0.06 |
| 300 | 1.53 | ± | 0.06 |
| 200 | 1.20 | ± | 0.06 |
| 100 | 0.94 | ± | 0.06 |
| 20 | 0.75 | ± | 0.07 |

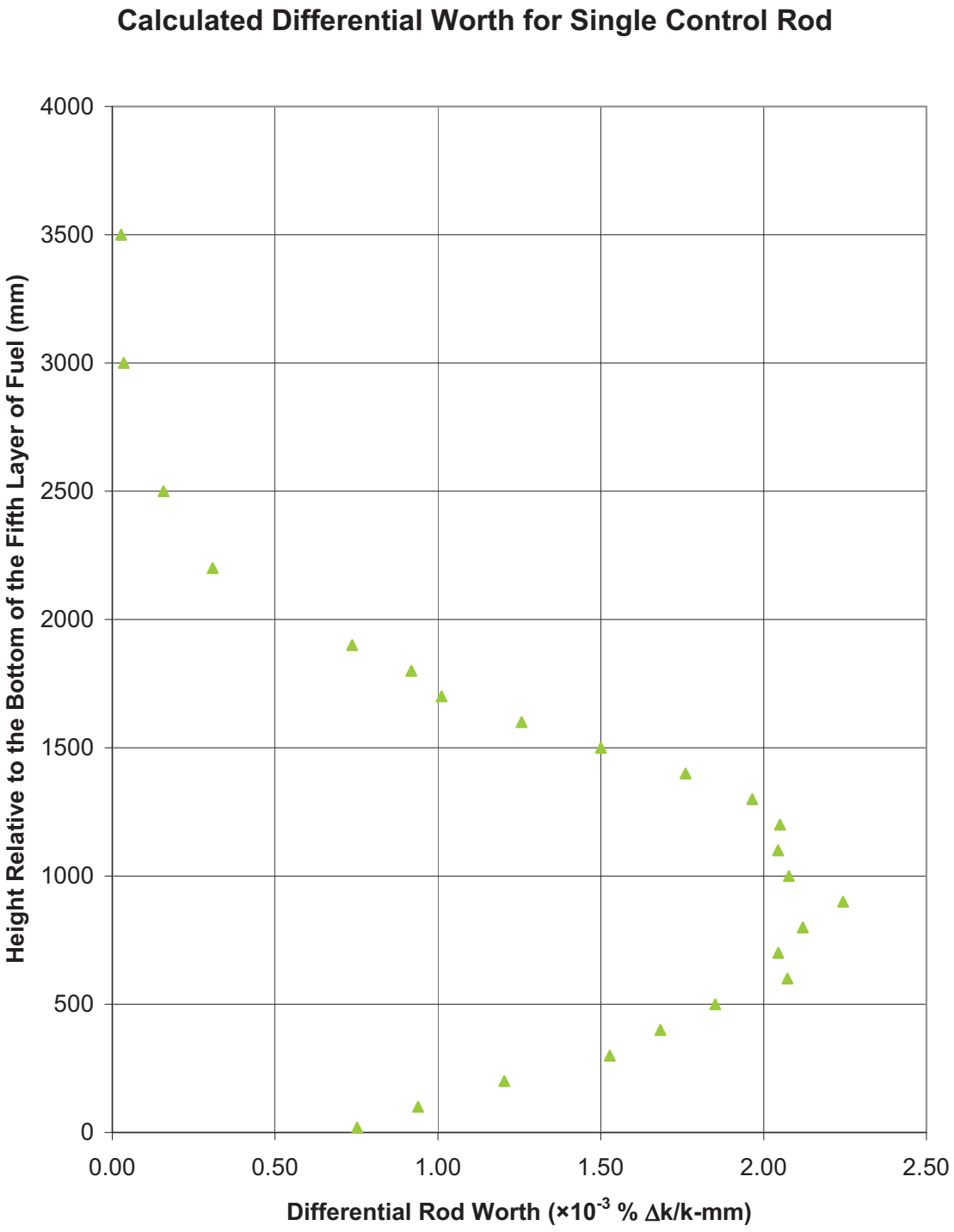


Figure D.3. Calculated Differential Center Control Rod Worth Chart for a Single Rod.

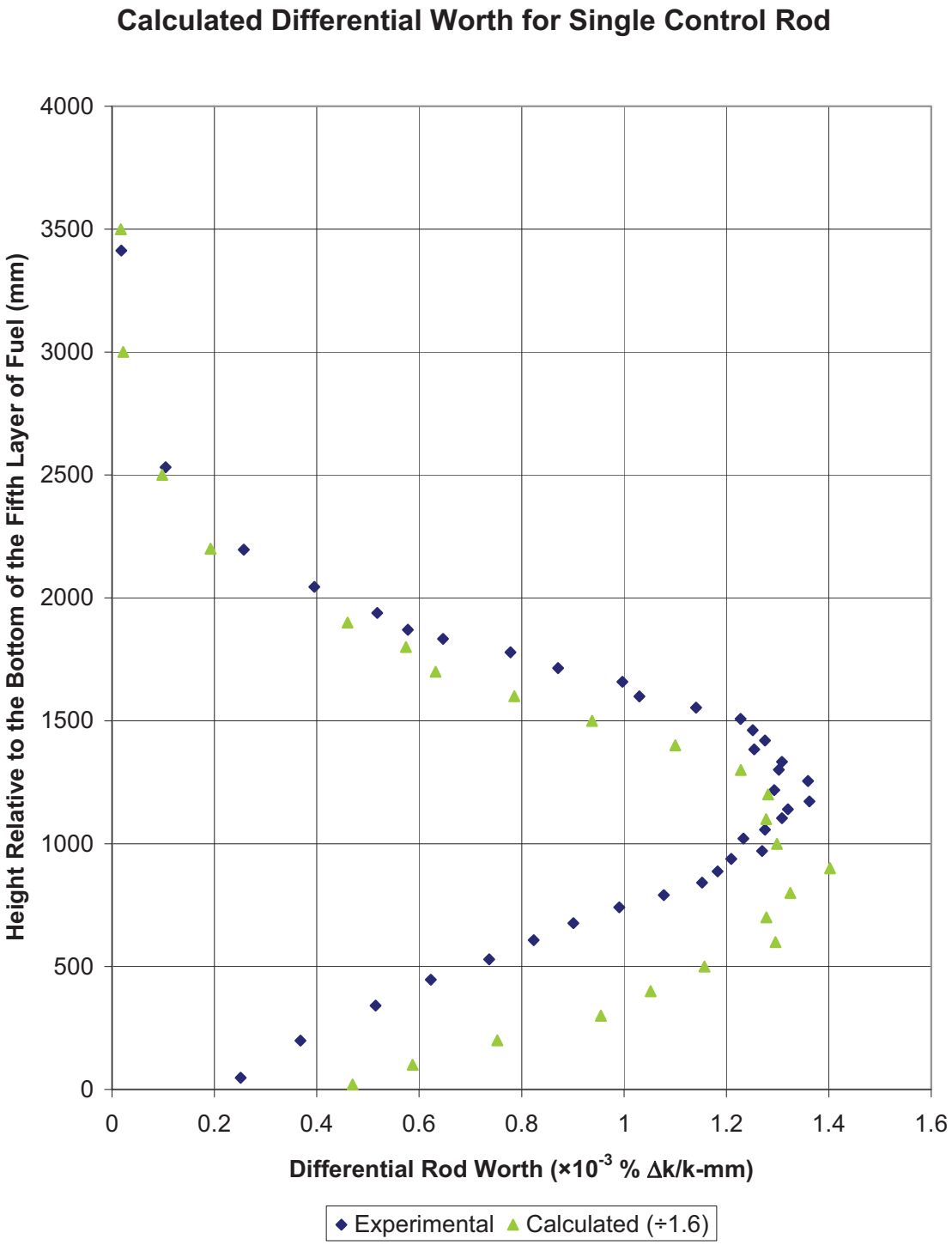


Figure D.4. Comparison of Experimental Rod Worth to Calculated Worth of a Single Rod.